



**University of
Nottingham**

UK | CHINA | MALAYSIA

**Development of An Electrical Impedance Tomography
System for Imaging and Measurement Applications**

Abdalla Mohamed Ahmed Mahmoud Salama

014198

Department of Electrical and Electronic Engineering

A thesis submitted to the University of Nottingham for the degree of

Master of Philosophy (MPhil)

Abstract

Electrical impedance tomography (EIT) is a non-invasive imaging technique that reconstructs the internal conductivity distribution of a medium using voltage or current measurements obtained via electrodes. Despite its potential, conventional EIT systems face challenges such as hardware complexity, high computational demands, and limited adaptability for diverse applications. This research addresses these limitations by developing a novel EIT system, termed Single-Ended Electrical Impedance Tomography (SEEIT), which introduces significant advancements in both hardware design and measurement methodology.

The SEEIT system's primary innovation lies in its unique electrode configuration and measurement approach, which reduces the number of required channels by 50% compared to traditional EIT systems. Unlike conventional systems that rely on differential signaling, SEEIT employs a simplified single-ended signaling method, where only one stationary electrode acts as the receiver for each measurement. This design minimizes hardware complexity and reduces the number of computations required for image reconstruction, thereby improving efficiency and reducing data errors. Additionally, the system incorporates custom-designed titanium alloy electrodes, which enhance durability and signal quality, addressing a critical limitation of existing EIT systems.

Experimental evaluations were conducted using cylindrical tanks equipped with 16 electrodes to assess the SEEIT system's ability to detect, locate, and reconstruct images of hidden objects. Results demonstrated that the system can detect objects as small as 1.5 mm in diameter within a tank of 134 mm diameter, achieving a spatial resolution of approximately 1.1% of the tank diameter. Furthermore, the system successfully reconstructed images of multiple non-conductive object shapes, showcasing its capability for accurate spatial mapping. Stability tests confirmed robust performance, with continuous data acquisition maintained over a one-hour period without degradation in signal quality.

To enhance flexibility and adaptability, a programmable LabVIEW interface was developed, enabling the SEEIT system to be easily customized for diverse applications without requiring hardware redesign. This feature significantly reduces costs and

accelerates deployment across different use cases. MATLAB, integrated with the open-source Electrical Impedance and Diffuse Optical Tomography Reconstruction Software (EIDORS) toolbox, was utilized for 2D image reconstruction based on processed data from LabVIEW.

The key contributions of this research include: (1) the development of a novel electrode configuration and measurement methodology that simplifies hardware requirements while maintaining high accuracy; (2) the demonstration of enhanced detection capabilities, including the ability to identify small objects and reconstruct non-conductive shapes; and (3) the creation of a flexible, cost-effective system adaptable to various industrial and biomedical applications. These advancements address critical gaps in current EIT technology and contribute to the broader body of knowledge by providing a more efficient and reliable solution for real-world challenges.

Acknowledgement

From the very depths of my soul, I want to begin by expressing my heartfelt gratitude to my supervisor, Dr. S. Anandan Shanmugam. Your unwavering guidance, compassion, and inspiration have been the backbone of this journey. You've not only been a mentor but also a source of light during moments when I felt lost in the shadows of self-doubt. From the bottom of my heart, thank you for believing in me, even when I struggled to believe in myself. If there were ever times when I caused you discomfort or frustration, please know it was never intentional—I deeply regret any pain I may have caused.

This research journey has been one of the most emotionally taxing experiences of my life. It came with sleepless nights, endless challenges, and moments where frustration seemed insurmountable. Yet, through it all, there were glimmers of hope—trust from those who believed in me, encouragement from voices that reminded me why I started. To everyone who stood by me, offered their support, or simply said a kind word: I owe you more than words can convey. Because of your kindness and belief, I've been able to push forward, and I hope that my work will somehow make others' lives just a little bit easier.

To my parents, Victoria and Mohammed—you are my first teachers, my greatest supporters, and the foundation upon which I stand. Thank you for every sacrifice you made to ensure I had the opportunities I needed. I am eternally grateful for your financial and emotional support, but my heart breaks as I reflect on the moments I wasn't there for you. When you faced critical health struggles, when you endured the pain of losing loved ones—I wasn't present. Mom, Dad, I am so incredibly sorry for failing you during those times when you needed me most. Please forgive me for not being the son you deserved.

And to my wife, my dearest companion—how do I even begin to thank you? You’ve been my rock, my safe haven, and the person who has loved me unconditionally despite my flaws. But I failed you too. There were moments when you needed me, and I wasn’t there. Life pulled me in different directions, but no excuse can justify my absence. My love, I am profoundly sorry for letting you down. Thank you for standing by me, even when I didn’t deserve it. You are my everything, and I vow to be better for you.

To my children—you are my greatest blessings, my reason to keep going when the weight of the world feels too heavy. Watching you grow, seeing your smiles, and hearing your laughter remind me of what truly matters in life. I want to thank you for your patience, for understanding when I couldn’t always be there, and for loving me even when I was consumed by this journey. I offer you my deepest apologies for the moments I missed, the bedtime stories left untold, or the hugs that weren’t given soon enough. You mean the world to me, and I promise to cherish every moment with you moving forward.

If there is anyone else I’ve hurt, knowingly or unknowingly, I humbly ask for your forgiveness. It was never my intention to cause pain—I am human, and I make mistakes. But I am learning, growing, and striving to be someone who deserves the love and trust you’ve given me. To everyone who has touched my life in some way, I wish you nothing but boundless happiness, radiant health, and a future filled with peace and joy.

Finally, I bow my head in gratitude to Almighty God. Thank You for seeing me through this journey, for blessing me with strength when I thought I had none left, and for surrounding me with people who loved and supported me. Everything I am and everything I have achieved is because of Your grace.

Table of Contents

Abstract.....	I
Acknowledgement	III
Table of Contents.....	V
List of Figures	IX
List of Tables	XIV
List of Abbreviations	XVII
List of publications	XIX
1 Chapter 1 Introduction	1
1.1 Research background.....	1
1.1.1 Problem statement and research motivation.....	2
1.2 Aims and objectives	3
1.3 Scopes and limitation.....	4
1.4 Thesis Organisation.....	7
2 Chapter 2 Literature Review	9
2.1 Electromagnetic tomography	9
2.1.1 Electrical capacitance tomography.....	10
2.1.2 Magnetic induction tomography	10
2.1.3 Electrical impedance tomography	11
2.2 Electrical impedance tomography (EIT) measurement strategies.....	13
2.2.1 Adjacent measurement strategy	13
2.2.2 Opposite measurement strategy	14
2.2.3 Cross measurement strategy	15
2.3 Literature Review	16
2.3.1 Image reconstruction using voltage-current system in electrical impedance tomography.....	16
2.3.2 A 4.9 m Ω -sensitivity mobile electrical impedance tomography ic for early breast-cancer detection system	18
2.3.3 Multi-frequency electrical impedance tomography system with automatic self-calibration for long-term monitoring.....	18
2.3.4 Code-division-multiplexing using orthogonal codes for fast electrical impedance tomography.....	19
2.3.5 Use of electrical impedance tomography to monitor regional cerebral edema during clinical dehydration treatment.....	20
2.3.6 System description and first application of an FPGA-based simultaneous multi-frequency electrical impedance tomography	21

2.3.7	Localized electrical impedance Myography of the biceps brachii muscle during different levels of isometric contraction and fatigue	22
2.3.8	Adaptive techniques in electrical impedance tomography reconstruction	23
2.3.9	A deformable smart skin for continuous sensing based on electrical impedance tomography.....	24
2.3.10	A FPGA-based broadband EIT system for complex bioimpedance measurements—design and performance estimation.....	25
2.3.11	Electrical impedance tomography (EIT) system for radiation-free medical imaging based on LabVIEW.....	26
2.3.12	A local region of interest imaging method for electrical impedance tomography with internal electrodes.....	27
2.4	Comparison of recent EIT based imaging systems	31
Table 2.1: The recent EIT system feature.		31
2.5	Electrical impedance tomography image reconstruction theory	32
2.5.1	Forward problem	34
2.5.2	Inverse problem.....	35
2.6	EIT reconstruction algorithms.....	36
2.6.1	GREIT.....	36
2.6.2	Modified newton-raphson method	37
2.6.3	Finite element method	37
2.6.4	Jacobian matrix	38
2.6.5	Linear back projection.....	38
2.6.6	D-bar	38
2.7	Electrode arrays and signaling methods.....	39
2.8	Image reconstruction methods.....	39
3	Chapter 3 Methodology.....	40
3.1	Electrical impedance tomography system.....	41
3.1.1	Electrical impedance tomography system software.....	42
3.1.1.1	Indirect LabVIEW program.....	42
3.1.1.2	Direct LabVIEW program.....	48
3.1.1.2.1	The function of the program	48
3.1.1.2.2	Front panel description	49
3.1.1.2.3	User interface.....	50
3.1.1.2.4	“Settings & Results” tab	50
3.1.1.2.5	Software architecture.....	53
3.1.1.2.6	State transition diagram of the program	55
3.1.1.3	Measurement methods	57

3.2	Electrical impedance tomography system hardware	68
3.2.1	EIT hardware block diagram	70
3.2.1.1	16-Electrode Array	70
3.2.1.2	I/O Signal Switching Box.....	71
3.2.1.3	BNC-terminal-shielded connector blocks	73
3.2.1.4	Multifunction Data Acquisition NI PCI-6281 Unit	74
3.2.1.5	Host PC.....	75
3.2.2	Electrodes	76
3.2.3	Relay.....	78
3.1.3	Current EIT system advantages and disadvantages.....	79
4	Chapter 4 Measurements and injection signalling	82
4.1	Differential signalling	82
4.2	Single-ended signalling	93
4.2.1	Measurements of single-ended signaling	93
4.2.1.1	Measurements of single-ended signaling without using the switching box	93
4.2.1.2	Measurements of single-ended signaling using switching box.....	97
4.2.2	Comparison of measurements of single-ended signalling with and without using switching box.....	100
4.3	Conclusion.....	103
5	Chapter 5 Single-ended electrical impedance tomography (SEEIT) system	105
5.1	System architecture of the SEEIT system.....	106
5.2	SEEIT system hardware and software.....	107
5.3	Results and discussion	110
6	Chapter 6 A novel measurement technique using single-ended signalling for electrical impedance tomography (SEEIT).....	123
6.1	Principle of measurement.....	123
6.2	Data collection	125
6.3	Results and discussion	126
	Test 1:.....	126
	Test 2:.....	127
	Test 3:.....	128
6.4	Conclusion.....	135
7	Chapter 7 Application of SEEIT.....	136
7.1	Data collection	138
7.2	Results and discussion	139

7.2.1	Tap water detection test using the SEEIT system	141
7.2.2	Muddy water detection test using SEEIT system.....	147
7.2.2.1	RMS	148
7.2.2.2	Standard deviation.....	155
7.2.2.3	Variance	161
7.2.3	Gas and tap water detection test using SEEIT system	169
7.2.4	Electrically non-conductive object shape detection test using SEEIT system	170
7.2.5	Chicken tissue chunk detection test using the SEEIT system.....	173
7.2.6	SEEIT system stability test.....	174
7.3	Conclusion.....	188
8	Chapter 8 Conclusion and Future Work.....	189
8.1	Conclusion.....	189
8.2	Future work.....	190
9	Bibliography	192
10	Appendix A.....	209
11	Appendix B	227

List of Figures

Figure 1.1: The key chart of the research.....	6
Figure 1.2: Overall flowchart of the research	8
Figure 2.1: X-ray tomographic projections.....	9
Figure 2.2: Example of EIT electrode arrangements.....	11
Figure 2.3: Example of lung imaging using EIT.....	12
Figure 2.4: Generic process tomography system architecture.....	13
Figure 2.5: EIT adjacent electrode strategy.....	14
Figure 2.6: EIT opposite electrode strategy.....	15
Figure 2.7: EIT cross electrode strategy.....	16
Figure 2.8: EIT system complete measurement setup.....	17
Figure 2.9: Reconstructed images for two data collection system setups.....	17
Figure 2.10: Breast cancer detection system.....	18
Figure 2.11: KHU Mark 2.5 EIT system setup.....	19
Figure 2.12: CDM EIT system.....	20
Figure 2.13: Cerebrospinal fluid EIT system.....	21
Figure 2.14: Prototype of the mfEIT system.....	22
Figure 2.15: Actual testing of EIM system on human biceps brachii muscle.....	23
Figure 2.16: The 2D reconstruction images of the first four iterations; simulated results using MATLAB when electrically conductive and non-conductive objects were placed in the tank.....	24
Figure 2.17: (a) The developed artificial skin, using eight channels that are connected by alligator clip to the measurement system. (b) Possible application scenario attached over a dummy doll arm.....	25
Figure 2.18: Complete measurement setup for FPGA-based EIT.....	26
Figure 2.19: EIT system prototype hardware.....	27
Figure 2.20: ROI EIT system.....	28
Figure 3.1: SEEIT system's linking elements are shown as a sequence in a cycle.....	42
Figure 3.2: Indirect EIT system software flowchart.....	43
Figure 3.3: Program block diagram part 1.....	44
Figure 3.4: Program block diagram part 2.....	45
Figure 3.5: LabVIEW VI data acquisition assistant.....	45
Figure 3.6: LabVIEW VI configure simulate signal window.....	46
Figure 3.7: DAQ assistant for digital generator.....	47
Figure 3.8: LabVIEW front panel.....	47

Figure 3.9: Direct EIT system software flowchart.....	48
Figure 3.10: LabVIEW project.....	49
Figure 3.11: Front panel of application.....	49
Figure 3.12: The injection array.....	50
Figure 3.13: “Data” tab.....	51
Figure 3.14: “Graph” tab.....	51
Figure 3.15: “Injection Array” tab.....	52
Figure 3.16: “Settings” tab.....	53
Figure 3.17: Software architecture.....	54
Figure 3.18: State transition diagram of program.....	56
Figure 3.19: Flowchart of LabVIEW program adjacent measurement strategy.....	57
Figure 3.20: Full electrode injection cycle RMS measurements.....	66
Figure 3.21: Opposite measurement strategy.....	67
Figure 3.22: Random measurement strategy.....	67
Figure 3.23: Set-up of the developed EIT system.....	69
Figure 3.24: Current EIT hardware block diagram.....	70
Figure 3.25: Three different electrode arrays.....	71
Figure 3.26: Switching box component block diagram of the current EIT system.....	72
Figure 3.27: Schematic diagrams of EIT switching box.....	72
Figure 3.28: EIT system switching box PCB layout.....	73
Figure 3.29: BNC-2090A Front Panel.....	73
Figure 3.30: Blinking RGB LEDs breadboard.....	74
Figure 3.31: The Multifunction Data Acquisition Unit main parts.....	75
Figure 3.32: The host PC.....	76
Figure 3.33: Electrode design layout using AutoCAD (left); the actual electrode (right); square contact areas are 13 x 13 x 0.5 mm ³	77
Figure 3.34: A shows the top view dimensions of the testing tank; B is the top view of the actual testing tank.....	77
Figure 3.35: EIT electrode design layout using Diptrace software (left) and the testing breaker with the electrodes attached.....	78
Figure 3.36: Footprint and schematic symbol of G6K-2P.....	79
Figure 4.1: Actual location of plastic object.....	83
Figure 4.2: Actual location of object.....	83
Figure 4.3: Differential measurements which process 8 RMS measurements.....	84
Figure 4.4: Differential measurements which process 16 RMS measurements.....	84
Figure 4.5: RMS voltage of the vessel with and without object.....	86

Figure 4.6: RMS percent of total of the vessel with and without object.....	86
Figure 4.7: Zero method RMS measurements sequence.....	87
Figure 4.8: Modified RMS voltage of the vessel with and without object using the zero method.....	88
Figure 4.9: Modified RMS percent of total X1000 using the zero method.....	89
Figure 4.10: The 2D reconstructed image with (B) and without (A) object using modified results from zero method.....	89
Figure 4.11: Average method RMS measurements sequence.....	90
Figure 4.12: Modified RMS voltage of the vessel with and without object using the average method.....	91
Figure 4.13: Modified RMS change difference of the vessel with and without object using the average method....	92
Figure 4.14: The 2D reconstructed image with (B) and without (A) object using modified results from average method.....	92
Figure 4.15: Schematic diagram of resistor network circuit without using switching box.....	94
Figure 4.16: Schematic diagram of resistor network circuit with added 1k Ω resistor without using switching box.....	94
Figure 4.17: RMS voltage of 16-Channel resistor network; simulated measurements without using switching box.....	95
Figure 4.18: RMS voltage of 16-channels resistor network, simulated measurements.....	96
Figure 4.19: RMS voltage difference of 16-channels resistor network, simulated measurements.....	96
Figure 4.20: Schematic diagram of resistor network circuit using switching box.....	97
Figure 4.21: Schematic diagram of resistor network circuit with 1k Ω resistor added, using switching box.....	97
Figure 4.22: RMS voltage of 16-channels resistor network; simulated measurements using switching box.....	98
Figure 4.23: RMS voltage of 16-channels resistor network comparison with and without 1k Ω resistor; simulated measurements using switching box.....	99
Figure 4.24: RMS voltage difference of 16-channels resistor network; simulated measurements using switching box.....	99
Figure 4.25: The 2D reconstructed image with added 1k Ω resistor using switching box.....	100
Figure 4.26: Comparison of RMS voltage measurements of 16-channels resistor network using SB and NSB...	102
Figure 4.27: RMS voltage difference of 16- channels resistor network using SB and NSB.....	103
Figure 5.1: SEEIT system architecture.....	107
Figure 5.2: SEEIT hardware block diagram consists of a four-part testing vessel, switching box, data acquisition (DAQ) system, and operating program.....	108
Figure 5.3: SEEIT system LabVIEW program: a) Controller panel of the analogue input and output, and b) Program block diagram of the SEEIT system.....	109
Figure 6.1: Simplified block diagram of the proposed electrical impedance measurement system.....	124
Figure 6.2: (a) Photograph of real resistor network circuit with 16 channels; (b) basic scheme of the resistor network circuit with 16 channels.....	124
Figure 6.3 (a) The proposed measurement strategy flowchart and (b) Impedance data collection for complete steps of procedure is clarified.....	125

Figure 6.4: Homogeneous Root Mean Square data (RMSHD) and the data when a 1-k Ω resistor is added to Channel 2, Channel 7, and Channel 12.....	127
Figure 6.5: RMSHD and the data when a 1-k Ω resistor is added to Channel 2, Channel 7, and Channel 12.....	128
Figure 6.6: RMSHD and data when 1-k Ω , 2-k Ω , and 3-k Ω resistors are added to Channel 2, Channel 7, and Channel 12.....	129
Figure 6.7: RMSHD and data when 1-k Ω , 2-k Ω , and 3-k Ω resistors are attached to Channels 8, 10, and 12 at the same time.....	129
Figure 6.8: RMSHD and data when 1-k Ω , 2-k Ω , and 3-k Ω resistors are attached to Channels 8, 10, and 12 at the same time.....	130
Figure 6.9: RMS voltage difference when there is no object and when there is a non-conductive object in the centre of the vessel.....	131
Figure 6.10: Non-conductive object in the centre of the testing beaker (top view).....	131
Figure 6.11: RMS voltage difference when there is no object and when there is a non-conductive object near Channels 3, 4, and 5 of the testing beaker.....	132
Figure 6.12: Non-conductive object near Channels 3, 4, and 5 in the testing beaker (real location).....	132
Figure 6.13: RMS voltage difference when there is no object and when there is a non-conductive object near Channels 8, 9, and 10.....	133
Figure 6.14: Non-conductive object near Channels 8, 9, and 10 in the testing beaker (top view).....	133
Figure 6.15: RMS voltage difference when there is no object and when there is a non-conductive object near Channels 11, 12, and 13.....	134
Figure 6.16: Non-conductive object near Channels 11, 12, and 13 in the testing beaker (top view).....	134
Figure 6.17: Connectivity measurements different estimation object coordination based on the obtained measurements results. (a) The object in the centre. (b) The object near channels 3, 4, and 5. (c) The object near channels 8, 9, and 10. (d) Object near channels 11, 12, and 13.....	135
Figure 7.1: Flowchart of the stages of the process for the programmable SEEIT system.....	139
Figure 7.2: Channel configuration and signal generator configuration controls.....	140
Figure 7.3: A. Chicken skin and fat location in the vessel filled with raw chicken breast chunks. B. 2-D reconstructed image of the chicken skin and fat.....	174
Figure 7.4: The reconstructed images of the electrically non-conductive object with a diameter of 14 mm using two types of measurement results.....	178
Figure 7.5: The reconstructed images of the electrically non-conductive object with a diameter of 25 mm using two types of measurement results.....	179
Figure 7.6: The reconstructed images of the electrically non-conductive object with a diameter of 5 mm using two types of measurement results.....	180
Figure 7.7: The reconstructed image of the electrically non-conductive object shape, made of Styrofoam (circle shape).....	181
Figure 7.8: The reconstructed image of the electrically non-conductive object shape, made of Styrofoam (large rectangular shape).....	181
Figure 7.9: The reconstructed image of the electrically non-conductive object shape, made of Styrofoam (small rectangular shape).....	182

Figure 7.10: The reconstructed image of the electrically non-conductive object shape, made of Styrofoam (large triangle shape).....	182
Figure 7.11: The reconstructed image of the electrically non-conductive object shape, made of Styrofoam (small triangle shape).....	183
Figure 7.12: The reconstructed image of the electrically non-conductive object shape, made of Styrofoam (L shape shape).....	183
Figure 7.13: The reconstructed image of the electrically non-conductive object shape, made of Styrofoam (C shape shape).....	184
Figure 7.14: The reconstructed images of the electrically non-conductive object shape, made of Styrofoam (E shape shape).....	184
Figure 7.15: The reconstructed image of the electrically conductive object with a diameter of 1.5 mm.....	185
Figure 7.16: The reconstructed images of the electrically non-conductive object with a diameter of 2 mm.....	185
Figure 7.17: The reconstructed image of the gas bubble during gas has been pumped around electrodes 15, 16, 1, and 2 (Sample 1).....	186
Figure 7.18: The reconstructed image of the gas bubble during gas has been pumped around electrodes 15, 16, 1, and 2 (Sample 2).....	186
Figure 7.19: The reconstructed image of the gas bubble during gas has been pumped around electrodes 15, 16, 1, and 2 (Sample 3).....	187
Figure 7.20: Left side Chicken skin and fat location in the tank filled with raw chicken breast chunks. Right side image reconstructed of the chicken skin and fat.....	187

List of Tables

Table 2.1: The recent EIT system feature.....	31
Table 2.2: A selection of EIT system applications in industrial and medical arenas.....	33
Table 3.1: Full Electrode Injection Cycle Based on Adjacent Measurement Strategy.....	58
Table 3.2: Some of EIT system advantages and disadvantages.....	79
Table 3.3: Recent EIT systems and comparison with exiting EIT system.....	81
Table 4.1: Measurement results of differential voltage using adjacent measurement strategy.....	85
Table 4.2: Modified measurement results of differential voltage using adjacent measurement strategy and zero method.....	87
Table 4.3: Measurements of differential voltage with the average of RMS using the adjacent measurement strategy and average method.....	90
Table 4.4: Measurement results of single-ended voltage using the adjacent measurement strategy without switching box.....	95
Table 4.5: Measurements of single-ended voltage using switching box and the adjacent measurement strategy.....	98
Table 4.6: Measurement results of single-ended voltage using SB and NSB.....	101
Table 5.1: Conductive objects at different positions; images for four different rod sizes using 12.5 kHz for injection frequency.....	111
Table 5.2: Conductive objects at different positions; images for four different rod sizes using 35 kHz for injection frequency.....	112
Table 5.3: Conductive objects at different positions; images for four different rod sizes using 70 kHz for injection frequency.....	113
Table 5.4: Conductive objects at different positions; images for four different rod sizes using 350 kHz for injection frequency.....	114
Table 5.5: Conductive objects at different positions; images for four different rod sizes using 1 MHz for injection frequency.....	115
Table 5.6: Non-conductive objects at different positions; images for four different rod sizes using 12.5 kHz for injection frequency.....	116
Table 5.7: Non-conductive objects at different positions; images for four different rod sizes using 35 kHz for injection frequency.....	118
Table 5.8: Non-conductive objects at different positions; images for four different rod sizes using 70 kHz for injection frequency.....	119
Table 5.9: Non-conductive objects at different positions; images for four different rod sizes using 350 kHz for injection frequency.....	120
Table 5.10: Non-conductive objects at different positions; images for four different rod sizes using 1 MHz for injection frequency.....	121
Table 7.1: Conductive objects at different positions; reconstructed images for three conductive object diameters (26 mm, 12 mm, 4 mm).....	142

Table 7.2: Conductive objects at different positions; reconstructed images for three different conductive object diameters (3 mm, 2 mm, 1.5 mm).....	144
Table 7.3: Non-conductive objects at different positions; reconstructed images for three non-conductive object diameters (25 mm, 14 mm, 7 mm).....	145
Table 7.4: Non-conductive objects at different positions; images for two non-conductive object diameters (4 mm, 2 mm).....	146
Table 7.5: Non-conductive objects at different positions; images for three different non-conductive object diameters (50 mm, 25 mm, 14 mm) with injection frequency 12.5 kHz.....	149
Table 7.6: Non-conductive objects at different positions; images of three non-conductive object diameters (50 mm, 25 mm, 14 mm) with an injection frequency of 300 kHz.....	150
Table 7.7: Non-conductive objects at different positions; images for three non-conductive object diameters (50 mm, 25 mm, 14 mm) with the injection frequency of 1000 kHz.....	151
Table 7.8: Conductive objects at different positions; reconstructed images for three conductive object diameters (50 mm, 26 mm, 12 mm) with the injection frequency of 12.5 kHz.....	152
Table 7.9: Conductive objects at different positions; reconstructed images for three conductive object diameters (50 mm, 26 mm, 12 mm) with the injection frequency of 300 kHz.....	153
Table 7.10: Conductive objects at different positions; reconstructed images for three conductive object diameters (50 mm, 26 mm, 12 mm) with the injection frequency of 1000 kHz.....	154
Table 7.11: Non-conductive objects at different positions; images for three non-conductive object diameters (50 mm, 25 mm, 14 mm) with the injection frequency of 12.5 kHz.....	155
Table 7.12: Non-conductive objects at different positions; images for three non-conductive object diameters (50 mm, 25 mm, 14 mm) with the injection frequency of 300 kHz.....	156
Table 7.13: Non-conductive objects at different positions; images for three non-conductive object diameters (50 mm, 25 mm, 14 mm) with the injection frequency of 1000 kHz.....	157
Table 7.14: Conductive objects at different positions; reconstructed images for three conductive object diameters (50 mm, 26 mm, 12 mm) with the injection frequency of 12.5 kHz.....	158
Table 7.15: Conductive objects at different positions; reconstructed images for three conductive object diameters (50 mm, 26 mm, 12 mm) with the injection frequency of 300 kHz.....	159
Table 7.16: Conductive objects at different positions; reconstructed images for three conductive object diameters (50 mm, 26 mm, 12 mm) with the injection frequency of 1000 kHz.....	160
Table 7.17: Non-conductive objects at different positions; images for three non-conductive object diameters (50 mm, 25 mm, 14 mm) with the injection frequency of 12.5 kHz.....	162
Table 7.18: Non-conductive objects at different positions; images for three non-conductive object diameters (50 mm, 25 mm, 14 mm) with the injection frequency of 300 kHz.....	163
Table 7.19: Non-conductive objects at different positions; images for three non-conductive object diameters (50 mm, 25 mm, 14 mm) with the injection frequency of 1000 kHz.....	164
Table 7.20: Conductive objects at different positions; reconstructed images for three conductive object diameters (50 mm, 26 mm, 12 mm) with the injection frequency of 12.5 kHz.....	165
Table 7.21: Conductive objects at different positions; reconstructed images for three conductive object diameters (50 mm, 26 mm, 12 mm) with the injection frequency of 300 kHz.....	166

Table 7.22: Conductive objects at different positions; reconstructed images for three conductive object diameters (50 mm, 26 mm, 12 mm) with the injection frequency of 1000 kHz.....	167
Table 7.23: Air hose placed at different positions; reconstructed cross-section images for five air hose setups.....	169
Table 7.24: Non-conductive objects (Styrofoam) with different shapes; reconstructed images for different non-conductive object shapes.....	171
Table 7.25: Plastic rod object with diameter of 25 mm at different positions; reconstructed image samples using 1000 kHz as the injection frequency.....	175

List of Abbreviations

2D.....	Two-dimensional
3D.....	Three-dimensional
AC.....	Alternating Current
APT.....	Atom Probe Tomography
BEM.....	Boundary Element Method
BNC.....	British Naval Connector
BPSK.....	Binary Phase Shift Keying
CDM.....	Code Division Multiplexing
CryoET	Electron Cryotomography
CT.....	Computed Tomography
CTIS.....	Computed Tomography Imaging Spectrometer
CV.....	Current to voltage
DAQ	Data Acquisition
DDS.....	Direct Digital Synthesizers
DIP.....	Dual In-Line Package
ECT.....	Electrical Capacitance Tomography
EIDORS	Electrical Impedance and Diffuse Optical Tomography Reconstruction Software
EIM.....	Electrical Impedance Myography
EIT.....	Electrical Impedance Tomography
FDM	Finite Difference Method
FEM.....	Finite Element Method
FMRI.....	Functional Magnetic Resonance Imaging
FPGA	A Field-Programmable Gate Array
GREIT	Graz Consensus Reconstruction Algorithm
HT.....	Hydraulic Tomography
IC	Integrated Circuit
IE	Electrical Impedance
LAT.....	Laser-Aided Tomography
LBP.....	Linear Back Projection
LED	Light Emitting Diode
LSCM.....	Laser Scanning Confocal Microscopy
MFEIT.....	Multi-Frequency Electrical Impedance Tomography
MIT.....	Electromagnetic Induction
NI.....	National Instruments

NSB.....	No Switching Box
OCT.....	Optical Coherence Tomography
ODT.....	Optical Diffraction Tomography
OPT.....	Optical projection tomography
PAT.....	Photoacoustic Computed Tomography
PC.....	Personal Computer
PCB.....	Printed Circuit Board
PET.....	Positron-Emission Tomography
PET-CT.....	Positron Emission Tomography–Computed Tomography
RGB	Red, Green and Blue
RMS.....	Root Mean Square
ROI.....	Region of Interest
SB.....	Switching Box
SD.....	Standard Deviation
SEEIT.....	Single-Ended Electrical Impedance Tomography
SINAD	Signal-to-Noise and Distortion Ratio
SNR.....	Signal-to-Noise Ratio
Sonar.....	Sound Navigation and Ranging
SPECT.....	Single Photon Emission Computed Tomography
TAT.....	Thermoacoustic Tomography
TDMS	Technical Data Management Streaming
UI	User Interface
UNMC.....	University of Nottingham Malaysia Campus
V.....	Variance
VC.....	Voltage to Current
VI.....	Virtual Instrument

List of publications

A) Publications with peer review process

[1] A. Salama, A. Malekmohammadi, and S. Mohanna, “Single-Ended Electrical Impedance Tomography (SEIT),” J. Eng., no. 4, pp. 1–17, 2018.

Link < [Single-ended electrical impedance tomography | The Journal of Engineering](#)>

[2] A. Salama, A. Malekmohammadi, S. Mohanna, and R. Rajkumar, “A Multitasking Electrical Impedance Tomography System Using Titanium Alloy Electrode,” Int. J. Biomed. Imaging, vol. 2017, pp. 1–20, 2017.

Link< <https://www.ncbi.nlm.nih.gov/pubmed/29225613>>

Chapter 1 Introduction

1.1 Research background

Traditional industrial processes have long relied on point sensors, such as pressure and temperature sensors, for operational control and monitoring (Scott and McCann, 2005; Hermann, Pentek, and Otto, 2016; Herterich, Uebernickel, and Brenner, 2015). However, as industrial processes grow increasingly complex and demanding, there is a growing need for advanced visualization techniques to observe internal events within process media, such as tanks or pipes (Johansen and Wang, 2008; Wei et al., 2015; Precup et al., 2015; Metrics, 2015). For example, critical industrial measurements often include monitoring particulate shape, detecting contamination, and ensuring compliance with product standards (Scott and McCann, 2005). While sensors installed in pipes or tanks provide continuous data streams for process control, the instrumentation required for certain imaging techniques, such as ionizing radiation imaging (e.g., X-ray imaging), can be too complex, large, or hazardous for many industrial applications (Sun, Yang, and Tian, 2015).

To address these challenges, researchers are exploring non-ionizing and non-invasive imaging and monitoring techniques, such as electrical impedance tomography (EIT), electrical capacitance tomography (ECT), and electrical resistance tomography (ERT) (Rasteiro et al., 2011). These methods are particularly valuable because they do not damage or alter the original form of the object being imaged, making them suitable for both industrial and medical applications. In industrial settings, non-invasive imaging is essential for risk mitigation, process optimization, and quality control. Similarly, in medical fields, such techniques are critical for real-time monitoring and diagnostics without compromising patient safety.

Electrical impedance tomography (EIT), the focus of this research, is a promising imaging modality that reconstructs internal conductivity distributions within an object by measuring electrical potentials on its surface. This technique is advantageous due to its portability, low cost, and lack of ionizing radiation. Other related imaging methods, such as ECT and ERT, also offer unique benefits depending on the application. For instance, ECT is particularly effective for imaging dielectric materials, while ERT is well-suited for conductive media. Each of these

techniques has been developed to address specific challenges in industrial and medical process control, providing valuable feedback to enhance safety, efficiency, and product quality. By leveraging these non-invasive methods, industries can achieve more accurate and safer process control, while medical applications can benefit from real-time, risk-free monitoring and diagnostics. Moreover, chapter 2 provides an overview of electrical impedance tomography and briefly discusses similar imaging techniques, highlighting their potential applications and advantages in both industrial and medical contexts.

1.1.1 Problem statement and research motivation

In recent years, numerous electromagnetic tomography systems that image different applications were implemented, but each technology has a specific application. Some of the existing tomography techniques are producing radiation, expensive, requiring an ample operation space, and requiring high power consumption. For medical and industrial applications, there is some challenging and promising application of EIT, such as monitoring brain stroke and chemical mixing. However, the EIT problems are mainly associated with complexity, computation, accuracy, and limited scope of place where it can be used. Our current work acknowledges some of the problems and addresses a way to make the system simplified with less computational, easy to use, and, hopefully, it can be used in a multi-environment settings. If that objective is achieved, it shall serve as a cheaper, more applicable impedance measurement system in a verity of applications. This research will focus on the development of electrical impedance tomography hardware and software. Moreover, most of the EIT researchers focus on the image reconstruction algorithm, with little attention given to its hardware, signals monitoring, and data processes. This work will include hardware and signal monitoring and processing to reconstruct an image using EIDORS.

There are many reasons for utilising EIT:

- I. **Radiation free:** Using radiation imaging techniques in some industrial and medical application risk are substantial and varied. The EIT imaging it only uses very low electrical current as an injection which means the aimed object will not be subjected to the radiation field, so it considers a radiation-free imaging technique.
- II. **Non-invasive:** Non-invasive mean that the developed EIT system will not damage or contaminate the object which subjected to electrical current injection.
- III. **Continuous:** The electrical impedance tomography system non-stopping will reconstruct image slice, that makes it ideal to monitor a process.
- IV. **Fast responsiveness:** The EIT system does not require a long time to reconstruct an image or even to set up the system.
- V. **Flexibility:** EIT system is adaptable to be used in several applications.
- VI. **Low cost:** EIT system implementation and operation cost lower than some other conventional tomography technique.
- VII. **Low power consumption:** EIT system operates using low power.

1.2 Aims and objectives

The goal of monitoring and imaging using electrical impedance is to provide an image that can be used to monitor a hidden object. Specifically, the aim is to

- Design, develop, and implement a novel electrical impedance tomography (EIT) system, including both hardware and software, for imaging and monitoring hidden objects.

- Enable imaging of various materials, including both electrically conductive and non-conductive substances, as well as fundamental geometric shapes such as triangles, squares, and circles.
- Enhance object detection capabilities by developing advanced control and monitoring software for the EIT system.

The objectives were achieved by integrating hardware and software. A LabVIEW program was developed and implemented to calibrate both the hardware and software components, involving extensive laboratory experimentation.

1.3 Scopes and limitation

This study will focus on investigation, implement, and develop an electrical impedance tomography system that can track, detect, and monitor hidden objects. The aim is to design a novel EIT system that improves some of the current EIT systems in terms of both hardware and software. The developed system will be able to be used in some different testing environments like water, muddy water. Some limitations include extra-low voltage (ELV) injections and measurements on electrodes due to safety and power consumption, the frequency within the range of injecting currents between 1Hz and 10MHz, relatively inexpensive within 250000RM, the speed of image processing based on measurements resolution, host PC speed, and signals switching speed. Moreover, this work will not include EIT imaging reconstruction algorithms development or implementation. However, in this research Electrical Impedance Tomography and Diffuse Optical Tomography Reconstruction Software (EIDORS), is an image reconstruction algorithm that will be used. Figure 1.1 shows the key chart of the current research. The key chart shows different imaging tomography technique based on power consumption (low voltage and high voltage). As seen, the research focuses on low voltage tomography. The left side of the key chart shows the tomography techniques which consume high electrical power and in the middle tomography, shows unknown techniques which their power consumption not known. On the other hand, the right side shows the tomography techniques which use low electrical power, which the current work

focusses on it. To develop a tomography system collection of techniques, methods, implementation steps should be connected, as shown on the Right Side of the key chart. The developed tomography technique system in this research was electrical impedance tomography (EIT), the injecting and measuring methods single-ended then the measurements need to be obtained through sensors (Electrode Array). The number of electrodes used 16 electrodes for both injection and measurement. There are several measurement strategies such as Cross, Opposite, Neighbouring, and Adaptive. In this research, the Neighbouring measurement method mainly used. Moreover, the image reconstruction measurements will be processed to be any of the three-data form Variance, RMS, and Standard deviation. The processed data will be processed further using MATLAB EIDORS Method even though other reconstruction algorithms are available such as LBP, SVD, and Tikhonov methods. The developed system to be continuous, the direct image reconstruction system has been developed. Overall, as seen, a key chart has been shown for the tomography types and the EIT system implementation guide.

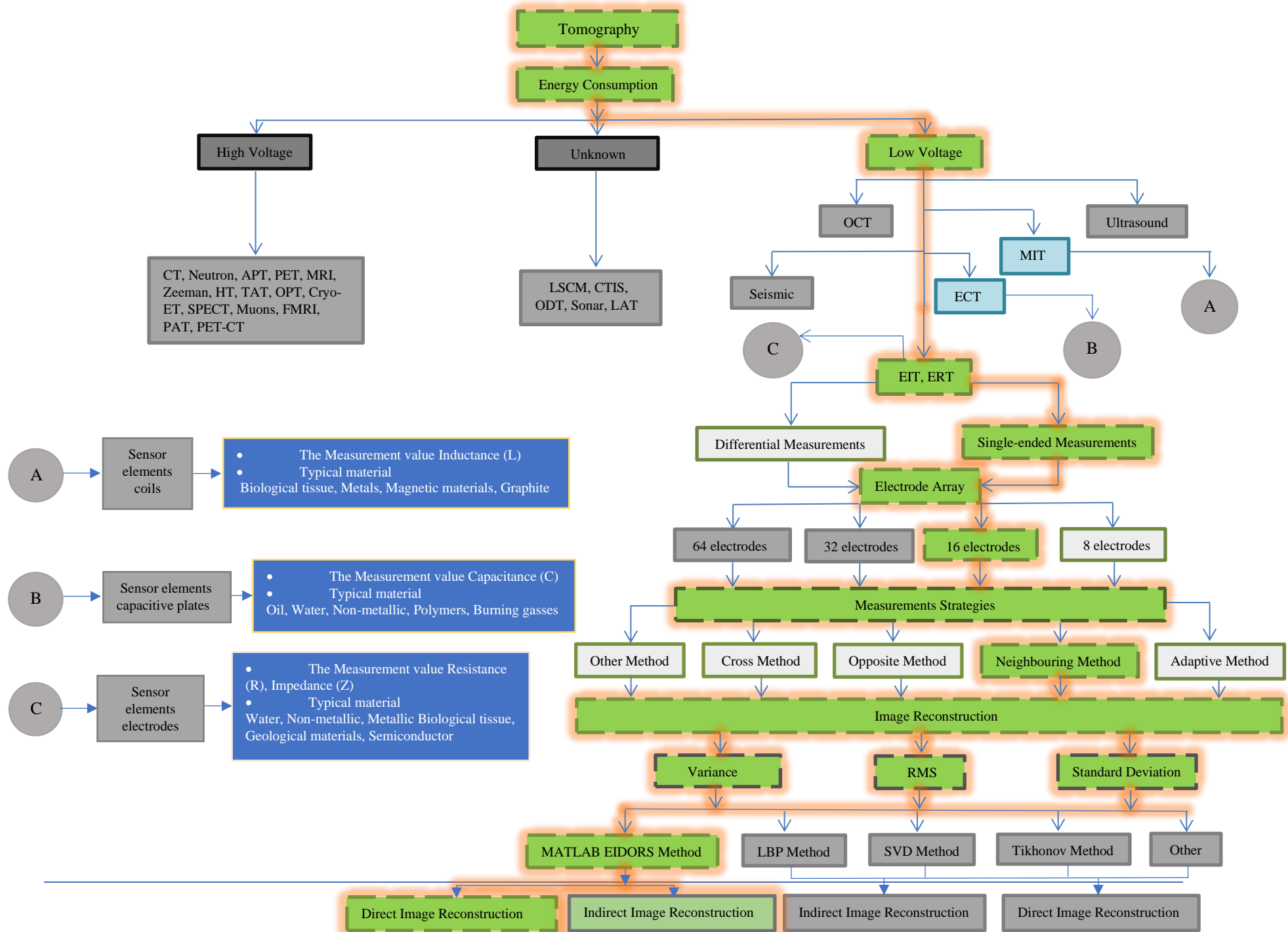


Figure 1.1: The key chart of the research.

1.4 Thesis Organisation

This thesis consists of eight chapters, which will cover A general background of EIT, the design, develop, and implement of novel electrical impedance tomography (EIT) system hardware and software to image and monitor hidden objects.

Chapter 1: Describes the problem statements, the need to develop a low voltage impedance tomography with the aim and limitations of this work.

Chapter 2: Literature Review briefly discusses the electromagnetic tomography, electrical impedance tomography (EIT) measurement strategies, reviews the recent literature concerning EIT and EIT image reconstruction theory.

Chapter 3: Methodology discusses SEEIT system software and hardware, measurement methods, and the developed EIT system in comparison to some of the latest EIT systems.

Chapter 4: Measurements and injection signalling where differential and single-ended signals measurement transformation and testing presented. Moreover, testing the single-ended signalling EIT system switching box and comparing their results.

Chapter 5: A single-ended electrical impedance tomography (SEEIT) system discusses the developed SEEIT system architecture, hardware, software, and some of the results.

Chapter 6: A novel measurement technique using the SEEIT system discusses the principle of the SEEIT system technique measurement with the obtained results.

Chapter 7: Application of SEEIT presents multiple experimental testing using the developed SEEIT prototype system. There are six experiments conducted to mimic several applications using the SEEIT system. And present and discusses the results.

Chapter 8: Conclusion and Future Work

Figure 1.2 show the flowchart that visually represents the relationships and progression between the chapters:

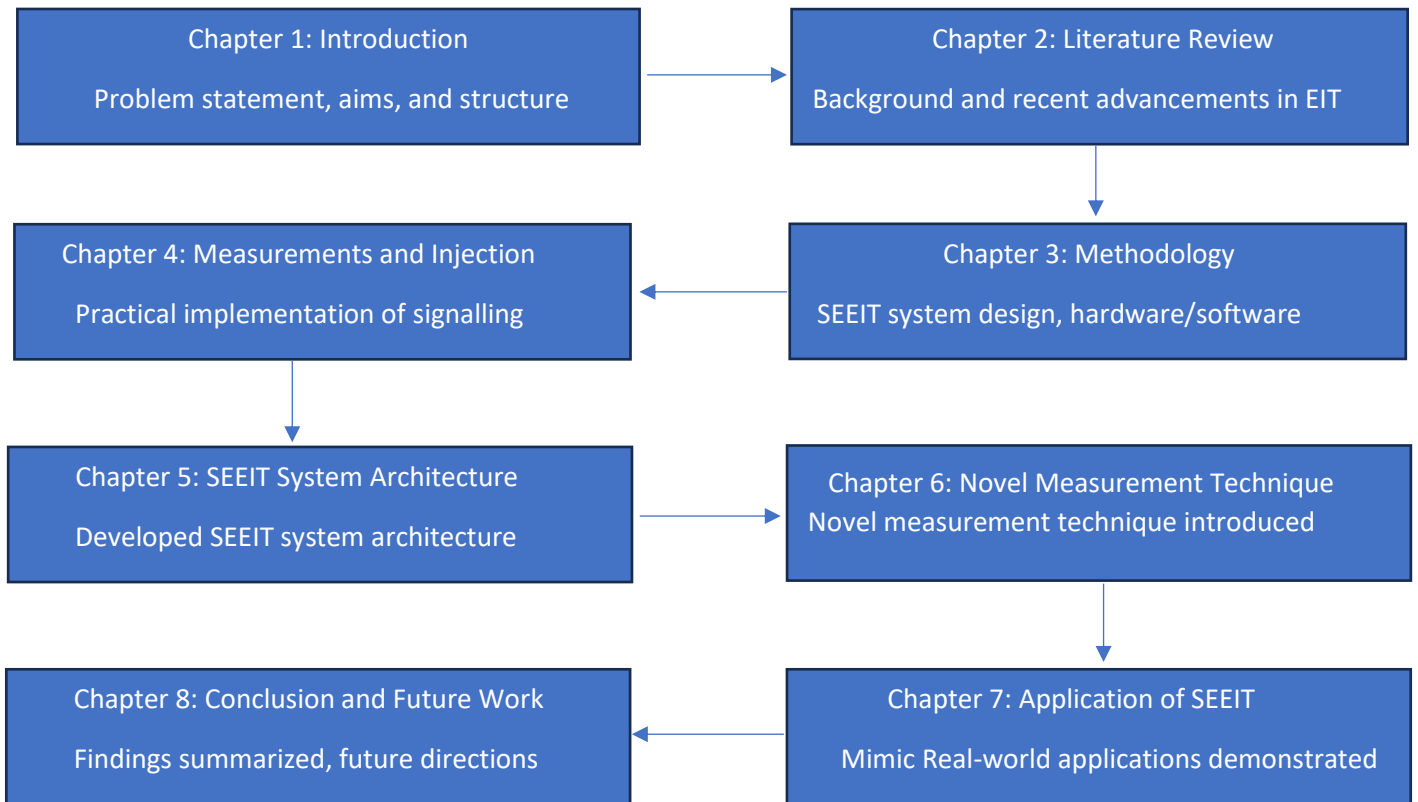


Figure 1.2: Overall flowchart of the research.

The flowchart above illustrates the logical progression of the research. Each chapter builds upon the previous one, ensuring a cohesive narrative:

Chapters 1 and 2 lay the groundwork by introducing the problem and reviewing relevant literature.

Chapters 3 and 4 focus on the theoretical and practical aspects of the SEEIT system.

Chapters 5 and 6 detail the system's architecture and validate its novel measurement technique.

Chapter 7 applies the system to real-world scenarios through experiments.

Chapter 8 concludes the research and provides recommendations for future work.

Chapter 2 Literature Review

2.1 Electromagnetic tomography

Objects moving in a magnetic field experience electromotive energy acting in a direction perpendicular to the magnetic field and to the motion (Shercliff, 1987). Hans Christian Oersted announced the discovery of the magnetic effects of the electrical current in July 1820 (Daniel, 1992; Guarnieri, 2014). Tomography derived from two Greek words, “*tomos*” for slice and “*graph*” for image (Ferrari et al., 2017; Ghanem et al., 2017; Spartalis et al., 2017; Zhang et al., 2018). Tomography refers to the rebuilding of the interior distribution of any materials from numerous external perspectives, hence providing transversal slices through the material (O’Donnell and Wright, 2016; Choi and Popovics, 2015; Sanders et al., 2017; He et al., 2016). The tomography term is often found in therapeutic diagnostics, where computerised tomography (CT) X-ray scanning systems are widely used (Scott, and McCann, 2005; Maskery et al., 2016). Radon derived the basic mathematical description of projections and tomographic reconstructions in 1917 (Scott and McCann, 2005; Kharfi, Yahiaoui, and Boussahoul, 2015). Figure 2.1 illustrates the fundamental systems of radon X-ray tomographic projections.

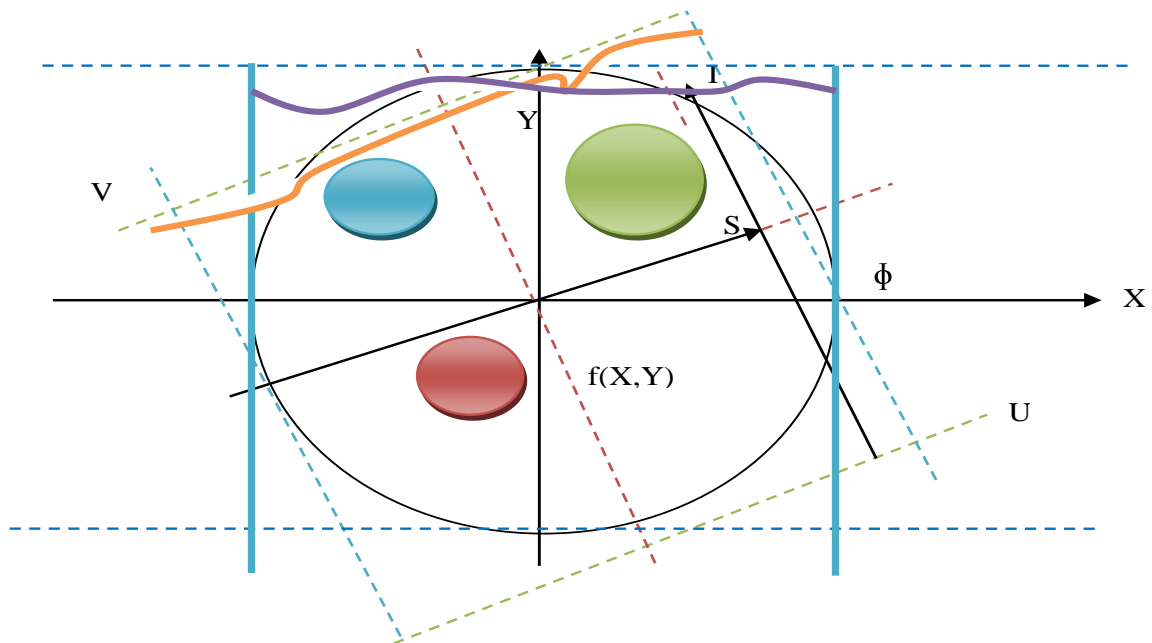


Figure 2.1: X-ray tomographic projections.

Radon defined the tomography projections as shown in Equation 2.1.

$$\rho(S, \varphi) = \int f(X, Y) d1 \quad \text{for all } S \text{ [adapted from Scott and McCann, 2005] Equation 2.1}$$

In brief, the X-ray CT beam moves through space to be exposed to the aimed object to create an image that will be mirrored on photographic film. On the other hand. In EIT tomography, low electrical current will be injected to the subjected object then electrical current change will be processed to reconstructed images based on electrical energy changes. So, the means different between the X-ray CT and EIT imaging is the X-ray imaging using an X-ray beam, and the EIT uses electrical current.

2.1.1 Electrical capacitance tomography

In the 1980s, the first electrical capacitance tomography (ECT) system was developed at the University of Manchester (Chen, Yang, and Deng, 2010). ECT is the latest electrical process technique used for imaging industrial processes. Typically, it is used to measure the permittivity of the object being imaged by measuring the changes in capacitance from capacitor electrodes to reconstruct the cross-section imaging from measured information. The ECT system has many advantages, such as being low cost, non-invasive, robust, involving no radiation, having a fast imaging speed and being able to withstand high pressures (Zhang et al., 2014; Yang, Peng and Jia, 2017; Cui, Wang, and Yin, 2015). The ECT system can obtain cross-sectional images from the inner area of vessels or pipelines. Usually, ECT consists of attaching a capacitance electrode array around a pipeline. Hence, the pipeline should be made of dielectric materials (Gamio, 2005).

2.1.2 Magnetic induction tomography

The first study was reporting magnetic induction tomography (MIT) published in 1968. The MIT system images magnetic permeability and conductivity of the inner object (Darrer et al., 2015; Dekdouk et al., 2016; Saiful et al., 2015; Li et al., 2017). Typically, the MIT system uses coils instead of electrodes for transmitting and receiving electrical signals to measure perturbation, inducing voltage changes that will be used to reconstruct the object image (Zhang, Ma and Soleimani, 2015; Ann, Su-shi and Zakaria, 2017; Li et al., 2017; Wang et al., 2017). The conductive object must be within magnetic propagation regions. The measurements of object conductivity are used to determine the object location. According to various studies, the MIT system is

the best technique for two-phase monitoring (Zhang, Ma, and Soleimani, 2015; Zhai et al., 2016; Lima, Félix, and Reis, 2015). MIT is a very stable technique because it is contactless (Yang et al., 2017). The prime advantage is the ability to detect different conductivity materials (Wei and Soleimani, 2012).

2.1.3 Electrical impedance tomography

Electrical impedance tomography (EIT) is a non-invasive imaging method based on measurements of electrical conductivities in any object (Holder, 1992; Manuel, 2010; Frerichs et al., 2016; Khan et al., 2015). This technique based on the electrical conductivities (current and voltages) of any conductive object depending on the element characteristics (Avery, 2017; Zhou, Harrach and Seo, 2018). Typically, EIT involves a collection of electrodes attached to the surface of any object, and electric currents fed into it through those electrodes (Grychtol, Müller and Adler, 2016). There are many applications of the EIT system, such as medical imaging, industrial process monitoring, and underground prospecting (Aristovich et al., 2016; Garde and Knudsen, 2016; Murphy, Mahara and Halter, 2016). For instance, if employed in chest imaging, the electrodes can be attached, as shown in Figure 2.2:

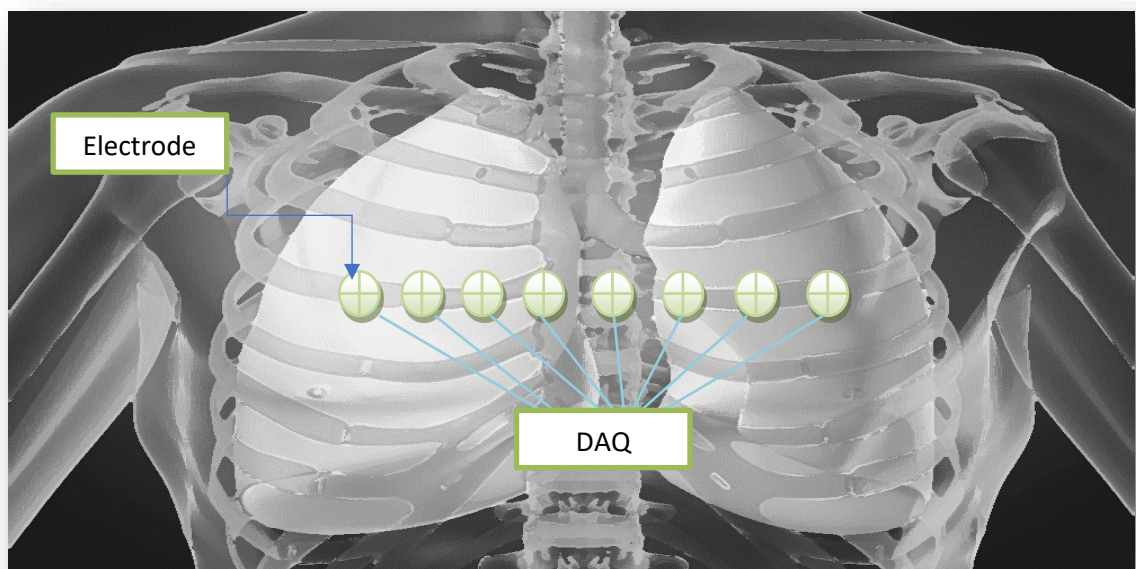


Figure 2.2: Example of EIT electrode arrangements [Adapted from LRMC, 2014].

The voltage is measured at each electrode after the electrical current is injected to the other electrodes. This estimates the electric conductivity at grid spots by using the measured information. The outcome is a reconstructed image of the inner structure of the object, similar to that in Figure 2.3. The main limitation of EIT data is its nonlinear response and extreme sensitivity to noise measurements.

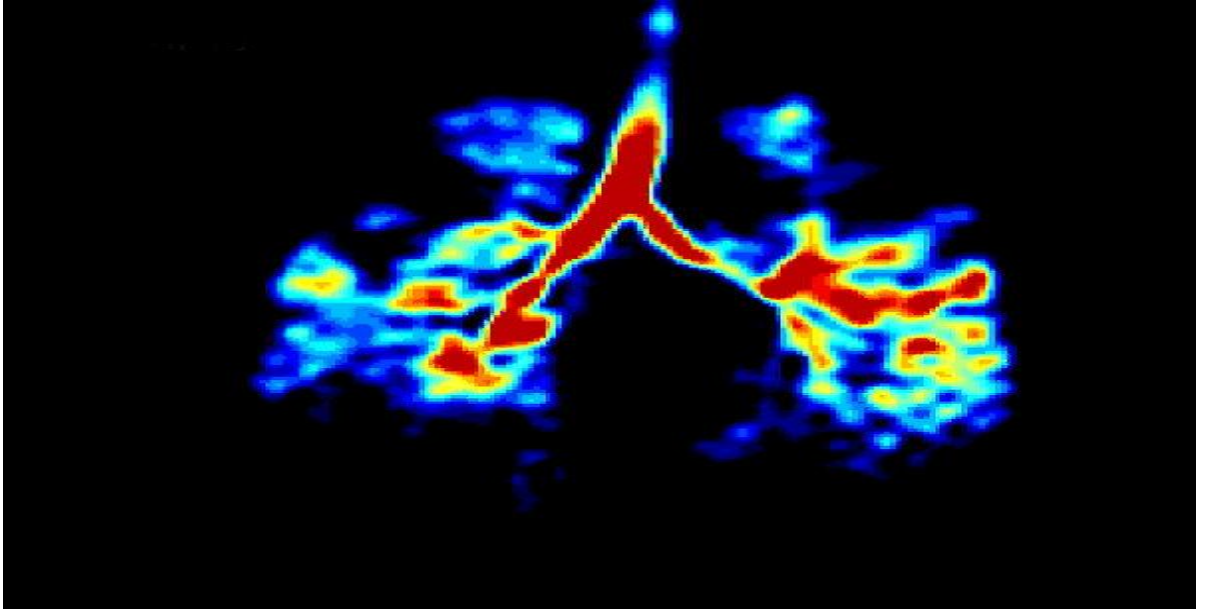


Figure 2.3: Example of lung imaging using EIT [Adapted from Tami Freeman, 2008].

A typical EIT system is a compact set of modules that includes: (1) a data acquisition unit that reads the potential values induced by the current, (2) a current generator that injects current to the object, (3) an electrode array, (4) a multiplexing system that drives the signal injection according to an appropriate sequence, (5) possible amplifiers and signal filters, and (6) computer software for image reconstruction.

Figure 2.4 demonstrates the generic architecture operation of a process tomography system. An electrode array is a collection of electrodes arranged around cylindrical vessels and pipes or any object. This defines the method of tomography to be implemented and employed for subsequent tomography system modules. The electrode DAQ module is for process control and providing the energy source to the electrode array. The reconstruction processing module for processing the raw data originates from an electrode array and yields an estimated image. The analysis processing module requires the extraction of relevant process information from the tomographic image.

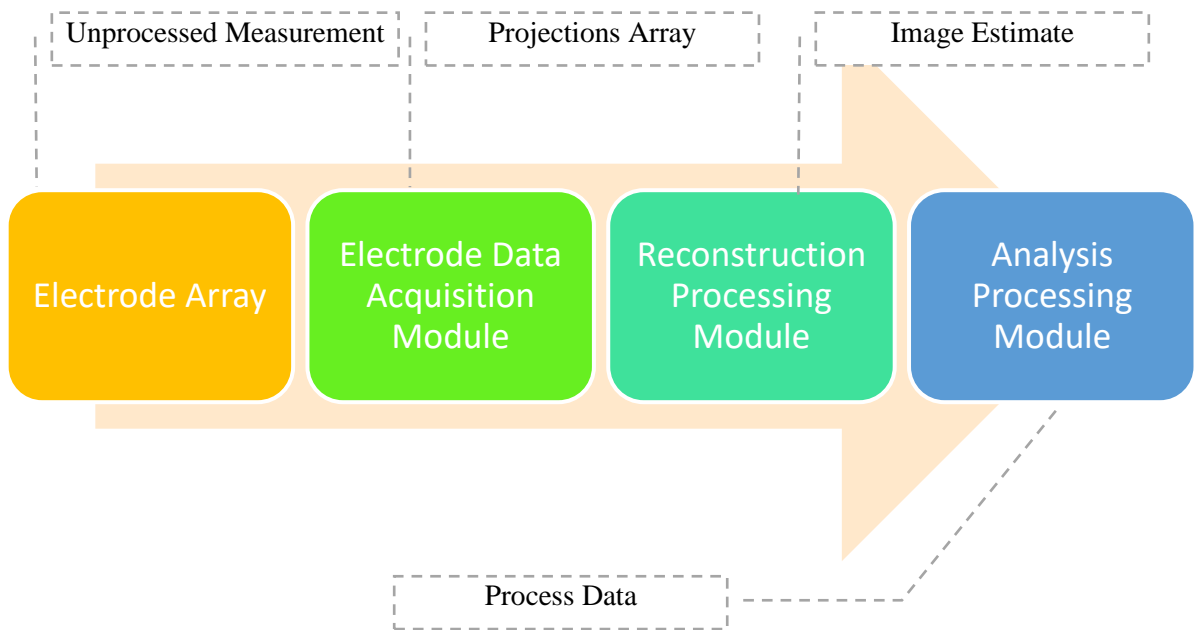


Figure 2.4: Generic process tomography system architecture.

2.2 Electrical impedance tomography (EIT) measurement strategies

Different data collection strategies exist for extracting complete data set measurements of electric potential at the boundary walls of any conductive object. In this section, several EIT measurement strategies will be briefly described.

2.2.1 Adjacent measurement strategy

In this strategy, the electrical current will be injected at two adjacent electrodes. Then, the voltage will be measured simultaneously or sequentially between all other neighbouring electrodes. After that, the electric injection will be shifted to another pair of electrodes for the second set of measurements. Since there are two electrodes used for excitation, the number of independent measurements decreases (Chang, 1997). For example, the number of independent measurements will be 464 for a 32-electrode array, which calculated using Equation 2.2. Figure 2.5 shows how electrical current (A) is being injected, and voltage (V) is being measured using the adjacent measurement strategy.

$$M = N(N - 3)/2 \quad [\text{Adapted from Chang, 1997}] \quad \text{Equation 2.2}$$

N = total number of electrodes

M = number of independent measurements for strategy

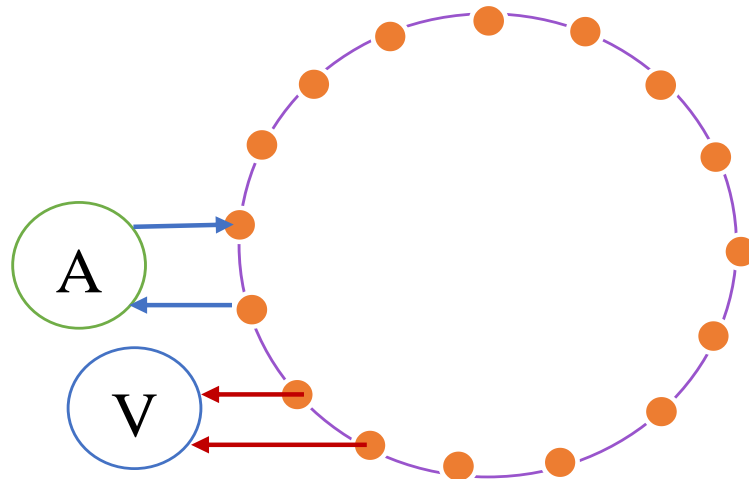


Figure 2.5: EIT adjacent electrode strategy.

2.2.2 Opposite measurement strategy

In the opposite measurement strategy, the electrical current is applied to two opposite-side electrodes and the voltage is obtained from other electrodes (Wang, 2015). For example, the electrical current injected into electrode number one and number nine, and then voltage from the rest of the electrodes will be measured. The full data set is obtained by shifting the excitation to the next pair of opposite electrodes. For every switching of the electrode injection, the measuring electrodes will switch to the unused electrode so as to continue in the formation with the excitation electrode. However, the conductivity changes as current flows through the centre point of the cross-section. Figure 2.6 demonstrates the typical opposite electrode strategy parameters.

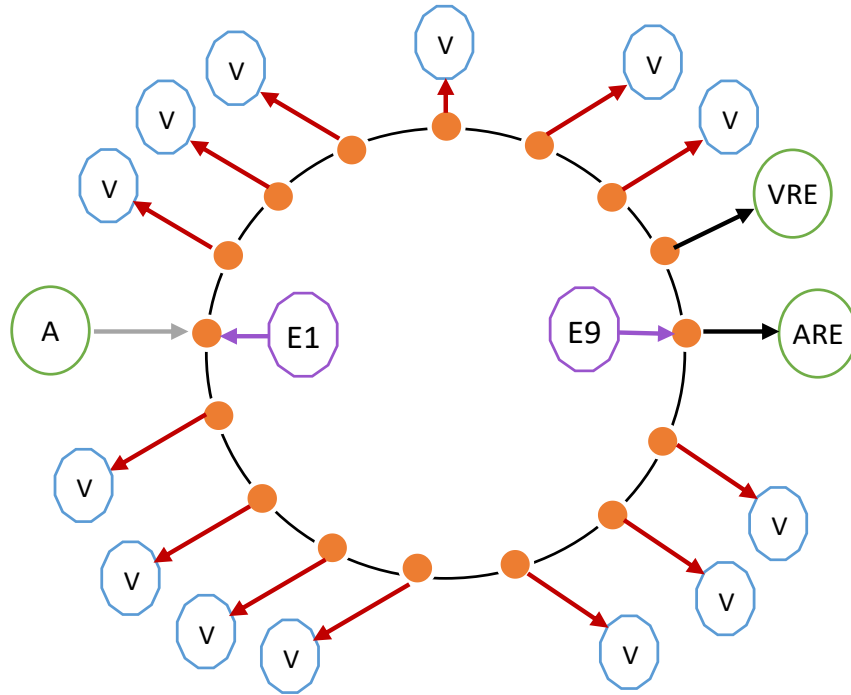


Figure 2.6: EIT opposite electrode strategy.

2.2.3 Cross measurement strategy

The cross method was suggested by Tompkins (Jaakko and Robert, 1995). In the cross method, two electrodes are selected as voltage and current references (Harikumar, Prabu and Raghavan, 2013). For example, Figure 2.7 shows how 13 voltage measurements are obtained using electrode number 2 (E2) as the reference for 13 voltage electrodes, whereas the current is applied to electrodes number 1 (E1) and number 3 (E3). Moreover, the cross method provides 13 differential voltage measurements. Subsequently, the current is injected into electrodes 1 and 5 while 13 differential voltage measurements are obtained when electrode 2 is set as the reference.

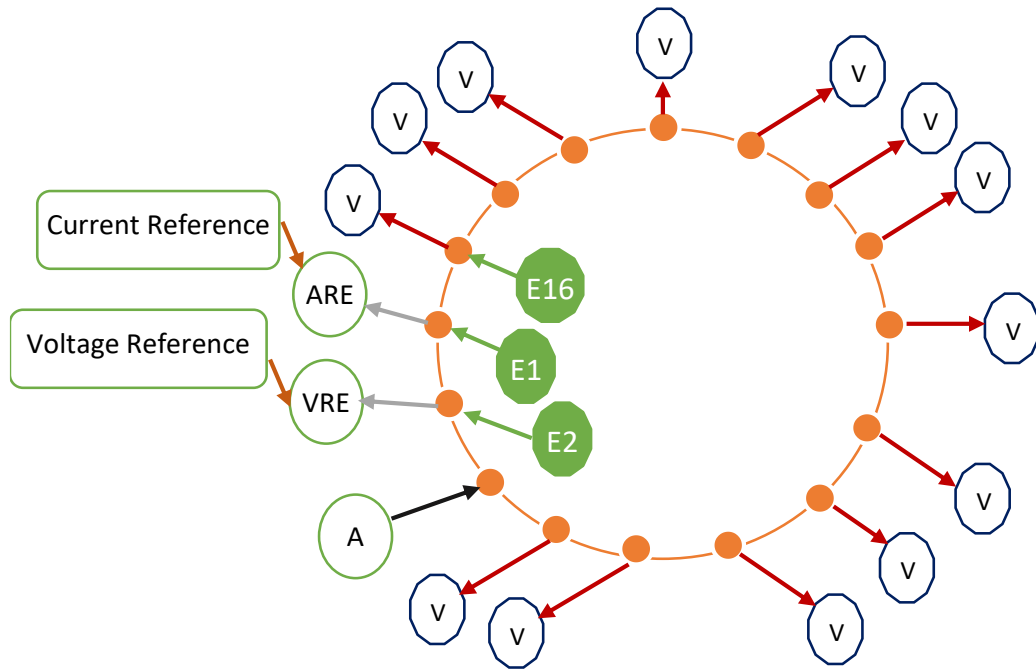


Figure 2.7: EIT cross electrode strategy.

2.3 Literature Review

This section reviews the recent literature concerning EIT.

2.3.1 Image reconstruction using voltage-current system in electrical impedance tomography

This study was conducted by Seok, Kumar, Jun, Youn, and Kim from Jeju National University & Chung-Ang Universities Republic of Korea. They investigated voltage-current (VC) and current-voltage (CV) systems for two-phase applications. With the VC system, first, voltage is injected; then, the electrical current is measured. The researchers solved the forward problem by formulating with a conductance matrix. Moreover, they estimated the conductivity distribution by a non-iterative inverse method. Compared to conventional systems, the methods used in the study involved more complex hardware. The placements of the electrodes on the human skin was difficult because of the contact impedance between the electrodes and the human body. Jacobian Matrix algorithms were used to measure the internal conductivity distribution. Two collection methods were employed: an adjacent CV system and a new excitation method for VC. Figure 2.8 shows the test setup. Circle A indicates the test vessel; B is used for data acquisition (Agilent 34970A), and C is the LCR meter (Agilent 4284A).

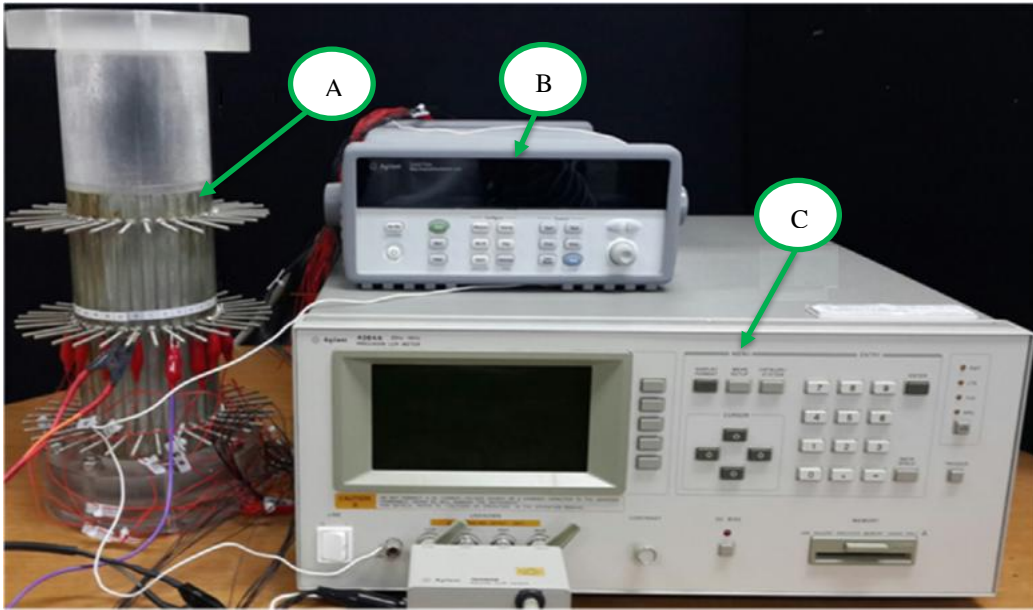


Figure 2.8: EIT system complete measurement setup [Adapted from Seok et al., 2014].

Figure 2.9 reveals the reconstructed images for two data collection setups. The black circle represents the position of the object, and the black line indicates the electrode position. Image A shows the CV system configuration, and image B illustrates the VC system configuration.

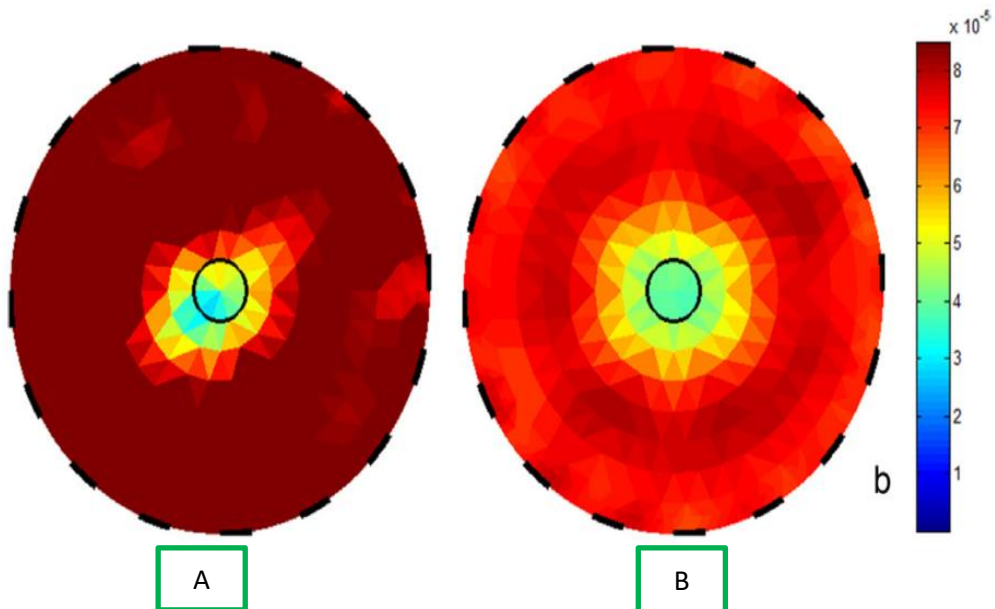


Figure 2.9: Reconstructed images for two data collection system setups [Adapted from Seok et al., 2014].

2.3.2 A 4.9 mΩ-sensitivity mobile electrical impedance tomography ic for early breast-cancer detection system

Hong et al. (2015) implemented an EIT integrated circuit (IC). Their IC was proposed for an early breast cancer detection system using a mobile phone (see Figure 2.10). The system can be divided into three parts: imaging device, electrode array, and electronic circuitry. They used a multi-layered fabric circuit that supports up to 90 electrodes for enhanced image quality. The IC has three operation modes: electrical impedance tomography, gain scanning, and contact impedance monitoring modes. A six-channel voltage sensing amplifier was developed for better gain control. The IC chip dimensions are 2.5×5 mm. The EIT system was able to detect cancerous tumours as small as 5 mm. However, the electrode array contact is unstable due to the electrode fabrication material.

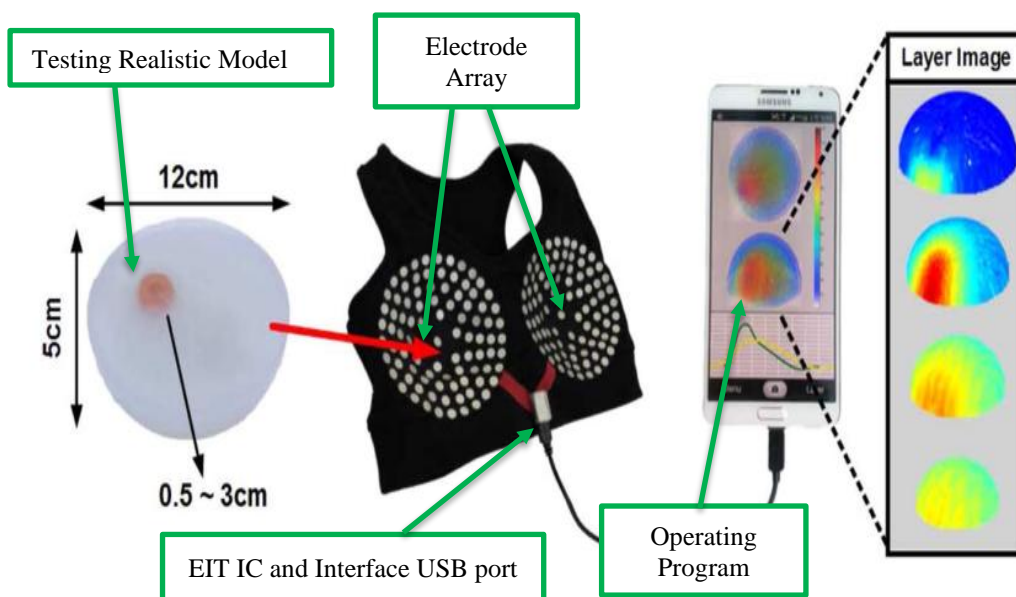


Figure 2.10: Breast cancer detection system [Adapted from Hong et al., 2015].

2.3.3 Multi-frequency electrical impedance tomography system with automatic self-calibration for long-term monitoring

The multi-frequency EIT developed by Wi, Sohal, McEwan, Woo, and Oh (2014) is a radiation-free system used to diagnose the condition of biological tissues. The researchers collected induced voltages from an electrode array attached to the human

body after injecting it with a safe amount of current. They used a finite element model (FEM) to solve the inverse problem. Their system, known as the KHU Mark 2.5, can support other electrical impedance electrode arrays, so it can be modified for various applications. Figure 2.5 shows the setup of the system. The system architecture is based on a digital signal processor (TMS 320f2812) controllers. The main feature of the KHU Mark 2.5 is self-calibration with a frequency range from 50 to 500000 Hz. The longest system operation period of the KHU Mark 2.5 was 72 hours of continuous operation. The KHU Mark 2.5 device is a stable, high-performance electrical impedance tomography system. They plan to use it to detect stroke, cardiac activity, and bleeding. As shown in Figure 2.11, the EIT system is divided into three sections: operating program, 16-channel KHU Mark 2.5 DAQ data acquisition, and testing vessel.

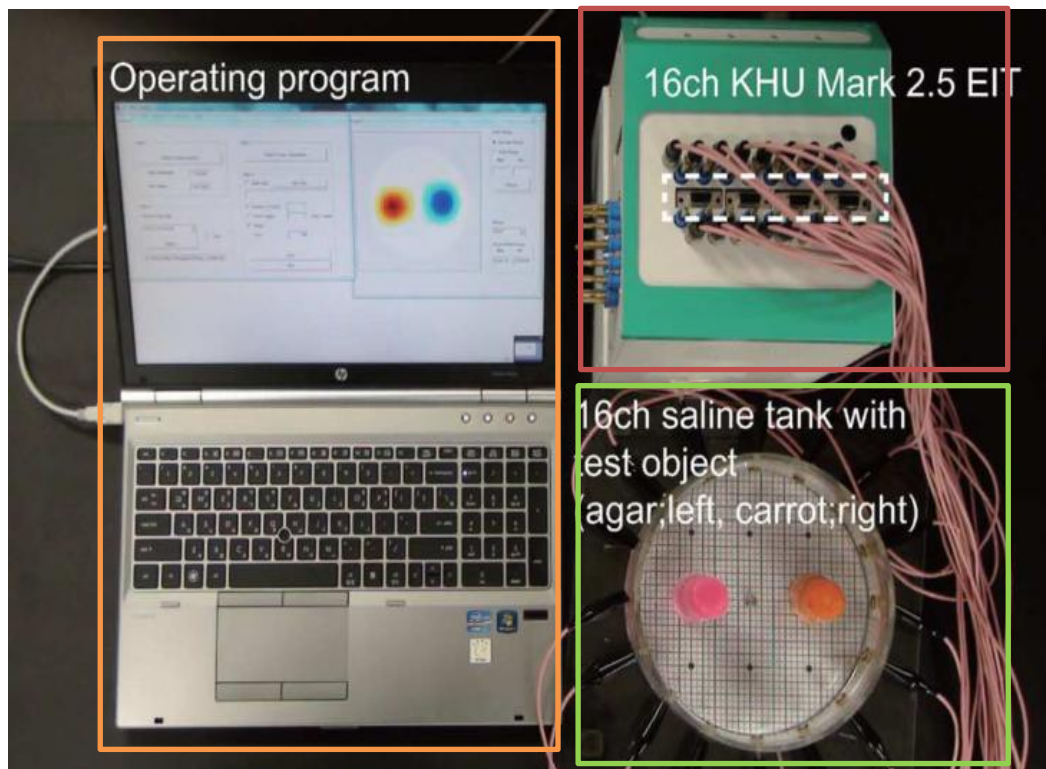


Figure 2.11: KHU Mark 2.5 EIT system setup [Adapted from Wi et al., 2014].

2.3.4 Code-division-multiplexing using orthogonal codes for fast electrical impedance tomography

Geyers, Gebhardt, Vogt, and Musch (2014) developed an EIT system that used the code-division-multiplexing (CDM) technique. CDM is a channel access method that

employs spread spectrum technology. The CDM excitation technique will increase the measurement rates for parallel measurement. Their sampling frequency set to 2 MHz and the carrier frequency set to 250 kHz. The direct digital synthesizers (DDS) controlled by binary phase-shift keying (BPSK). Orthogonal codes were applied to optimize dynamic range and channel separation. Tests were performed on a sealed pipe filled with tap water. An 18 electrical current injection was used for a full measurement cycle with a total number of electrodes 36. The researchers compared the reconstructed conductivity distribution images to those of frequency division multiplexing (FDM), EIT, and CDM systems measurements. Figure 2.12 displays the EIT system, which consists of three sections. Section 1 shows a screenshot of the operating program, Section 2 is the data acquisition box, and Section 3 shows the pipes filled with tap water for testing.

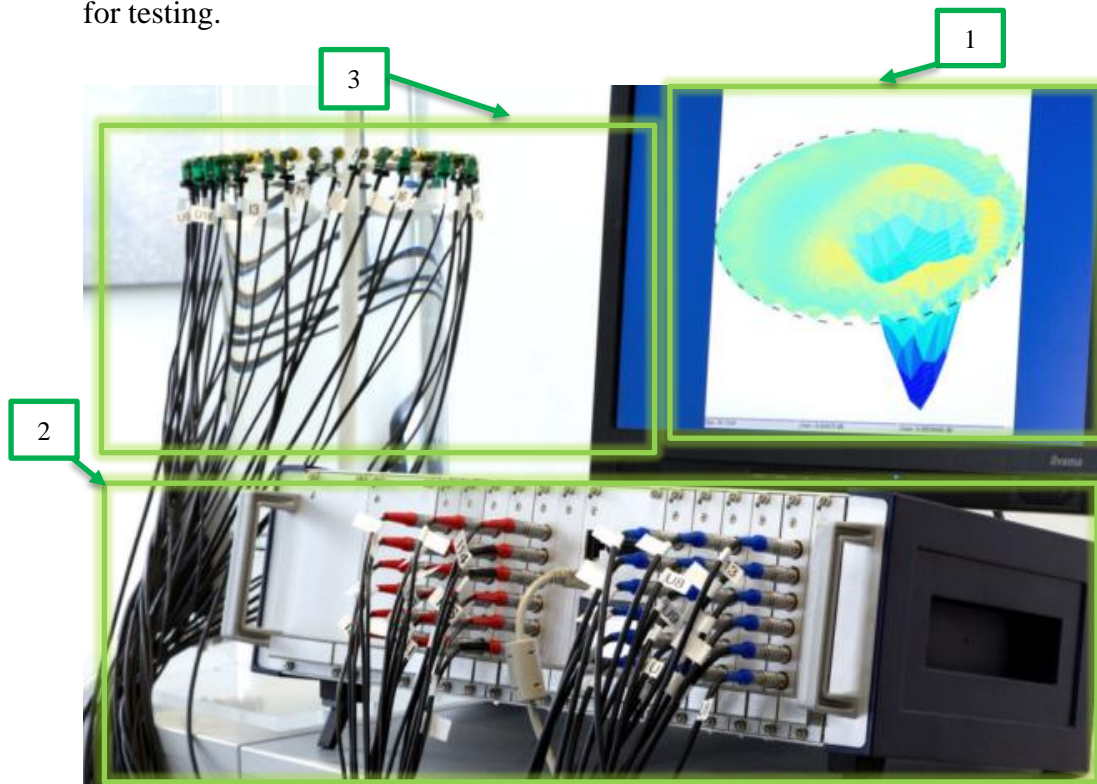


Figure 2.12: CDM EIT system [Adapted from Gevers et al., 2014].

2.3.5 Use of electrical impedance tomography to monitor regional cerebral edema during clinical dehydration treatment

A group of scientists from China and the United Kingdom worked on developing a system that can monitor brain fluid content using electrical impedance tomography (Fu et al., 2014). They used an electrical impedance tomography system for the first time

to evaluate cerebrospinal fluid contents. The main reasons for using EIT systems are that they are safe because they use very low current injection, and they have a fast imaging process. This EIT system can measure data in real-time and can be used in emergency situations. The simulated results prove that the system can detect and track the impedance change while the position of the object changed in the realistic skull model. However, the researchers faced a few problems, including variation of patient skull thickness. In the beginning, they evaluated their EIT system on the realistic human head model. Subsequently, they tested it on 23 patients with brain cerebral edema. The injected frequency range was between 1 kHz and 190 kHz. Figure 2.13 shows a complete set of measurements that consists of six diverse object positions. The EIT system is divided into three parts: a realistic head model with electrodes, operating program, and data acquisition box.

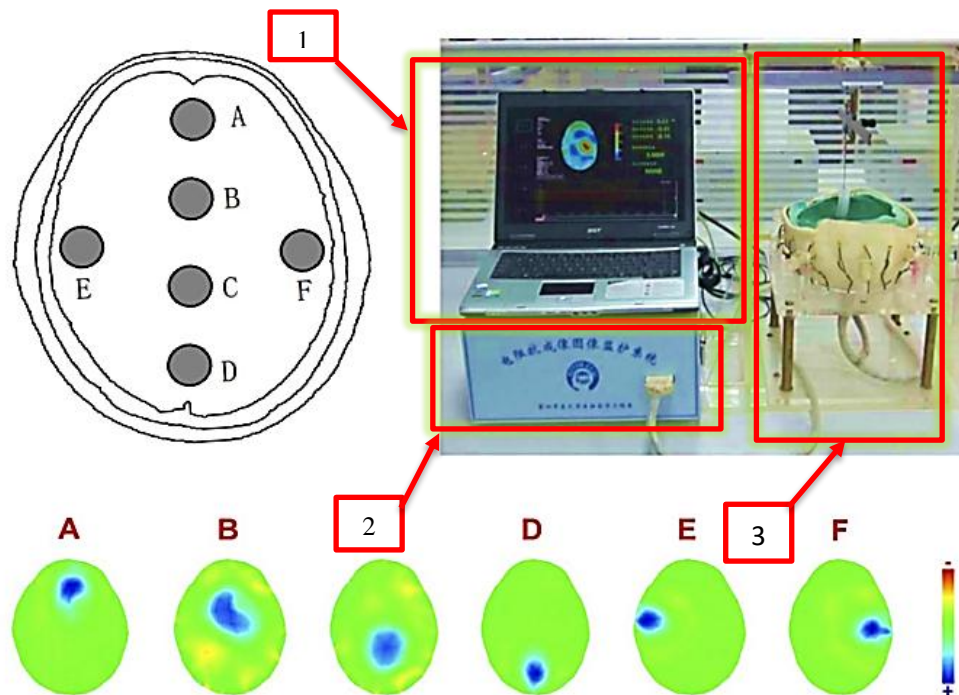


Figure 2.13: Cerebrospinal fluid EIT system [Adapted from Fu et al., 2014].

2.3.6 System description and first application of an FPGA-based simultaneous multi-frequency electrical impedance tomography

A study conducted by Santos, Robens, Boehm, Leonhardt, and Teichmann (2016) implemented a prototype multi-frequency electrical impedance tomography (mfEIT) system. The researchers developed a 16-electrode mfEIT system with a composite waveform that was configured to record electrical impedance simultaneously at

different frequencies uses a field-programmable gate array as the primary controller. They used preliminary frequency-difference images for the first time for in-vivo experiments. The system was tested using different dual-injection frequency range 60-960 kHz for both frequency-difference and time-difference imaging. They compared the results of time-difference imaging with simulated results and found that the prototype system operated well within the frequency ranges. The developed system can select two different frequencies simultaneously using graphical user interface control panels without the need to upgrade the hardware, which increases system flexibility. However, the system is incomplete and requires further development, particularly for frequency-difference images for which improvement of algorithms and the normalisation process is required to reconstruct accurate 2D images. The mfEIT system was primarily developed for medical applications: specifically, the thoracic area. The implementation of a graphical user interface within the basic configuration of the mfEIT system makes it easy to change and increases flexibility. Figure 2.14 shows the prototype EIT system, which consists of two main units. Unit 1 shows the DAQ box; Unit 2 is the host PC, which has the operating program.

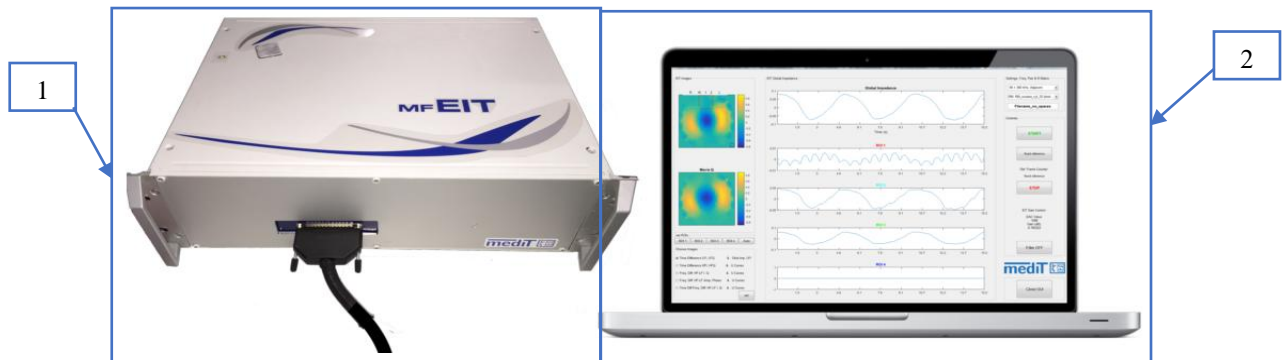


Figure 2.14: Prototype of the mfEIT system [Adapted from Aguiar Santos et al., 2016].

2.3.7 Localized electrical impedance Myography of the biceps brachii muscle during different levels of isometric contraction and fatigue

A group of scientists from China and the United States investigated isometric muscle contractions and fatigue levels using an EIT system (L. Li et al., 2016). They found that the conductivity of the muscle changes significantly during different muscle contraction levels. Their electrical impedance myography (EIM) system can detect the electrical conductivity when muscle contractions increase and decrease. This study conducted testing of the biceps brachii muscle of 19 subjects. The researchers claimed that they

were the first individuals to use the electrical impedance (EI) system to detect electrical impedance changes during muscle contraction. The main reason for developing the EIM system was to enhance the clinical evaluation of changes in muscles during muscle activation in patients with neurological disease. As displayed in Figure 2.15, a biceps brachii muscle was put to the test to evaluate the use of the EIM system to examine the human body. However, the EIM system only can measure the impedance results and cannot obtain the reconstructed image.

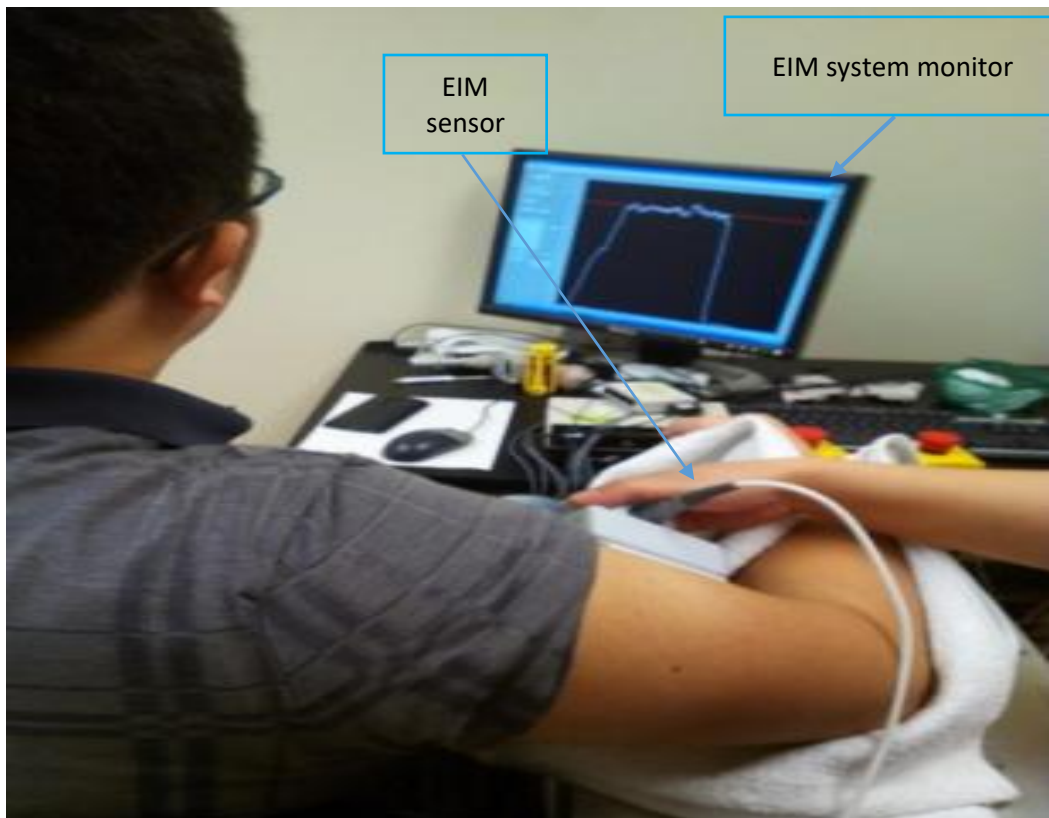


Figure 2.15: Actual testing of EIM system on human biceps brachii muscle [Adapted from L. Li et al., 2016].

2.3.8 Adaptive techniques in electrical impedance tomography reconstruction

Researchers from Rensselaer Polytechnic Institute developed a novel image reconstruction technique using adaptive algorithms to solve the inverse problem for an EIT system (Li et al, 2014). Essentially, they combined two adaptive reconstruction algorithms to refine the reconstruction 2D image and achieved improved image resolution. They claimed that their adaptive algorithm combination improves current patterns to avoid unnecessary elements for better spatial resolution of 2D reconstructed

images. Moreover, they stated that this technique reduces the EIT system cost. They evaluated their algorithm method by simulation, and their results reveal the stable performance of the EIT system using adaptive algorithms. Figure 2.16 shows the 2D reconstructed images, based on the measured data, using a combination of two algorithm methods: adaptive Kaczmarz and mesh refinement.

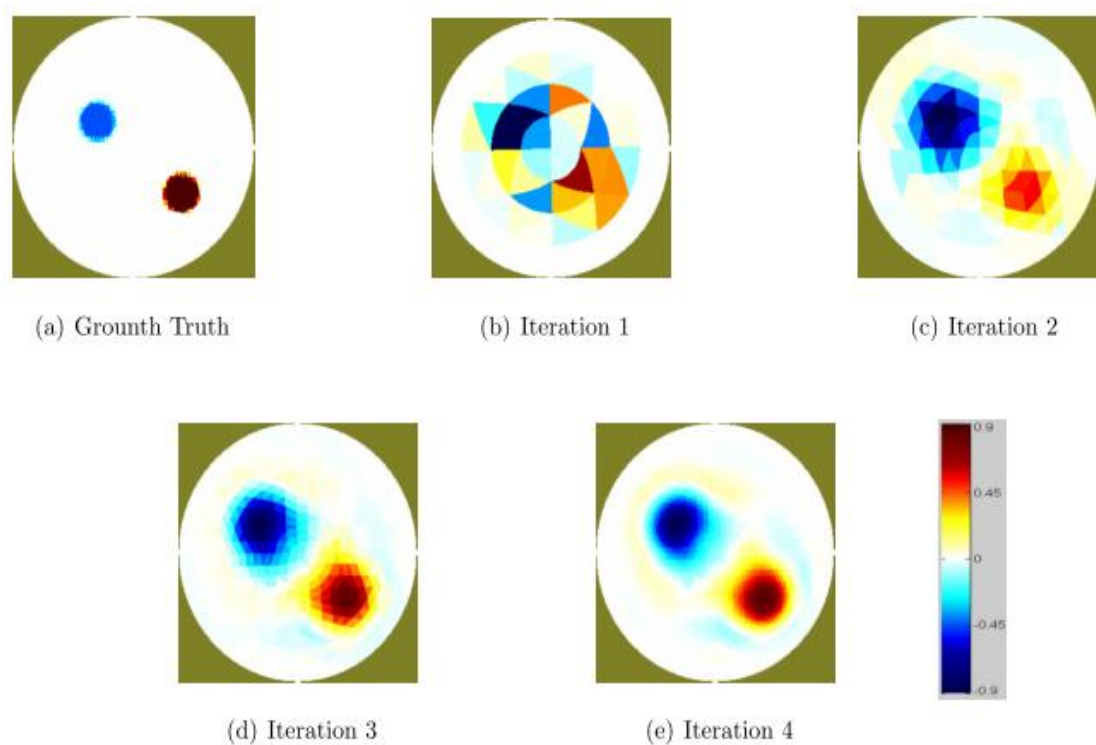


Figure 2.16: The 2D reconstruction images of the first four iterations; simulated results using MATLAB when electrically conductive and non-conductive objects were placed in the tank [Adapted from T. Li et al., 2014].

2.3.9 A deformable smart skin for continuous sensing based on electrical impedance tomography

Visentin, Fiorini, and Suzuki (2016) developed a flexible, low-cost EIT pressure sensor, which is used as a smart skin and overcomes the flexibility problem experienced with sensors of traditional EIT systems. The researchers tested their system in different environments by changing the number of channels, size, and shape to evaluate the feasibility of the EIT sensor. However, they were not able to correctly distinguish the terminal shapes of the different electrode channels. They were able to detect the location in the space of the terminals and estimate their size. All of the tests of the EIT

artificial skin showed good performance, even when the skin was applied over different geometries. The main objective of the research was to create a smart, low-cost EIT system sensor that can be adapted for use in different configurations without affecting the sensing abilities. Figure 2.17 shows the artificial skin in the actual testing environment; image (b) shows that the skin can operate even on informal electrode arrangements.

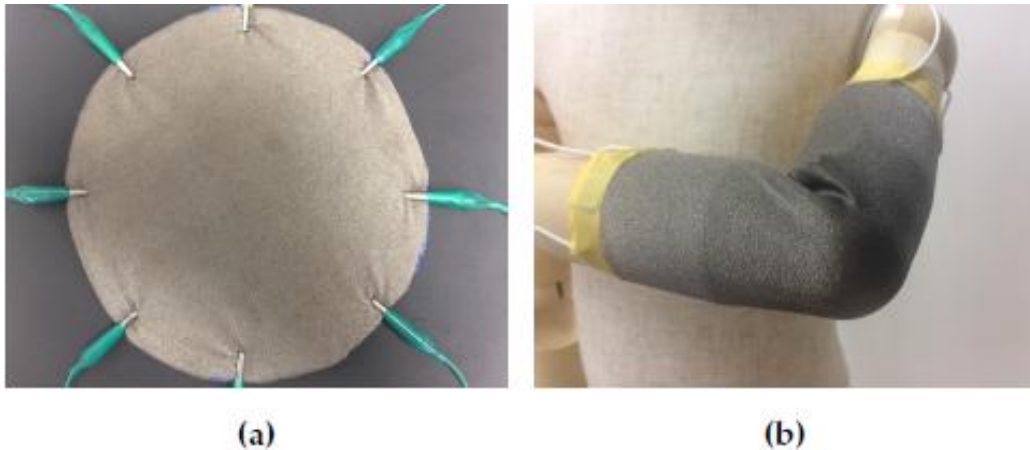


Figure 2.17: (a) The developed artificial skin, using eight channels that are connected by alligator clip to the measurement system. (b) Possible application scenario attached over a dummy doll arm [Adapted from Visentin, Fiorini and Suzuki, 2016].

2.3.10 A FPGA-based broadband EIT system for complex bioimpedance measurements—design and performance estimation

Kusche et al. (2015) designed an FPGA mEIT system (16 channels) to monitor and image the conductivity changes in living tissue. To show the system features, the system was tested against an impedance phantom and in actual physiological measurements. Moreover, physiological measurements of the EIT system were taken with three different tests: micro-tank, tank, and thorax. The system injected diverse signals of frequency and form, with a frequency range up to 0.5 MHz and low excitation currents up to 5 mA. However, the system is not complete and is ongoing within the LUMEN research group. Figure 2.18 shows the recent mEIT system complete measurement setup.

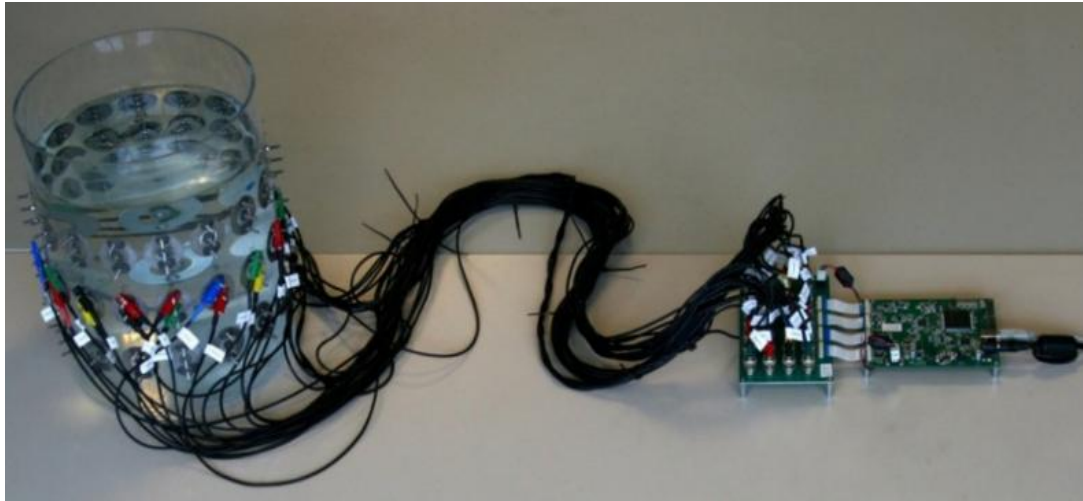


Figure 2.18: Complete measurement setup for FPGA-based EIT system [Adapted from Kusche et al., 2015].

2.3.11 Electrical impedance tomography (EIT) system for radiation-free medical imaging based on LabVIEW

Bera and Nagaraju (2011) implemented an EIT system using 16 electrodes and employing a low-amplitude current injection. The EIT system consists of three parts: the host PC, electrodes, and electronic instrumentation. The main advantage of the developed system is that it can use diverse types of electrodes, such as silver and stainless steel. However, the EIT system was calibrated by testing it on dissimilar materials, both organic and non-organic. An injection current of 1 mA was used, so the system is medically safe for use in the human body. The purpose of developing the EIT system was to investigate the physiological status of a human body to monitor and diagnose diverse diseases. Figure 2.19 shows a prototype of the EIT system based on National Instruments (NI) data acquisition hardware run by LabVIEW software.

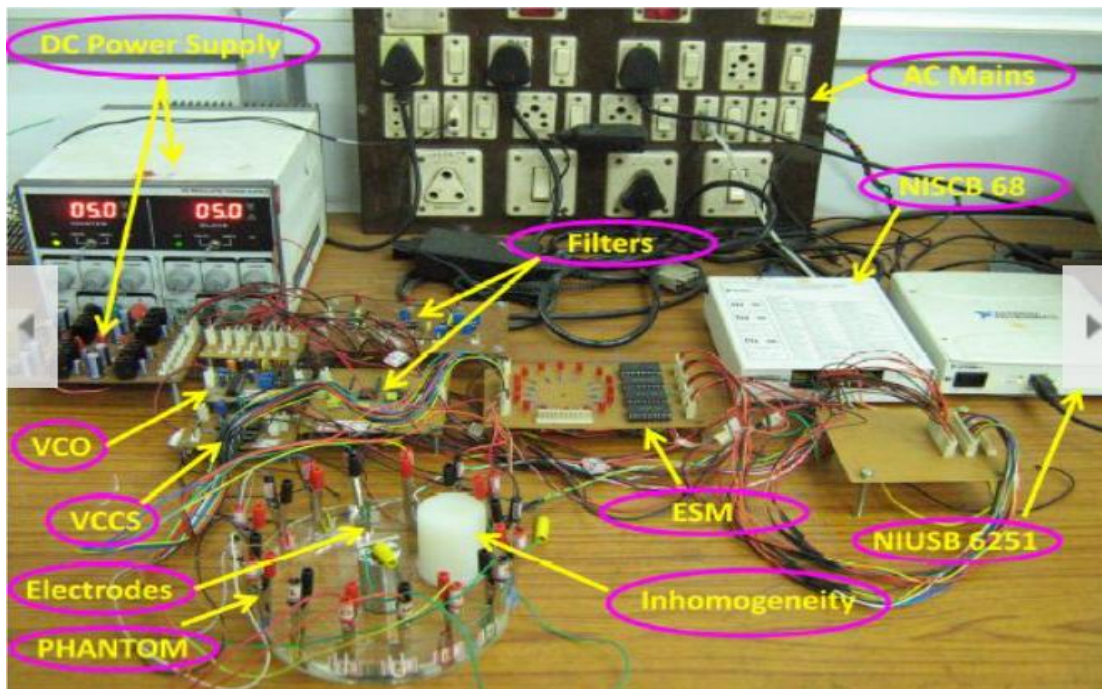


Figure 2.19: EIT system prototype hardware [Adapted from Bera and J Nagaraju, 2011].

2.3.12 A local region of interest imaging method for electrical impedance tomography with internal electrodes

A group of scientists from Korea and Australia developed an EIT system with a method known as region of interest (ROI), which uses internal electrodes. The researchers performed simulations and physical measurements to evaluate the ROI method. Their results, which obtained with multiple targeted objects that were examined simultaneously, illustrate the merits of introducing the internal electrode ROI method. The electrodes in the ROI EIT system are unequally spaced, unlike the typical EIT system in which the electrodes are equally spaced. The purpose of the system is to monitor and treat liver tumors, particularly for patients with medical situations that do not allow them to face surgical procedures. Because liver tumor tissue has a higher electrical conductivity characteristic than liver tissue, differentiating the tissues is simple using the EIT system. The results obtained from numerous experiments conducted over an injection frequency range of 10 Hz to 1 MHz. However, further investigation of the ROI EIT system is required. Figure 2.20 shows a full setup for the ROI system using internal electrodes.

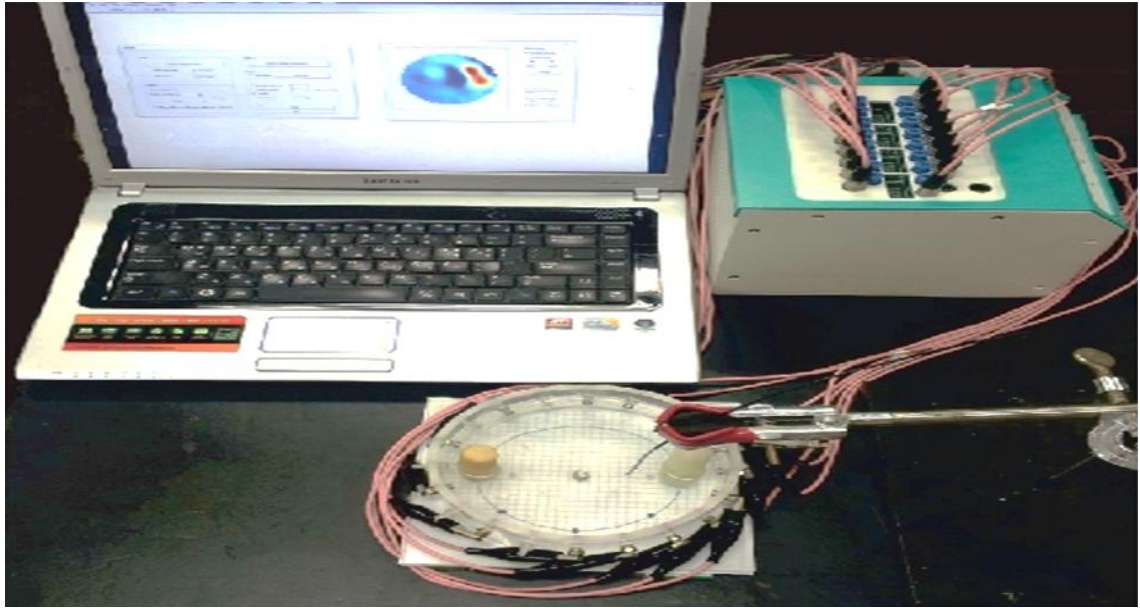


Figure 2.20: ROI EIT system [Adapted from Kwon et al., 2013]. Synthesis

Based on the twelve projects using the EIT system, some aspects of each project, such as the limitations of the research, are worth discussing. For the first study, which can be seen in Figure 2.8, the setup of the EIT system was implemented by scientists whose investigation focused on a VC system for a two-phase application. Nevertheless, the researchers solved the forward problem by formulating with a conductance matrix. Moreover, they estimated the conductivity distribution by a non-iterative inverse method, which resulted in inaccurate reconstructed image quality. A more accurately reconstructed picture with fewer input data could be obtained by using an iterative method instead of a non-iterative method (Tamburrino, Rubinacci and Ventre, 2014).

Regarding the second research case, the early breast cancer detection system developed by the Institute of Electrical and Electronics Engineers (IEEE) is quite adjustable. This is because the engineers built an integrated circuit (IC) that can be connected to a mobile phone, and then can be processed by mobile software to generate an image of a cancerous tumour. Although the system can support up to 90 electrodes for a better reconstructed image, the researchers encountered a problem with electrode placements, which will affect the reconstructed image quality.

The third research case, which can be seen in Figure 2.11, shows the multi-frequency KHU Mark 2.5 EIT system. The researchers collected induced data from an array of 16

electrodes attached to the human body. Of all the cases, the KHU Mark 2.5 has the longest operation period of approximately 72 hours. Therefore, it can be used as a monitoring system for industrial processes.

For the fourth research case, researchers from Ruhr University Bochum uniquely designed an EIT system using a channel access method, with code division multiplexing (CDM) and frequency division multiplexing (FDM) techniques. Nonetheless, as shown in Figure 2.12, their reconstructed image was not very accurate even with using 36 electrodes.

The fifth research case, which used a prototype of an EIT system, was developed to monitor brain cerebrospinal fluid contents (Figure 2.13). This system can track and detect the position of an object in a realistic skull model. Nevertheless, the variation of patient skull thickness will affect the accuracy of the reconstructed image.

For the sixth research case, researchers from RWTH Aachen University developed mfEIT system for medical applications. They used preliminary frequency-difference images for the first time with in-vivo experiments. However, further development of the technology for frequency-difference images is required, primarily for algorithms and the normalisation process for accurate 2D images.

The seventh research case involved the development of an EIM system to detect conductivity of muscle changes during different muscle contraction levels. This will enhance the clinical evaluation of changes in muscle strength in patients with neurological diseases. Nevertheless, the developed EIM system only produces raw data and does not create reconstructed images.

For the eighth research case, researchers from Rensselaer Polytechnic Institute combined two adaptive reconstruction algorithms to refine the reconstructed 2D image, which improved the algorithm technique to solve the inverse problem of the EIT system. The researchers evaluated their algorithm method by simulation and showed the reliable performance of the EIT system. However, larger regularization is required

for finer meshes, and smaller regularization is required for coarser meshes, to enable accurate solutions for different meshes.

The ninth research case involved a pressure sensor used for the EIT system to overcome the flexibility problem with the electrode, which exists in typical EIT systems. The researchers evaluated the feasibility of their system by changing the number of channels, size, and shape. Furthermore, their sensor was able to estimate the size of the testing object. However, the developed sensor was not able to distinguish the different electrode shapes.

For the tenth research case, researchers implemented an FPGA EIT system to diagnose living tissue. The system precisely determined the complex impedance data. The reconstruction algorithm can be improved in the future when phase data of the impedance are used. However, the high number of channels that had to be attached to the patient should be reduced since the current system uses 32 electrodes.

Regarding the eleventh research case, scientists at the Indian Institute of Science Bangalore implemented an EIT system using 1 mA for the injection current, which made the system medically safe. Nevertheless, the developed system should have a current-seeking electrode, and the differential injection technique that it employs will restrict the flexibility of the system.

For the twelfth research case, scientists developed an EIT system using a method region ROI with internal electrodes, which made it possible to diagnose and watch liver tumours. Furthermore, they investigated their ROI EIT system via both simulation and actual testing. Despite the positive results of the tests, further investigation of the ROI EIT system required.

2.4 Comparison of recent EIT based imaging systems

Table 2.1 shows the modern developed EIT system features highlighted. The number 1 means the system has the feature, and 0 does not have it, and NA not provided by the developer. However, the table shows the article title, where the EIT system has been used.

Table 2.1: The recent EIT system feature.

Feature / The article title in which the developed system used	Two-phase applications	EIT integrated circuit	Multi-frequency	Self-calibration	Multi injection signals	Double signals injection	FPGA based	Electrode unequally spaced	Number of electrodes 16 and less than 16	Number of electrodes more than 16
Image reconstruction using voltage-current system in electrical impedance tomography	1	0	0	0	0	0	NA	NA	1	0
A 4.9 mΩ-sensitivity mobile electrical impedance tomography IC for early breast-cancer detection system	0	1	0	0	0	0	NA	NA	0	1
Multi-frequency electrical impedance tomography system with automatic self-calibration for long-term monitoring	0	NA	1	1	NA	0	NA	NA	1	0
Code-division-multiplexing using orthogonal codes for fast electrical impedance tomography	0	0	1	0	1	0	NA	NA	0	1
Use of electrical impedance tomography to monitor regional cerebral edema during clinical dehydration treatment	0	NA	1	0	NA	0	NA	NA	1	0
System description and first application of an FPGA-based simultaneous multi-frequency electrical impedance tomography	0	NA	1	0	NA	1	1	NA	1	0
Localized electrical impedance myography of	0	0	1	0	0	0	NA	NA	0	1

the biceps brachii muscle during different levels of isometric contraction and fatigue											
Adaptive techniques in electrical impedance tomography reconstruction	NA	0	1								
A deformable smart skin for continuous sensing based on electrical impedance tomography	NA	1	0								
A FPGA-based broadband EIT system for complex bioimpedance measurements—design and performance estimation	0	NA	1	0	NA	NA	1	NA	1	0	
Electrical impedance tomography (EIT) system for radiation-free medical imaging based on LabVIEW	0	0	0	0	0	0	0	NA	0	1	
A local region of interest imaging method for electrical impedance tomography with internal electrodes	NA	1	NA	NA							

2.5 Electrical impedance tomography image reconstruction theory

A tomographic image can be produced by mainly measuring the impedance, conductivity, and permittivity of an object using measurements obtained from the electrode surface. The concept of EIT is based on the fact that each and every targeted object is capable of permitting electrical conductivity (penetration). In the operation process, numerous conducting electrodes are attached to the surface of the targeted object being tested. Then, AC currents of small magnitude are injected into the object using selected or all electrodes (Hong et al., 2015). Next, the data differences in conductivity among the electrodes are measured and recorded. Several measurement sets obtained by recording and comparing the measurement values are combined to produce a 2D tomographic image. In EIT data, the challenge of reconstructing an image is treated as a nonlinear problem, which is highly sensitive to the measurement noise

(Gallo and Thostenson, 2016). This factor will make it difficult to reconstruct an image with high resolution, so several methods have been developed by scientists to improve the resolution and clarity of the reconstructed image (Ammari et al., 2015).

A brief description of several algorithms is presented in this chapter. The EIT reconstruction algorithms can be divided into two categories: analytical reconstruction algorithms and algebraic reconstruction algorithms. Algebraic reconstruction algorithms make up a class of iterative algorithms and are used to reconstruct the image from a series of angular projections. Moreover, the first-time algebraic reconstruction algorithms were employed to produce an image was by Gordon, Bender and Herman (1970). On the other hand, analytical reconstruction algorithms are based on a continuous representation of the problem by mathematical equations, and they generally do not consider the statistical nature of the measurement noise. Therefore, they are fast and easy.

However, two problems should be solved to reconstruct an image using EIT (Jehl et al., 2015; Silvera-Tawil et al., 2015; Alberti et al., 2016). The first is the forward problem and the second is the inverse problem. Both problems are discussed briefly in this chapter. EIT system applications consist of several types and primarily focus on two fields: industrial and medical. A list of some of the EIT processes is shown in Table 2.2.

Table 2.2: A selection of EIT system applications in industrial and medical arenas.

Industrial	Medical
Monitoring multi-component flows in pipes such as water, gas and oil (Tapp et al., 2003; Abdul Wahab et al., 2015)	Detecting breast cancer (Zain and Kanaga, 2015)
Pneumatic transport (Tapp et al., 2003)	Confirm correct placement of double-lumen tube (Steinmann et al., 2008)
Soil water infiltration (Gutiérrez Gnechi et al., 2012)	Assessment of stroke volume variation (Trepte et al., 2017)
Anisotropic carbon fiber-reinforced polymer composite laminate for damage localization (Nonn et al., 2018)	Predicting failure of spontaneous breathing trials (Bickenbach et al., 2017)

Nuclear fuel process and plant decommission (Wang et al., 2007)	Quantification of pulmonary edema in acute lung injury (Trepte et al., 2016)
-----------------------------------------------------------------	------------------------------------------------------------------------------

2.5.1 Forward problem

The Solution of the EIT forward problem begins when the electrical current or voltage is injected into the object of interest using an electrode attached to the targeted area. The conductivity distribution is known, and the corresponding induced electrical potential is determined from the nonlinear Laplace equation, which is derived from partial differential equations, second-type boundary condition, and ohms law. To solve the forward problem, scientists have developed methods for calculating and reconstructing an image. However, numerous methods can be used to solve the forward problem, and each has its own limitations and image accuracy. One example is the finite element method (FEM), which permits an individual set of meshes to be generated from given geometric information obtained from the targeted object (Bayford et al., 2001).

The forward problem starts with the computation of electrical voltages and proceeds to formulating the solution by evaluating the conductivity. The valuation is performed when the injected current and the distribution pattern of the conductivity element are known. Viewed from another perspective, the forward problem is concerned with the simulation of the measurements for the electrical boundary using a conductivity that is close enough to the true conductivity value (Grabb, 2017). The forward problem is needed when the object under study has a shape that cannot be conveniently described. In such a case, an approximation is made to ensure that the object under analysis can assume a similar 2D or 3D model.

The forward problem in EIT requires the computation of electric voltage potentials at the boundary electrodes using the current injected at the electrodes and the conductivity for the geometric model. In the majority of scenarios involving the forward problem, Maxwell's equations are used to model the problem. Grabb (2017) goes on to add that the forward problem can be solved by the linear finite elements, as mentioned earlier, whereby a mesh is used to reduce the inaccuracies between the electrode potentials. Various approaches are used to solve the EIT forward problem; the majority of them are used to measure or establish the boundary conditions. The complete

electrode model is an approach that takes into consideration the impedance generated by the electrodes when they are in contact with the object surface (Grabb, 2017).

Another approach used to solve the EIT forward problem is through the use of the boundary element method (BEM). As further noted by de Munck, Faes and Heethaar (2000), the boundary element method works by replacing flat surfaces with polygonal ones. This is motivated by the fact that polygonal surfaces have more accurate computational results when using EIT algorithms. However, FEM is the most popular method of solving the forward problem; it uses numerical values and has applications in domains with curved boundaries. FEM is also capable of producing sparse matrix results, especially in conductivities with inhomogeneous attributes (Grabb, 2017).

Another approach used to solve the forward EIT problem involves the use of the finite difference method (FDM). This method is designed to simplify the process of creating the mesh used for image processing (Grabb, 2017). It is worth noting that FDM uses more memory and has a lower accuracy rate compared to FEM or BEM. Additionally, FDM requires the use of noise filtering techniques to enhance the process of edge detection in EIT. Nonetheless, FDM is regarded as a useful numeric solver for the forward EIT problem and can be used for both 2D and 3D image reconstruction.

2.5.2 Inverse problem

The inverse EIT problem is concerned with estimating the internal conductivity of an object using the electrical voltage measurements taken on the object's surface as well as the existing knowledge of the current being injected. Unlike the forward problem, the inverse problem starts with the results of the EIT process and proceeds backward to identify the causes. Viewed from another perspective, the inverse problem is primarily concerned with establishing a conductivity value that reduces the difference between the measured and estimated electrical voltages or currents. Simply, the inverse problem is concerned with establishing the conductivity that produced the known and predicted electrical voltages or current.

The EIT inverse problem is basically regarded as being ill-posed; as such, it requires the knowledge of prior information to ensure that a mathematical model can be used to transform it into a well-posed problem. The ill-posed nature of the inverse problem implies that the approach only serves to produce an image with modest quality.

Consequently, mathematical models and algorithms have been proposed aimed at improving the conductivity at the object's surface. The inverse problem can be solved by a multi-frequency approach that involves the linearization of the mathematical model (Alberti et al., 2016). Unlike the forward problem, there are no major approaches that have been established and approved for solving the inverse problem. Instead, there are various individual works aimed at solving the inverse problem, although they are only on a small-scale implementation. For instance, the Gauss-Newton and conjugate gradient (nonlinear) are some of the notable approaches that use logarithmic conductivity to solve the inverse problem (Pellegrini, Trigo and Lima, 2018). The two approaches use physical boundaries to perform the estimates of conductivity that is then employed to produce the electrical voltages or currents at the object's surface.

2.6 EIT reconstruction algorithms

Reconstruction algorithms in EIT are primarily used for the process of recreating the images from the tomography procedure. There are various reconstruction algorithms, each designed to serve a specific purpose, although the end result is the reconstruction of images (Malone et al., 2015; Halter et al., 2015). Moreover, they are used to improve the process of reconstructing images. In particular, EIT reconstruction algorithms are used to solve either forward or inverse problems. Most algorithms can only solve a single problem and not two problems at once.

2.6.1 GREIT

The Graz consensus reconstruction algorithm (GREIT) is specifically designed to assist in lung EIT and uses the linear reconstruction approach (Roth et al., 2015). The algorithm obtained its name in 2007 when discussions about the framework took place in Graz, Austria during an ICEBI conference. GREIT's popularity is based on the fact that it provides a nonlinear framework that makes it possible to solve the inverse problem in a 2D environment (Orschulik and Antink, 2015). The algorithm assists in thoracic imaging and employs spatial data for the development of the training framework (Yerworth, Frerichs and Bayford, 2017; Orschulik and Antink, 2015). Notable features found in GREIT include the ability to reconstruct a 2D image model as well as to reconstruct an image of up to 32x32 pixels (Graf and Riedel, 2017;

Ambrisko et al., 2015). GREIT can also support quantitative reconstruction using configurations made from single-ring electronic nodes (Antink and Pikkemaat, 2015).

2.6.2 Modified newton-raphson method

The Newton-Raphson method is a reconstruction algorithm that uses the least-square method for image reconstruction (Anand et al., 2015; Pisa, Pittella and PiuZZi, 2017). The least-square method is a popular approach that minimizes the error function generated when performing the reconstruction process. The modified version is designed to accommodate various resistivity values when operating under a specific set of voltage measurements (Yorkey, Webster and Tompkins, 1987). The functionality and performance of the modified Newton-Raphson method is further enhanced by using region of interest in EIT (Karsten et al., 2016). The region of interest method is particularly designed to solve EIT inverse problems that take the form of ill-posedness (Nguyen and Yang, 2016). From the basis, the region of interest is used with the modified Newton-Raphson method to manage linearization and distribution of voltage in EIT (Yorke, Webster and Tompkins, 1987). This algorithm has been found to be particularly effective in solving the EIT inverse problem as well as increasing the visualization of the reconstructed image.

2.6.3 Finite element method

The finite element method (FEM) is a reconstruction algorithm that is used to solve the forward problem in EIT (Hyvönen and Leinonen, 2015; Jehl et al., 2015; Harrach and Ullrich, 2015). The framework is better applied in scenarios that involve non-homogenous distributions as well as irregularly placed domains. FEM is used in both 2D and 3D implementations and is mostly employed in the implementation of the complete electrode model (CEM) (Lionheart, 2004; Jehl, Avery, et al., 2015). CEM in this context is used to improve the accuracy and precision of the electrode voltages (Dunlop and Stuart, 2016). FEM has been found to be successful in situations where accuracy is given priority. It is widely used in both commercial and custom medical applications (Lionheart, 2004). FEM is capable of enhancing efficient results through the use of system matrix and mesh generation (Crabb, 2017). A key aspect of FEM is that it takes a considerable amount of time to reconstruct an image with FEM, but the quality of the image is greatly improved.

2.6.4 Jacobian matrix

The Jacobian matrix, otherwise known as sensitivity matrix, is an algorithm used in EIT reconstruction (Jehl and Holder, 2016). Jacobian matrix is employed in the evaluation of the optimal network path that will be used to reconstruct an image. The Jacobian framework is primarily used to solve the forward inverse problem in EIT (Gong et al., 2015). It is used to evaluate the optimal voltage value as well the required current that must be submitted to the electrodes (Chen, 1990). The efficiency of the reconstruction process is further enhanced by conducting iterative processes of the adaptive network generated by the Jacobian matrix (Rymarczyk, 2016).

2.6.5 Linear back projection

The linear back projection (LBP) algorithm is the most widely used algorithm for EIT, primarily due to its capability to handle image processing in a dynamic manner (Sun et al., 2015). LBP is also capable of handling real-time imaging processing in as well as enhancing the generation and realization of image resolution (Sun and Yang, 2015). Back projection is used to solve the inverse problem by calculating and evaluating the optimal solution through an iterative process (Lionheart, 2004). Back projection is essential because it simplifies smoothing of the image during the reconstruction process (Devakumari and Punithavathi, 2018). A common implementation of the back-projection process takes the form of Tikhonov regularization, which makes it easy to process spatial data (Lionheart, 2004).

2.6.6 D-bar

The D-bar reconstruction method is nonlinear and is used to solve the inverse problem (Murphy and Mueller, 2009; Mueller, Siltanen and Isaacson, 2002; D. Liu, Kolehmainen, et al., 2015; Mellenthin et al., 2015). The D-bar algorithm was developed from the global uniqueness proof of Nachman (Isaacson et al., 2006; Hamilton, Mueller and Alsaker, 2017). Moreover, this method was based on a rigorous mathematical analysis that needed to be processed through a low-pass filter (Hamilton et al., 2016; Hamilton, Mueller and Alsaker, 2017). The advantage of the D-bar method is that it does not need intermediate approximation of the electrical conductivity from a forward model (Murphy and Mueller, 2009).

2.7 Electrode arrays and signaling methods

Selecting the appropriate electrode array and signaling method is essential for ensuring the performance and efficiency of Electrical Impedance Tomography (EIT) systems. In this study, a 16-electrode array was chosen because it strikes a good balance between measurement accuracy and system complexity. Single-ended signaling was preferred over differential signaling due to its simplicity and ability to reduce noise interference. Single-ended signaling requires only one wire connection for signal injection or measurement, simplifying the circuitry. While differential signaling offers better sensitivity and accuracy, it involves multiple wire connections, which increases system complexity and cost.

2.8 Image reconstruction methods

For image reconstruction, the EIDORS software was selected for its versatility in handling data from various electrode configurations and producing high-quality images. EIDORS utilizes several algorithms, including Linear Back Projection (LBP), Singular Value Decomposition (SVD), and Tikhonov regularization, to reconstruct images from voltage measurements. These algorithms were chosen for their ability to balance computational efficiency with image accuracy, ensuring the EIT system operates effectively in real-time industrial applications.

Our current study shall look at a novel 16 electrodes single-ended measurements adapted into an electrical impedance tomography system for imaging applications. This benefits by having a lower number of electrodes and simple computation. Its performance is comparable to many of the recent developments. The concept of using single-ended measurements halved the number of channels, and this considered a novel approach.

Chapter 3 Methodology

An electrical impedance tomography (EIT) system that uses single-ended signalling and analyses the electrical potential distribution within a medium of electrical measurements conducted through a series of electrodes was developed. Measuring the electrical impedance helps in analysing voltage potential of sparsity constraints for different material, whether it is electrically conductive or non-electrically conductive based on boundary electrical measurements. Moreover, In the development of Electrical Impedance Tomography (EIT) systems, several restrictions have historically impeded their routine use for non-destructive testing. These limitations include issues such as the high number of measurement channels required, which increases system complexity and cost, as well as challenges related to data acquisition speed and signal-to-noise ratio. Moreover, the developed EIT system incorporates specific enhancements that address and overcome several of these critical restrictions. For instance, the new system design reduces the number of required measurement channels by 50% compared to traditional EIT systems, thereby significantly decreasing hardware complexity and cost while maintaining high performance. This improvement not only enhances the practicality of the system but also makes it more suitable for routine non-destructive testing applications.

The single-ended electrical impedance tomography (SEEIT) system has evolved through the use of several resistor circuit networks, which help to stabilise the system for use in a real testing tank under multiple signal injection frequencies in the range of 12–1000 kHz. However, the SSEIT system requires one wire connection to make one signal injection or measurement, and this is controlled using a switching box. The developed SEEIT measurement method has been shown to reduce the EIT system complexity significantly because it uses only one electrode to measure (receiver), and it features a total of 15 measurements per image.

The modularity LabVIEW code was implemented to improve the SEEIT system's flexibility and to enable adaptation of the EIT system for different applications without the need to implement a new EIT system, which may reduce development time and costs. Furthermore, a series of experiments were conducted to simulate specific industrial scenarios relevant to the study, such as detecting and locating changes in

conductivity within a controlled environment. These experiments focused on a well-defined setup involving a vessel filled with different types of water, including muddy water, tap water, and brackish water. This approach allowed for the evaluation of the system's ability to identify conductivity variations under conditions that resemble certain industrial applications, such as monitoring liquid quality or detecting impurities in contained systems. The experimental results demonstrated the system's effectiveness in accurately detecting and locating these changes, validating its potential for practical use in similar industrial contexts.

The main reduction in the complexity of the EIT system was to provide simpler computation and faster data acquisition with the use of single-ended electrodes, instead of double-ended conductors, for sensing purposes. The developed prototype system was subjected to a stability test, in which the system runs continuously for one hour to record the data. Further development included the development of its associated algorithms and development of titanium alloy grade 2 and coated copper electrodes.

3.1 Electrical impedance tomography system

The SEEIT developed at University of Nottingham Malaysia campus includes hardware and software components. The hardware primarily consists of the host computer, data acquisition (DAQ) system, connector unit, a switching unit, and an electrode array. The software can be divided into three parts: Windows operating system, MathWorks' MATLAB, and National Instruments' LabVIEW. MATLAB was used to reconstruct the image based on the processed data received from the LabVIEW program using Electrical Impedance and Diffuse Optical Tomography Reconstruction Software (EIDORS) tool. The LabVIEW program was designed and implemented to control and monitor the EIT system. LabVIEW code was developed to control the switching unit to inject and record the signals, process the raw data, and then stream the information to MATLAB for further processing to reconstruct the cross-sectional image. The switching unit connects the DAQ with the electrode array. The switching unit is designed to handle the frequency range 12 kHz to 1 MHz, which is due to the use of an electromechanical low-signal relay. However, the frequency range which utilizes in the current EIT system tests 12 kHz to 1 MHz. Figure 3.1 shows the continuing sequence stages of cycle flow for the EIT system, which shows the data start from electrode array and end on the EIDORS.

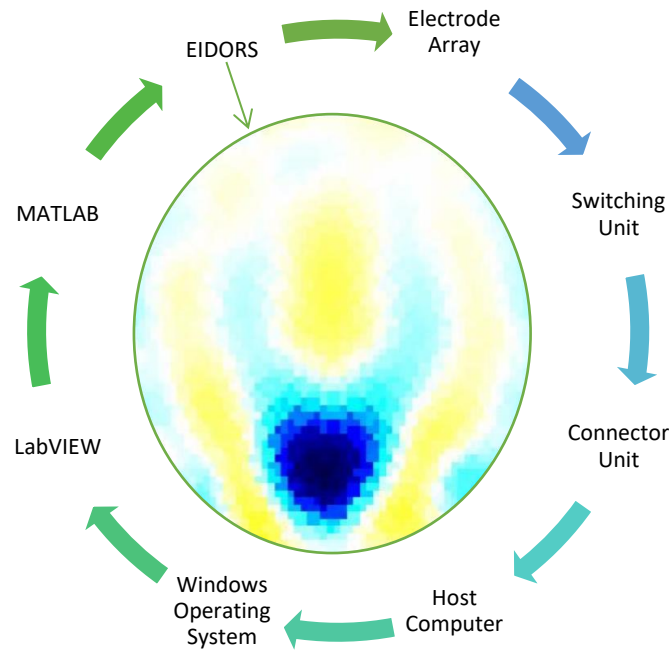


Figure 3.1: SEEIT system's linking elements are shown as a sequence in a cycle.

3.1.1 Electrical impedance tomography system software

Basically, two LabVIEW programs have been developed. The first program images objects indirectly, and the second program does it directly. The direct program can obtain raw data, process them, and sent them to EIDORS. Moreover, it can use the simulation mode, which helps to obtain random data to reconstruct an image; this feature was primarily developed for calibration purpose.

Conversely, the indirect program can obtain data without sending them to EIDORS, which mean it needs the user's interaction to move and process the data. The main difference between these two LabVIEW programs is the speed difference; the direct method is much faster than the indirect technique since it will export the image data automatically. The following sections describe the two types of the developed software program. They contain information about the structure of the program, methods of functioning, and descriptions of modules.

3.1.1.1 Indirect LabVIEW program

The indirect program is the first LabVIEW program that was implemented. The implementation steps are illustrated in Figure 3.2.

The process begins by setting the switching box to create a measurement method, setting up the injected signal amplitude, and establishing the frequency and sampling rate. Then, the voltage change is measured based on conductivity change in the targeted field, such as industrial processing vessel and human body. After that, the voltage change response is calculated to estimate the impedance distribution of the area, and the voltage calculation and variance are regularized. Then, the updated current configuration is employed. Finally, based on the voltage difference, the image is reconstructed using EIDORS. The indirect LabVIEW program is stable, but it should be improved to enhance the reliability as well as modify it for different applications.

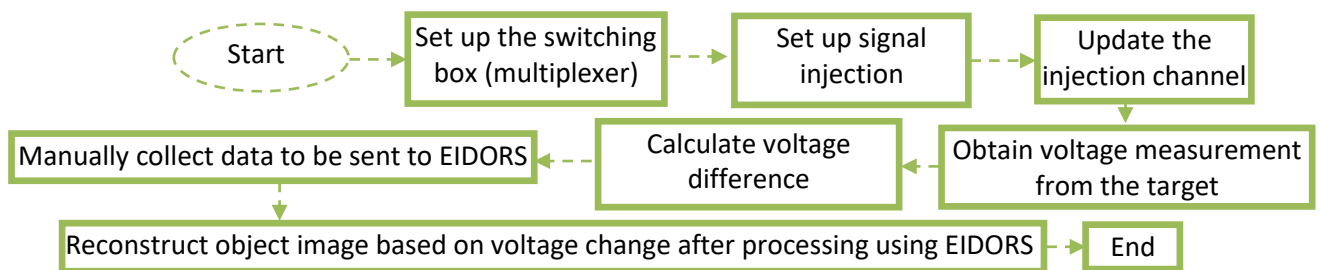


Figure 3.2: Indirect EIT system software flowchart.

Figure 3.3 shows the data acquisition (DAQ) assistant designed to measure 16 single-ended voltages simultaneously. As shown in the Figure, the signals are split based on the DAQ assistant set-up. Function for signal analysis and statistical calculation, is used to calculate the root mean square (RMS) from the measured signals for each channel. The RMS icon is a function used to indicate the processed signals. “Write to measurement file function” is used to read and save the measured RMS voltage, time, and date for each channel, respectively.

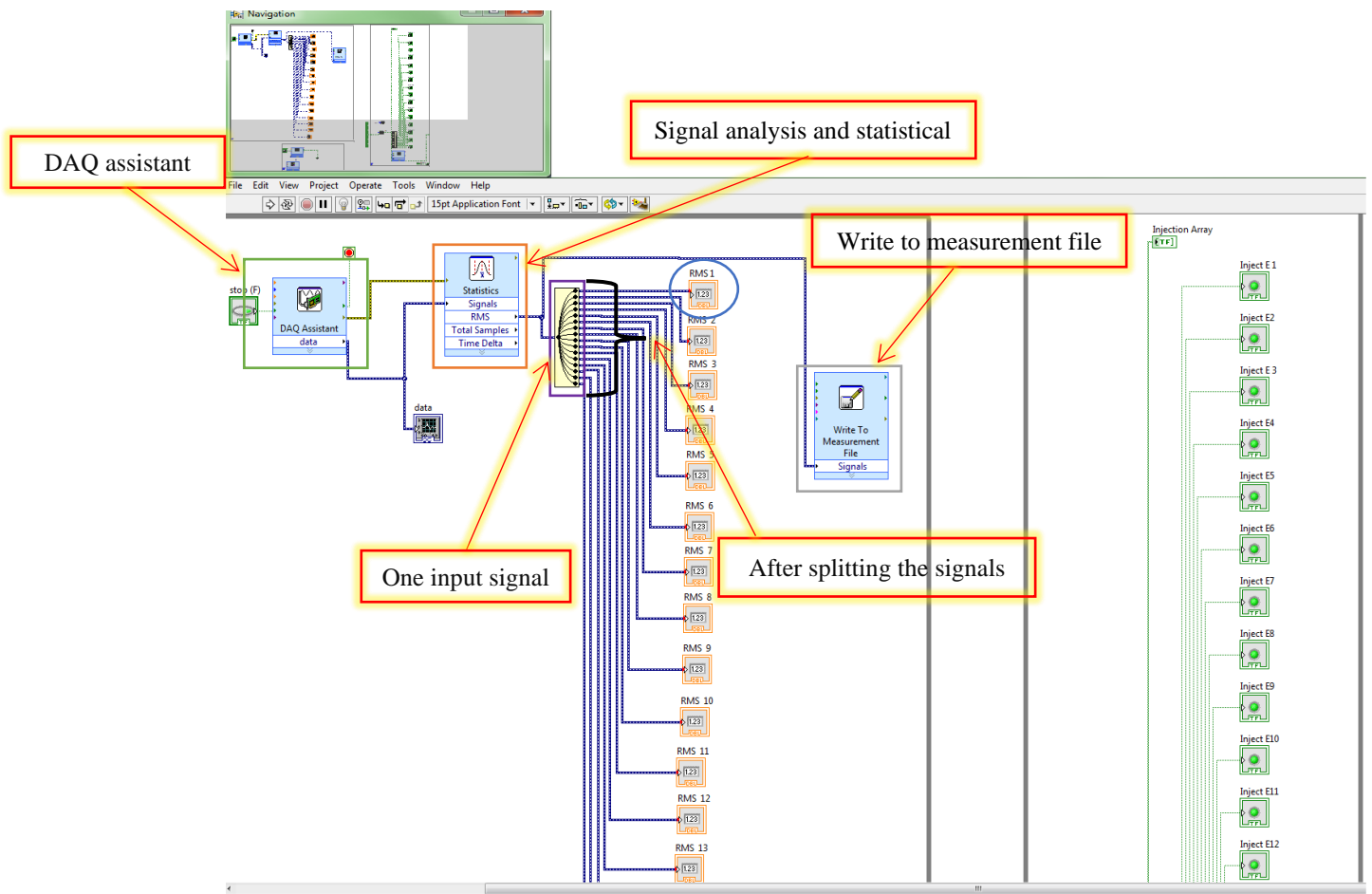


Figure 3.3: Program block diagram part 1.

The block diagram part 2 in Figure 3.4 shows the function generator and a digital control section. The DAQ assistant, which is designed to control the digital low and high signal that will switch ON and OFF the relays. The Index Array is a function indicates whether all the digital signals are ON or OFF. DAQ assistant3 is used as a digital signal generator. Moreover, the DAQ assistant2 is designed to generate a signal for one channel. The timer function is used as a time trigger for the 16-digital-line output. The DAQ system is designed to generate one signal for one channel.

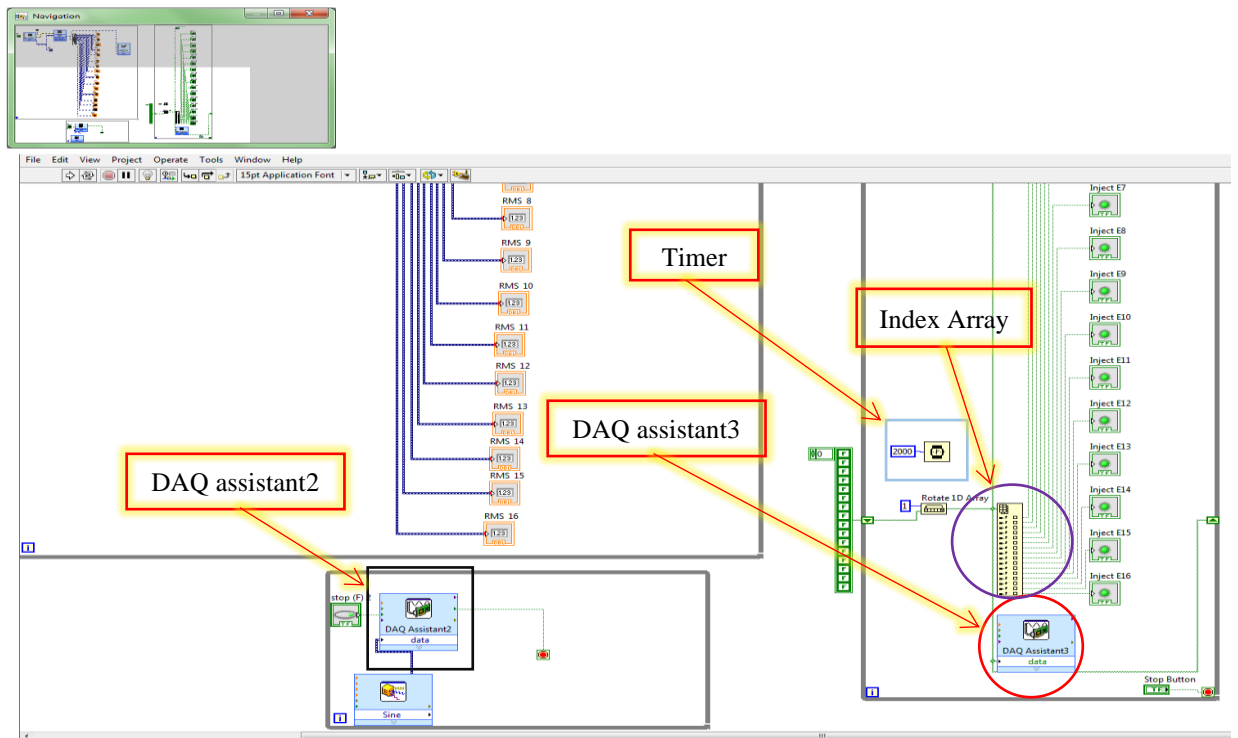


Figure 3.4: Program block diagram part 2.

Figure 3.5 shows the configuration of DAQ assistant windows. The signal input voltage ranges between -5 and 5, and it cannot exceed -10 to 10 V because of the DAQ input signal limitation. In this research, the current non-distractive testing does not exceed -5 to 5 V. The Single-ended (RSE) analogue input is selected for the terminal configuration. The main advantage is that it enables a greater number of readings compared to the differential measurement. Continuous samples mode is selected to provide a continuous real-time reading.

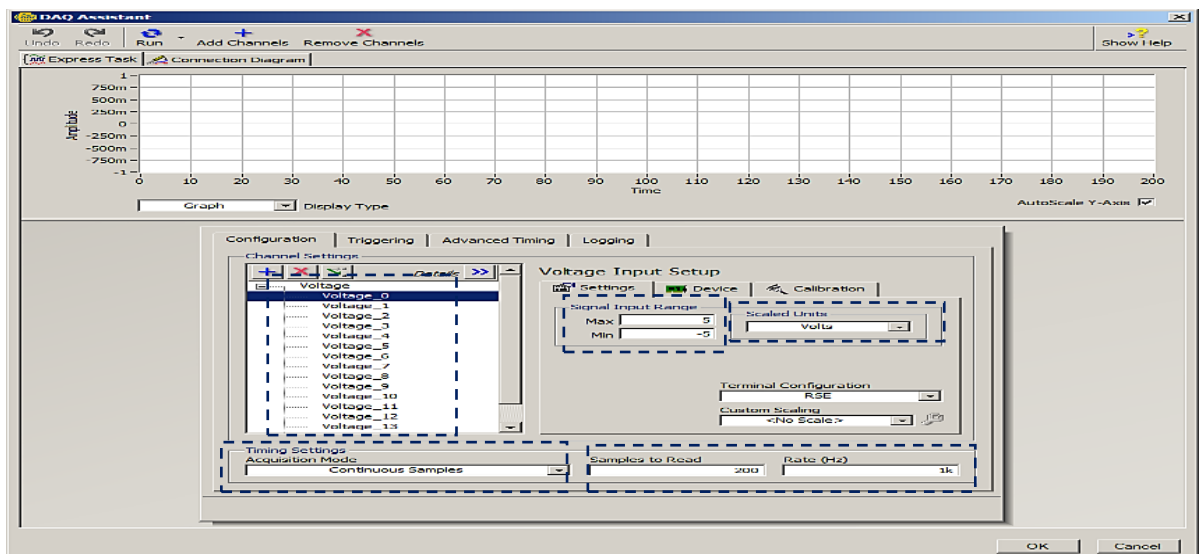


Figure 3.5: LabVIEW VI data acquisition assistant.

Figures 3.5 and 3.6 show the configuration set-up for the generated and the measured signals. The generated signal type, amplitude, phase, offset, and sampling rate were set as shown.

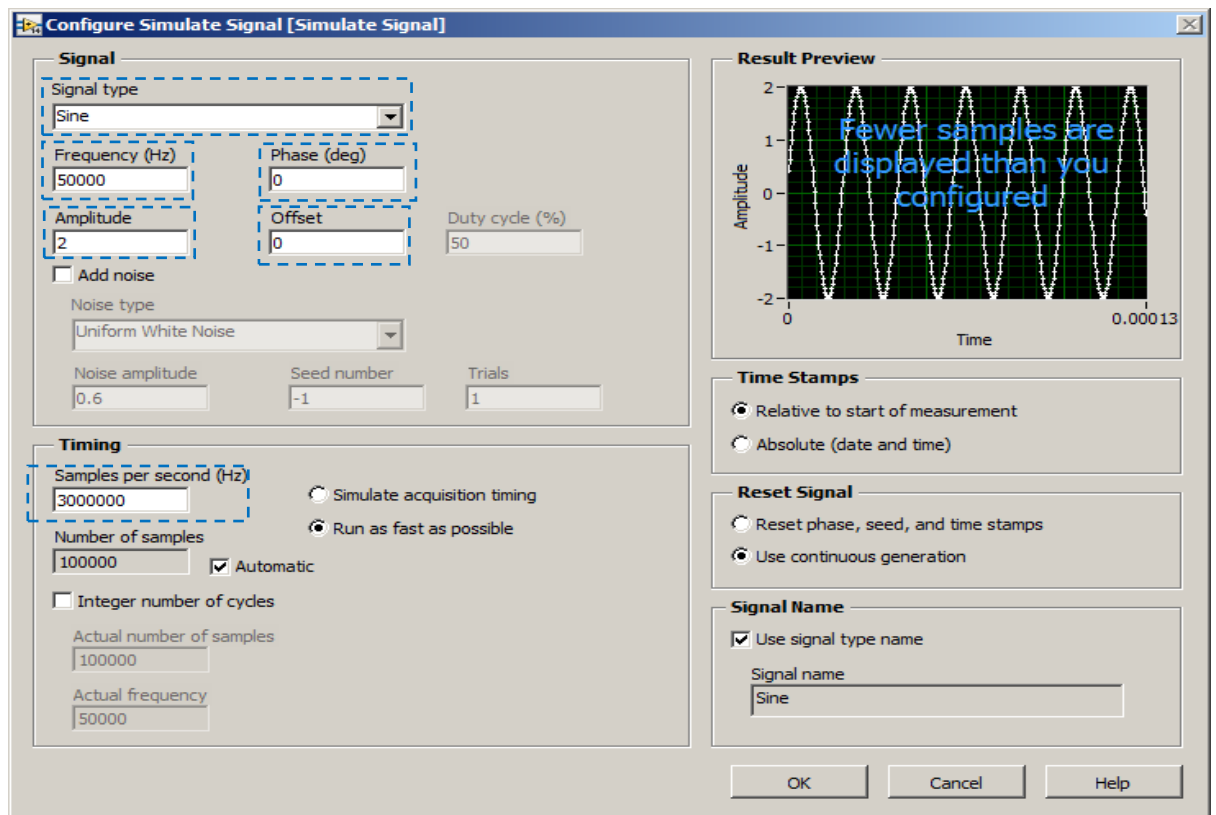


Figure 3.6: LabVIEW VI configure simulate signal window.

Figure 3.7 demonstrates the DAQ assistant configuration for the 16-digital-line output. Figure 3.8 displays the LabVIEW control and monitor front panel. The front panel can be divided into four sections, which they are the status indication of the 16-digital-signal output: either high or low, the real-time root mean square measurement for the 16 input channels, indicates and tracks the injection electrodes, and the waveform chart displays the 16 input-channel signals.

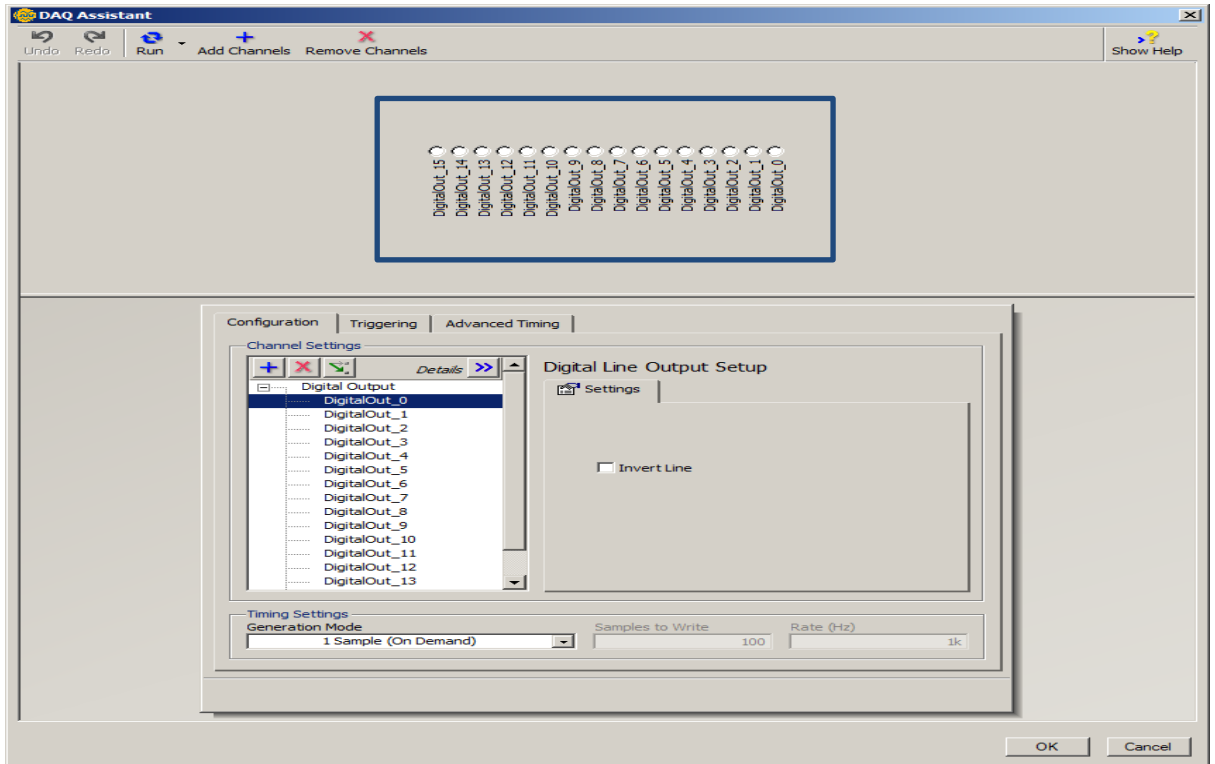


Figure 3.7: DAQ assistant for digital generator.

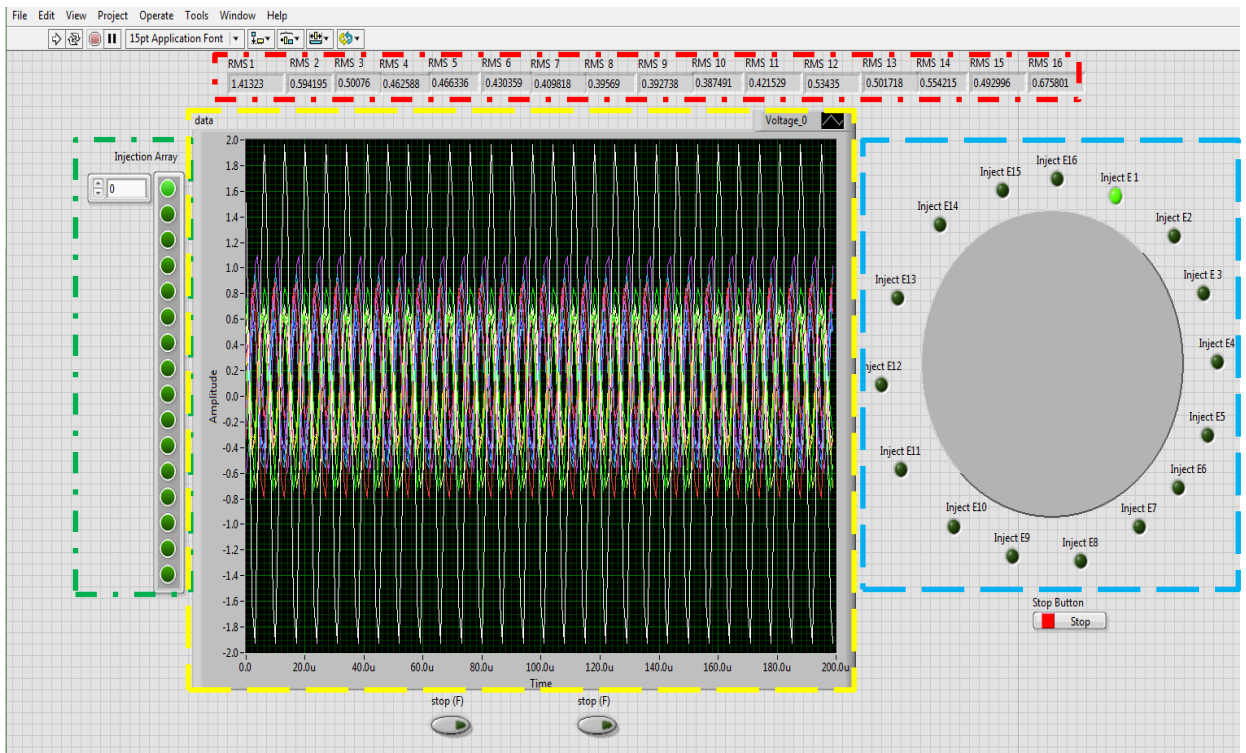


Figure 3.8: LabVIEW front panel.

3.1.1.2 Direct LabVIEW program

The direct program is the second LabVIEW program that was implemented. Figure 3.9 illustrates the basic steps of the direct EIT system software.

As shown in the figure, the process begins by setting up the I/O signals, which are set based on the application. For example, for application with a low electrical connectivity measurement environment, high injection is required for better electrical penetration, which leads to better signal reading. Then, the voltage change is calculated based on conductivity change for the targeted application. Next, voltage change response is calculated to estimate the impedance distribution of the area, and the voltage calculation and variance are regularized. Then, the processed data is sent directly to EIDORS to reconstruct the image. The direct LabVIEW program is stable, and it should be used efficiently to maximize its potential for each application.

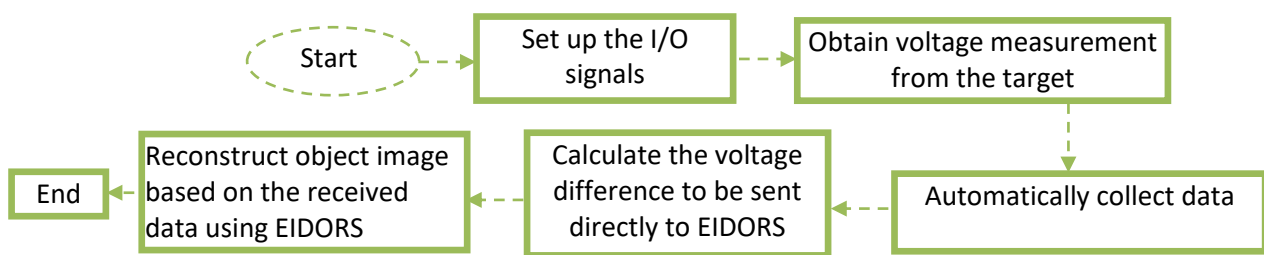


Figure 3.9: Direct EIT system software flowchart.

3.1.1.2.1 The function of the program

The software is designed to control the electrical energy which is applied to the surface electrodes on a targeted object. The software measures the resulting signals' voltages or currents on the periphery. The application can also work in simulation mode. The simulation mode can work without NI hardware and is designed for algorithm testing purposes. LabVIEW is used for excitation and data acquisition control as well as for data logging. MATLAB is employed for data processing.

The program, which is organized as a LabVIEW project, is depicted in Figure 3.10. The logical structure of the program includes the following software modules:

1. "Main.vi" is the main virtual instrument (VI) that contains all other program modules.
2. "DAQ.vi" is responsible for signal acquisition from electrodes and RMS calculation.

3. “DAQmxTask.vi” creates DAQmx task for signal acquisition from electrodes.
4. “WriteToDaq.vi” is responsible for digital signal generation to switch electrodes.

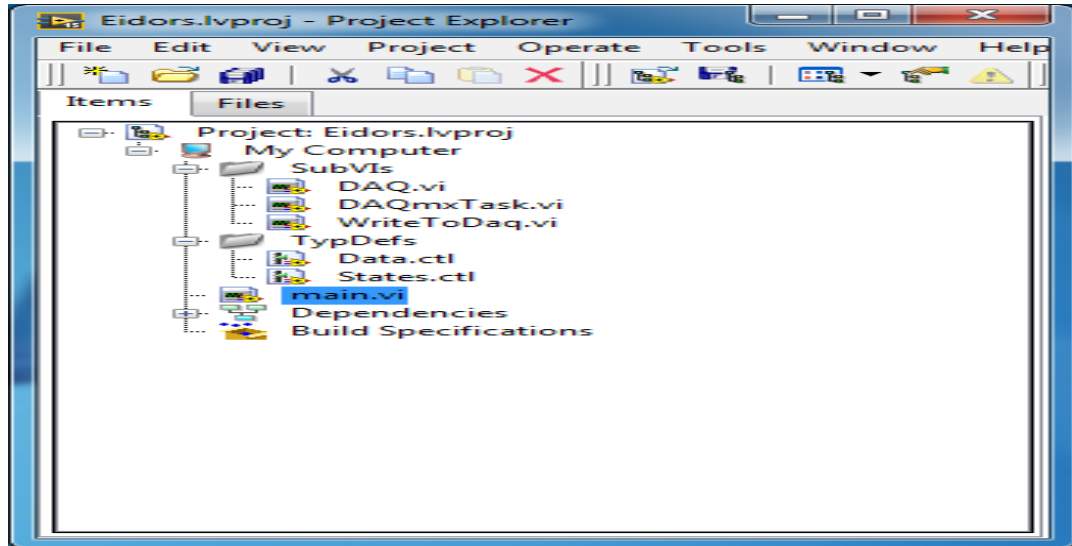


Figure 3.10: LabVIEW project.

3.1.1.2.2 Front panel description

The front panel of “Main.vi” is depicted in Figure 3.11.



Figure 3.11: Front panel of application.

The front panel window is the VI user interface. The Window toolbar is located at the top of the front panel.

3.1.1.2.3 User interface

The injection array, shown in Figure 3.12, is presented on the left side of the user interface (UI). The running program indicates the excited electrode (electrodes). The software execution mode switch is located next to the right side. The application can work both in real and simulation modes. The default mode is “Simulation”. The “Stop” button is located at the bottom of the switch.

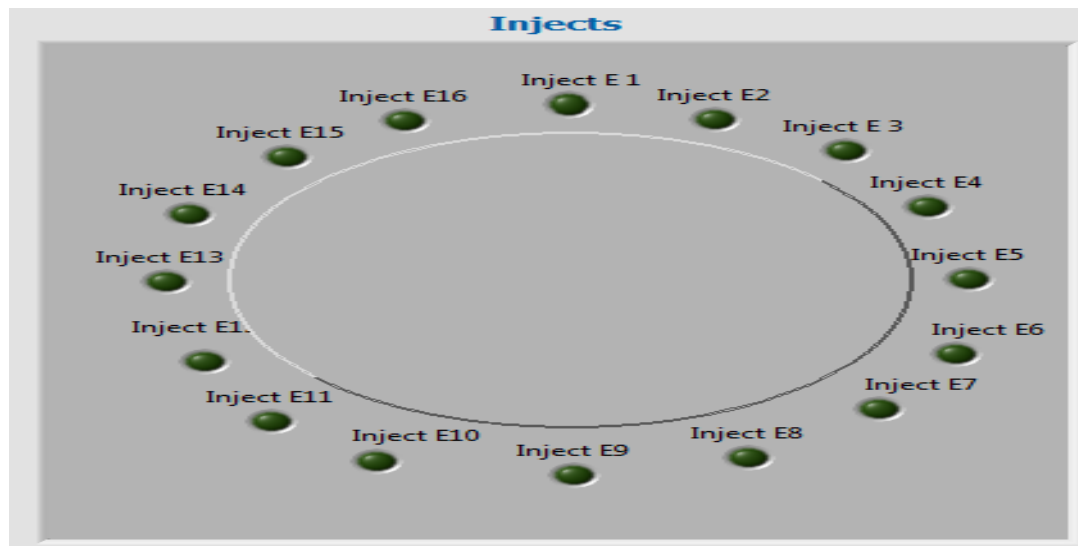


Figure 3.12: The injection array.

3.1.1.2.4 “Settings & Results” tab

The “Settings & Results” tab is located at the right side of the UI. It is designed to view data and the software configuration.

The homogeneous data and data arrays are indicated at the top of the “Data” tab, as shown in Figure 3.13. The indicator for the actual acquisition time is located below the “Data” tab. In the “Data acquisition” graph the same data are depicted as in “Data” array.

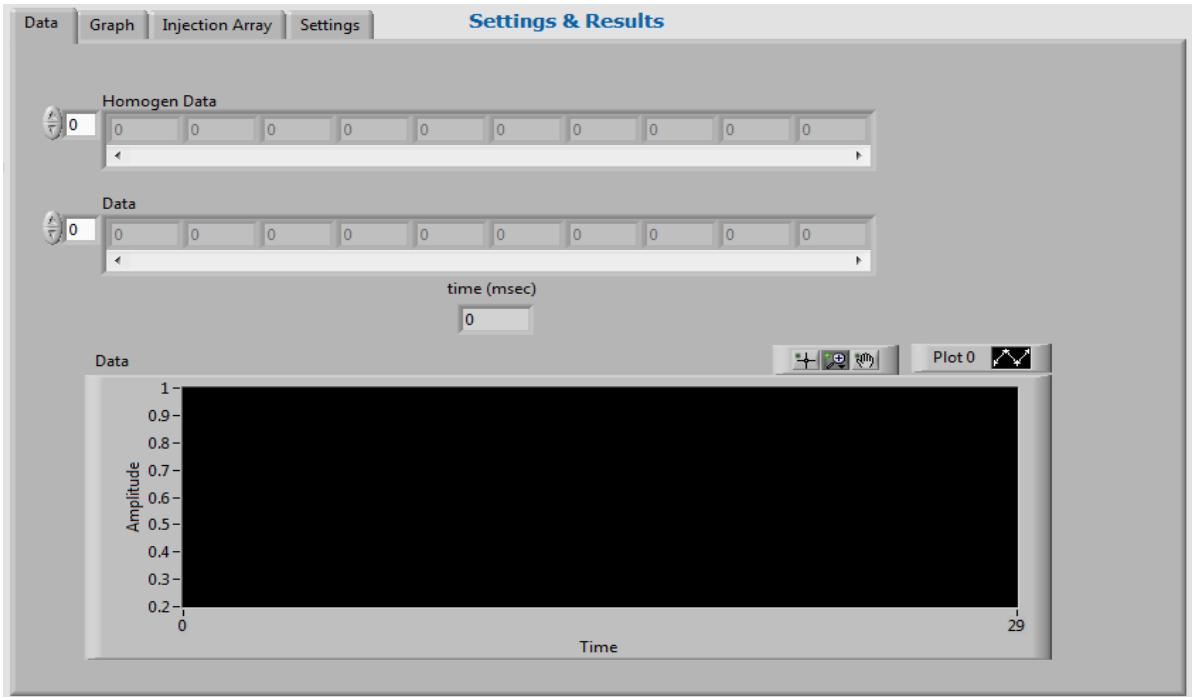


Figure 3.13: “Data” tab.

The RMS values for measurement from each electrode are displayed at the top of the “Graph” tab, as shown in Figure 3.14. The excitation signal is displayed at the bottom.

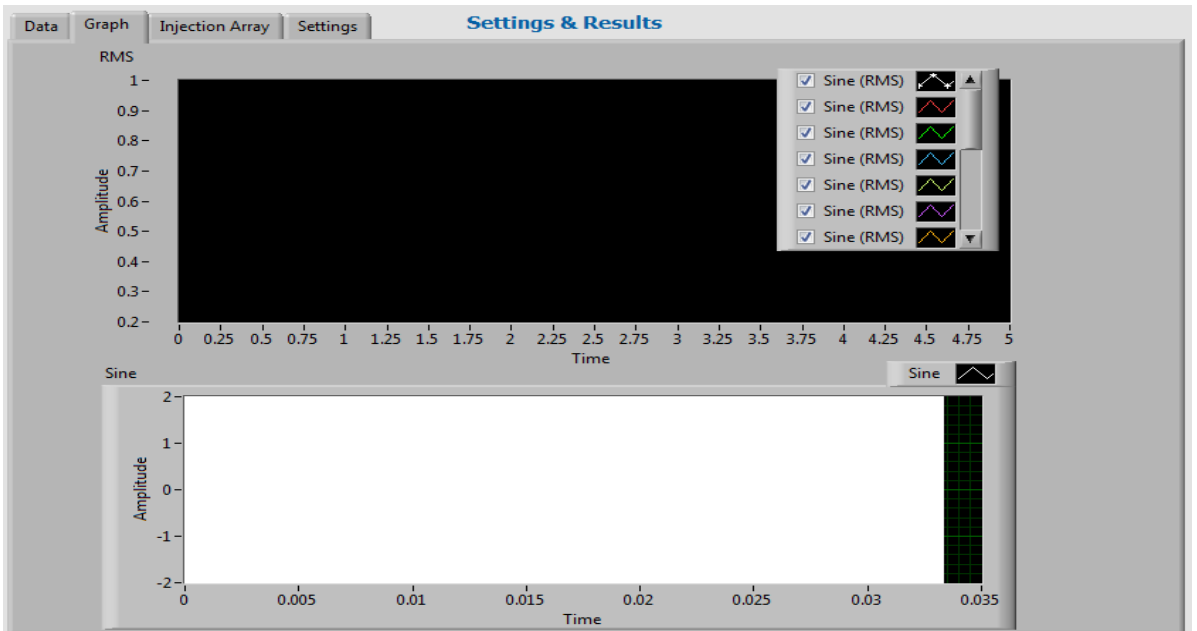


Figure 3.14: “Graph” tab.

The injection array is presented in the “Injection Array” tab, as shown in Figure 3.15. It indicates the excited electrode(s) as long as the program is running.



Figure 3.15: “Injection Array” tab.

The channels signal measurements configuration controls are located at the left side of the “Settings” tab, as shown in Figure 3.16.

The parameters for channel signal measurements configuration are the following:

- Physical channel – specifies the names of the physical channels to use to create virtual channels.
- Number of samples – specifies the number of samples to obtain for each channel.
- Rate – specifies the sampling rate in samples per channel and per second.
- Maximum –specifies in units the maximum value that is expected to be measured.
- Minimum –specifies in units the minimum value that is expected to be measured.
- Input terminal configuration – specifies the input terminal configuration for the channel.
- Channel name – specifies a name to assign to the virtual channel.
- Units – specifies the units to use to return voltage measurements.
- Custom scale name – specifies the name of a custom scale for the channel.

The excitation signal generator configuration controls are located at the right side of the “Settings” tab.

Parameters for channel excitation signal generator configuration are the following:

- Amplitude – waveform amplitude.
- Frequency (Hz) – waveform frequency in hertz.
- Offset – DC offset of the signal. The default value is 0.
- Phase (deg) – initial phase in degrees of the waveform. The default value is 0.

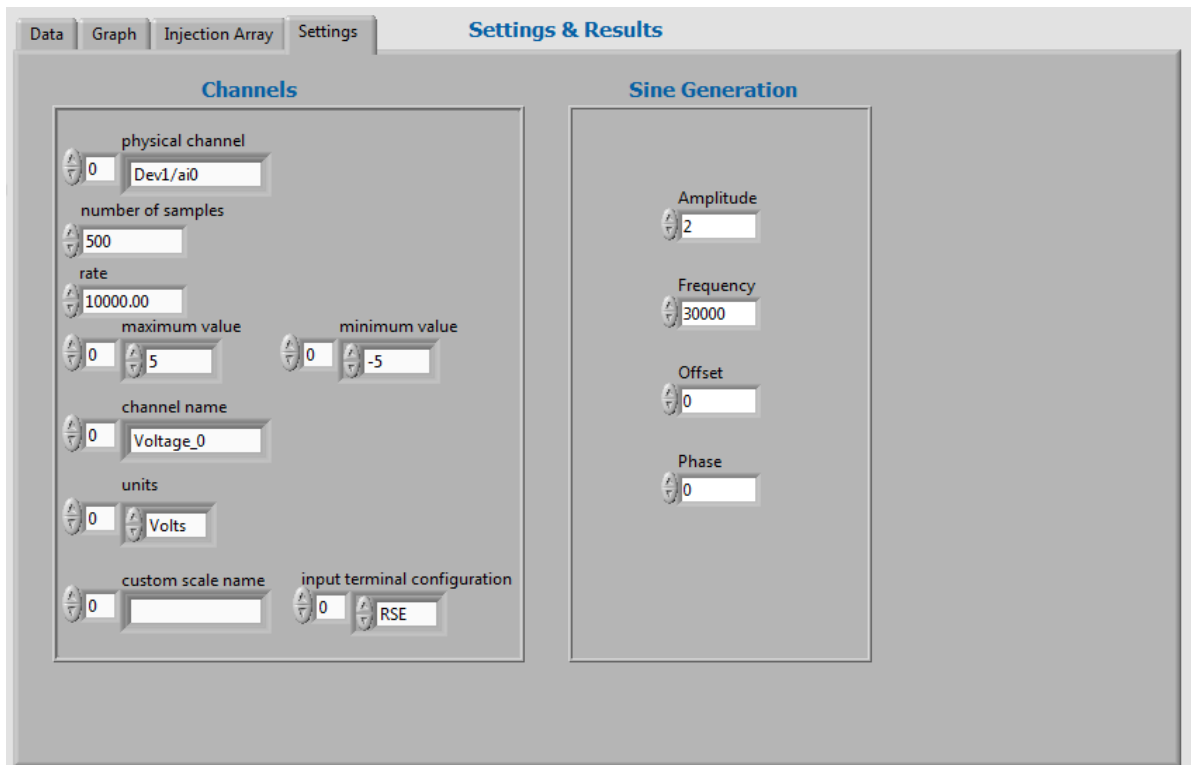


Figure 3.16: "Settings" tab.

3.1.1.2.5 Software architecture

The software consists of the following three loops: "Acquisition", "Processing & Save", and "Signal Generation", as shown in Figure 3.17. The "Acquisition" loop is responsible for electrode switching control and signal acquisition. The "Processing & Save" loop is responsible for data processing acquired from electrodes as well as data logging. The "Signal Generation" loop is responsible for electrode excitation. The communication between loops is based on shared variables, property node, and queue. The file path and stop command are transferred between loops by shared variables. The homogeneous data are transferred from "Acquisition" loop to "Processing & Save" via property node. The acquired signal data are transferred via queue. The program has an initialization part, which is organized as the "Initialization" case in the "Acquisition" loop. The deinitialization part is located at the right side of the "Acquisition" loop. It works after the "Stop" button is pressed from the UI and the loops are stopped. The deinitialization part is responsible for returning UI indicators to their initial state. In addition, it sets all digital channel values on the DAQ device to false. MATLAB is used for data processing. "MATLAB script node" is employed to run MATLAB code.

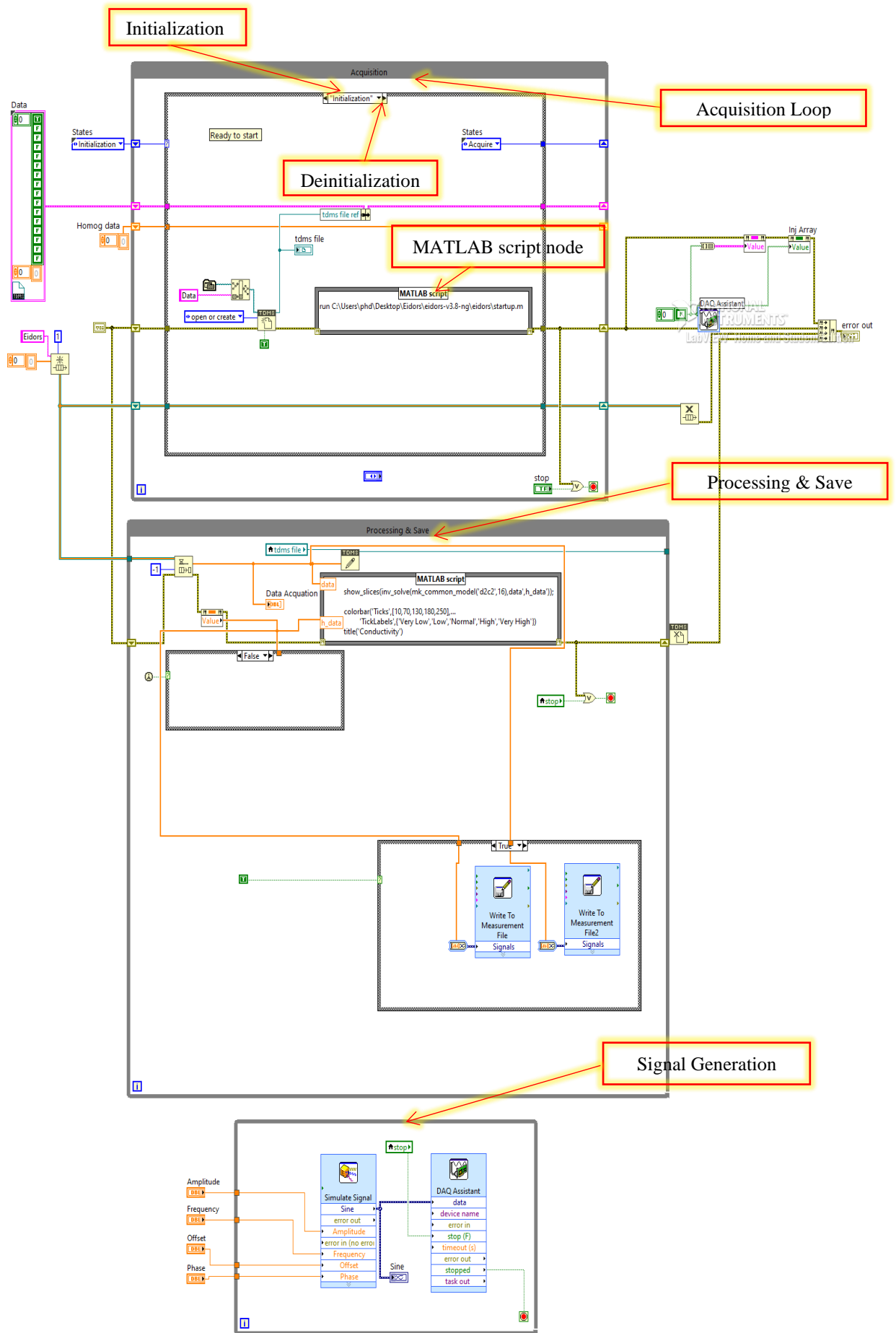


Figure 3.17: Software architecture.

3.1.1.2.6 State transition diagram of the program

The state transition diagram is depicted in Figure 3.18. The state diagram is used in different fields of sciences, especially in computer science, to define the behaviour of the system. It usually requires a system which contains a known number of states. There are three loops, and they are executed simultaneously. Each loop is presented as a sequence of states. In each state, some action takes place. Transitions from one state to another occur after state completion. The “Acquire” state of the “Acquisition” loop is a composite and has its own sub-states. The “Choice” node is designed to check if one full cycle is completed. One cycle means all 16 electrodes have been excited and 256 measurements have been taken from electrodes. All loops start when the “Run” button is pressed from the front panel of the application and stop when “STOP” is pressed. The Acquisition Loop starts with initialization. The initialization data file will be created to begin receiving processed measurement data at the same time, launching the Matlab to use EIDORS tools. The following states are sub-state for acquire state since it is responsible for obtaining the processed data. The first and second sub-state is the modify injection array to shift element with true value (Setting up the injection array measurements strategy) then run the injection array. The third sub-state is reading the samples from all the channels, then calculate the RMS values for all the channels. Formerly the data cycle, which contains 256 measurements it considered a completed data cycle, the data will be sent to Processing and Save Loop, but if it is not achieved, the data will be remeasured. In the Reset state, the data will be cleared. The last state in the acquisition loop is the Deinitialization, where return UI indicators states and “DO” states to “False”. The Processing and Save Loop have two states, the Wait for data and Data processing. After the data received, it will be executed using EIDORS tools. The last loop is Signal Generation only contain one repeated state, which is generating a signal with given parameters. For more Direct LabVIEW program details are attached to Appendix A.

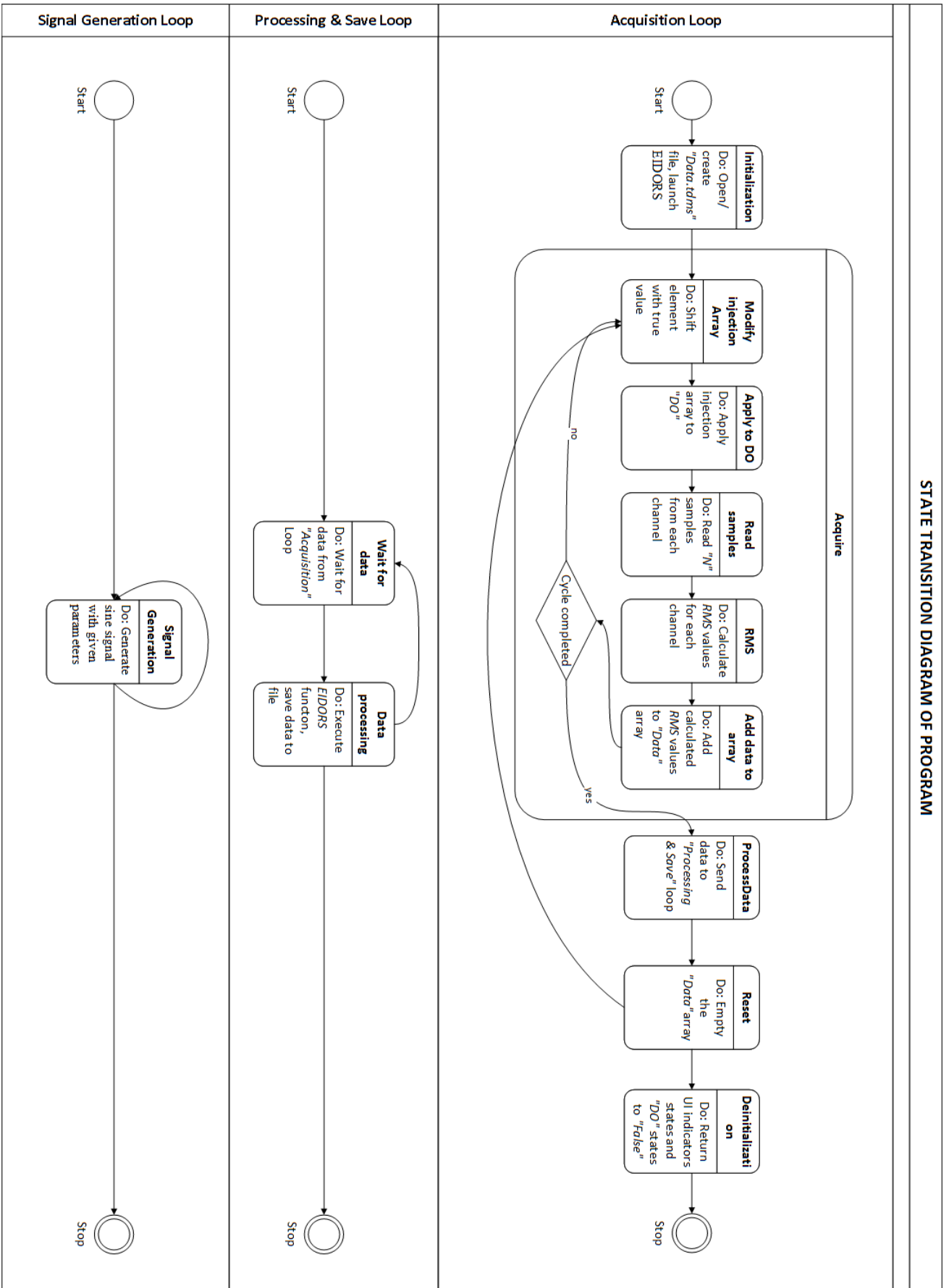


Figure 3.18: State transition diagram of program.

3.1.1.3 Measurement methods

The current EIT system can use several measurement methods, such as adjacent and opposite. In this research, the focus was on the adjacent method since it is employed by the EIDORS. To provide more insight into the current EIT monitoring system using LabVIEW, Figure 3.19 demonstrates the stages of the process in a flowchart. The electrical signals are injected into Channel 1 while the electrical signal measurements are taken simultaneously from all 16 channels. Then, the signal injection is shifted to the neighbouring channel, which is channel 2, and electrical signal measurements are obtained from all the channels. This procedure is repeated for each channel, in turn. All the channels are allocated to a dependent electrode. Furthermore, the number of independent measurements, M , is $N \times N$, where N is the total number of electrodes (16). Therefore, the total number of independent measurements, in this case, is 256. Basically, this process must be performed for every image slide, and the delay time is controlled; it depends on the measurement sampling rate. Therefore, a high measurement sampling rate requires a longer time to process than a lower sampling rate. Additionally, an electrode injection cycle is demonstrated in Table 3.1, which presents pictures for a full electrode injection cycle based on the adjacent measurement strategy using LabVIEW.

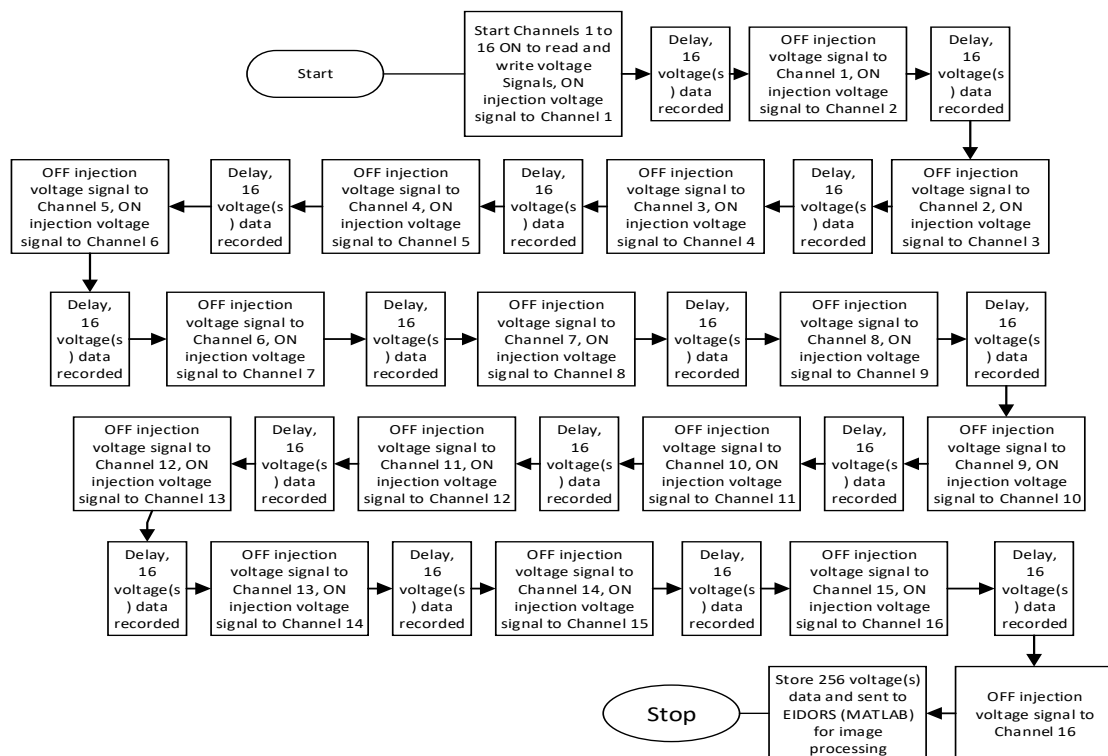
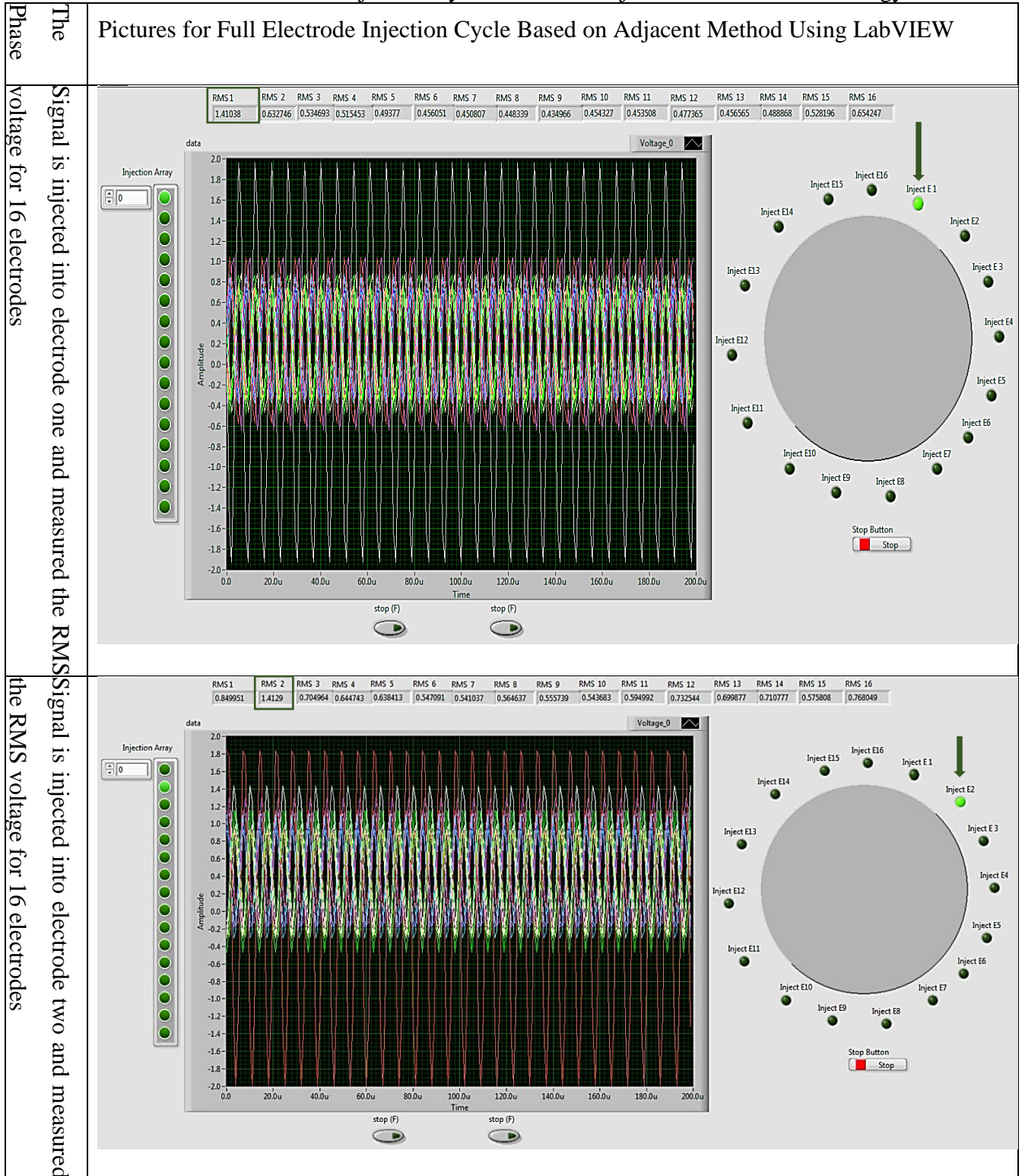


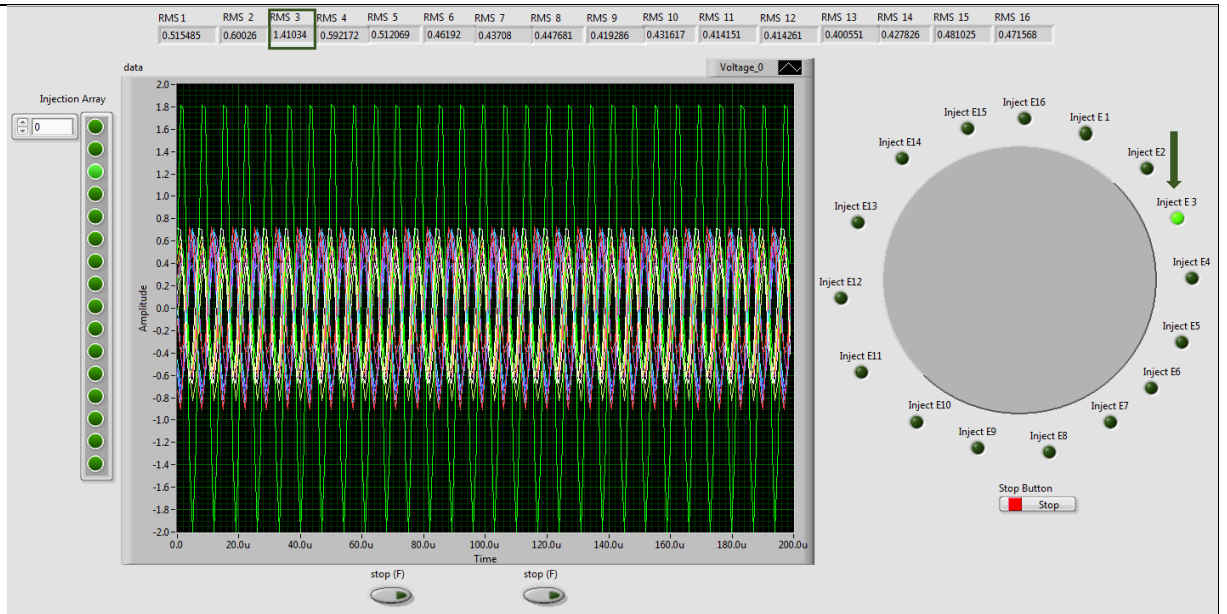
Figure 3.19: Flowchart of LabVIEW program adjacent measurement strategy.

Table 3.1: Full Electrode Injection Cycle Based on Adjacent Measurement Strategy.



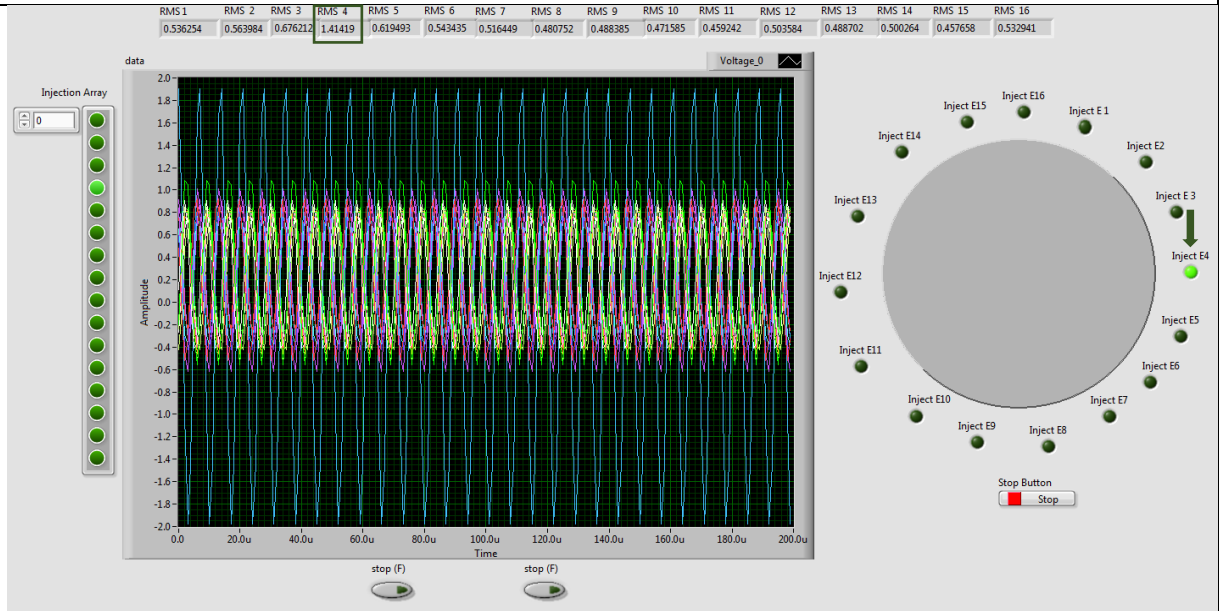
the RMS voltage for 16 electrodes

Signal is injected into electrode three and measured



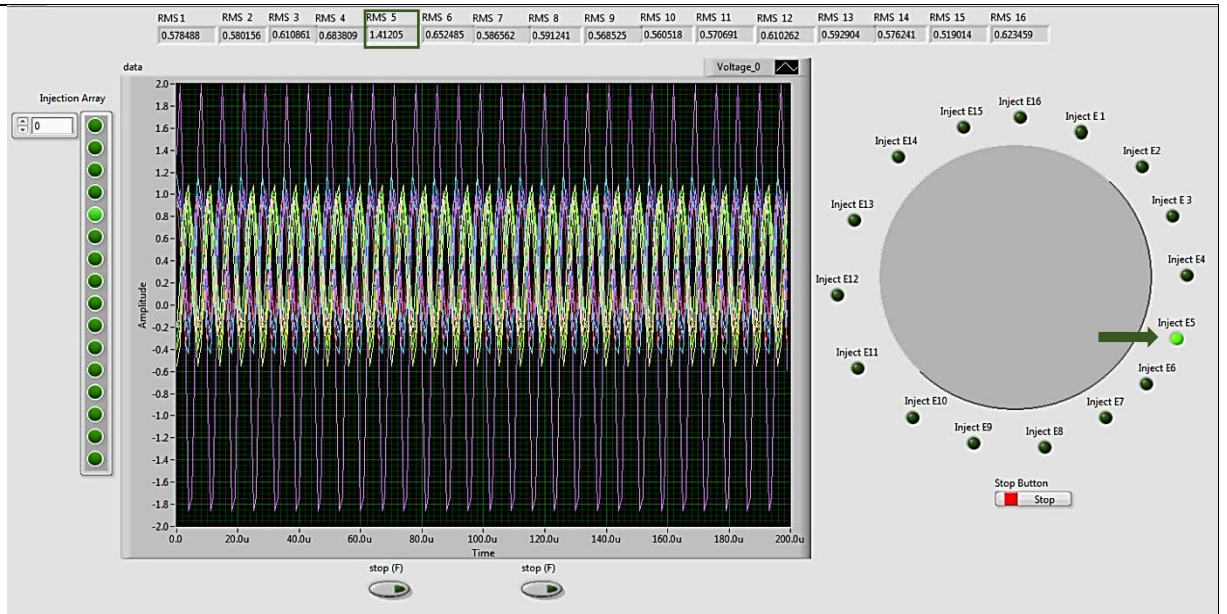
the RMS voltage for 16 electrodes

Signal is injected into electrode four and measured



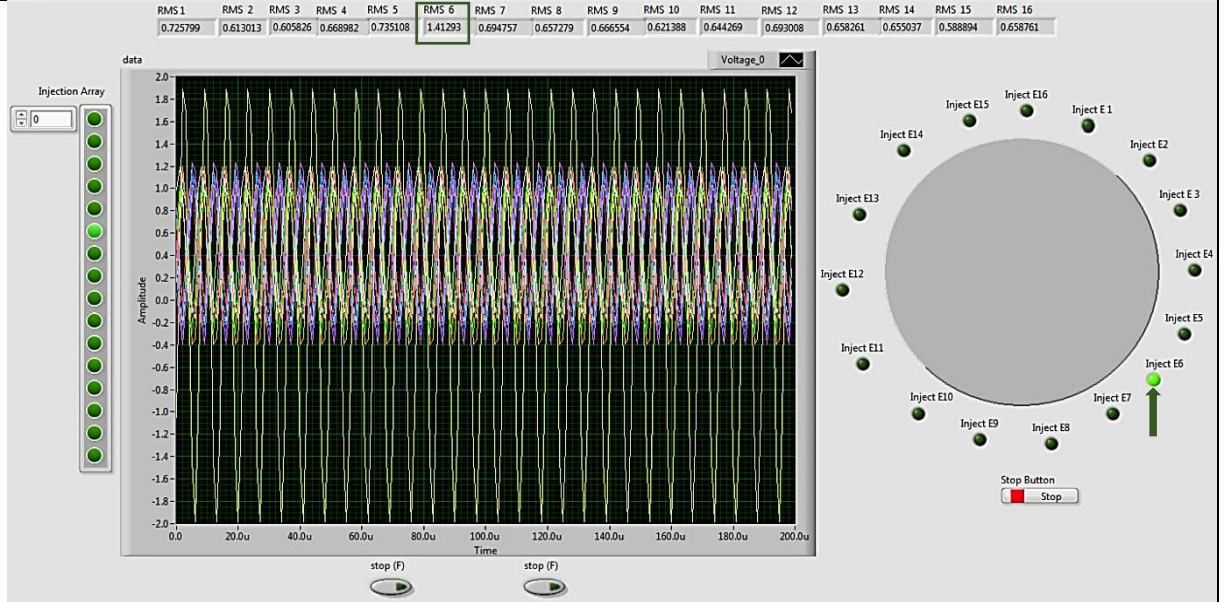
the RMS voltage for 16 electrodes

Signal is injected into electrode five and measured



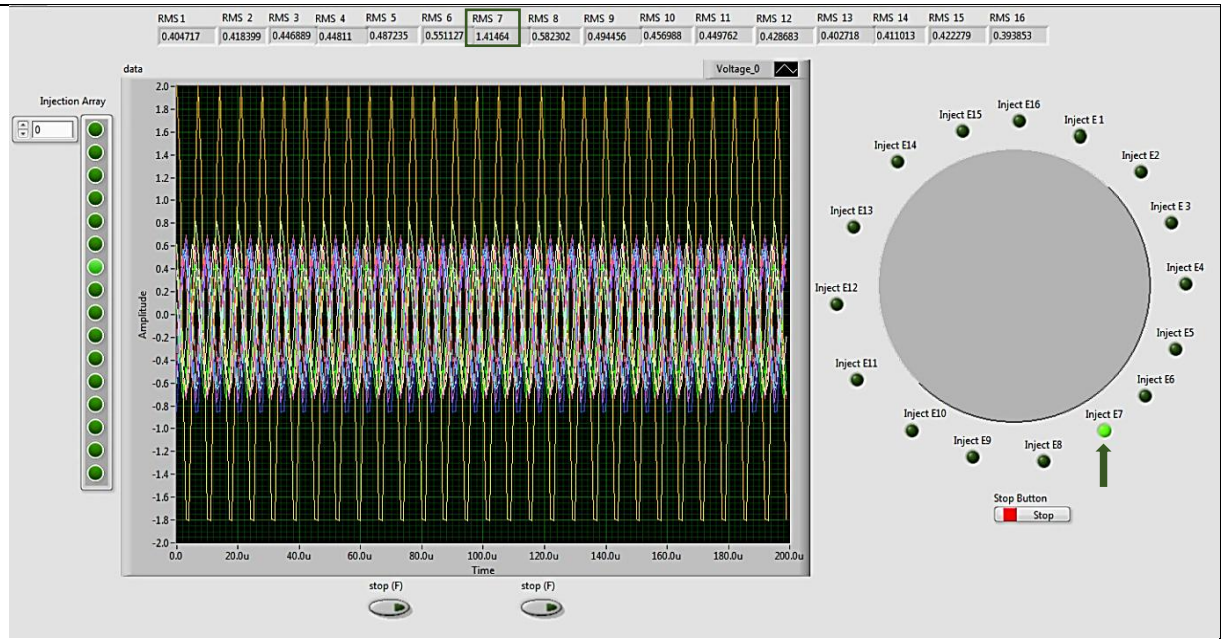
the RMS voltage for 16 electrodes

Signal is injected into electrode six and measured



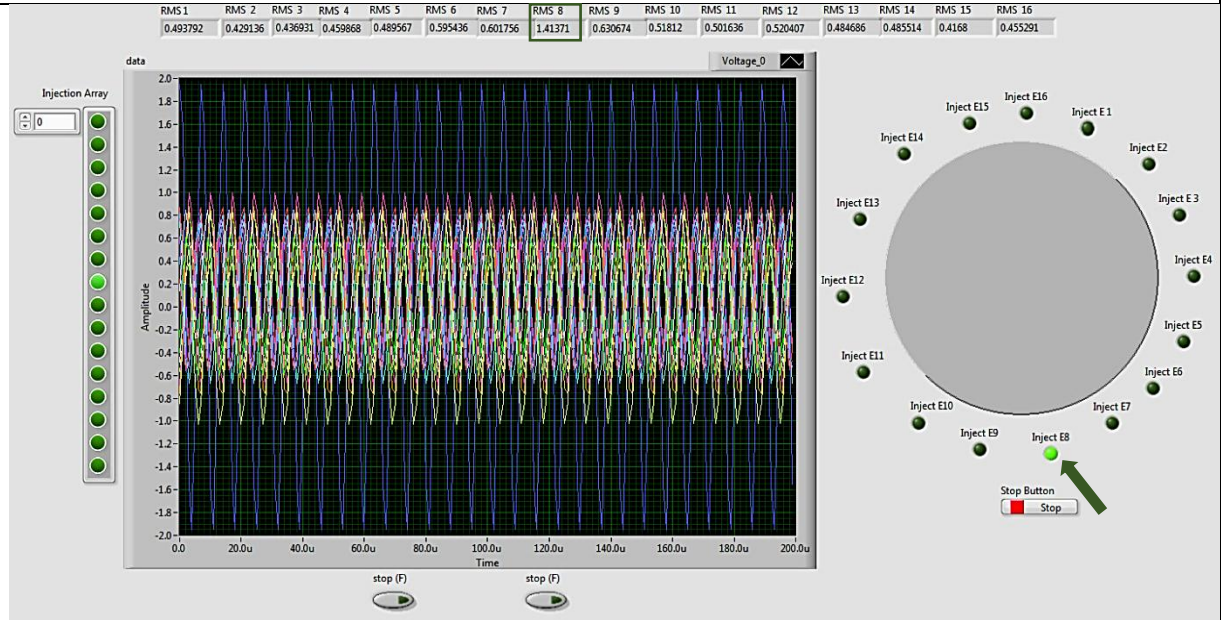
the RMS voltage for 16 electrodes

Signal is injected into electrode seven and measured



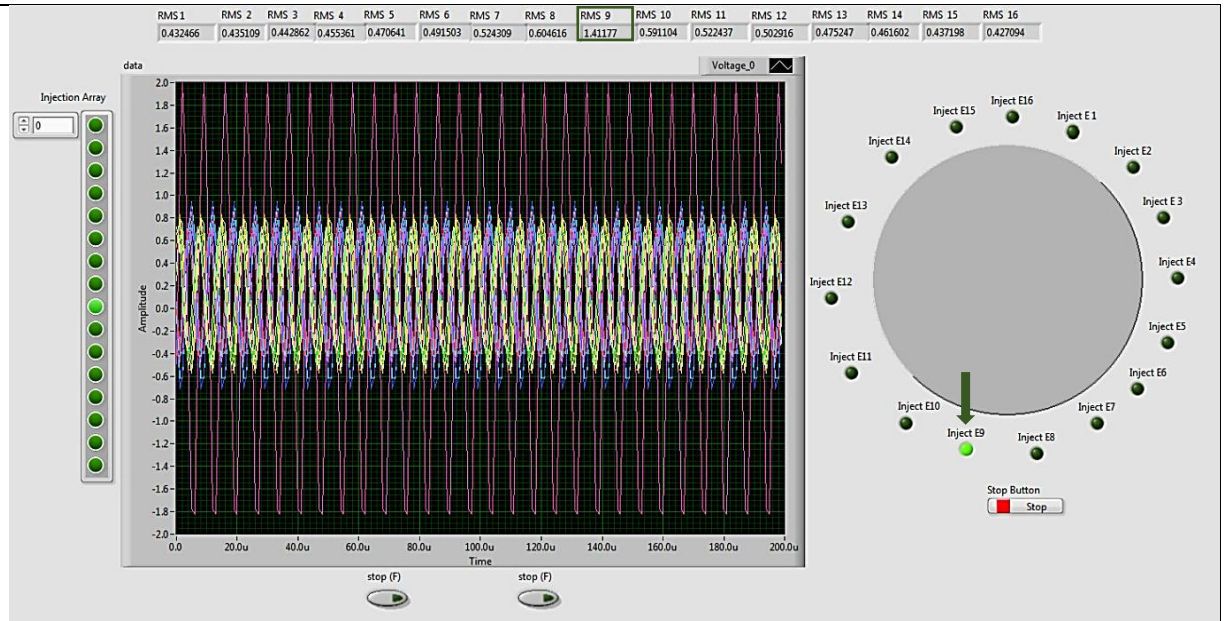
the RMS voltage for 16 electrodes

Signal is injected into electrode eight and measured



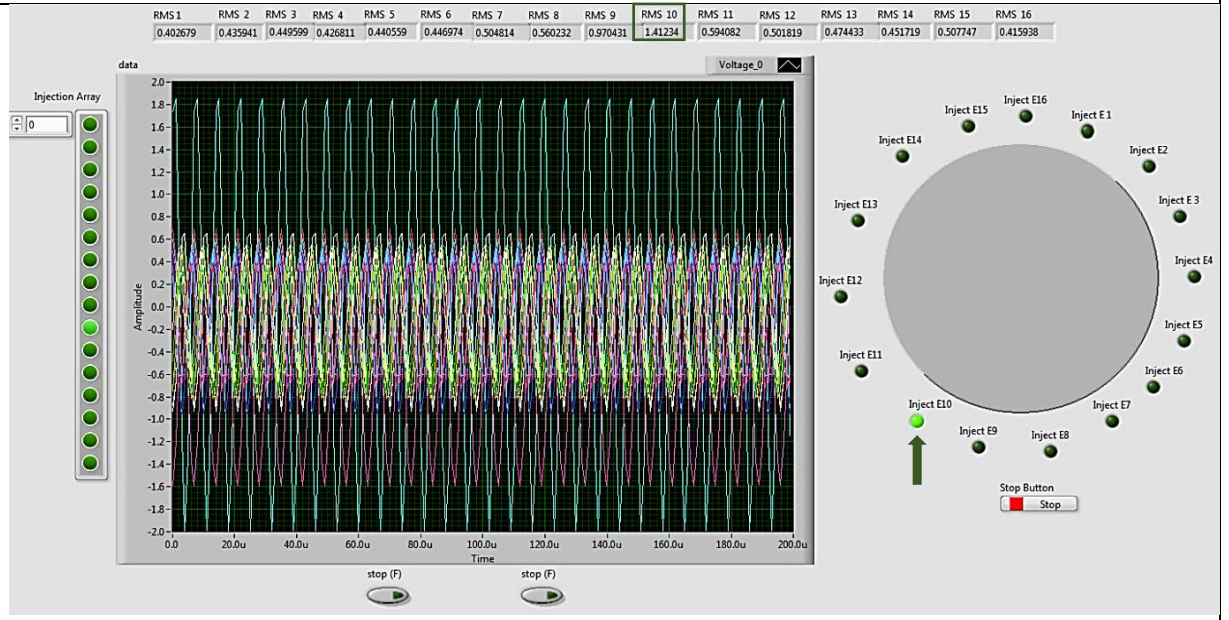
the RMS voltage for 16 electrodes

Signal is injected into electrode nine and measured

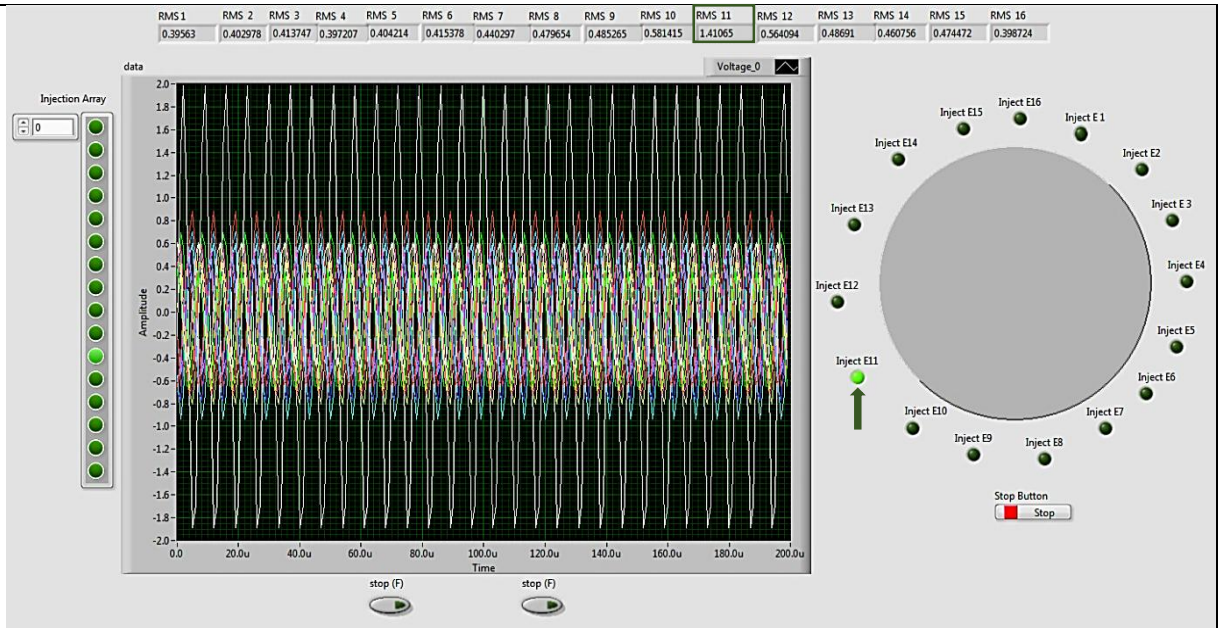


the RMS voltage for 16 electrodes

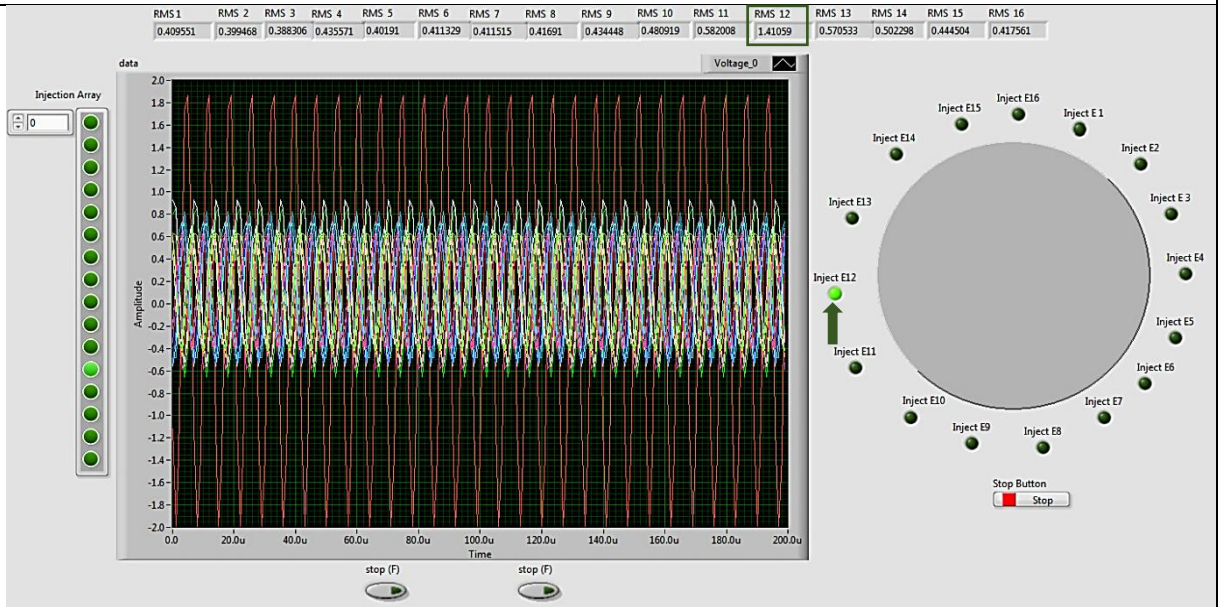
Signal is injected into electrode ten and measured



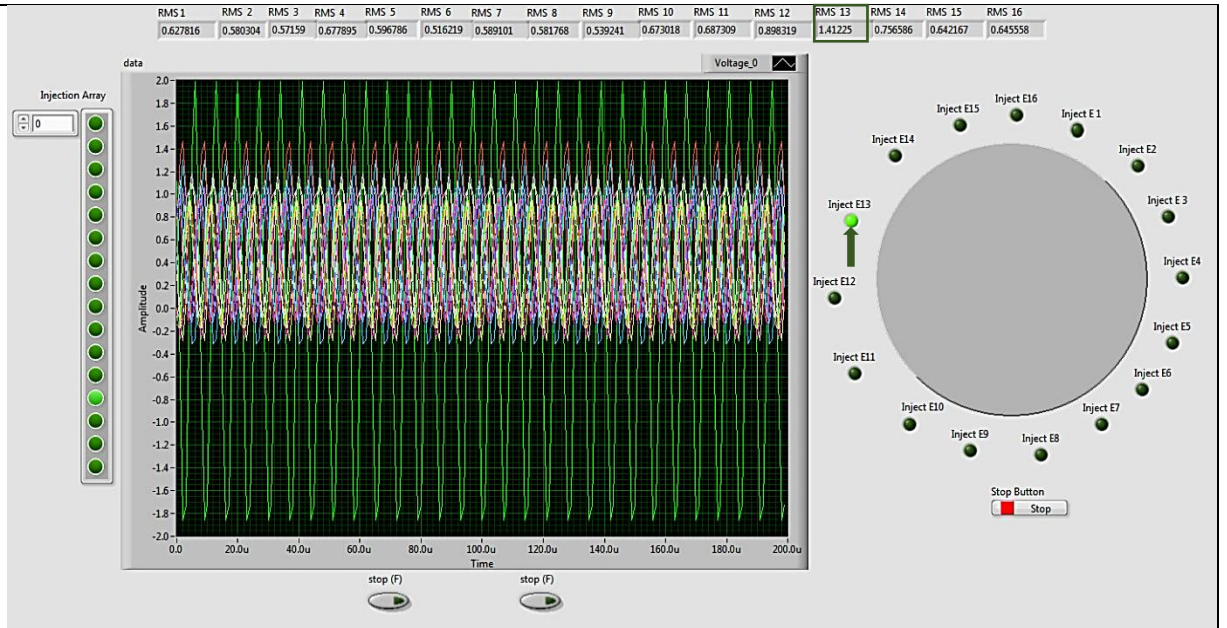
Signal is injected into electrode eleven and measured the RMS voltage for 16 electrodes



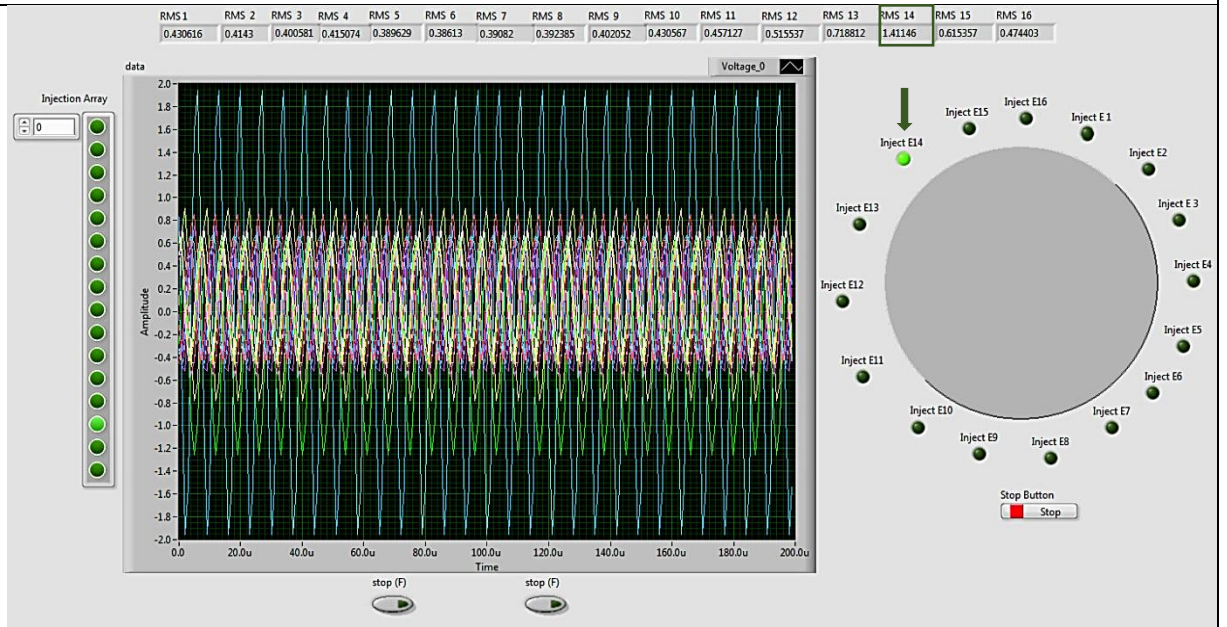
Signal is injected into electrode twelve and measured the RMS voltage for 16 electrodes



Signal is injected into electrode thirteen and measured the RMS voltage for 16 electrodes

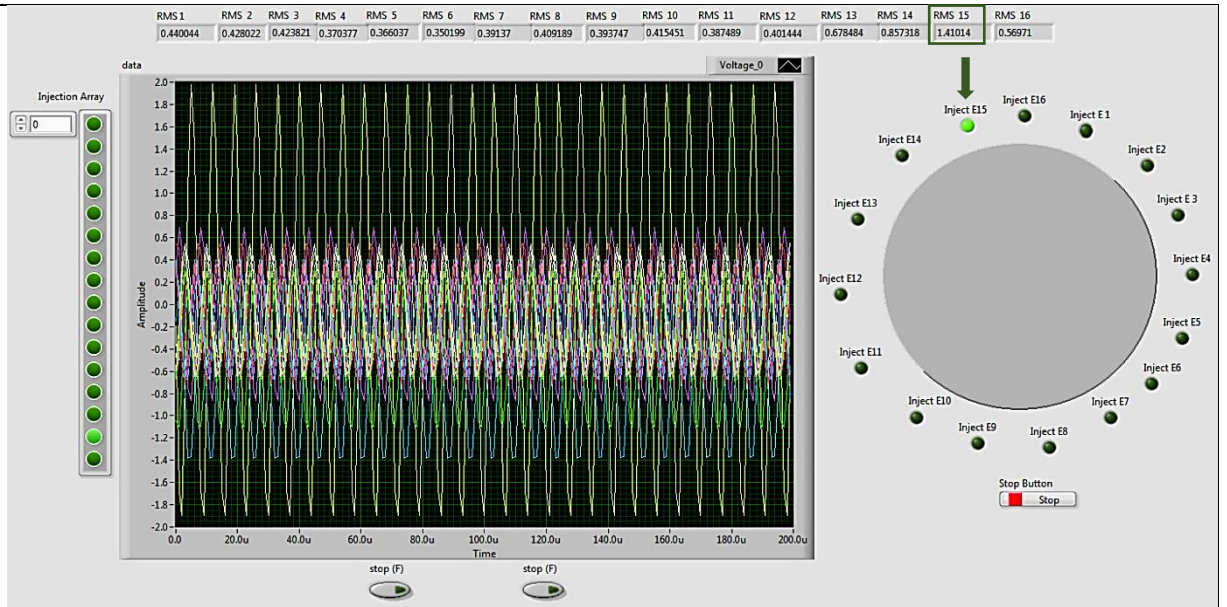


Signal is injected into electrode fourteen and measured the RMS voltage for 16 electrodes



measured the RMS voltage for 16 electrodes

Signal is injected into electrode fifteen and



measured the RMS voltage for 16 electrodes

Signal is injected into electrode sixteen and

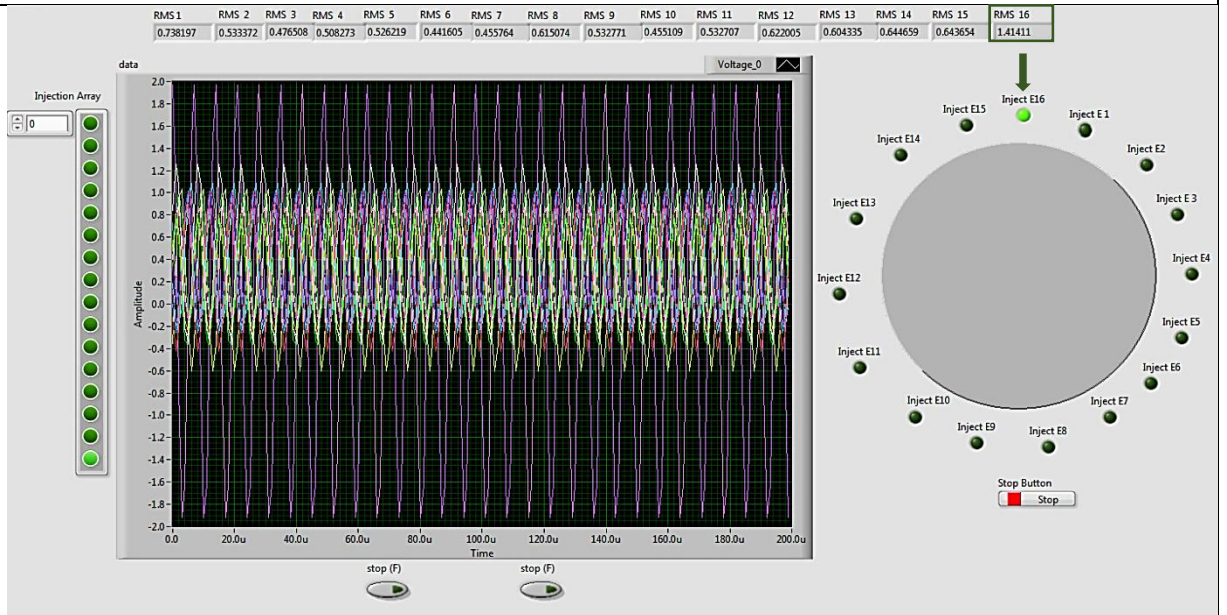


Figure 3.20 shows the full electrode injection cycle chart using real 256 RMS measurements obtained from 16 electrodes. This chart illustrated the operation sequence responses and functionality, which show reliable performances. Each electrode measurements and injection chart demonstrate in the Appendix.

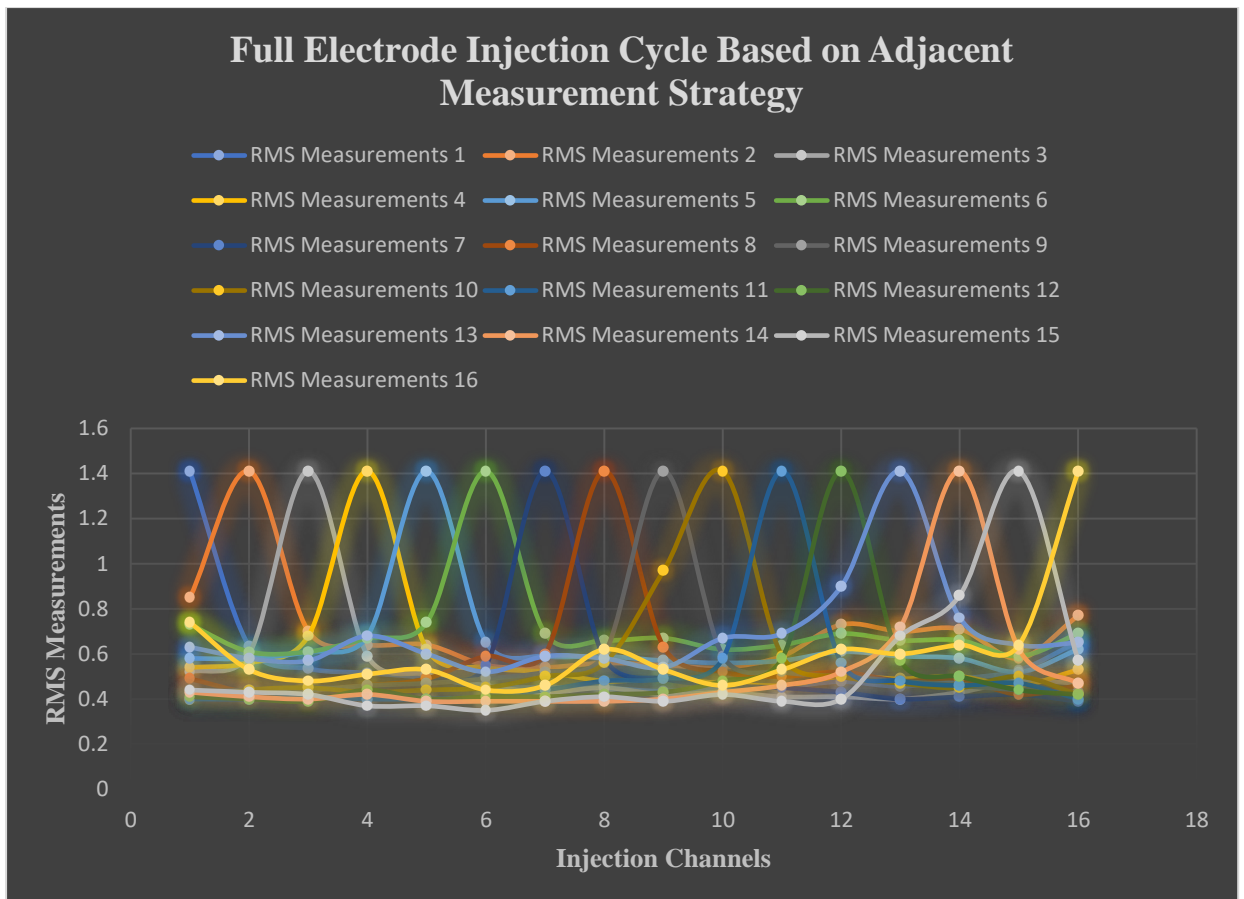


Figure 3.20: Full electrode injection cycle RMS measurements.

Figures 3.21 and 3.22 show an example of the current EIT system measurement strategy and the capability of applying some of the measurement methods, such as the opposite method. Though, different data collection strategies exist, such as opposite, cross, and adjacent measurement; these strategies are used for extracting complete dataset measurements of electric potential at the boundary walls of the object. The existent EIT system only uses one measurement strategy unlike the developed system. Applying different EIT measurement strategies will solve some of the electrical signal propagation issues and will improve the detecting and tracking of the resistivity change for certain EIT applications (Guermandi et al., 2014).

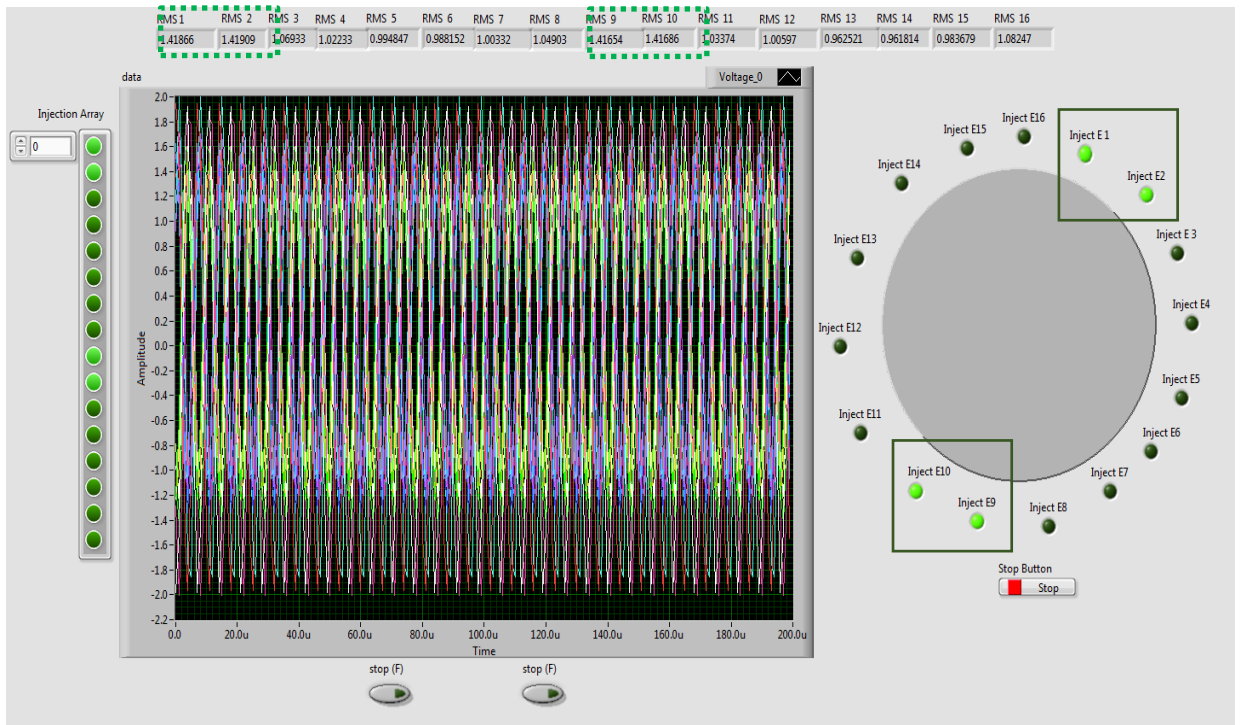


Figure 3.21: Opposite measurement strategy.

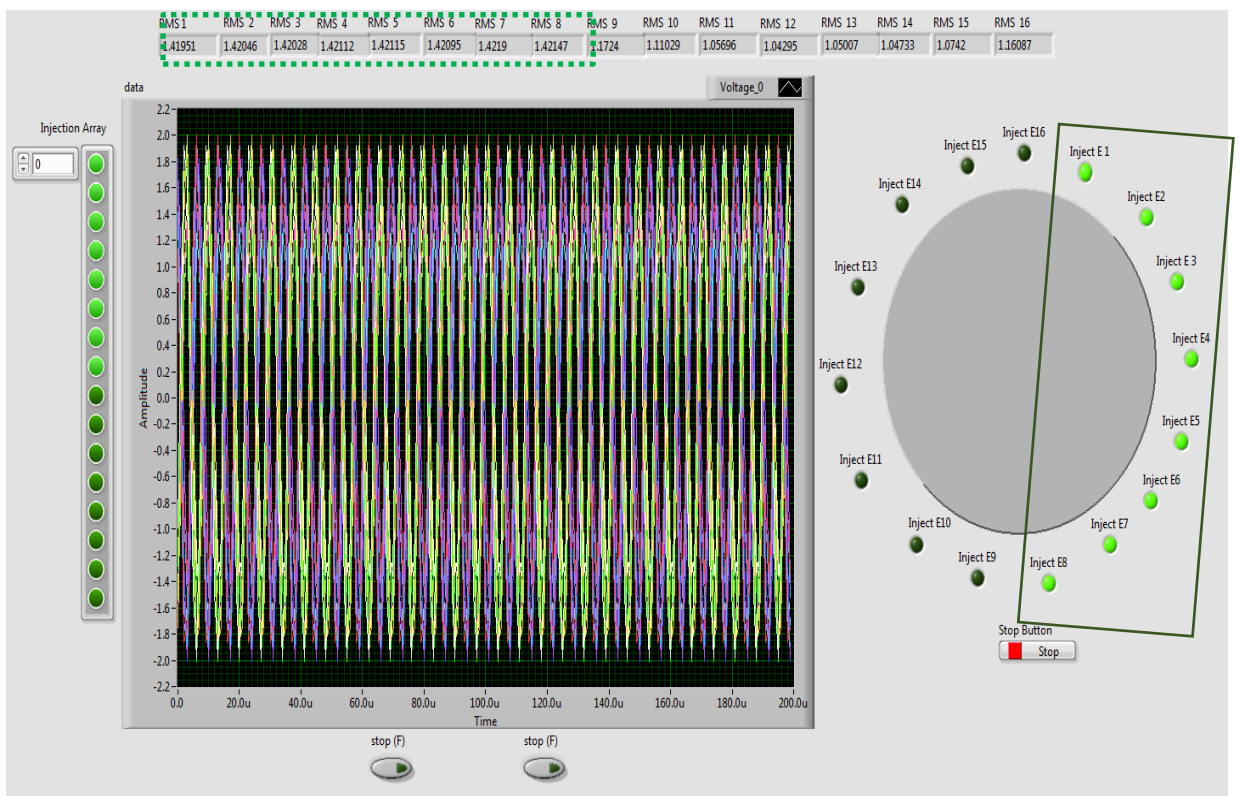


Figure 3.22: Random measurement strategy.

3.2 Electrical impedance tomography system hardware

EIT is a technique based on the electrical conductivities (current and voltage) of any conductive object based on the characteristics of the element (Ammari et al., 2017; Martin and Choi, 2016; Tallman and Wang, 2016; Y. Yang et al., 2017). A new EIT system was developed in this research and is shown in Figure 3.23. Fundamentally, the system consists of 16 electrodes made of electrically conductive materials which attach to the surface of an object. The electrical signal can be injected into all 16 electrodes through a controllable switching box. The injection switching box is controlled via a pre-programmed NI PCI-6281 data acquisition (DAQ) system using LabVIEW. The range of the injected signal frequency is 12 kHz to 1 MHz; sampling rate is up to 3000000 samples per second; and range of the voltage amplitude is -5 to 5. The current switching box allow the users to apply different impedance measurement methods, such as neighbouring, opposite, and cross methods. The EIT system can measure up to 16 single-ended and eight differential measurements. However, the eight differential measurements only can be used without the switching box since it only supports 16 single-ended channels. The system is calibrated using a 17-resistor network circuit. The EIT system consists of a five-part electrode array, testing vessels, switching box, DAQ system, and operating program. The 16-electrode data acquisition system was built and implemented inside different vessels to sense the impedance changes. The measurement sensitivity of the EIT system can be controlled through careful design and optimization of the injected signals. Key parameters include the amplitude, frequency, and waveform of the injected current or voltage. For instance, increasing the amplitude of the injected signal enhances the signal-to-noise ratio (SNR), enabling the detection of smaller impedance changes. Similarly, selecting an appropriate frequency ensures that the signal interacts effectively with the medium under study, as different materials exhibit varying impedance characteristics across frequencies. Additionally, using well-defined waveforms (e.g., sinusoidal or pulsed signals) minimizes distortion and improves the system's ability to resolve subtle conductivity variations. These adjustments, combined with proper calibration and filtering techniques, allow for precise control over the system's sensitivity.

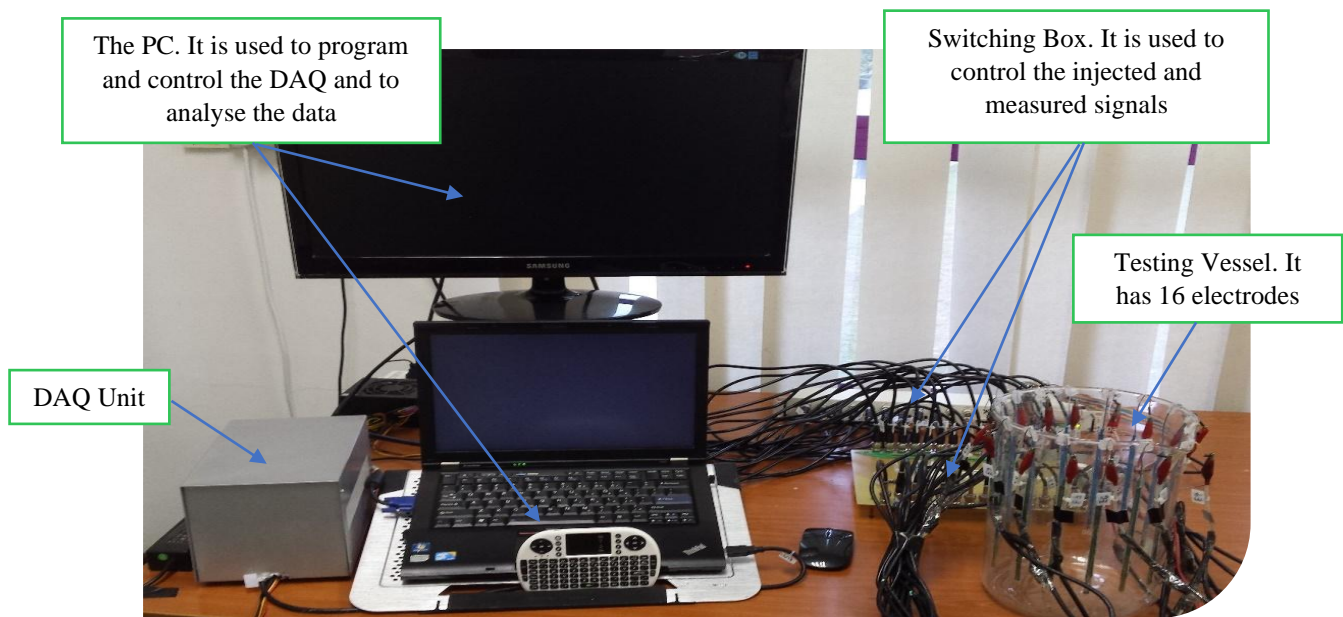


Figure 3.20: Set-up of the developed EIT system.

Figure 3.24 displays the basic EIT hardware block diagram. A sixteen-electrode array is attached to a cylindrical vessel to measure the voltage and current changes inside the beaker. The I/O switching box, controlled by 16 digital channels, is pre-programmed to control the DAQ system, monitor excitation signals for 16 electrodes, and simultaneously measure the voltage and current changes. The switching box schematic and layout are designed by Diptrace, as shown in Figures 3.27 and 3.28. Connector Blocks BNC-2090A are BNC-terminal-shielded connector blocks used as connectors between the electrodes and DAQ system for secure connectivity of input and output signals to determine whether they are digital or analog signals commanded by the DAQ system. The DAQ is monitored by a pre-programmed LabVIEW programme. The BNC-2090A supports 8 differential analog and 16 single-ended BNC input signals. Furthermore, it can generate up to 2 BNC analog and 24 digital I/O signals. The switching box and 16-electrode array are connected by 16 BNC to crocodile clip cables. The excitation signals are generated by NI PCI-6281 and then delivered to the switching box. Then, the switching box is monitored by the pre-programmed LabVIEW to direct the signals to the targeted electrode. Furthermore, it has an auto calibration technology to increase measurement accuracy. Additionally, it can be programmed via two well-known software packages, LabVIEW and MATLAB. The host PC will compute the measured data that is received from the DAQ system for image reconstruction using EIDORS.

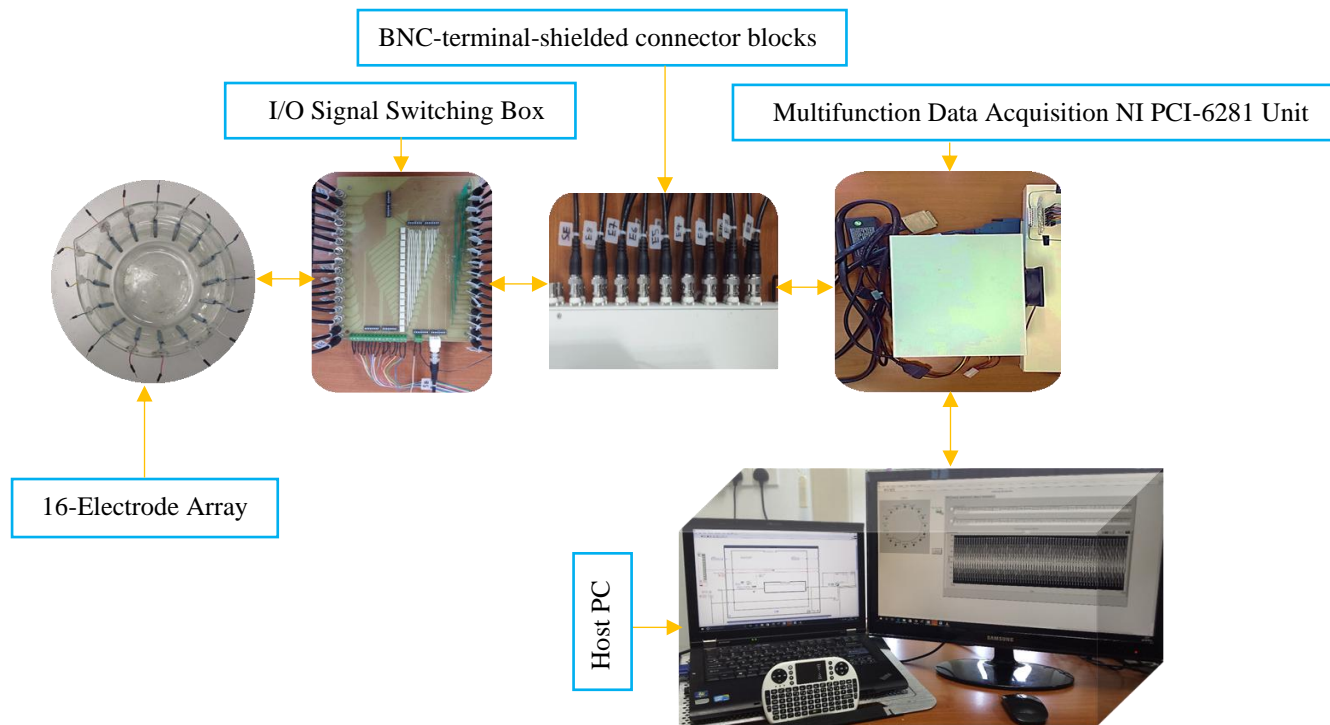


Figure 3.21: Current EIT hardware block diagram.

3.2.1 EIT hardware block diagram

3.2.1.1 16-Electrode Array

In the current developed system uses three different 16-Electrode Array used in three different testing vessels and they are Titanium alloy grade 2 electrodes with diameter $13 \times 13 \times 0.5 \text{ mm}^3$, Titanium alloy grade 2 electrodes with diameter $14 \times 14 \times 0.5 \text{ mm}^3$ and Copper electrodes with diameter $2 \times 0.5 \times 0.0035 \text{ cm}^3$ plated for rust protection. These electrodes array design to surround the aimed object, then injected and collected electrical energy to obtain the electrical energy distribution within the aimed object. The dimensions were chosen randomly, as they have negligible impact on signal injection and detection. The focus was on evaluating material properties, such as conductivity and corrosion resistance, which are more critical to system performance. The electrode array in the current system is connected through two ways either with shielded electrical cable or electrical wire to I/O Signal Switching Box. Figure 3.25 shows the developed three different electrode arrays.

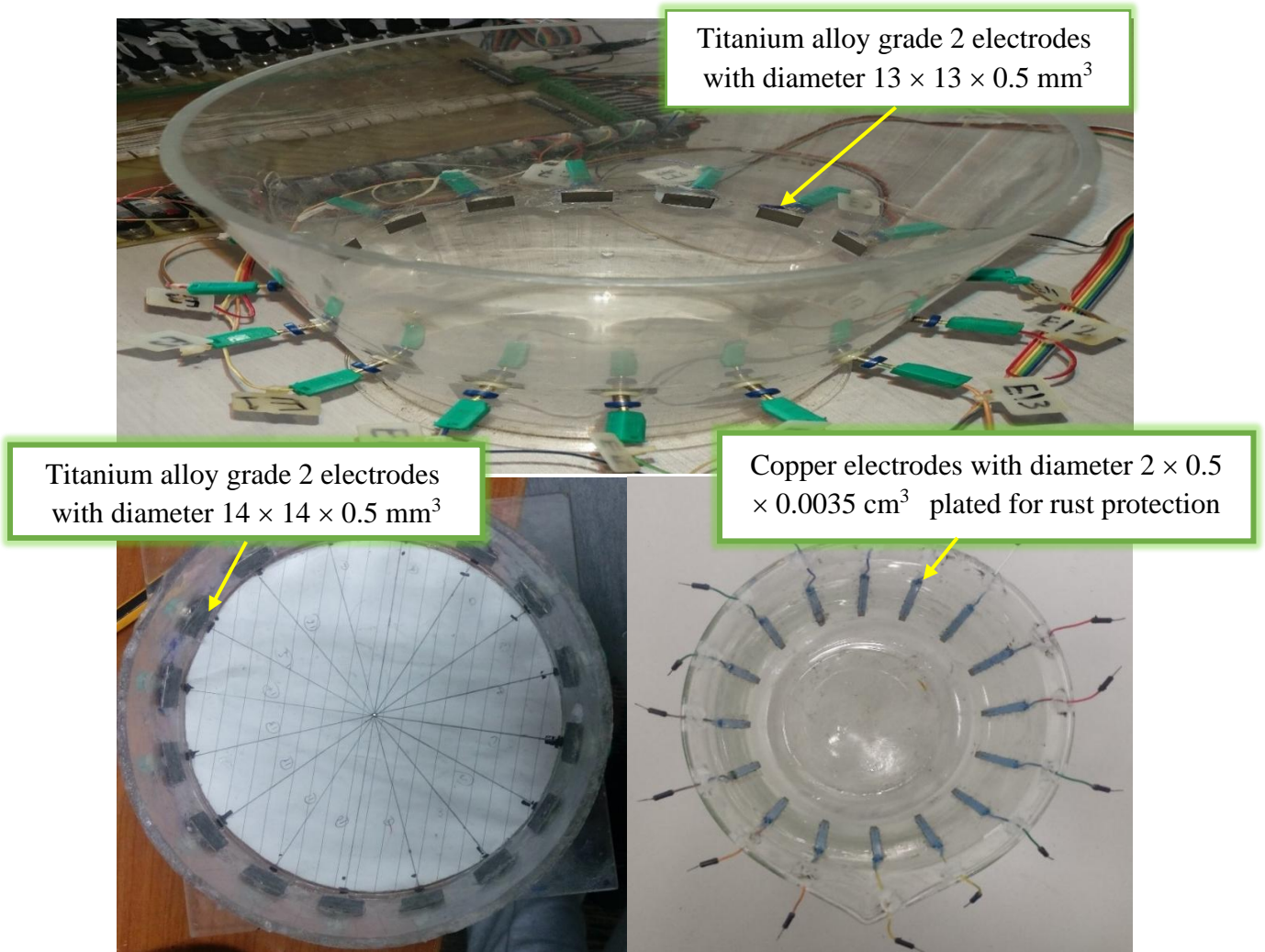


Figure 3.25: Three different electrode arrays.

3.2.1.2 I/O Signal Switching Box

The switching box is an electrical device that controls electrical signals, whether it is automatic or manually. The switching box, controlled by 16 digital channels and 4 DIP manually switching unite to monitor excitation signals for 16 electrodes, and simultaneously measure the voltage and current changes. Moreover, the switching box can be connected by 16 BNC to crocodile clip cables to a 16-electrode array. In additionally, the current switching units enable the developed EIT system to apply different impedance measurement methods, such as neighbouring, opposite, and cross methods. To shorten it is component Figure 3.26 shows the block diagram of the current switching box.

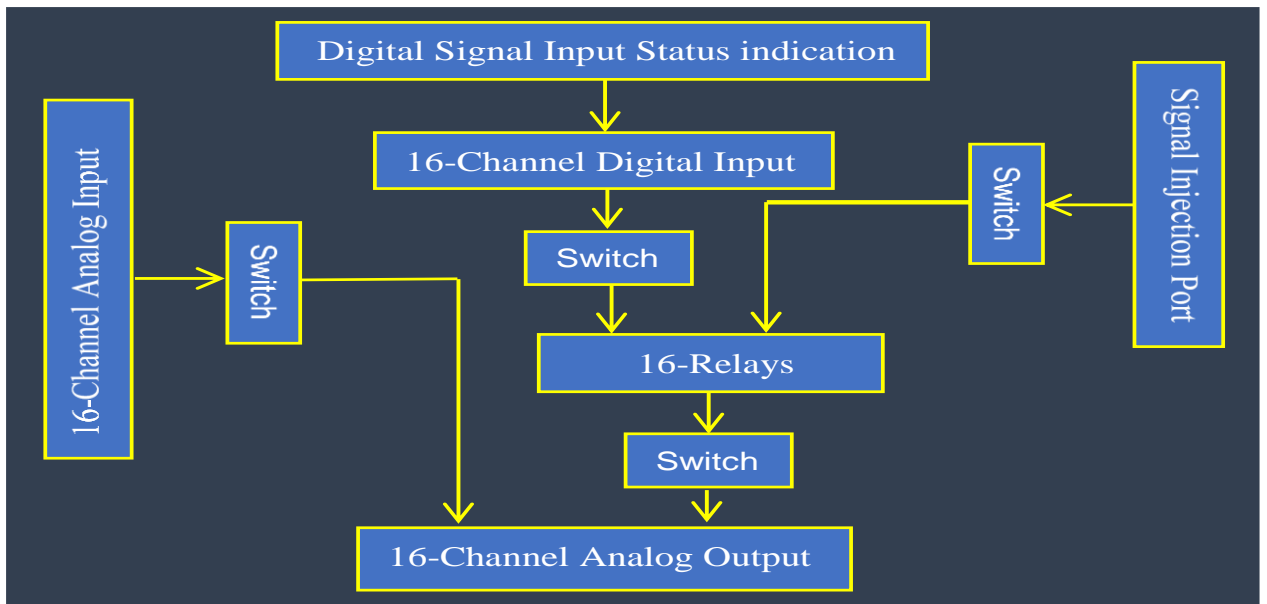


Figure 3.26: Switching box component block diagram of the current EIT system.

The schematic diagrams of EIT switching box shown in Figure 3.27. The developed schematic diagrams show the actual electrical connections of the switching box using Diptrace software.

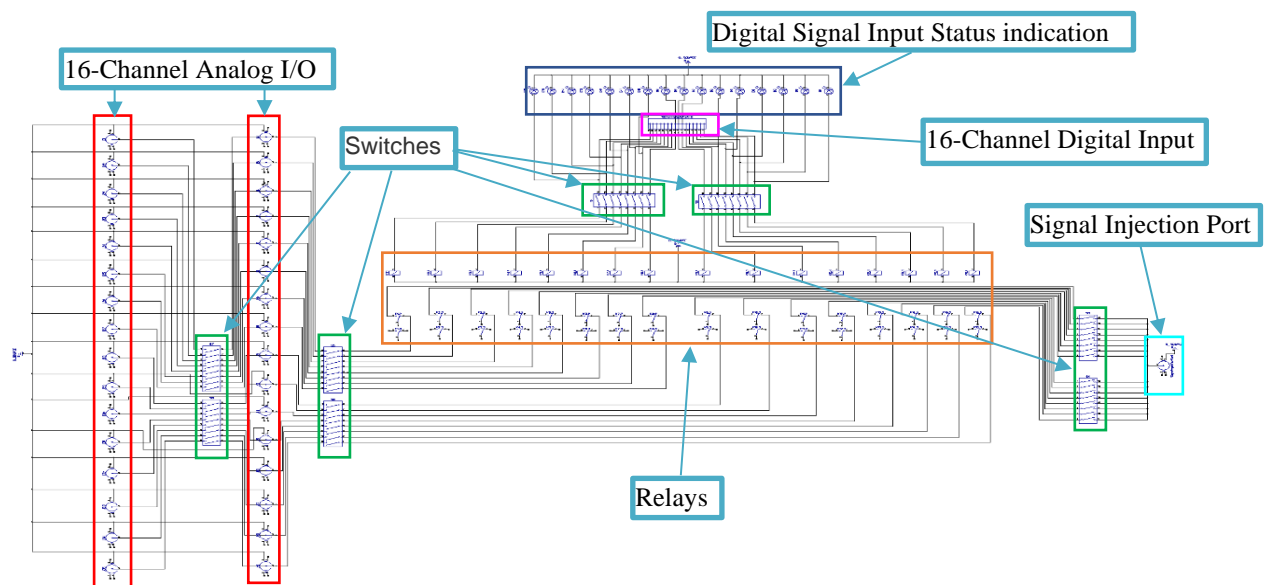


Figure 3.27: Schematic diagrams of EIT switching box.

Figure 3.28 shows the current EIT system switching box PCB layout using Diptrace software.

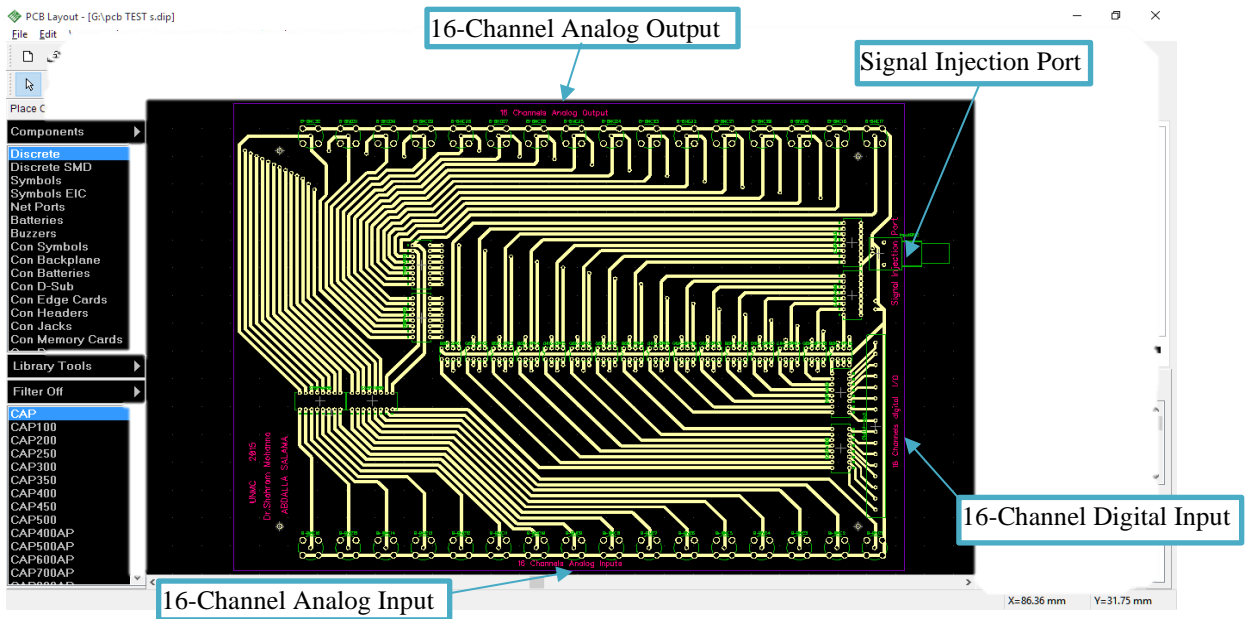


Figure 3.28: EIT system switching box PCB layout.

3.2.1.3 BNC-terminal-shielded connector blocks

The NI BNC-2090A is a shielded 19 in rack-mountable connector block with 22 signal BNC connectors used to connect I/O signals whether it is analogy or digital which it is compatible with 68-pin NI DAQ devices. Moreover, the Digital signals connectivity is provided over 29 spring terminals. Figure 3.29 shows the Front Panel of rack-mountable block BNC-2090A. The BNC-2090A is a stable connector used in the implementation of the SEEIT system.

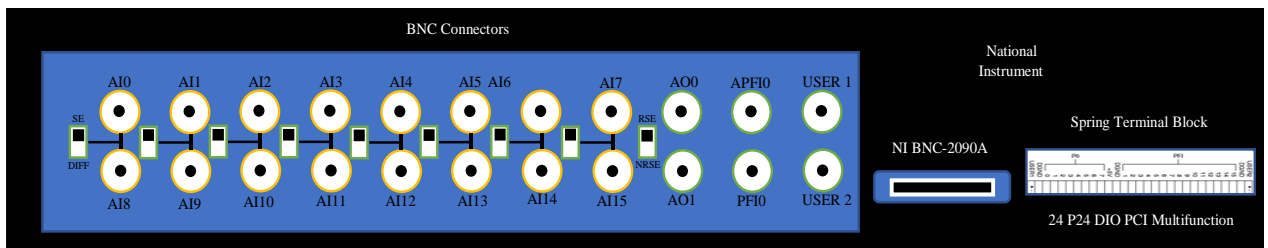


Figure 3.29: BNC-2090A Front Panel.

Blinking RGB LEDs breadboard has been attached to the BNC-2090a to shows digital signals indicator shown in Figure 3.30.

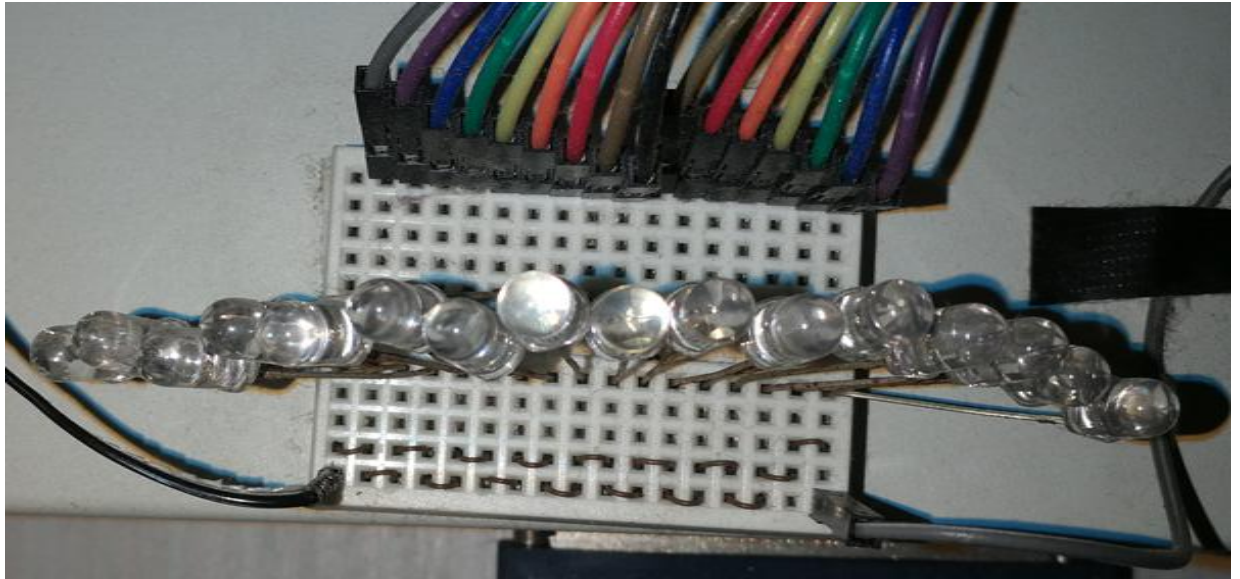


Figure 3.30: Blinking RGB LEDs breadboard.

3.2.1.4 Multifunction Data Acquisition NI PCI-6281 Unit

The Multifunction Data Acquisition Unit consists of six parts which are: NI PCI-6281 Card, Express Card 34mm Adapter, Enclosure Box PCI Expansion Slot, Expansion Card to Two 32bit PCI Slots Adapter, Shielded 68-Conductor Cable Terminated with a VHDCI 68-Pin Male Connector to 68-Pin Female D-type Connector, and Power Supply. Figure 3.31 shows all the parts of the Multifunction Data Acquisition Unit. The NI PCI-6281 Card is the most significant part since all the Signals measurements and generation are made within. Moreover, Expansion Card to Two 32bit PCI Slots Adapter can handle two NI PCI-6281 DAQ so it can be upgraded and then synchronized which will increase the number of measurements channels from 16 to 32 and injection signals from one source to two different signals generation.

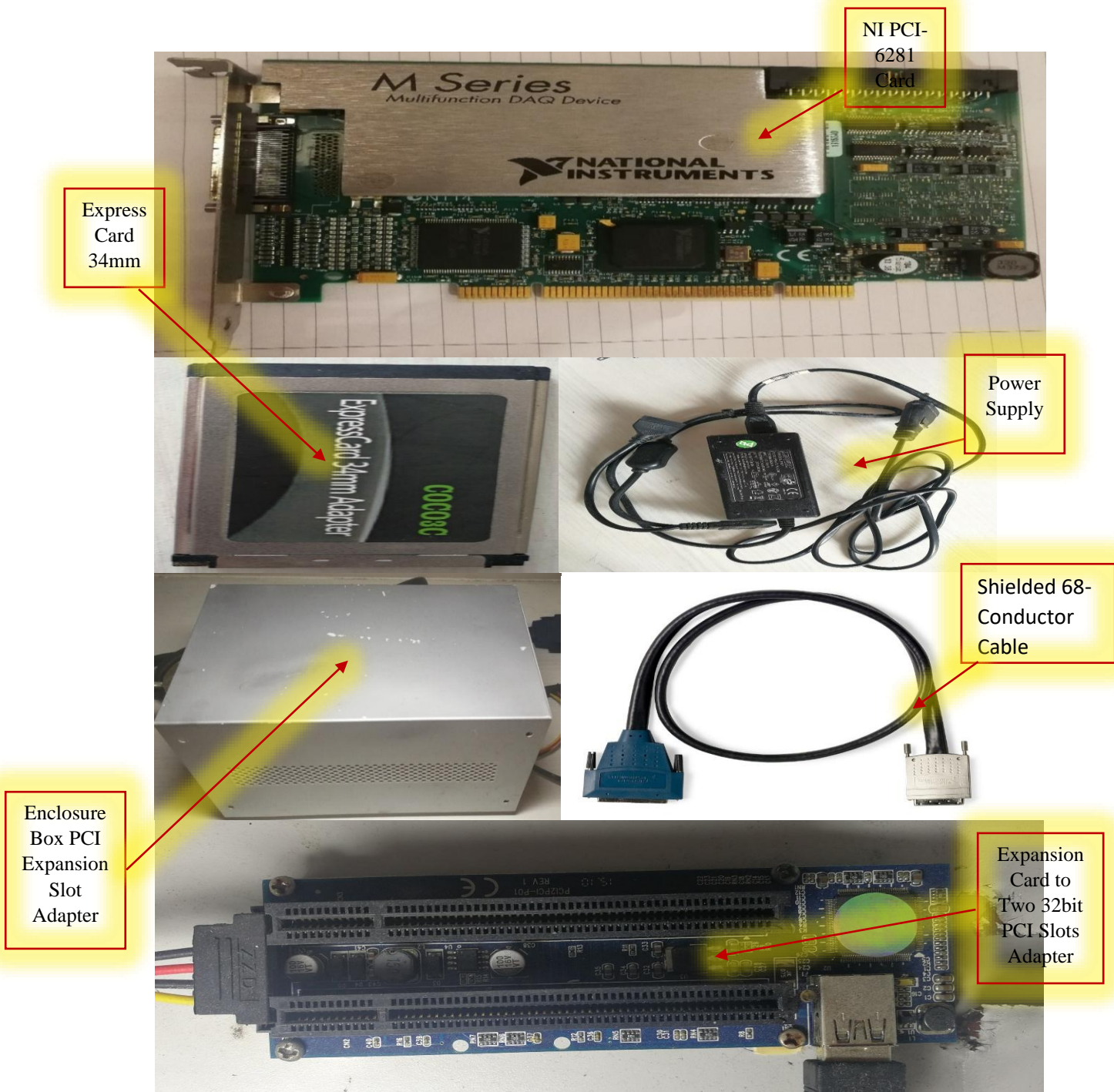


Figure 3.31: The Multifunction Data Acquisition Unit main parts.

3.2.1.5 Host PC

The utilize PC for the developed EIT system is the Lenovo ThinkPad T410 shown in Figure 3.32. The host PC equipped with i5 CPU 2.66 GHz, 8 GB RAM Memory, 250 GB Hard Drive, Windows 10 Pro operation system, and 512 MH Video Memory. However, the current PC can be upgraded for higher specification PC, which will speed up the EIT system processing data.



Figure 3.32: The host PC.

3.2.2 Electrodes

An electrode is an electrical conductor made of metallic material (or non-metallic) used to contact the medium of an object, through which a current, either alternating current (AC) or direct current (DC), enters or leaves a non-metallic substance medium (Fabrizi et al., 2009; Yan et al., 2001; Guermendi et al., 2015; Wang et al., 2016). Moreover, an electrode array is used in the EIT to detect and track electrical activity (Bas et al., 2016; Zhou et al., 2016; Jamil et al., 2017). Several material characteristics should be considered to make a suitable electrode for the EIT system; these include conductivity, durability, flexibility, light weight, corrosion resistance, lack of toxicity, long life, non-ferromagnetic properties, and low cost (Jin et al., 2016; Almuhammadi et al., 2015; Ruan and Poursaeed, 2017; Floroian et al., 2015; Tallman et al., 2015; Rymarczyk et al., 2016; Jehl and Holder, 2016). Hence, titanium alloy grade 2 electrodes were designed and implemented, as shown in Figure 3.33. The active area of the titanium alloy grade 2 electrodes is in direct contact with the medium of diameter $13 \times 13 \times 0.5 \text{ mm}^3$ (Vitalii, Andrey and Georgy, 2015; Niemczewska-Wójcik, 2017). Keeping in mind another electrode array made of titanium alloy grade 2 but with active area in direct contact with the medium of diameter $14 \times 14 \times 0.5 \text{ mm}^3$. The electrode used to apply signals is called the ‘injection electrode’; the electrode used to measure signals is called the ‘measurement electrode’. The same electrode was used for the

injections and measurements. In the present EIT system, a plurality of electrodes is arranged in a ring shape with equal spacing, as shown in Figure 3.34. The 16 electrodes were attached approximately 149.35 mm from the bottom of the testing tank.

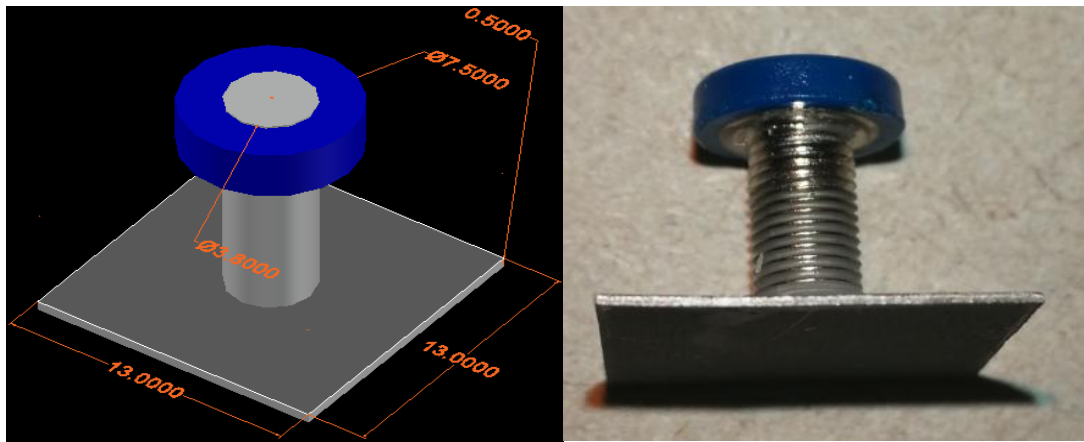


Figure 3.33: Electrode design layout using AutoCAD (left); the actual electrode (right); square contact areas are $13 \times 13 \times 0.5 \text{ mm}^3$.

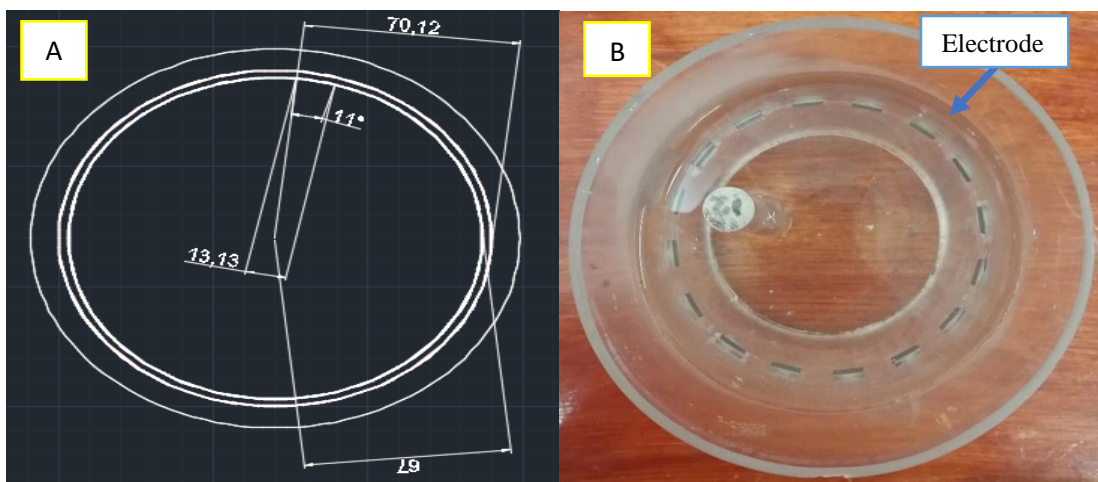


Figure 3.34: A shows the top view dimensions of the testing tank; B is the top view of the actual testing tank.

However, another 16 EIT electrodes were designed and fabricated at the beginning using the Diptrace PCB layout as shown in Figure 3.35. This electrode was designed to be attached to the breaker, as shown. The $2 \times 0.5 \text{ cm}$ copper area is plated for rust protection because it is the active region of the electrode. A $13 \times 0.5 \text{ cm}$ region of the electrode region is insulated by paint. The layout of the electrode is saved as a Gerber file and used to communicate scheme information for the printed circuit board. The electrodes were attached to the curved surface of the tank by carefully positioning them in predetermined locations to ensure consistent contact. Equal spacing was maintained between each electrode to ensure uniform distribution and avoid measurement

irregularities. The curvature of the tank was accounted for during placement to maximize the effective contact area, which is critical for reliable measurements. While the exact required contact area was not explicitly quantified, care was taken to ensure that each electrode maintained sufficient contact with the surface through precise alignment and secure attachment. Silicone-based adhesive was used to fix the electrodes in place, providing stability without interfering with electrical performance. This method ensured proper positioning and minimized the risk of measurement errors due to poor contact.

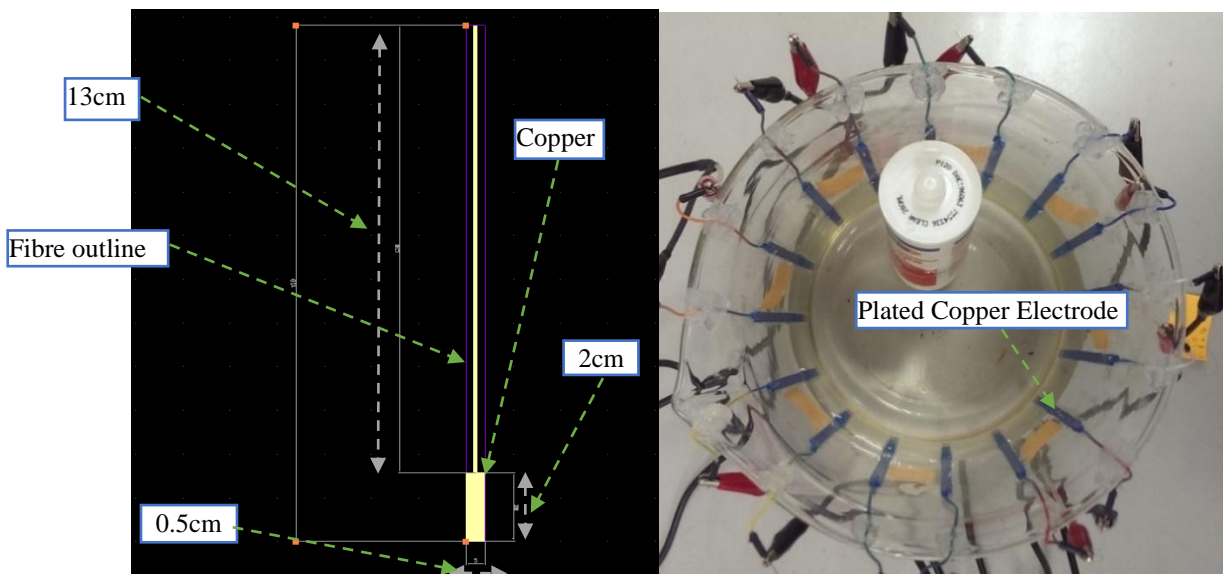


Figure 3.35: EIT electrode design layout using Diptrace software (left) and the testing breaker with the electrodes attached.

3.2.3 Relay

The EIT system measurements are sensitive to noise that is generated from switching the signals for injection and measuring results. Hence, a high noise insulation relay is needed (Cornelis et al., 2018; Angira and Rangra, 2016; Chieh et al., 2018; Ruan, Shen and Wheeler, 2001). Traditional relays such as solid state and electromagnetic will generate high noise for many reasons such as capacitive noise, long AC signal cable, leakage currents, switching point, and high-frequency suppression. Omron develops an especially low signal surface-mounting relay called G6K. The G6K is subminiature, as small as $5.2 \text{ mm} \times 6.5 \text{ mm} \times 10 \text{ mm}$, with a dielectric strength of 1500 VAC. Figure 3.36 shows the G6K-2P single-side stable with high insulation PCB mounting hole chip terminal arrangement and internal connections and dimensions.

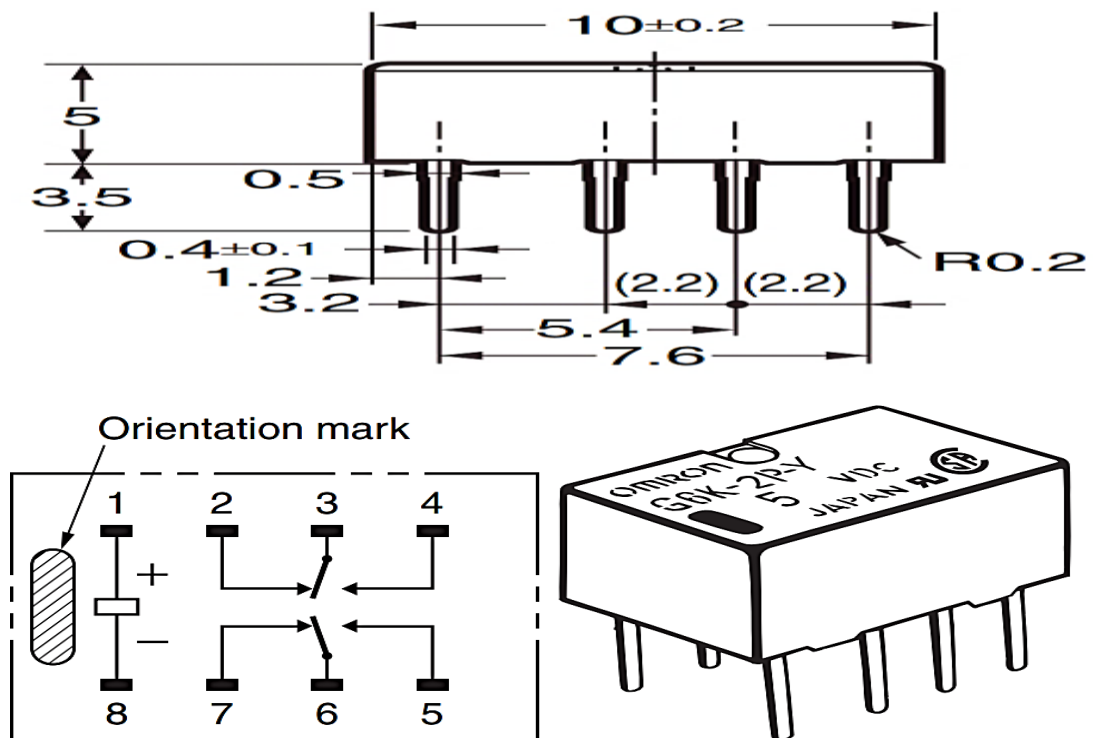


Figure 3.36: Footprint and schematic symbol of G6K-2P.

3.1.3 Current EIT system advantages and disadvantages

There are several advantages to the current EIT system. For instance, no radiation meaning there will be no hazard. However, there are some of the disadvantages. For example, low-quality image but this can be improving either by increasing the number of electrodes or improving the reconstruction algorithms. The main pros and cons of the current EIT system and they are listed in Table 3.2.

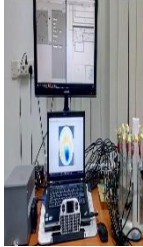
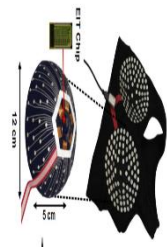
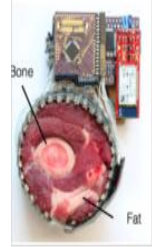
Table 3.2: Some of EIT system advantages and disadvantages.

Pros	Cons
High-speed monitoring system	Low-quality image
Non-invasive	Problem of setting electrodes and cable
Cheap installation of electrodes	Limited input signals frequency range
No radiation so less hazard	Challenging algorithm
Less expensive than alternative systems such as MRI	

<p>Image resolution will be improved by increasing the number of the electrodes</p>	
--------------------------------------------------------------------------------------------	--

Table 3.3 shows the developed EIT system in comparison to some of the latest EIT systems. The table shows six different EIT systems developer organization. Every EIT systems have unique techniques and parameters. As shown, the image dimension for all produces either 2-D or 3-D. The 3-D image required a higher number of electrodes comparing to the 2-D. However, the Mobecommm MEIK systems provide 2-D images even it uses 256 electrodes which is a high number that to detect an object as small as 3-5 mm in diameter. On the other hand, the developed system only uses 16 electrodes to detect an object as small as 1.5 mm in diameter. Most of the EIT systems use multi-frequency injection with different frequencies ranges. The electrodes materials vary between all the EIT systems based on the aimed application. However, titanium alloy and Paled copper electrodes used in the current EIT system. The signal to noise ratio SNR varies between all the displayed EIT system. Only very few systems have multi amplitude. The main benefit of the multi amplitude injection is to improve the ability of the EIT system to detect different conductivity object. The developed EIT system uses only Single-Ended measurements, unlike other EIT systems that use differential measurements. The processed signals in the developed EIT system uses three different types, unlike the other which uses one.

Table 3.3: Recent EIT systems and comparison with exiting EIT system.

EIT System Developer	Nottingham University Malaysia Campus	Dartmouth College (Halter et al., 2015)	KAIST University (Hong et al., 2015)	Aachen University (Aguar Santos et al., 2016)	Maltron Sheffield MK 3.5	Mobecomm MEIK	Carnegie Mellon University (Zhang, Xiao and Harrison, 2016)
System							
Dimension	134 mm diameter	600 mm	$300 \times 250 \times 50 \text{ mm}^3$	N/A	N/A	$160 \times 180 \times 100 \text{ mm}^3$	200 mm diameter
Image Dimension	2-D	3-D	3-D	2-D	2-D	2-D	2-D
Electrodes	16 (1 Layer)	64 (4 Layers)	92 (Flexible)	16 (2 Layers)	8 (1 Layer)	256 (Planar)	8,16,32 (1 Layer)
Electrode Materials	Copper, Titanium Alloy	N/A	N/A	N/A	N/A	N/A	Stainless Steel
Frequency	12 kHz – 1 MHz	10 kHz – 10 MHz	100 Hz – 100 kHz	60 kHz – 1 MHz	2 kHz–1620 kHz	10 kHz, 50 kHz	40 kHz
Multi Frequency	Yes	Yes	Yes	Yes	Yes	No	No
Amplitude	0.1–10 V, 5 mA	N/A	10 μA – 400 μA	N/A	N/A	0.5 mA	0–6 V, 300 μA
Multi Amplitude	Yes	No	No	No	N/A	No	Yes
SNR	SINAD 8 – 70 dB depends on channels and the injection frequency	94 dB	90 dB	109.6 dB	N/A	N/A	N/A
Minimum Detectable Size	1.5 mm (in 134 mm)	N/A	5 mm (in 120 mm)	N/A	N/A	3–5 mm	38.1 mm (in 200 mm)
Measurement Type	Single-Ended	Differential	Differential	Differential	Differential	N/A	Differential
Processed Signals	RMS, Variance, Standard deviations	N/A	N/A	N/A	N/A	N/A	RMS
Imaging Device	Computer	Computer	Mobile Device	Computer	Computer	Computer	Computer
Year	2016	2015	2015	2016	2014-2016	2010	2016

Chapter 4 Measurements and injection signalling

This chapter presents several EIT systems calibration and development techniques. The Electrical Impedance and Diffuse Optical Tomography Reconstruction Software (EIDORS) program was used to reconstruct the image based on the obtained measurements. EIDORS is a source code algorithm for EIT image reconstruction that was developed via open-source software. EIDORS has solved many image reconstruction difficulties, including forward and inverse problems (Adler & Lionheart, 2006). Two types of EIT signalling measurements and injection were calibrated and tested in this research. The switching box was introduced to improve the EIT system signalling I/O. The traditional EIT system uses Differential signalling which gives limitation to it. For example, in differential, each electrical measurement required two electrodes. Alternatively, single-ended required one electrode for each measurement. The single-ended EIT system makes the processes of obtaining electrical measurements more accurate since it only involved one electrode for a set location. The transformation from using differential signalling to the use of single-ended signalling presented. Two methods were used to apply the differential measurements to the EIDORS and improve the detection of the aimed object which they are the Zero and the Average methods.

4.1 Differential signalling

Differential signaling simultaneously sends and receives signals through two wires. Moreover, it uses a differential transmitter and a differential receiver, which provides better signal noise immunity than do single-ended signals (Thierauf, 2004). However, the differential signalling measurement was obtained and saved from an electrode array placed around a beaker filled with tap water. Then, another set of measurements was taken from a beaker filled with tap water and added object. Then, the measured data were processed to obtain the location of the object using the EIDORS program suite. EIDORS only supports 16 electrodes, and the adopted system uses 8 electrodes. However, the results were successfully developed to suit the EIDORS program. Two methods were used to reconstruct an image using the collected data: the zero results method and the average results technique. Because the differential measurements required two separate wire connections for each measurement, two electrodes were used. Figures 4.1 and 4.2 show the actual location of the object. The differential

measurements can be obtained from the testing tank in two ways, as illustrated in Figures 4.3 and 4.4. However, the developed EIT system only can get 8 differential measurements.

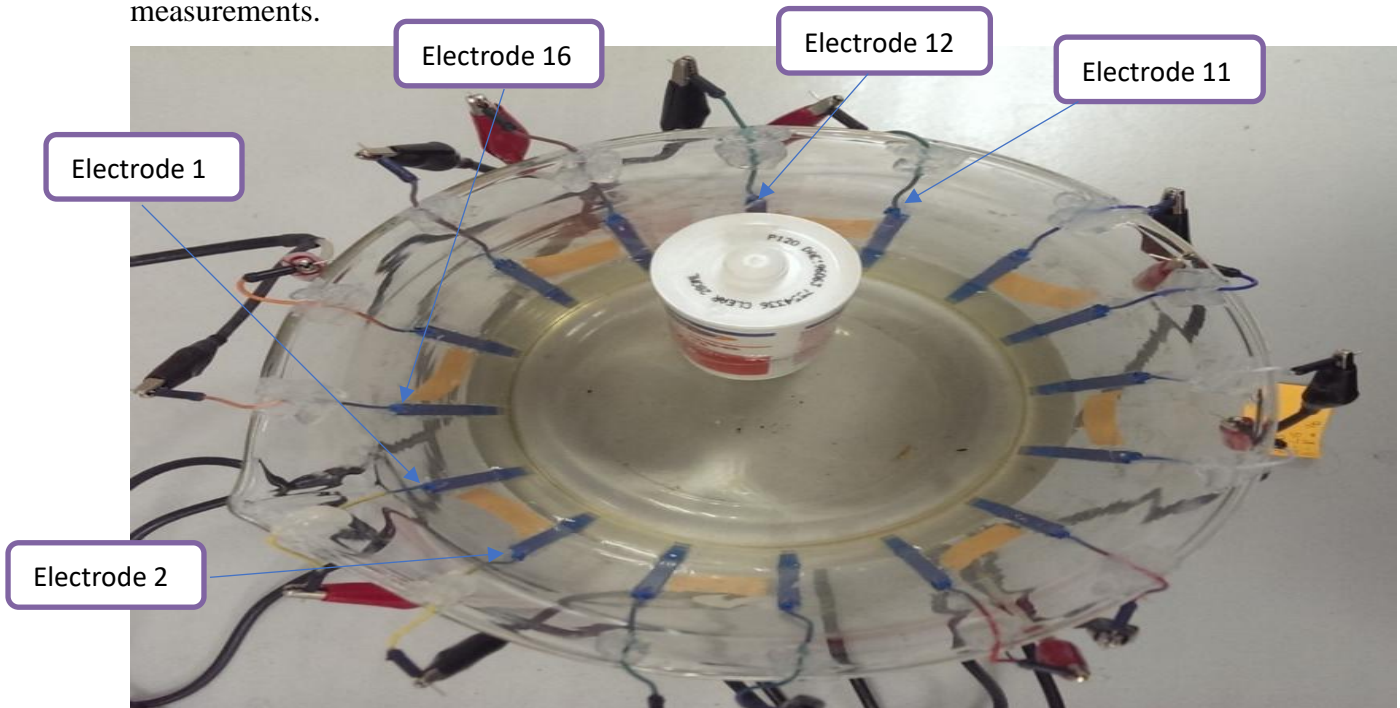


Figure 4.1: Actual location of plastic object.

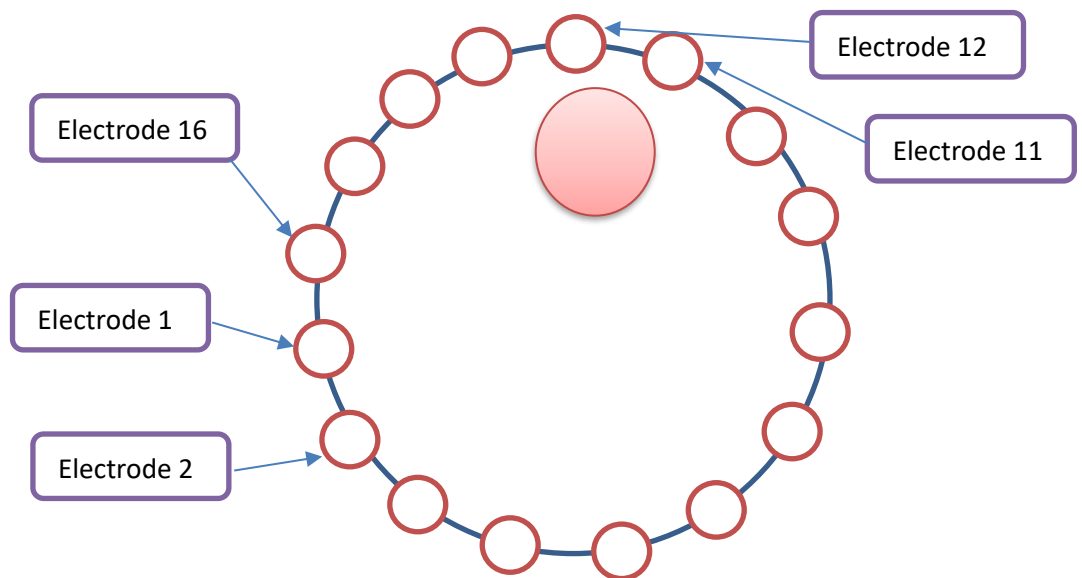


Figure 4.2: Actual location of object.

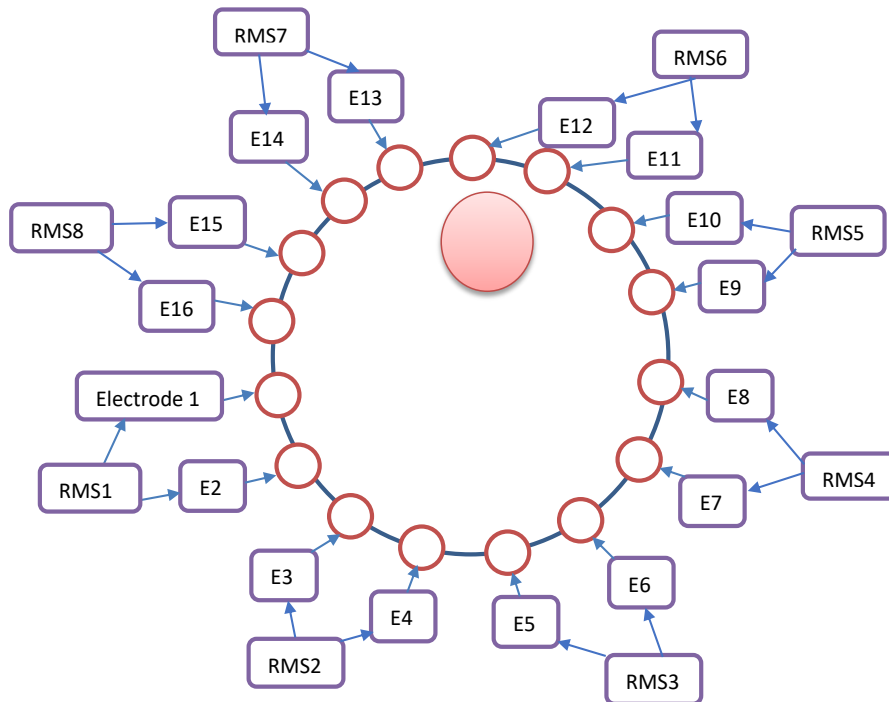


Figure 4.3: Differential measurements which process 8 RMS measurements.

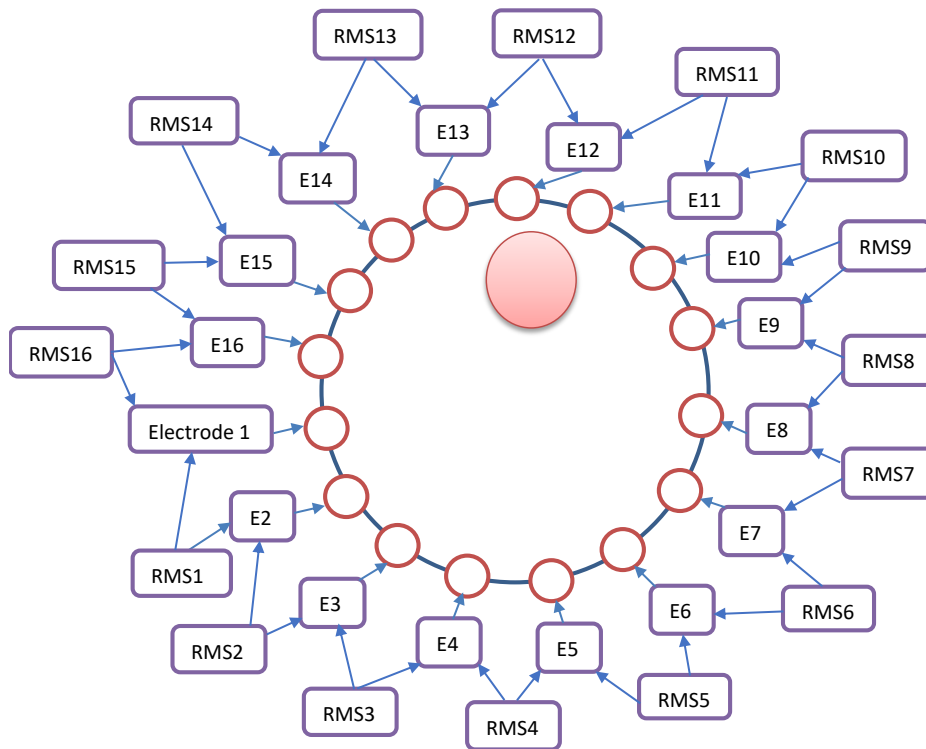


Figure 4.4: Differential measurements which process 16 RMS measurements.

Table 4.1 shows the original measurements of differential voltage using the adjacent measurement strategy after scaling up by multiplying the data measurements by 1000.

This step is necessary for the data to be processed in EIDORS since EIDORS does not identify low-signal data. The three equation which displayed in Equation 4.1, Equation 4.2, and Equation 4.3 used to process the measured signals to show the changes responses and present it. The percent of total which multiplies by 1000 results has been round numbers to the nearest integer.

$$\text{Percent of total} = \frac{\text{Difference}}{\text{Total}} \times 100 \quad \text{Equation 4.1}$$

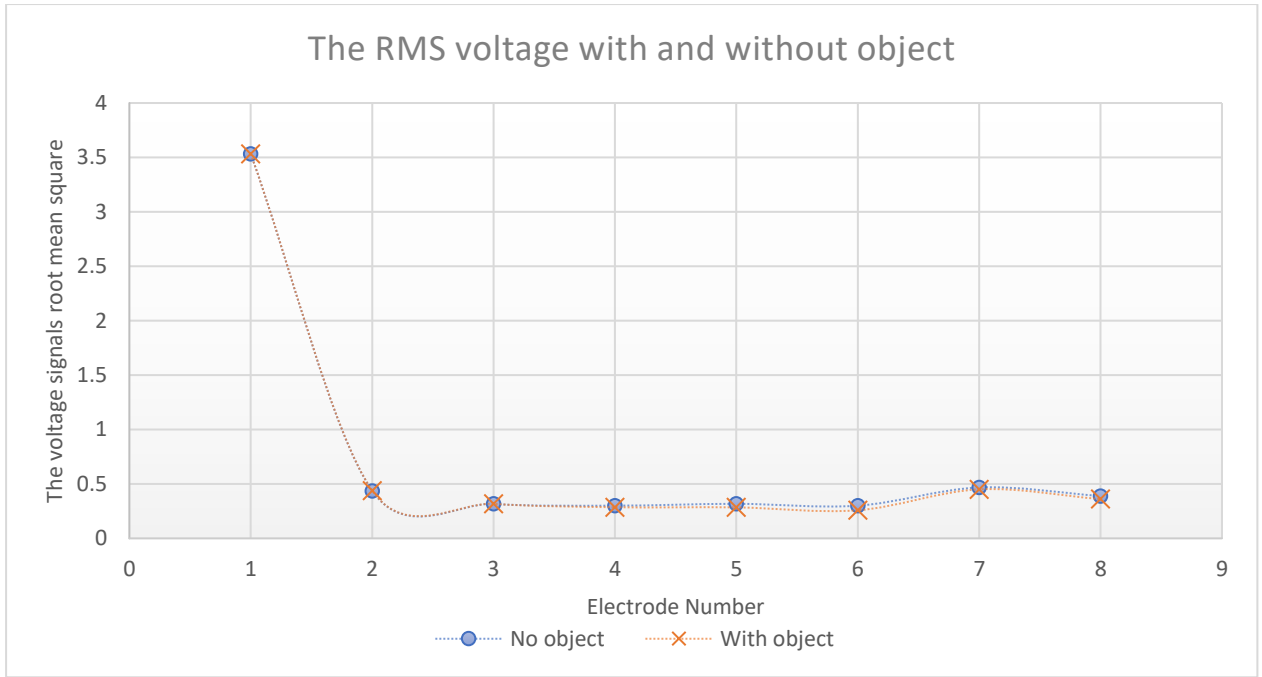
$$\text{Difference} = \text{With object} - \text{No object} \quad \text{Equation 4.2}$$

$$\text{Total} = \text{No object} + \text{With object} \quad \text{Equation 4.3}$$

Table 4.1: Measurement results of differential voltage using adjacent measurement strategy.

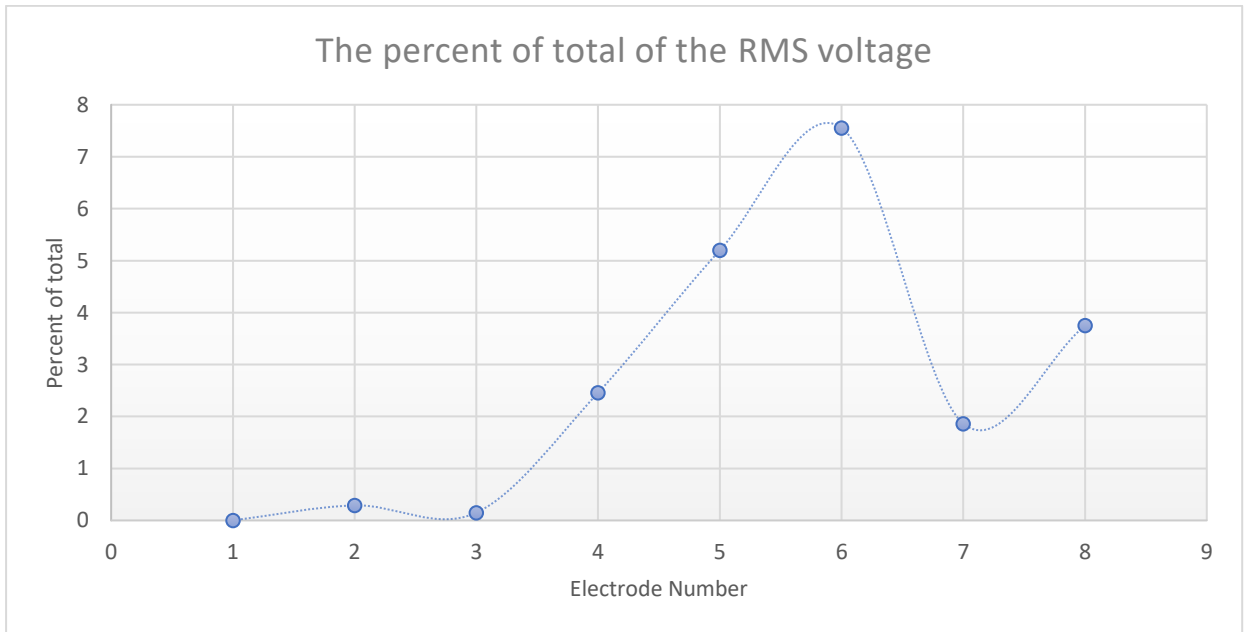
Vessel	RMS1	RMS2	RMS3	RMS4	RMS5	RMS6	RMS7	RMS8
No object (V)	3.5314055	0.4370413	0.3165336	0.3007933	0.3177637	0.3005614	0.4678531	0.389148
No object X1000	3531	437	317	301	318	301	468	389
With object (V)	3.5315315	0.4395836	0.3174853	0.2863587	0.2848515	0.2583347	0.4507355	0.3610065
With object X1000	3532	440	317	286	285	258	451	361
Difference	0.000125927	0.002542294	0.000951679	0.014434617	0.031404992	0.042226729	0.017117560	0.028141525
Total	7.062936995	0.87662493	0.634018881	0.587151993	0.604122368	0.558896029	0.918588634	0.750154465
Percent of total	0.00178293	0.2900093	0.1501026	2.4584123	5.1984488	7.5553818	1.8634631	3.7514307
Percent of total X1000	2	290	150	2458	5198	7555	1863	3751

Figure 4.5 presents a graph that compares the RMS results for the testing vessel with and without the plastic object. In the figure, slight changes in the RMS voltage signals between electrodes 5 and 7 can be seen, but the image is not clear. However, Figure 4.6 displays the calculated the RMS percent of total. As shown, the voltage difference between electrodes 5 and 7 is high, which indicates that the conductivity in that area changed.



No object	3.5314055	0.4370413	0.3165336	0.3007933	0.3177637	0.3005614	0.4678531	0.389148
With object	3.5315315	0.4395836	0.3174853	0.2863587	0.2848515	0.2583347	0.4507355	0.3610065

Figure 4.5: RMS voltage of the vessel with and without object.



Percent of total	0.00178293	0.2900093	0.1501026	2.4584123	5.1984488	7.5553818	1.8634631	3.7514307
------------------	------------	-----------	-----------	-----------	-----------	-----------	-----------	-----------

Figure 4.6: RMS percent of total of the vessel with and without object.

Since the EIDORS program is designed for a 16-electrode system, the RMS measurement was developed using the zero method, as shown in Table 4.2, and the average method, as illustrated in Table 4.3. However, Figure 4.7 shows the signals

obtaining arrangement the Zero Method where zero used in between two real measurements value to compensation the number of the RMS measurements needed by EIDORS to reconstruct an image.

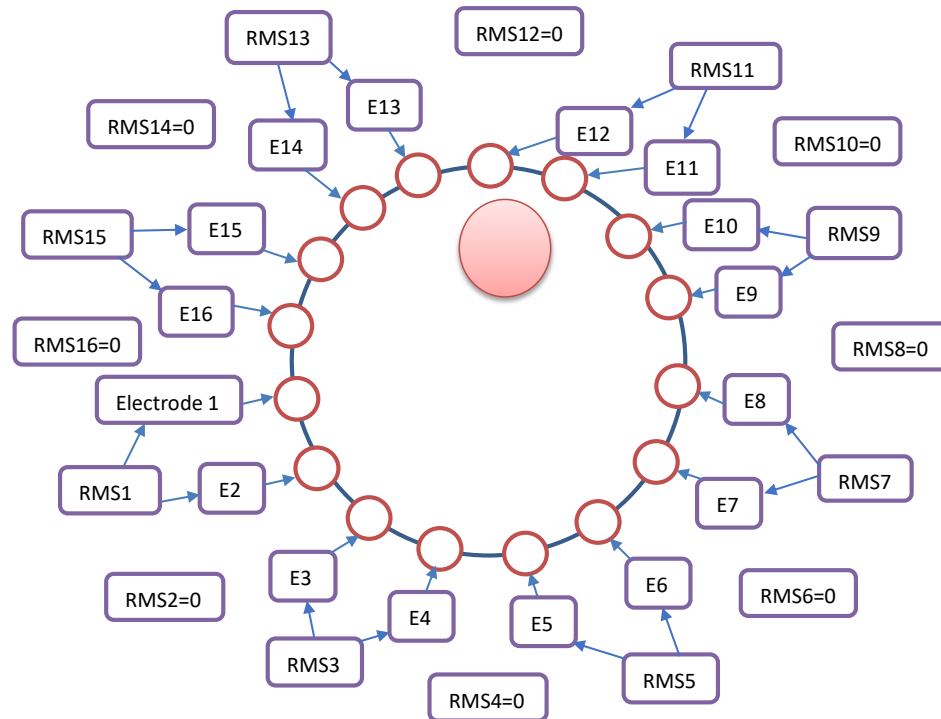
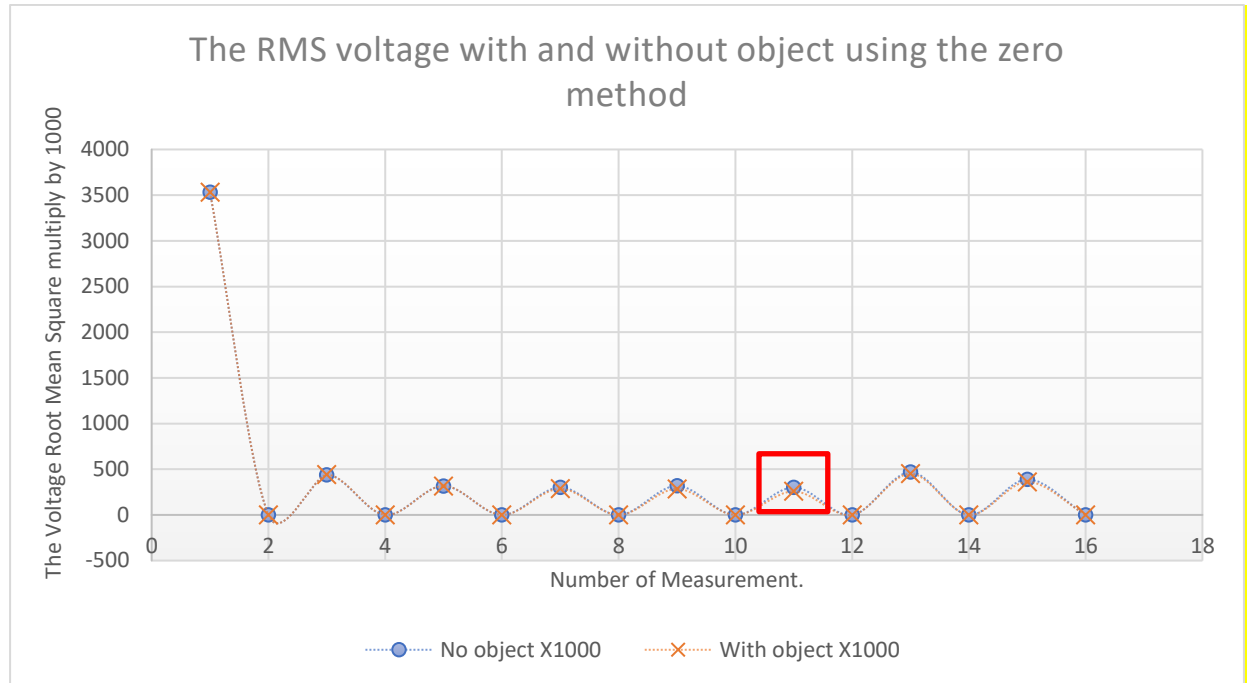


Figure 4.7: Zero method RMS measurements sequence.

Table 4.2: Modified measurement results of differential voltage using adjacent measurement strategy and zero method.

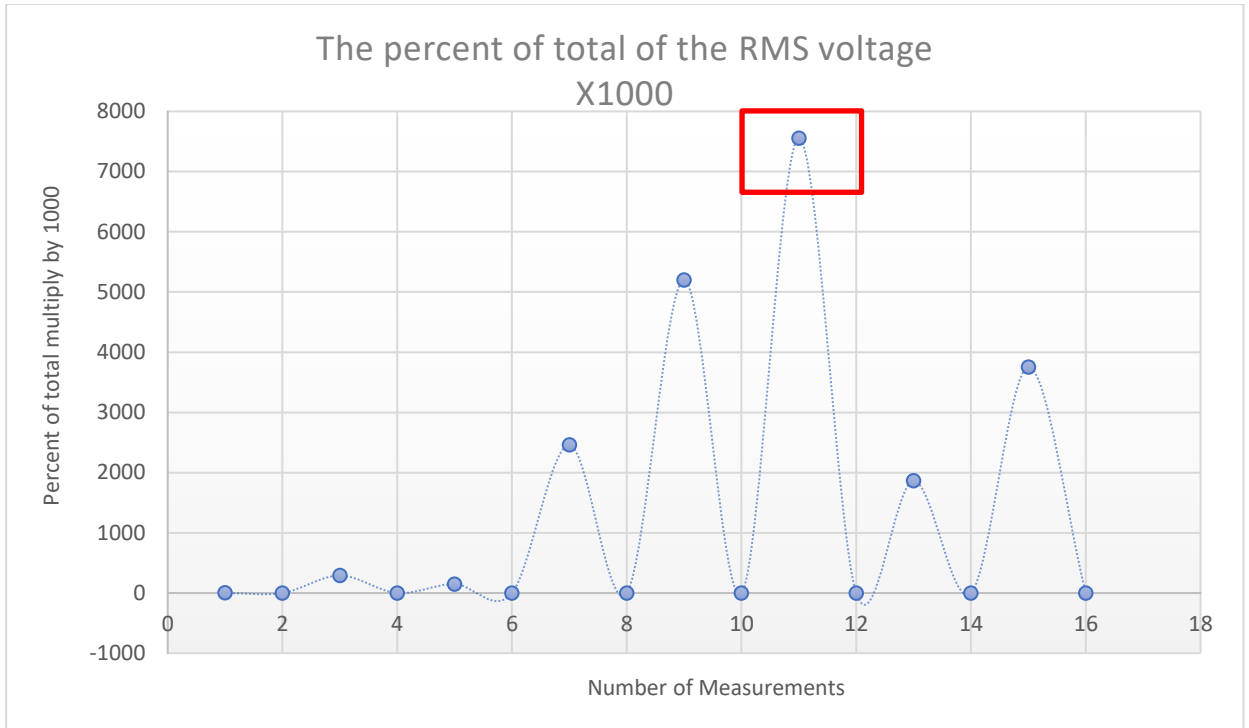
	Root mean square (V)	No object X1000	With object X1000	Percent of total X1000
1	RMS1	3531	3532	2
2	((RMS1+RMS2)X0)	0	0	0
3	RMS2	437	440	290
4	((RMS2+RMS3)X0)	0	0	0
5	RMS3	317	317	150
6	((RMS3+RMS4)X0)	0	0	0
7	RMS4	301	286	2458
8	((RMS4+RMS5)X0)	0	0	0
9	RMS5	318	285	5198
10	((RMS5+RMS6)X0)	0	0	0
11	RMS6	301	258	7555
12	((RMS6+RMS7)X0)	0	0	0
13	RMS7	468	451	1863
14	((RMS7+RMS8)X0)	0	0	0
15	RMS8	389	361	3751
16	((RMS8+RMS1)X0)	0	0	0

Figure 4.8 compares the modified RMS results for the testing vessel with and without the plastic object. The highest change in the RMS voltage signals is observed on RMS11. This is highlighted in Figure 4.9. Based on the calculated RMS voltage difference, the modified RMS difference is located between electrodes 10 and 12.



No object X1000	3531	0	437	0	317	0	301	0	318	0	301	0	468	0	389	0
With object X1000	3532	0	440	0	317	0	286	0	285	0	258	0	451	0	361	0

Figure 4.8: Modified RMS voltage of the vessel with and without object using the zero method.



Percent of total X1000	2	0	290	0	150	0	2458	0	5198	0	7555	0	1863	0	3751	0
------------------------	---	---	-----	---	-----	---	------	---	------	---	------	---	------	---	------	---

Figure 4.9: Modified RMS percent of total X1000 using the zero method.

Figure 4.10 shows the reconstructed cross-section graph based on the result using the developed EIDORS program when no object placed in the vessels (A). In contrast, (B) displays the 2D reconstructed image when an object is present. The colours in the image represent RMS voltage changes: blue indicates high impedance (larger voltage changes), and red indicates low impedance (smaller voltage changes). This visualization highlights how impedance variations affect voltage distribution, aiding in object detection.

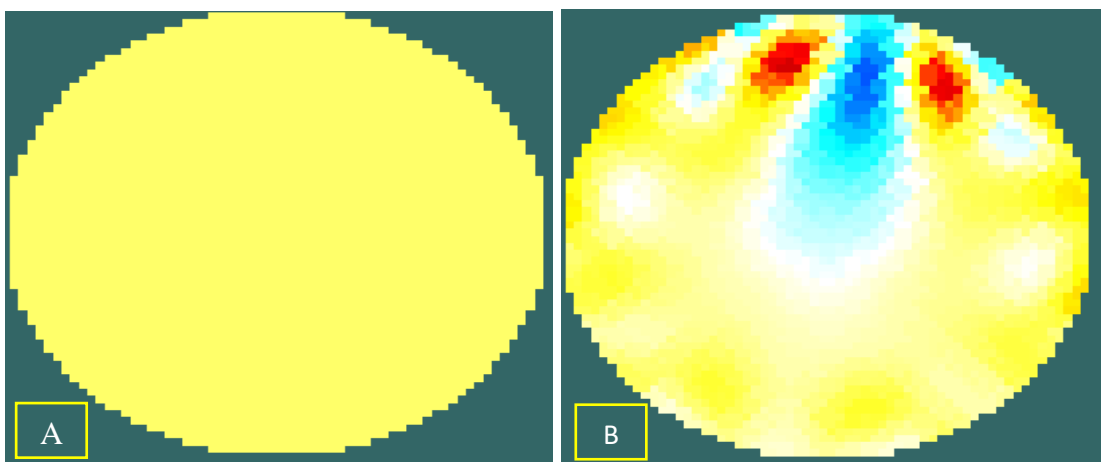


Figure 4.10: The 2D reconstructed image with (B) and without (A) object using modified results from zero method.

Employing the average method, Table 4.3 demonstrates the modified result measurements of differential voltage using the adjacent measurement strategy. Furthermore, the RMS average between each electrode is used to increase the number of measurements from 8 to 16 to be employed in EIDORS. Figure 4.11 shows the signals obtaining arrangement sequence using the average Method where two RMS measurements will be added then divided by 2 to compensation the number of the RMS measurements needed by EIDORS.

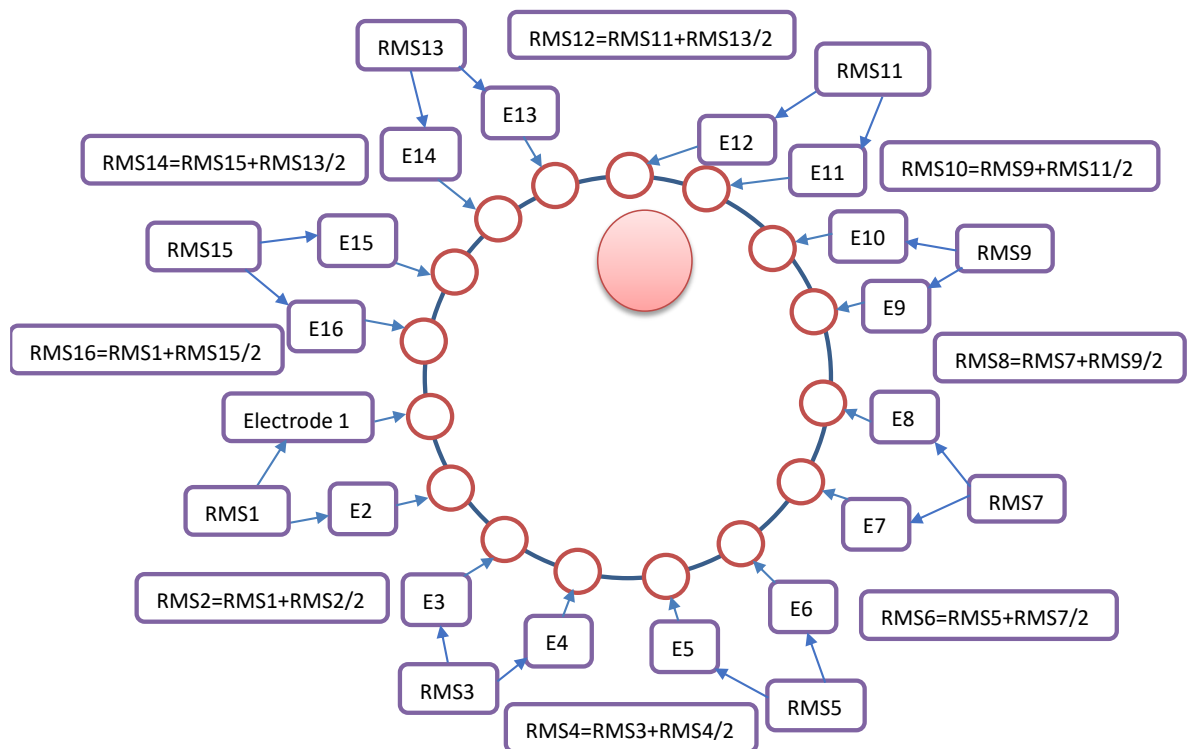


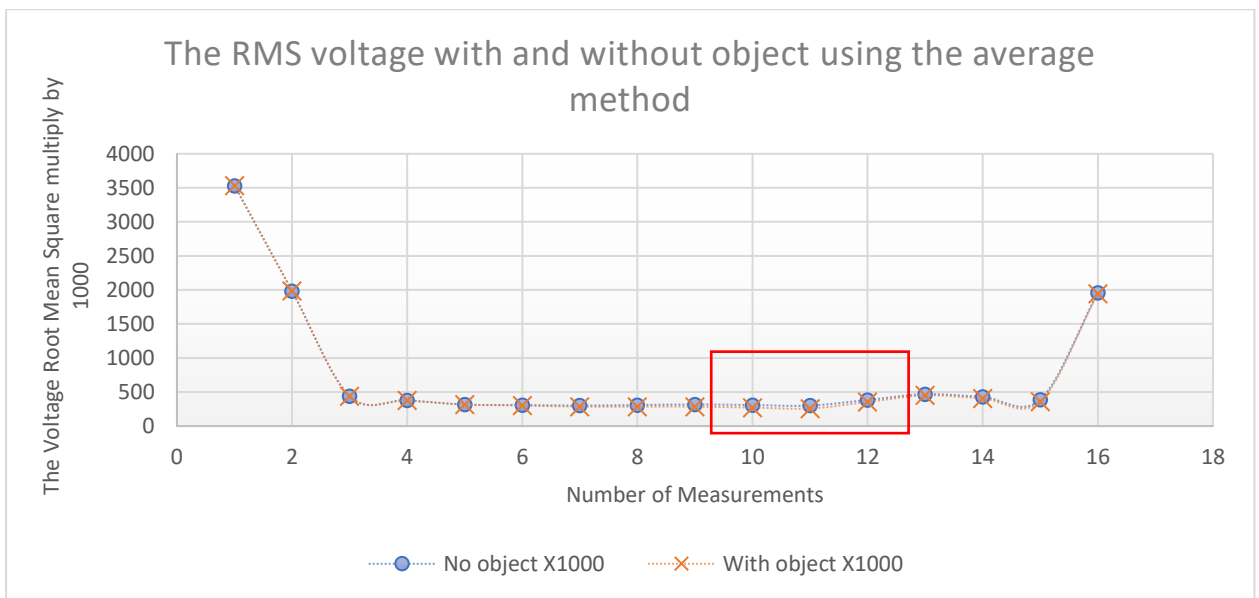
Figure 4.11: Average method RMS measurements sequence.

Table 4.3: Measurements of differential voltage with the average of RMS using the adjacent measurement strategy and average method.

	Root mean square (V)	No object X1000	With object X1000	Percent of total X1000
1	RMS1	3531	3532	2
2	((RMS1+RMS2)/2)	1984	1986	146
3	RMS2	437	440	290
4	((RMS2+RMS3)/2)	377	379	220
5	RMS3	317	317	150
6	((RMS3+RMS4)/2)	309	302	1304
7	RMS4	301	286	2458
8	((RMS4+RMS5)/2)	309	286	3828
9	RMS5	318	285	5198

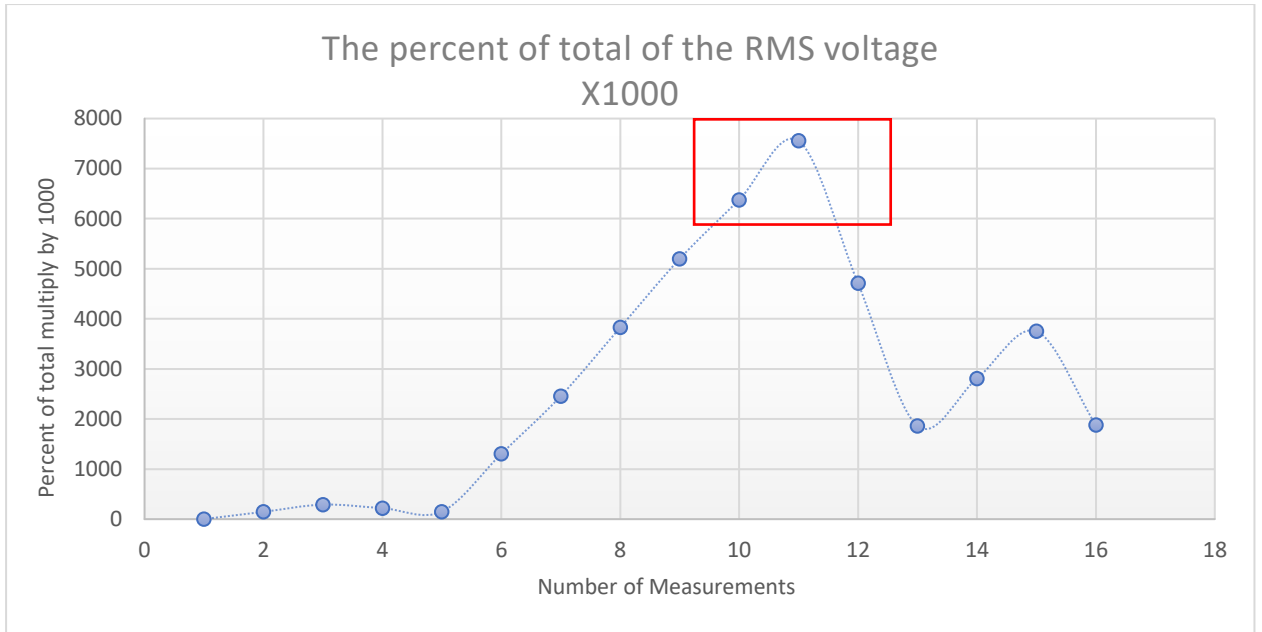
10	$((\text{RMS5}+\text{RMS6})/2)$	309	272	6377
11	RMS6	301	258	7555
12	$((\text{RMS6}+\text{RMS7})/2)$	384	355	4709
13	RMS7	468	451	1863
14	$((\text{RMS7}+\text{RMS8})/2)$	429	406	2807
15	RMS8	389	361	3751
16	$((\text{RMS8}+\text{RMS1})/2)$	1960	1946	1877

A comparison of the modified RMS results for the testing vessel with and without the plastic object is shown in Figure 4.12. Small changes can be seen in the RMS voltage signals between electrodes 8 and 13. Nevertheless, Figure 4.13 shows that the calculated RMS voltage difference between electrodes 8 and 12 is distinct. This indicates that the conductivity in that area changed.



No object X1000	3531	1984	437	377	317	309	301	309	318	309	301	384	468	429	389	1960
With object X1000	3532	1986	440	379	317	302	286	286	285	272	258	355	451	406	361	1946

Figure 4.12: Modified RMS voltage of the vessel with and without object using the average method.



Percent of total X1000	2	146	290	220	150	1304	2458	3828	5198	6377	7555	4709	1863	2807	3751	1877
------------------------	---	-----	-----	-----	-----	------	------	------	------	------	------	------	------	------	------	------

Figure 4.13: Modified RMS change difference of the vessel with and without object using the average method.

A cross-section reconstructed image based on the results obtained using the developed EIDORS program, when no object is in the vessel, is presented in Figure 4.14 (A). In contrast, (B) displays the 2D reconstructed image after using the RMS measurements with the object.

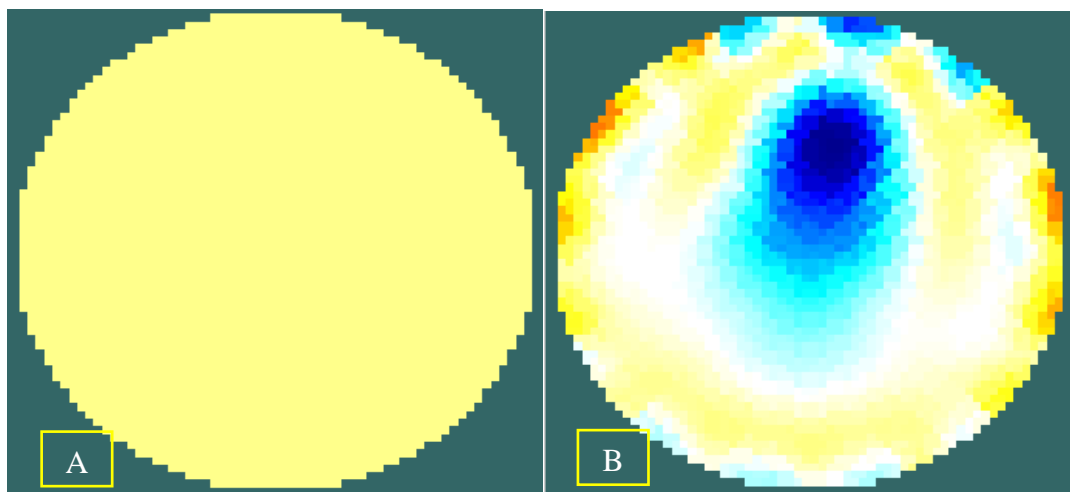


Figure 4.14: The 2D reconstructed image with (B) and without (A) object using modified results from average method.

Both the average and the zero methods are data processing configurations that help to improve the measurement results. However, as proven, the reconstructed image using the average method is much more apparent than the reconstructed image using the zero method. Figure 4.1 and Figure 4.2 shows the actual object location. The average method shows a more realistic image with fewer artifacts than the zero-method image since the average method uses the real obtained measurements to compensation missing measurements obtained from two actual measured numbers. The EIT system injection and measurement have been tested and calibrated using the resistor circuit network to check whether responses using single-ended signalling.

4.2 Single-ended signalling

Single-ended signalling is imbalanced signalling which is conducted on two wires, one of which is grounded and the other which carries the actual voltage signals (Fei, 2007). This means that one electrode is used for each signal measurement. However, the single-ended signalling measurement was measured and saved from the resistor network circuit, which has sixteen channels and 16 resistors. Then, another set of the measurements was taken after a resistor was introduced to the resistor network circuit. Subsequently, the measured data was processed using EIDORS to locate the resistivity change that was caused by the additional resistor. These tests were used to evaluate the possibility of using single-ended signalling in the EIT system to improve the system flexibility, transmission line, and complexity (Jose & Hubert, 2016). Finally, the switching box was tested and calibrated to control and monitor the I/O of the single-ended signals.

4.2.1 Measurements of single-ended signaling

The resistor network circuit is a collection of 16 resistors. The resistors are used to simulate the impedance change for all 16 channels.

4.2.1.1 Measurements of single-ended signaling without using the switching box

The sixteen-channel single-ended EIT system was tested using a resistor network circuit. The 16 channels are arranged in sequence in the system, as shown in Figure 4.15. Figure 4.16 showed a resistor network circuit when 1k Ω added. The resistor network circuit consists of a network of 16 470 Ω resistors to mimic a homogeneous environment that will be stable to test and calibrate the EIT system. One 1k Ω resistor

used to imbalance the circuit to detect the change of conductivity through the measured data. 470Ω and $1k\Omega$ both resistors selected randomly with 1% tolerance of error.

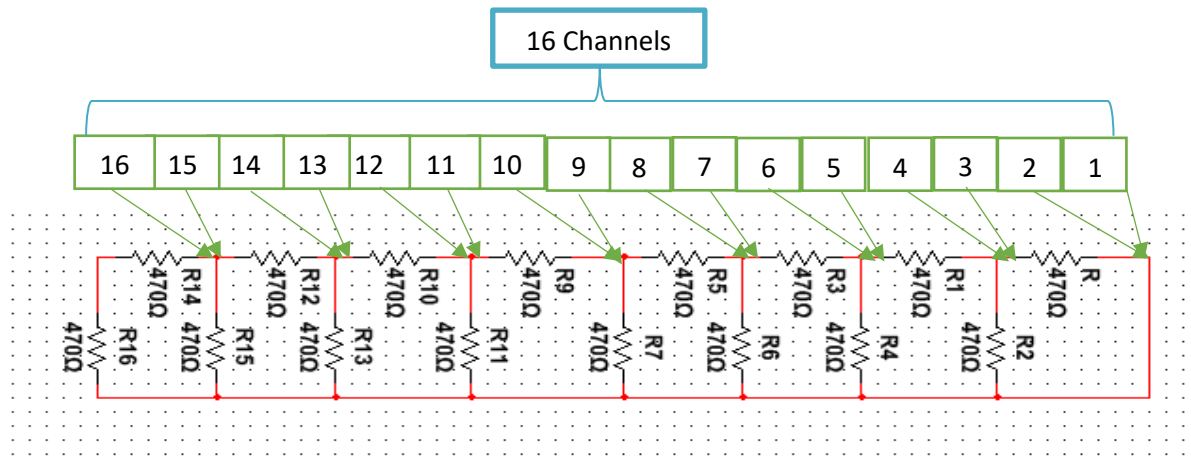


Figure 4.15: Schematic diagram of resistor network circuit without using switching box.

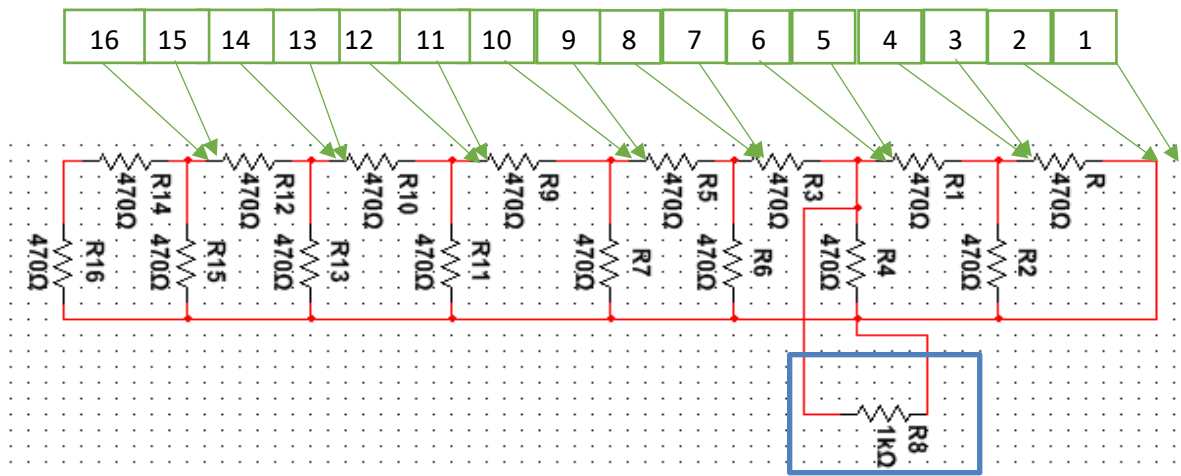
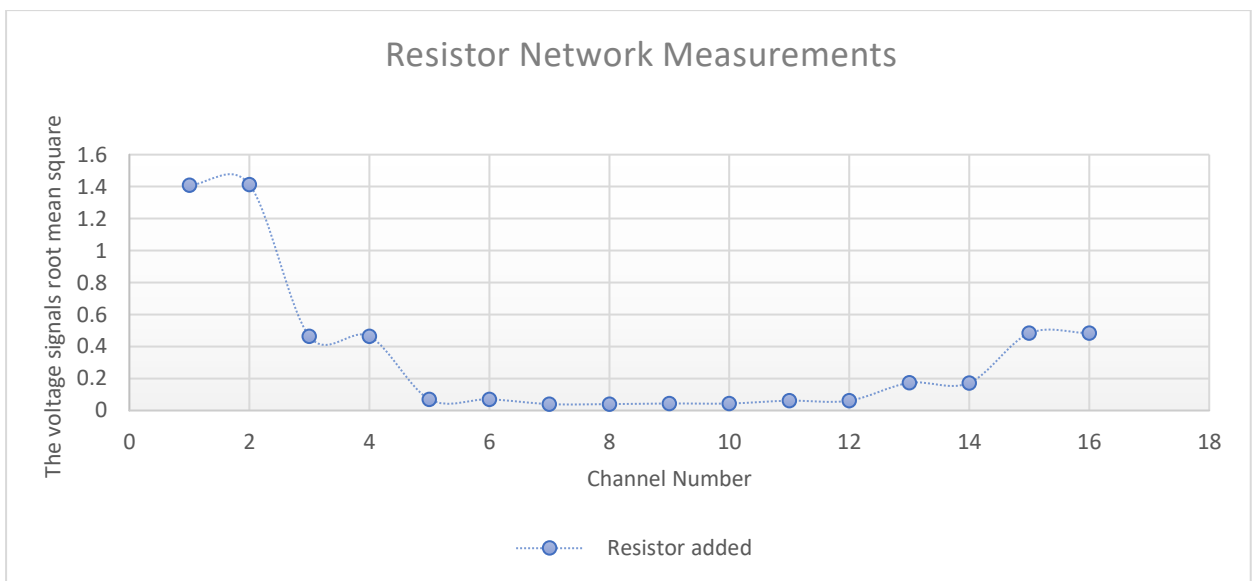


Figure 4.16: Schematic diagram of resistor network circuit with added $1k\Omega$ resistor without using switching box.

Figure 4.17 plots the RMS voltage for the situation when resistor is added. Alternatively, Figure 4.18 presents the RMS voltage when a $1k\Omega$ resistor is added and without added. As displayed in the highest change was observed between electrodes 5 and 6 when $1k\Omega$ resistor was added, as shown in Figure 4.19. The measurements of voltage root mean square (RMS) of 16 channels without using the switching box are displayed in Table 4.4. The results were obtained from the resistor circuit board after the signal was injected into channels 1 and 2 of the circuit board.

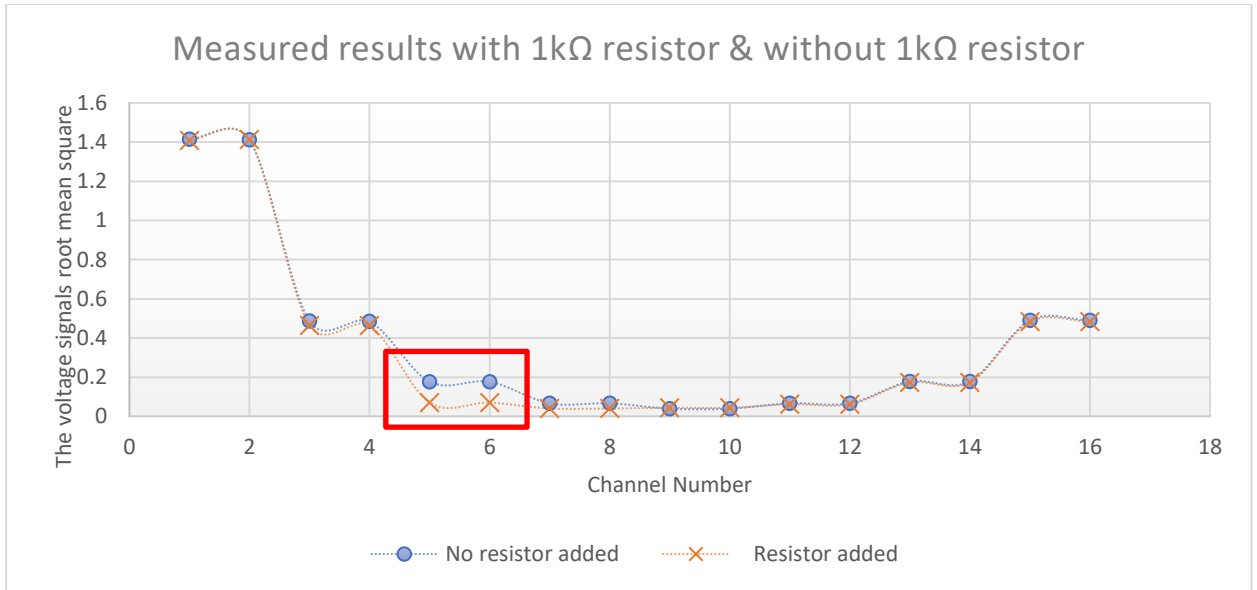
Table 4.4: Measurement results of single-ended voltage using the adjacent measurement strategy without switching box.

Root Mean Square(V)	No resistor added	Resistor added	Difference
RMS1	1.4157832	1.4090955	0.0066876
RMS2	1.411813	1.4131512	-0.0013382
RMS3	0.486092	0.4637466	0.0223454
RMS4	0.4849974	0.4646224	0.020375
RMS5	0.1766696	0.0704	0.1062696
RMS6	0.1767369	0.0701934	0.1065435
RMS7	0.0664885	0.0399371	0.0265513
RMS8	0.0666482	0.0399394	0.0267088
RMS9	0.0391929	0.0439346	-0.0047417
RMS10	0.0391176	0.0439057	-0.0047881
RMS11	0.0669235	0.061478	0.0054455
RMS12	0.0668067	0.0615244	0.0052823
RMS13	0.1781734	0.1729938	0.00518
RMS14	0.1786026	0.1724831	0.00612
RMS15	0.4906963	0.48312	0.007576
RMS16	0.4901229	0.4838239	0.006299



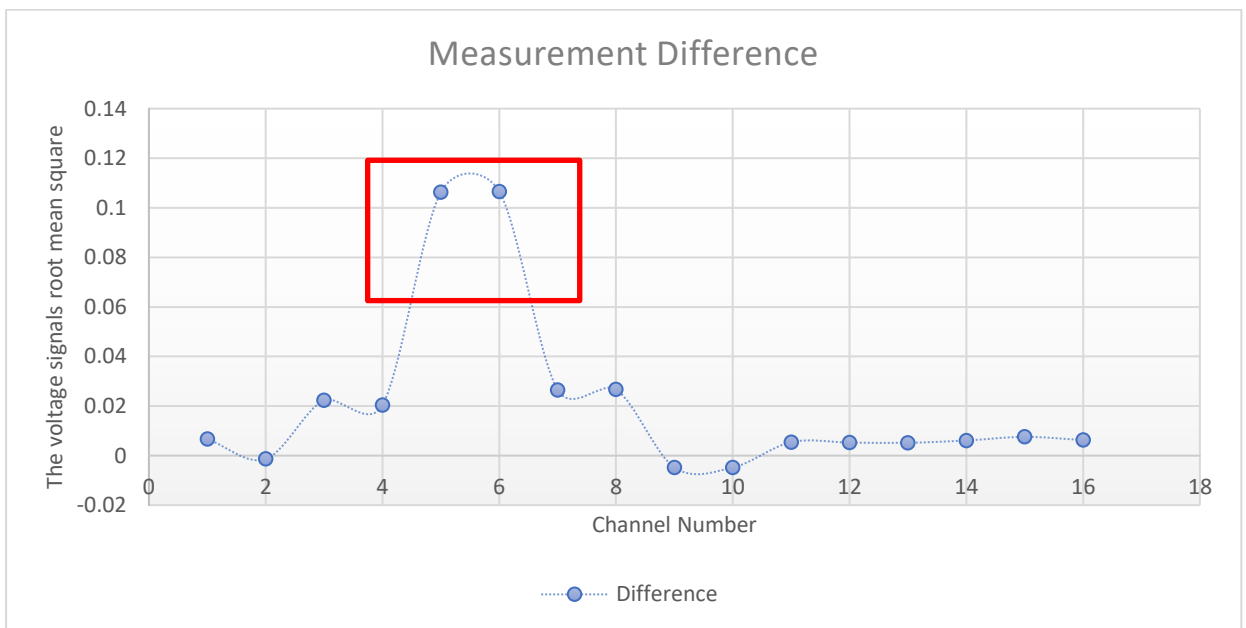
Resistor added	1.4091	1.4132	0.4638	0.4637	0.0704	0.0702	0.0399	0.0399	0.0439	0.0439	0.0615	0.0615	0.1729	0.1725	0.4831	0.4838
	91	315	375	462	04	019	994	994	393	391	148	152	299	248	312	2

Figure 4.17: RMS voltage of 16-Channel resistor network; simulated measurements without using switching box.



Resistor added	1.40 91	1.41 315	0.46 375	0.46 462	0.07 04	0.07 019	0.03 994	0.03 994	0.04 393	0.04 391	0.06 148	0.06 152	0.17 299	0.17 248	0.48 312	0.4 83 82
No resistor added	1.41 578	1.41 181	0.48 609	0.48 5	0.17 667	0.17 674	0.06 649	0.06 665	0.03 919	0.03 912	0.06 692	0.06 681	0.17 817	0.17 86	0.49 07	0.4 90 12

Figure 4.18: RMS voltage of 16-channels resistor network, simulated measurements.



Difference	0.00 6687 6	- 0.00 1338	0.022 3454	0.02 0375	0.106 2696	0.10 6543 5	0.026 5513	0.026 7088	- 0.00 4742	- 0.00 4788	0.00 5445 5	0.005 2823	0.00 518	0.00 612	0.00 7576	0.00 6299
------------	-------------------	-------------------	---------------	--------------	---------------	-------------------	---------------	---------------	-------------------	-------------------	-------------------	---------------	-------------	-------------	--------------	--------------

Figure 4.19: RMS voltage difference of 16-channels resistor network, simulated measurements.

4.2.1.2 Measurements of single-ended signaling using switching box

The sixteen-channel single-ended EIT system was tested using a resistor network circuit. The 16 channels arranged the same as arranged in sequence, as shown in Figure 4.20, and Figure 4.21 with a $1\text{k}\Omega$ resistor. In this section, the same producers repeated but this time using a switching box.

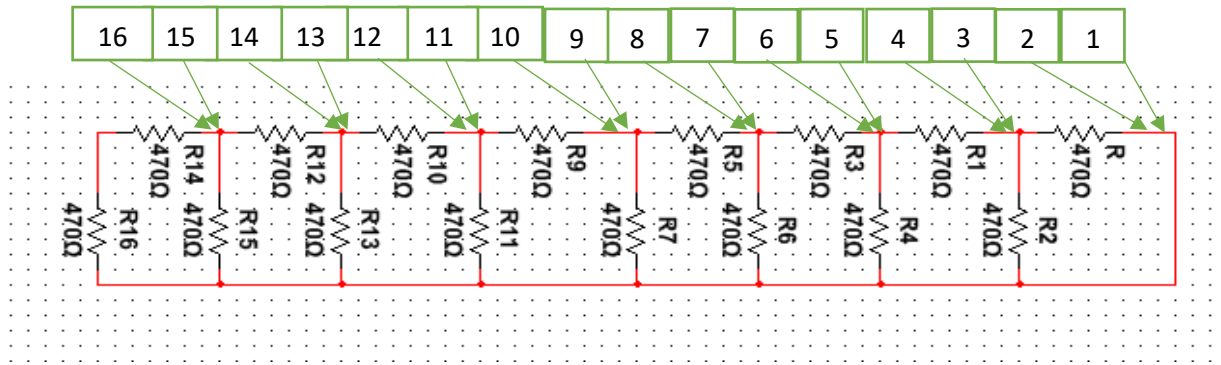


Figure 4.20: Schematic diagram of resistor network circuit using switching box.

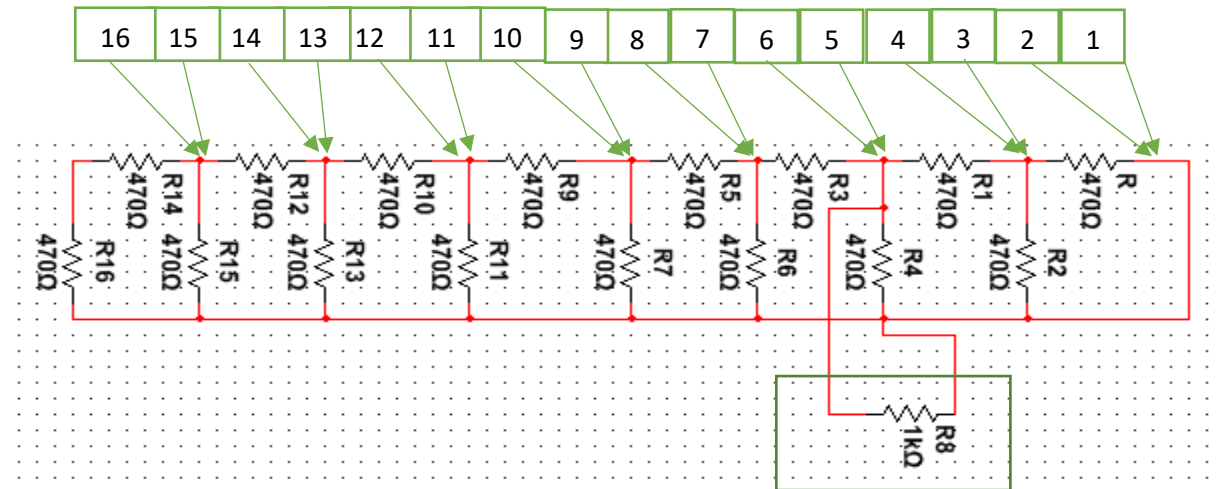


Figure 4.21: Schematic diagram of resistor network circuit with $1\text{k}\Omega$ resistor added, using switching box.

The measurements of RMS voltage of 16 channels are shown in Table 4.5. These results were obtained from the resistor circuit board after the signal was inserted into terminals 1 and 2 of the circuit board using the switching box.

Table 4.5: Measurements of single-ended voltage using switching box and the adjacent measurement strategy.

Root Mean Square(V)	No resistor added	Resistor added	Difference
RMS1	1.412928077	1.410147	0.002781
RMS2	1.408733423	1.414198	-0.00546
RMS3	0.466986388	0.453297	0.013689
RMS4	0.466601174	0.454276	0.012325
RMS5	0.166908606	0.071641	0.095268
RMS6	0.167256767	0.071511	0.095746
RMS7	0.063406779	0.04718	0.016227
RMS8	0.063464449	0.047166	0.016298
RMS9	0.042945311	0.050135	-0.00719
RMS10	0.0429673	0.050145	-0.00718
RMS11	0.061173225	0.061353	-0.00018
RMS12	0.061190465	0.061344	-0.00015
RMS13	0.157845732	0.15647	0.001376
RMS14	0.158341811	0.156005	0.002337
RMS15	0.463625305	0.4599	0.003726
RMS16	0.462595451	0.460677	0.001919

Figure 4.22 shows the graph of the RMS voltage when no resistor is added using the switching box.

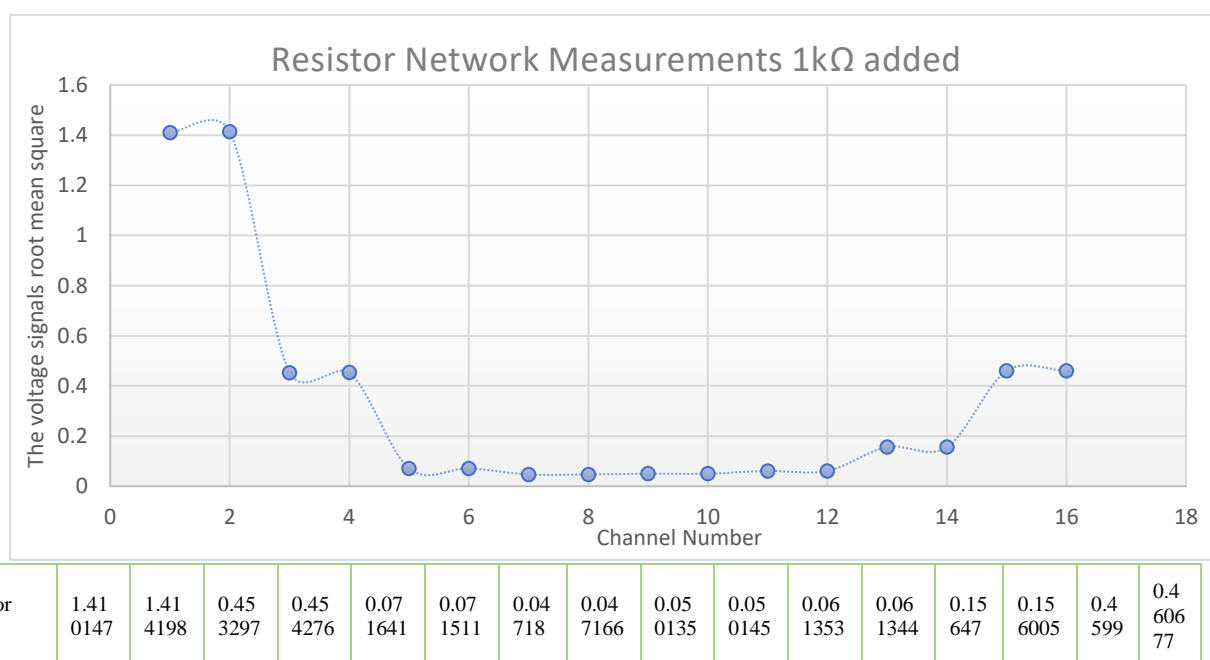


Figure 4.22: RMS voltage of 16-channels resistor network; simulated measurements using switching box.

Figure 4.23 shows the RMS voltage when a 1kΩ resistor is added and the switching box is used. As displayed in Figure 4.24, the highest change occurred between electrodes 5 and 6 when a 1kΩ resistor was added using the switching box.

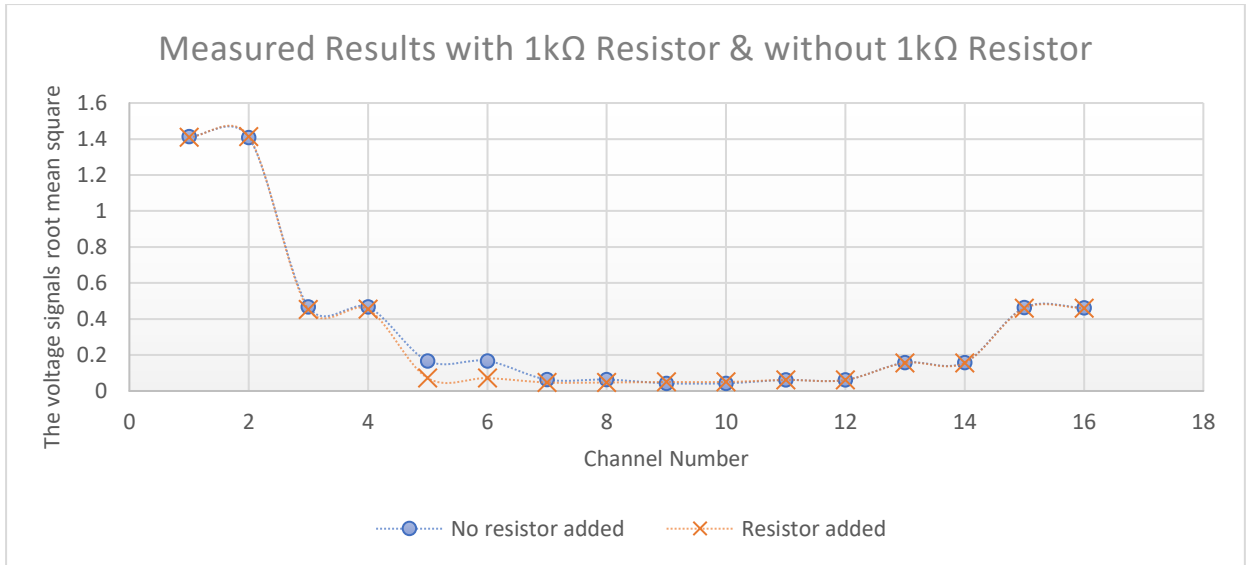


Figure 4.23: RMS voltage of 16-channels resistor network comparison with and without 1kΩ resistor; simulated measurements using switching box.

No resistor added	1.4129 281	1.408733 4	0.466986 4	0.466601 2	0.166908 6	0.167256 8	0.063406 8	0.063464 4	0.042945 3	0.042967 3	0.061173 2	0.061190 5	0.157845 7	0.158341 8	0.463625 3	0.462595 5
Resistor added	1.4101 47	1.414198 4198	0.453297 3297	0.454276 4276	0.071641 1641	0.071511 1511	0.04718 718	0.047166 7166	0.050135 0135	0.050145 0145	0.061353 1353	0.061344 1344	0.15647 647	0.156005 6005	0.4599 99	0.460677 0677

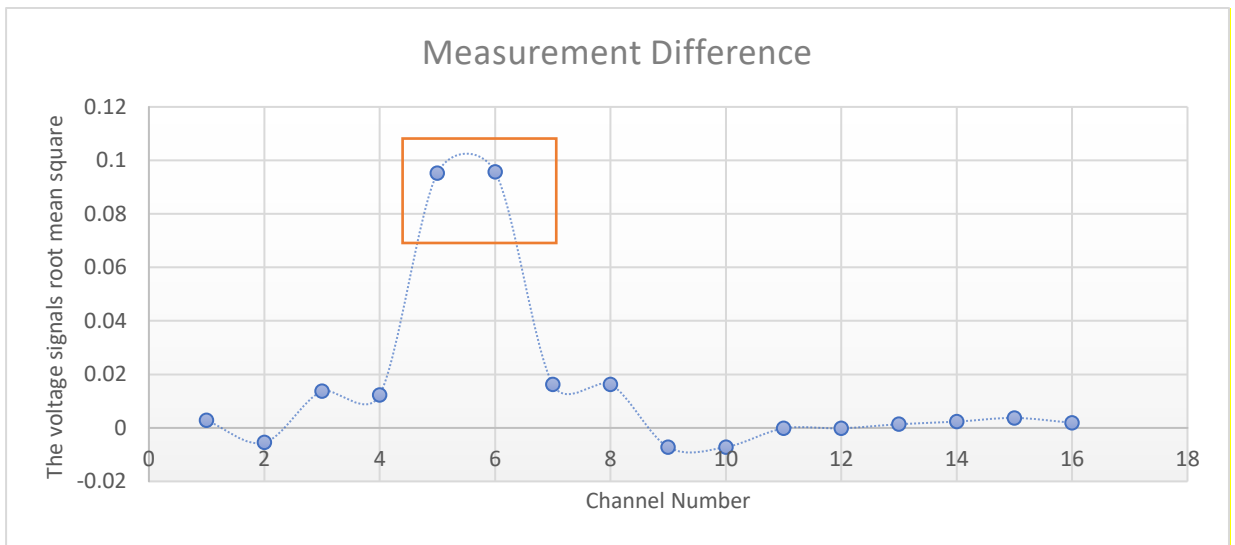


Figure 4.24: RMS voltage difference of 16-channels resistor network; simulated measurements using switching box.

Difference	0.002781	-0.00546	0.013689	0.012325	0.095268	0.095746	0.016227	0.016298	-0.00719	-0.00718	-0.00018	-0.00015	0.001376	0.002337	0.003726	0.001919
------------	----------	----------	----------	----------	----------	----------	----------	----------	----------	----------	----------	----------	----------	----------	----------	----------

As shown in Figure 4.25, the impedance change location was detected using the EIDORS program.

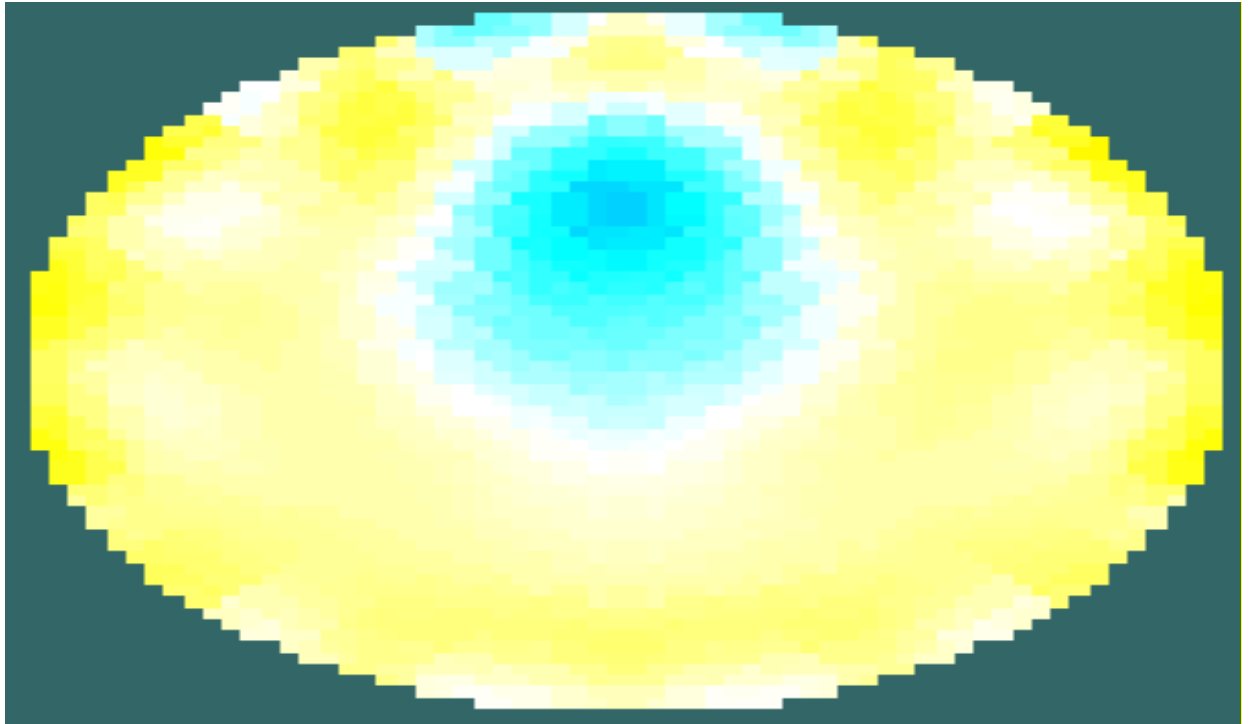


Figure 4.25: The 2D reconstructed image with added $1\text{k}\Omega$ resistor using switching box.

4.2.2 Comparison of measurements of single-ended signalling with and without using switching box

The EIT system configuration for both using the switching box (SB) and not using the switching box (NSB) is as shown below:

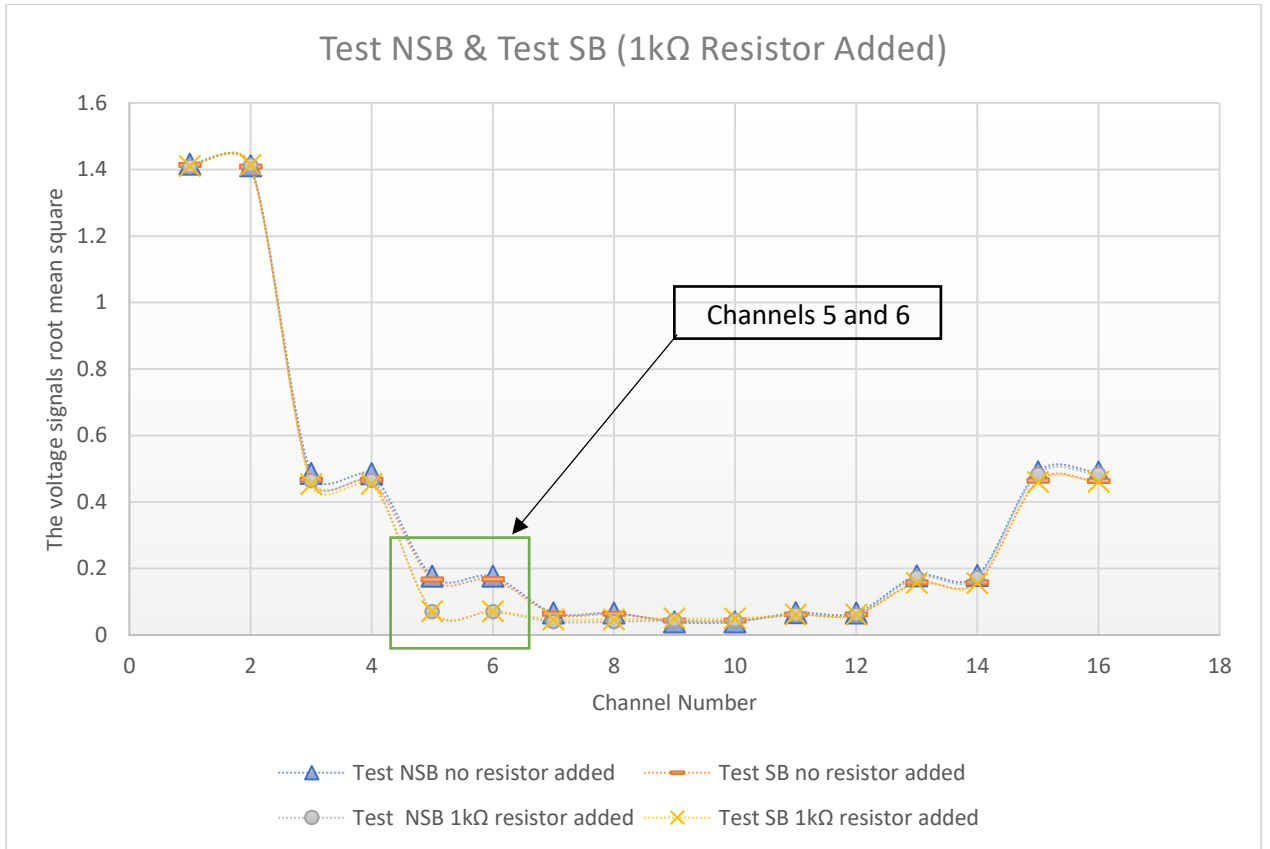
- ✓ Frequency: 50 kHz
- ✓ Sampling Rate: 3000000
- ✓ Amplitude: 2 V
- ✓ Samples to read 200
- ✓ Rate: 1 kHz
- ✓ Voltage injected into channels 1 and 2 for the experiments

Table 4.6 shows the measurement results of the single-ended voltage for SB and NSB when the resistance distribution of the resistor network circuit board is changed by attaching a $1\text{k}\Omega$ resistor to the circuit board.

Table 4.6: Measurement results of single-ended voltage using SB and NSB.

Root Mean Square(V)	Test NSB no resistor added	Test SB no resistor added	Test NSB 1kΩ resistor added	Test SB 1kΩ resistor added	Difference NSB	Difference SB
RMS1	1.4157832	1.4129281	1.409096	1.410147	0.006688	0.002781
RMS2	1.411813	1.4087334	1.413151	1.414198	-0.00134	-0.00546
RMS3	0.486092	0.4669864	0.463747	0.453297	0.022345	0.013689
RMS4	0.4849974	0.4666012	0.464622	0.454276	0.020375	0.012325
RMS5	0.1766696	0.1669086	0.0704	0.071641	0.10627	0.095268
RMS6	0.1767369	0.1672568	0.070193	0.071511	0.106544	0.095746
RMS7	0.0664885	0.0634068	0.039937	0.04718	0.026551	0.016227
RMS8	0.0666482	0.0634644	0.039939	0.047166	0.026709	0.016298
RMS9	0.0391929	0.0429453	0.043935	0.050135	-0.00474	-0.00719
RMS10	0.0391176	0.0429673	0.043906	0.050145	-0.00479	-0.00718
RMS11	0.0669235	0.0611732	0.061478	0.061353	0.005446	-0.00018
RMS12	0.0668067	0.0611905	0.061524	0.061344	0.005282	-0.00015
RMS13	0.1781734	0.1578457	0.172994	0.15647	0.00518	0.001376
RMS14	0.1786026	0.1583418	0.172483	0.156005	0.00612	0.002337
RMS15	0.4906963	0.4636253	0.48312	0.4599	0.007576	0.003726
RMS16	0.4901229	0.4625955	0.483824	0.460677	0.006299	0.001919

Figure 4.26 shows the results of resistivity change when switching unite has been used and without using it as demonstrated that the measurements are stable. Figure 4.27 shows the highest change in conductivity observed from channels 5 and 6, which indicated the ability of the system to track detect the difference with and without using the switching box.



Test NSB no resistor added	1.41 578 32	1.4 118 13	0.4 86 09 2	0.4 849 974	0.17 6669 6	0.17 6736 9	0.06 6488 5	0.066 6482	0.03 9192 9	0.03 9117 6	0.0 66 92 35	0.06 6806 7	0.17 8173 4	0.17 8602 6	0.4 906 963	0.490 1229
Test SB no resistor added	1.41 292 81	1.4 087 334	0.4 66 98 64	0.4 666 012	0.16 6908 6	0.16 7256 8	0.06 3406 8	0.063 4644	0.04 2945 3	0.04 2967 3	0.0 61 17 32	0.06 1190 5	0.15 7845 7	0.15 8341 8	0.4 636 253	0.462 5955
Test NSB 1kΩ resistor added	1.40 909 6	1.4 131 51	0.4 63 74 7	0.4 646 22	0.07 04	0.07 0193	0.03 9937	0.039 939	0.04 3935	0.04 3906	0.0 61 47 8	0.06 1524	0.17 2994	0.17 2483	0.4 831 2	0.483 824
Test SB 1kΩ resistor added	1.41 015	1.4 142	0.4 53 3	0.4 542 8	0.07 164	0.07 151	0.04 718	0.047 17	0.05 014	0.05 015	0.0 61 35	0.06 134	0.15 647	0.15 601	0.4 599	0.460 68

Figure 4.26: Comparison of RMS voltage measurements of 16-channels resistor network using SB and NSB.

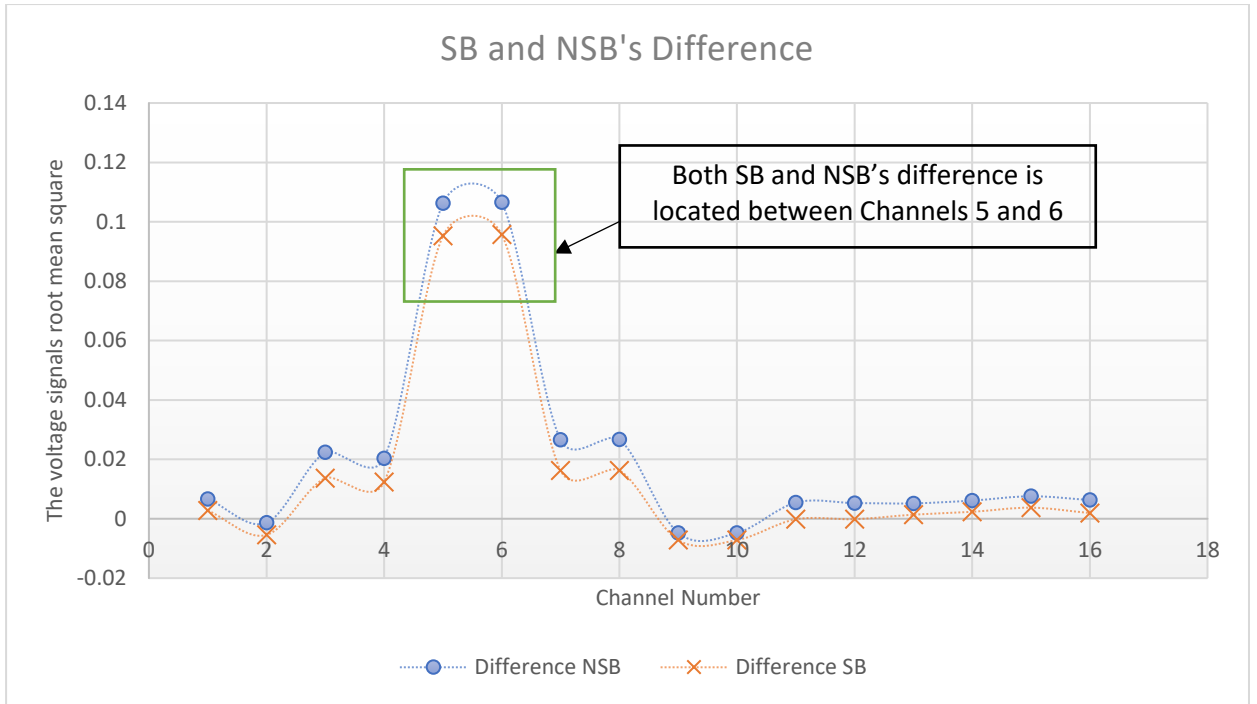


Figure 4.27: RMS voltage difference of 16- channels resistor network using SB and NSB.

4.3 Conclusion

This chapter investigates advancements in Electrical Impedance Tomography (EIT) systems, transitioning from traditional 8-channel differential signaling to a 16-channel single-ended signaling approach using a switching box (SB). Differential signaling, which uses two electrodes per measurement, was adapted to EIDORS software via the Zero Method (inserting zeros between measurements) and Average Method (interpolating adjacent values), with the latter yielding clearer reconstructed images. Single-ended signaling, using one electrode per measurement, improves spatial resolution and data density, eliminating the need for interpolation. A calibrated SB enabled seamless scaling to 16 channels, stabilizing measurements even when a 1kΩ resistor simulated conductivity changes in resistor network tests. Results showed that single-ended systems with SB detect impedance variations more accurately than differential systems, with the Average Method reducing artifacts. Resistor networks

validated the system's reliability, demonstrating that SB configurations enhance scalability and stability for practical EIT applications.

Chapter 5 Single-ended electrical impedance tomography (SEIT) system

EIT system, which is one type of electromagnetic tomography, operates under the principle that image electrical distribution image changes inside the area of interest (Aguiar Santos et al., 2016). Ordinary EIT systems use a set of electrodes that is placed on the surface of the aimed object, into which alternating current (AC) is applied, and voltage(s) or current(s) from the electrodes are measured, recorded, and processed to reconstruct a two-dimensional (2D) image (Aguiar Santos et al., 2016; Van der Burg et al., 2014; Hong et al., 2015; Zhang et al., 2015; Sarode, Patil and Cheeran, 2014; Li and Soleimani, 2013; Dowrick, Blochet and Holder, 2015; Guermandi et al., 2014). However, limited attention has been devoted to the way in which the measurements themselves are made. Therefore, most EIT system developers try to increase the image quality by only improving the reconstruction algorithms. However, the quality of the image also depends upon the sensitivity of the measuring system and varies with distance from the electrodes (Kauppinen, Hyttinen and Malmivuo, 2005). Because of this, the typical measurement strategy requires connection of a pair of electrodes for single data measurement, which will result in increased complexity of the control program read and wiring data since there will be more wires required for each data measurement. However, different data collection strategies exist, such as opposite, cross, and adjacent measurement; these strategies are used for extracting complete dataset measurements of electric potential at the boundary walls of the object. Applying different EIT measurement strategies will solve some of the electrical signal propagation issues and will improve the detecting and tracking of the resistivity change for certain EIT applications (Guermandi et al., 2014; Jaakko and Robert., 1995). However, in some systems, the switching box or the multiplexer should be modified or replaced to support the collection strategies. The single-ended EIT system has been implemented to improve the flexibility, reliability, and cost-efficiency of the measurement system. In a typical EIT system, a signal can be injected by using two wires for each injection, and this is controlled via a multiplexer or switching box. Moreover, the measured data required two wires for single data measurements. Thus, the existing system required more wires and a more complex circuit to control the I/O signals. That will result in an increased data error rate (Guermandi et al., 2014) and will

increase the cost significantly. On the other hand, the developed single-ended EIT system requires one wire connection to produce one signal injection, and this is controlled using a switching box. Similarly, the measured data required one wire connection for a single data measurement. Therefore, the SEEIT system will reduce the number of wires required to measure or inject a signal by 50%. The developed SEEIT system can use most of the electrical impedance measurement methods such as opposite, cross, and adjacent, employing single-ended signalling. Using the SEEIT system will enable the number of channels needed to measure or apply signals through an electrode to be reduced. Furthermore, this SEEIT system will overcome the need for a current (I) sinking source that is required in traditional EIT systems, which would decrease the measurement error (Aw el at., 2014).

5.1 System architecture of the SEEIT system

The SEEIT system that was designed and developed incorporating hardware consists of the host computer, data acquisition system (DAQ), switching box (multiplexer unit), and testing object. The architecture and operating process of the SEEIT system is shown in Figure 5.1. The electrode array is a collection of electrodes arranged around cylindrical vessels. The multiplexer controls the electrical signal direction of 16 electrodes through a pre-programmed NI PCI-6281 data acquisition system using LabVIEW, while the acquisition module is used to monitor and provide the energy source to the electrode array. At the same time, the reconstruction processing module processes the raw data that is measured from the electrode array. Finally, image processing is used to analyse the processed data and reconstruct an image.

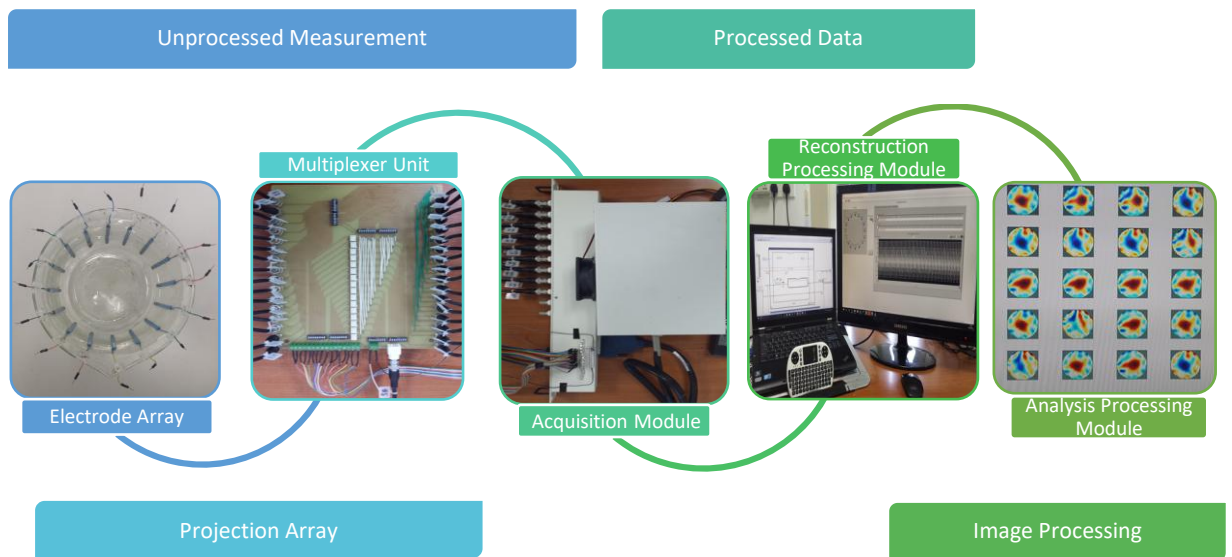


Figure 5.1: SEEIT system architecture.

5.2 SEEIT system hardware and software

The SEEIT system operates based on the electrical conductivities (current(s) and voltage(s)) of any conductive object and depends on the characteristics of the element. The original SEEIT system which was developed shown in Figure 5.2. The system consists of three sets of 16 electrode array, which were designed and fabricated. The first electrode array set made of copper strip plated with soldering lead to resist corrosion, and the rest of the electrode array sets made of titanium alloy grade 2; they described in chapter 3. The switching box, which was designed to handle single-ended signals, is controlled by 16 digital channels, monitors excitation signals for 16 electrodes, and measures the voltage(s) or current(s) signal changes. Only 16 lines connected to the electrode; they can be used for signal injection or extraction and can be adjusted using the control elements on the developed software. The BNC connector block has 22 BNC connectors for analogue I/O and 29 spring terminals for digital I/O connectivity and two user-defined BNC connectors. The connector block is connected to the data acquisition system using high-performance 68-pin shielded cable. The data acquisition box features the power supply, DAQ card (NI PCI-6281), and PCI to ExpressCard 34 board. Moreover, two analogue outputs, which have an adjustable frequency range of 1 Hz to 1 MHz and voltage amplitude range of -10 to +10 V, are provided. The host laptop is used to control, monitor, processes, and compute the

measured data received from the DAQ system for image reconstruction using the EIDORS tool. The SEEIT system was calibrated using a 32-resistor network circuit and a 16-resistor network circuit.

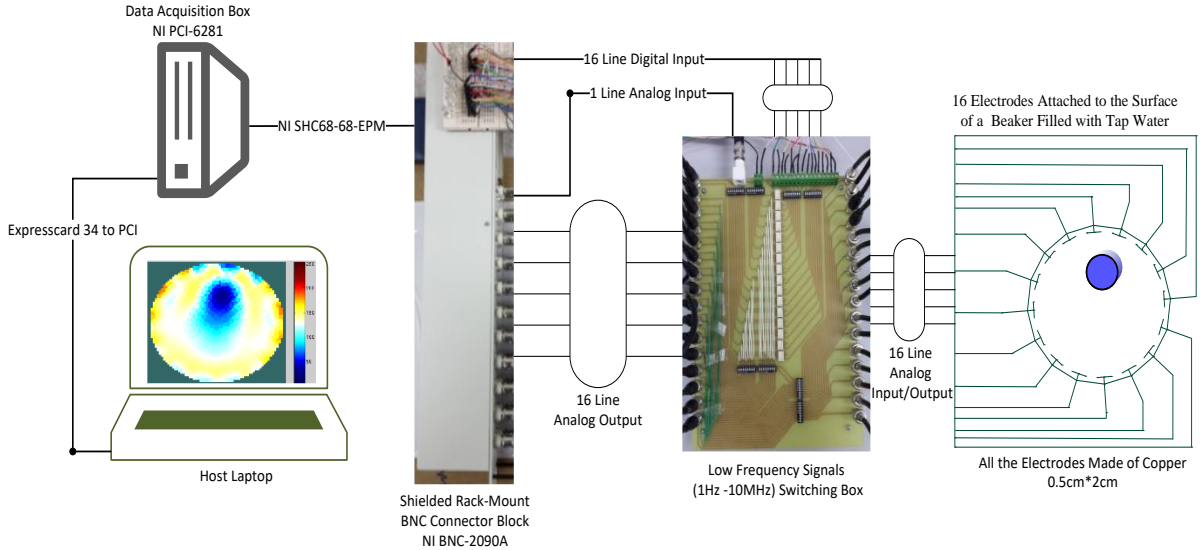


Figure 5.2: SEEIT hardware block diagram consists of a four-part testing vessel, switching box, data acquisition (DAQ) system, and operating program.

However, the SEEIT system LabVIEW program can be simplified to three main loops, which are executed simultaneously which has been clarified in chapter 3 section 3.1.1.2.6.

Figure 5.3 (a) shows the channel configuration and signal generator configuration controls. The channel configuration controls are located on the left side of the Settings tab. The parameters for channel configuration for both measured and generated signals have been illustrated in chapter 3 section 3.1.1.2.4. The SEEIT system automatically chooses the appropriate gain for each channel. The smallest detectable measurement change called Code Width determined by the DAQ resolution and the input signals range (Maximum Value/Minimum Value). Moreover, the input signals resolution for the current system is 18-bits. The Equation 5.1 below shows the formula needed to calculate the Voltage Code Width.

$$V_{CW} = \frac{(\text{Maximum value}) - (\text{Minimum value})}{2^{\text{resolution}}} \quad \text{Equation} \quad 5.1$$

These settings will prepare the system for ideal use in experimental SEEIT applications because the user can regulate signal input and output parameters. Figure 5.3 (b) shows the program block diagram of the SEEIT system.

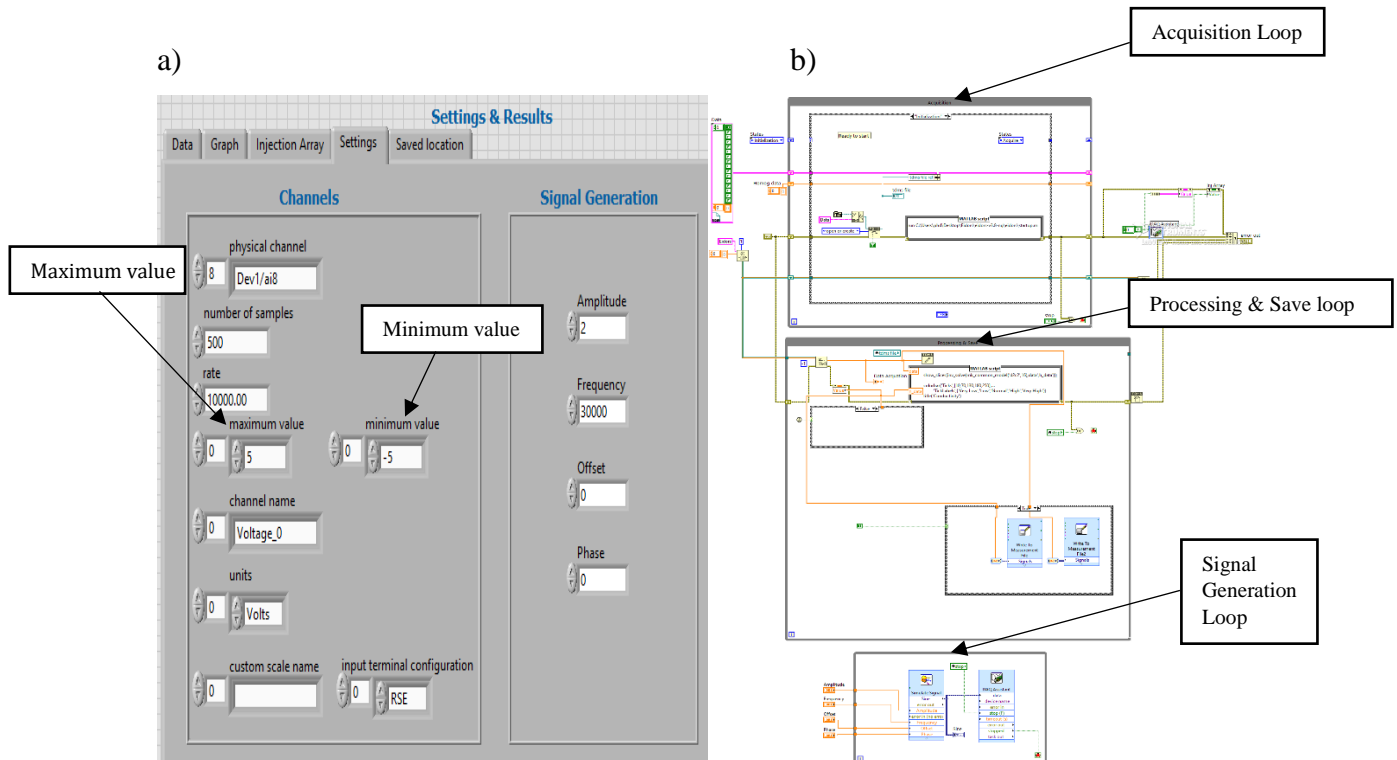


Figure 5.3: SEEIT system LabVIEW program: a) Controller panel of the analogue input and output, and b) Program block diagram of the SEEIT system.

Every measurement strategy has advantages and disadvantages, so specific applications require individual strategies. Furthermore, the use of different measurement strategies will improve the sensitivity and quality of the measured data. For example, the neighbouring (adjacent) measurement strategy is faster in terms of computational memory and requires a smaller amount of hardware to develop (Yang, and Spink, 1999). Alternatively, the current (I) distribution is unpredictable and current (I) density will drop in the center of the vessel, so the changes will be undetectable (shadow area). In another example, the diagonal strategy has a lower sensitivity than the neighbouring strategy, and the image quality is significantly better (Breckon, and Pidcock, 1987). However, the SEEIT system can apply most of the measurement strategies without the need for upgrading the hardware. The examples of measurement strategies presented in chapter 3 section 3.1.2.

5.3 Results and discussion

To validate the SEEIT system, including its ability to detect and track hidden conductive and non-conductive objects, the experiments were conducted using a beaker (cylindrical shape) of 180 mm diameter and 280 mm height filled with 3000 mL of tap water. Copper strips were used to make 16 electrodes, which were attached approximately 50 mm from the bottom of the beaker. The conductivity of the tap water, which was measured using an electrical conductivity meter, was 108 microS/cm at 24.6°C. Stainless steel and Teflon rods with different diameters were placed in a constant various position in the beaker, one after another. The first variance measurements were obtained when there was only water in the beaker. For the second variance measurements, the stainless steel and Teflon rods were placed in different locations inside the beaker. The two measurements were saved and compared by imaging them using EIDORS. In these experiments, a single-ended adjacent measurement strategy was used with a voltage amplitude of 2v and frequency ranging from 12–1000 kHz. The results of the measurements performed with the SEEIT system are presented in Tables 5.1–10. The reconstruction of both the conductive and non-conductive images were obtained. The conductive objects were stainless steel rod with wide diameters (50, 38, 26, and 12mm). Moreover, the non-conductive objects were Teflon rod with diameters of 50, 40, 25, and 14 mm. Basically, every rod, whether conductive or non-conductive, was placed in five different locations inside the testing beaker and exposed to five different injection signal frequencies: 12.5, 35, 70, 350, and 1000 kHz. Every table includes the real object location and the reconstructed image of the object. The five positions are listed below:

1. Nearby electrode 1, 2, 3, 4
2. Nearby electrode 5, 6, 7, 8
3. Nearby electrode 9, 10, 11, 12
4. Nearby electrode 13, 14, 15, 16
5. In the centre

Table 5.1: Conductive objects at different positions; images for four different rod sizes using 12.5 kHz for injection frequency.

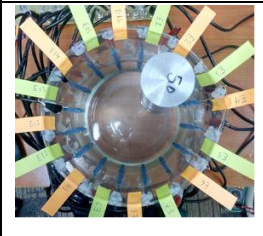
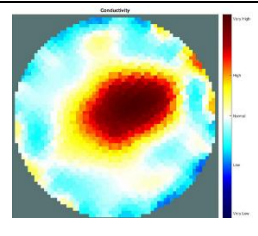
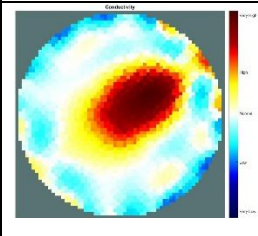
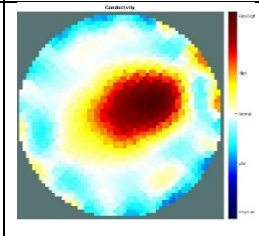
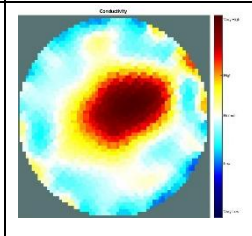
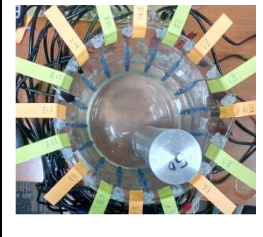
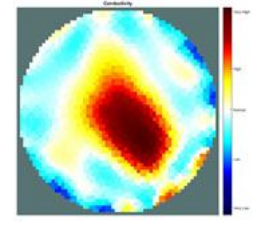
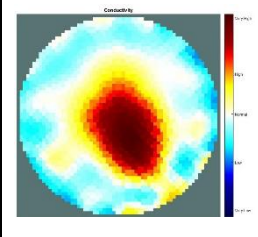
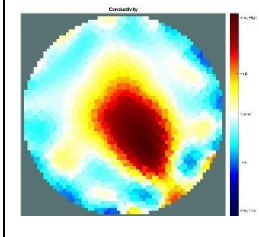
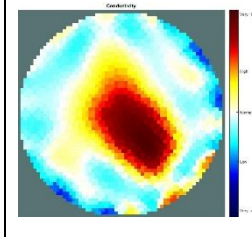
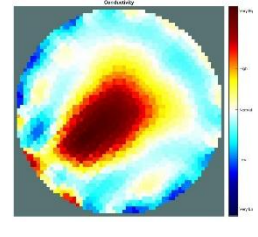
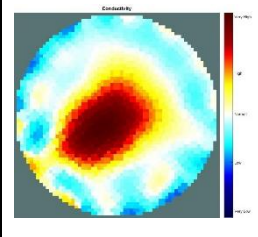
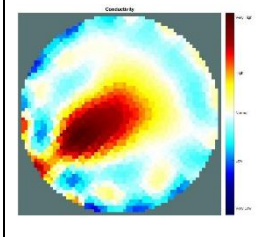
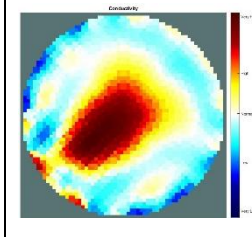
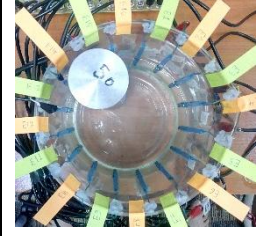
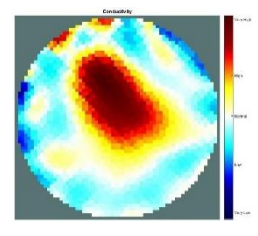
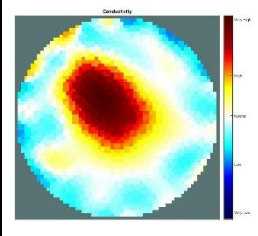
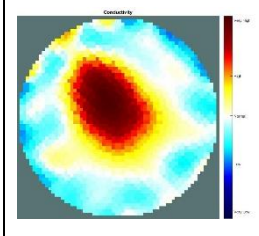
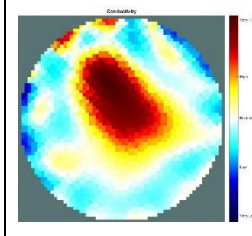
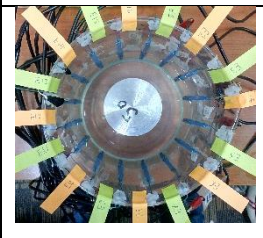
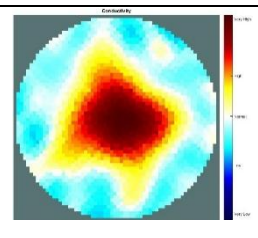
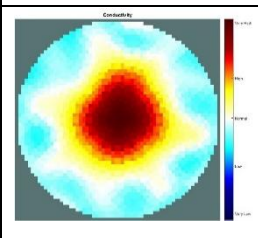
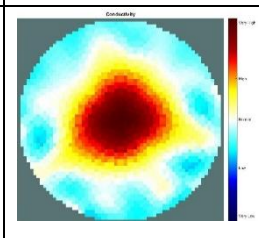
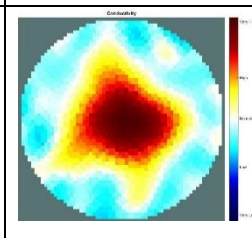
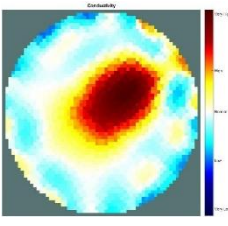
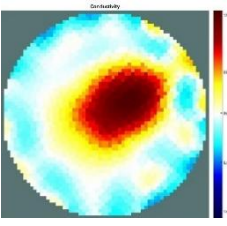
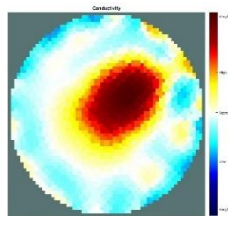
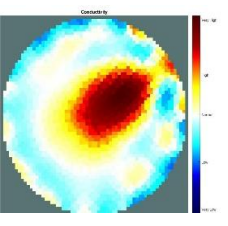
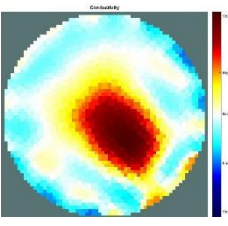
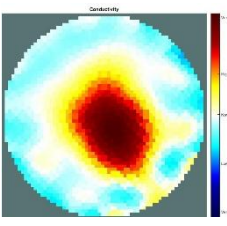
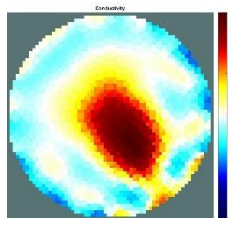
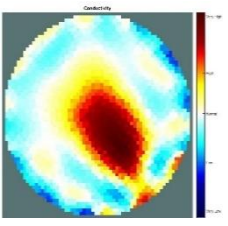
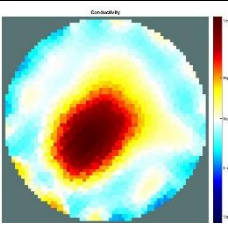
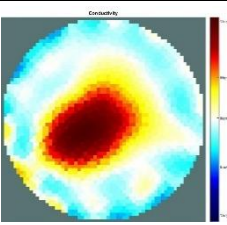
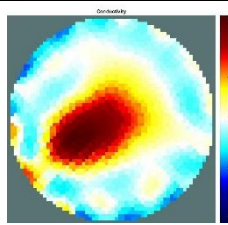
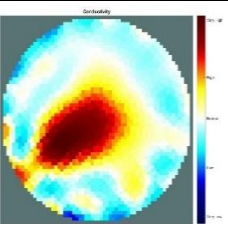
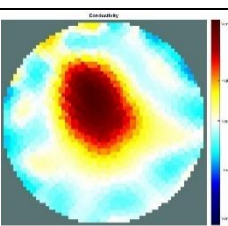
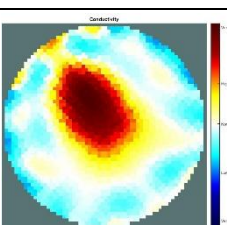
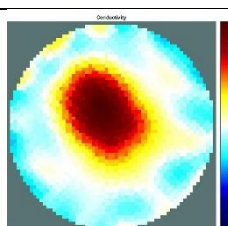
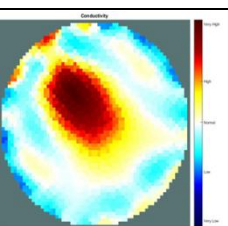
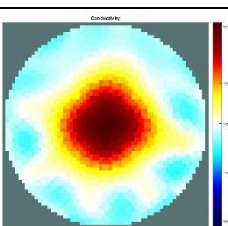
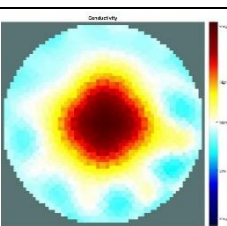
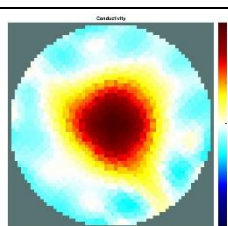
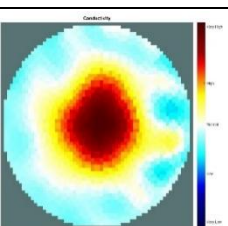
Injection frequency 12.5 kHz	Reconstructed images of conductive objects			
Real location	Stainless Steel Rod (50 mm diameter)	Stainless Steel Rod (38 mm diameter)	Stainless Steel Rod (26 mm diameter)	Stainless Steel Rod (12 mm diameter)
				
				
				
				
				

Table 5.1 shows the locations of stainless-steel rod objects of different sizes that are placed in various positions using 12.5 kHz for injection signals. The color scale illustrates the states of the conductivity changes. The red color means that the conductivity increased in that area, and the blue color means that the conductivity in that area dropped. However, as observed using the 12.5 kHz frequency, the SEEIT system can detect and provide information about positions of rods of all sizes. On

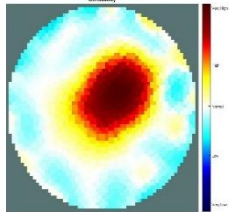
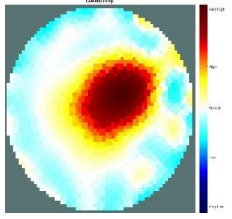
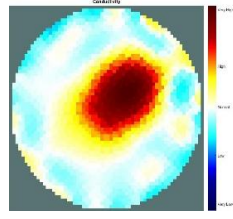
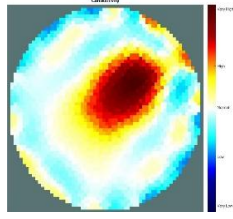
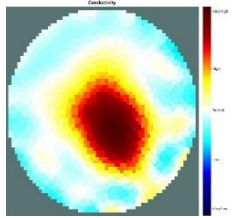
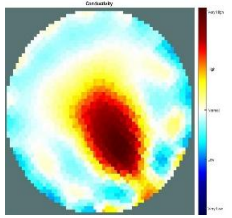
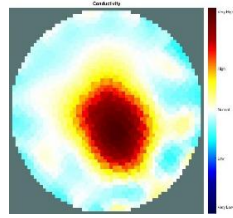
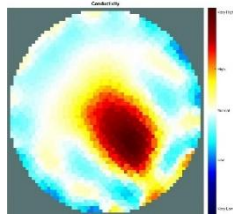
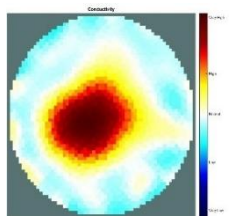
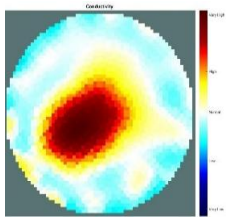
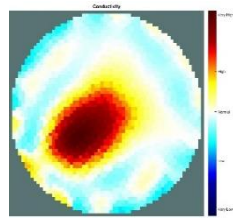
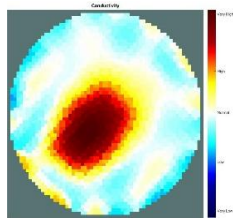
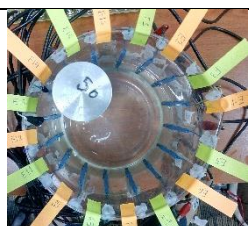
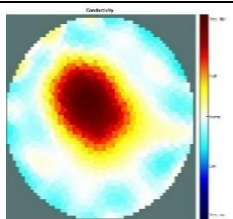
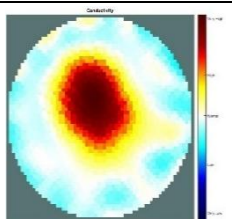
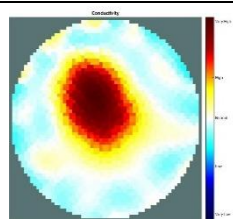
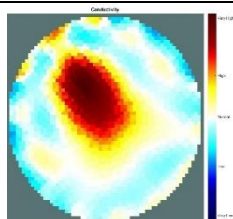
another note, all the reconstructed images show that the conductivity also increased in the center of the beaker, and that might be caused by a distant object or might cause by electrical current sinking and current discharge since the detected object good conductive.

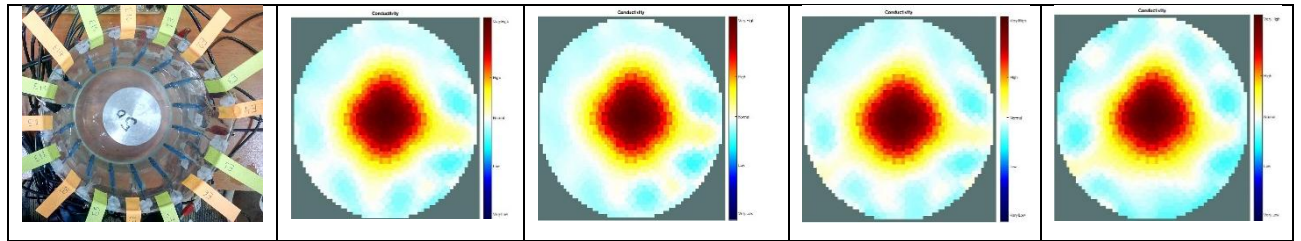
Table 5.2: Conductive objects at different positions; images for four different rod sizes using 35 kHz for injection frequency.

Injection frequency 35 kHz	Reconstructed images of conductive objects			
Real location	Stainless Steel Rod (50 mm diameter)	Stainless Steel Rod (38 mm diameter)	Stainless Steel Rod (26 mm diameter)	Stainless Steel Rod (12 mm diameter)
				
				
				
				
				

The reconstructed image using a frequency of 35 kHz is significantly better than the reconstructed image using 12.5 kHz, as observed. Note from the reconstructed images in Table 5.2 that the real object diameter changes almost imperceptibly, especially in the central positions. Moreover, the central detection problem is reduced in the 35 kHz reconstructed images compared to the 12.5 kHz images. However, the object detection and tracking works, as shown using the 35 kHz frequency. Table 5.3 shows the reconstructed images of the conductive object at different positions using 70 kHz. The results illustrate that, with 35 kHz and 70 kHz, detection and tracking behaviours are almost identical, but the background noise is less using the 70 kHz excitation frequency.

Table 5.3: Conductive objects at different positions; images for four different rod sizes using 70 kHz for injection frequency.

Injection frequency 70 kHz	Reconstructed images of conductive objects			
Real location	Stainless Steel Rod (50 mm diameter)	Stainless Steel Rod (38 mm diameter)	Stainless Steel Rod (26 mm diameter)	Stainless Steel Rod (12 mm diameter)
				
				
				
				



As seen in Table 5.4 using 350 kHz for the injection frequency to detect and track the conductive object, more accurate results were achieved than when using 12.5, 35, and 70 kHz. Also, the rod region diameter is more precise and consistent. However, the rod diameter problem when it placed in the central region is still present but improved because the reconstructed image is more accurate when the object is placed in a different location than when it is placed in the central region.

Table 5.4: Conductive objects at different positions; images for four different rod sizes using 350 kHz for injection frequency.

Injection frequency 350 kHz	Reconstructed images of conductive objects			
Real location	Stainless Steel Rod (50 mm diameter)	Stainless Steel Rod (38 mm diameter)	Stainless Steel Rod (26 mm diameter)	Stainless Steel Rod (12 mm diameter)

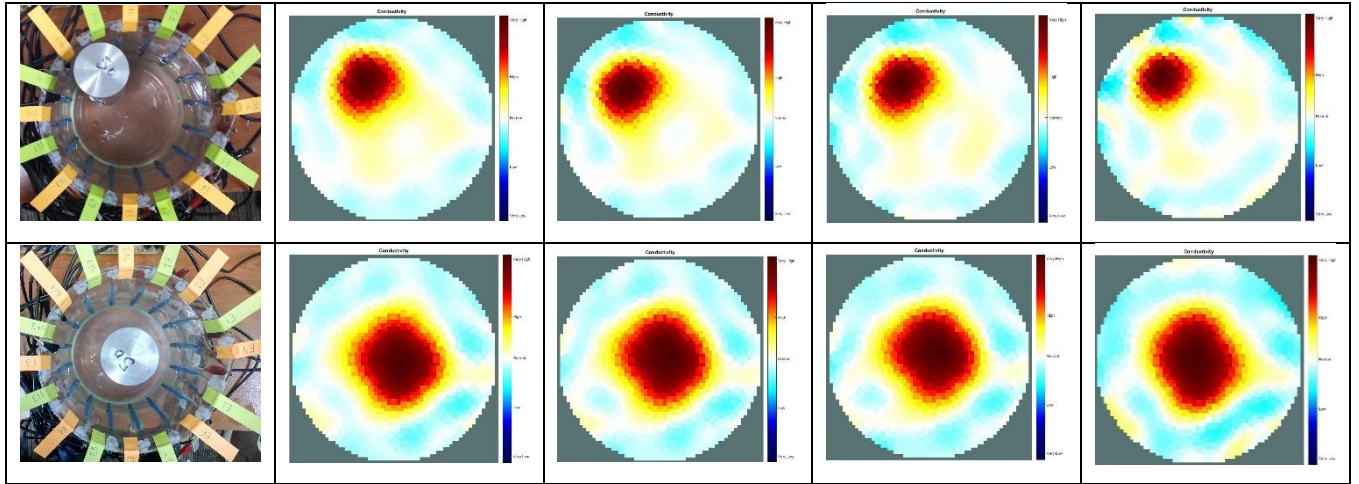
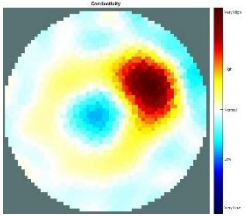
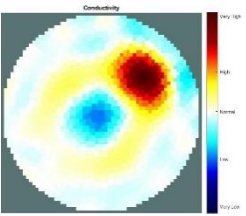
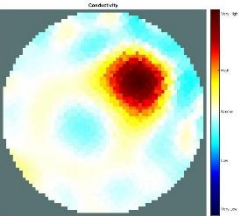
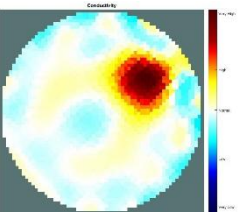


Table 5.5 shows that all the conductive rods were detected and tracked using the 1 MHz injection frequency. The 1 MHz reconstructed image is as accurate as the 350 kHz reconstructed image. Conversely, the amount of image background noise using 350 kHz is less than when using the 1 MHz reconstructed image. Moreover, it can be seen that the rod diameter problem in the central region using 1 MHz is elevated with 50 and 38 mm diameter rod. However, the most consistent excitation frequency to detect and track conductive objects with minimum image background noise at the four different rod diameters is observed to be 350 kHz. Furthermore, it is evident that the rod reconstructed image position precision using both 350 and 1000 kHz is better than that using 12.5, 35, and 70 kHz excitation frequencies.

Table 5.5: Conductive objects at different positions; images for four different rod sizes using 1 MHz for injection frequency.

Injection frequency 1 MHz	Reconstructed images of conductive objects			
Real location	Stainless Steel Rod (50 mm diameter)	Stainless Steel Rod (38 mm diameter)	Stainless Steel Rod (26 mm diameter)	Stainless Steel Rod (12 mm diameter)
				

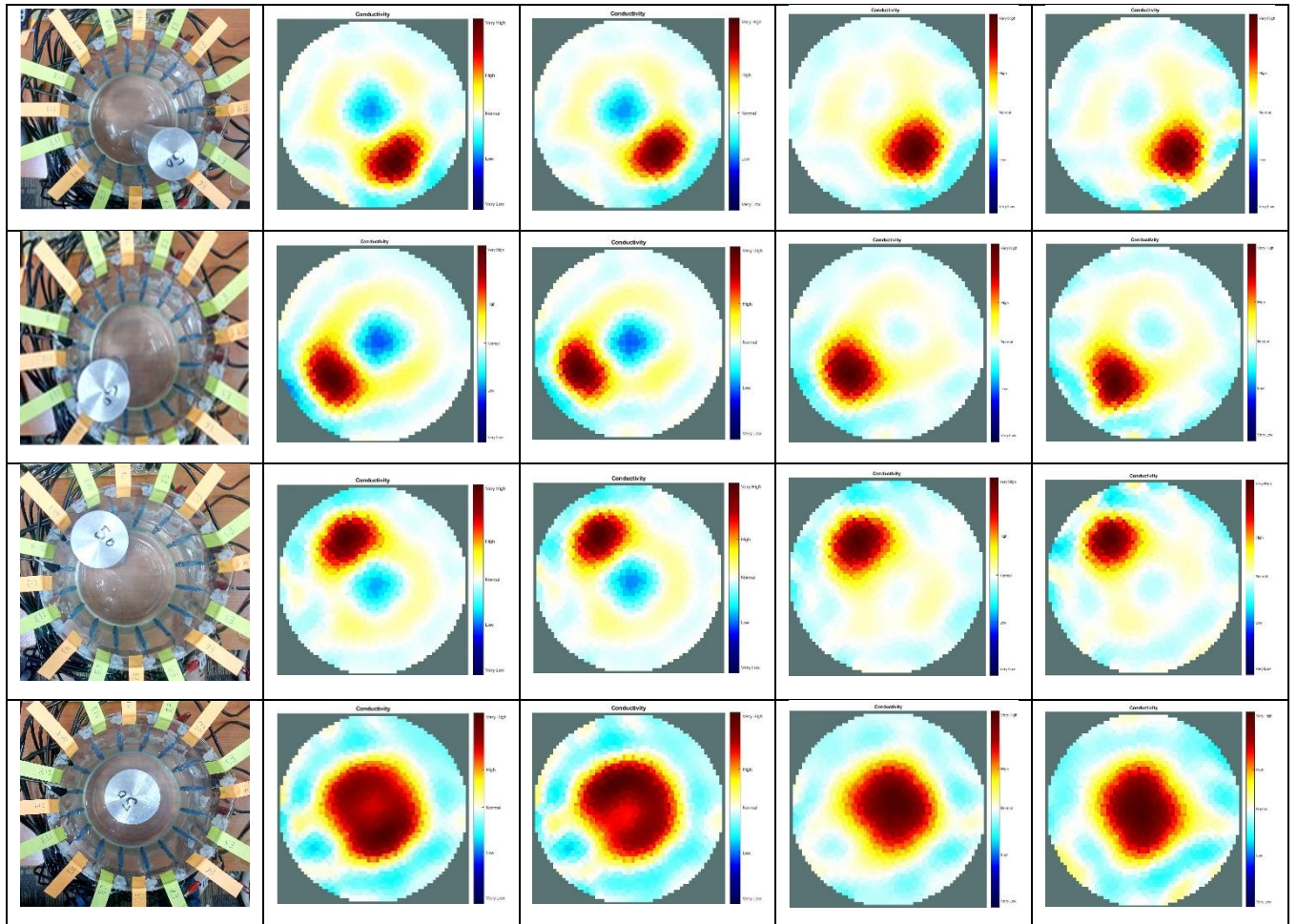


Table 5.6 shows the cross-sectional reconstructed images and locations of non-conductive rod objects with diverse diameters that are placed in different positions using 12.5 kHz for excitation signals. As observed at a low excitation frequency of 12.5 kHz, the SEEIT system can provide information about rod positions. However, all the reconstructed images show that the conductivity drops for all diameters except when they are placed in the center of the beaker position system, where the non-conductive object is undetectable.

Table 5.6: Non-conductive objects at different positions; images for four different rod sizes using 12.5 kHz for injection frequency.

Injection frequency 12.5 kHz	Reconstructed images of non-conductive objects			
Real location	Teflon rod (50 mm diameter)	Teflon rod (40 mm diameter)	Teflon rod (25 mm diameter)	Teflon rod (14 mm diameter)

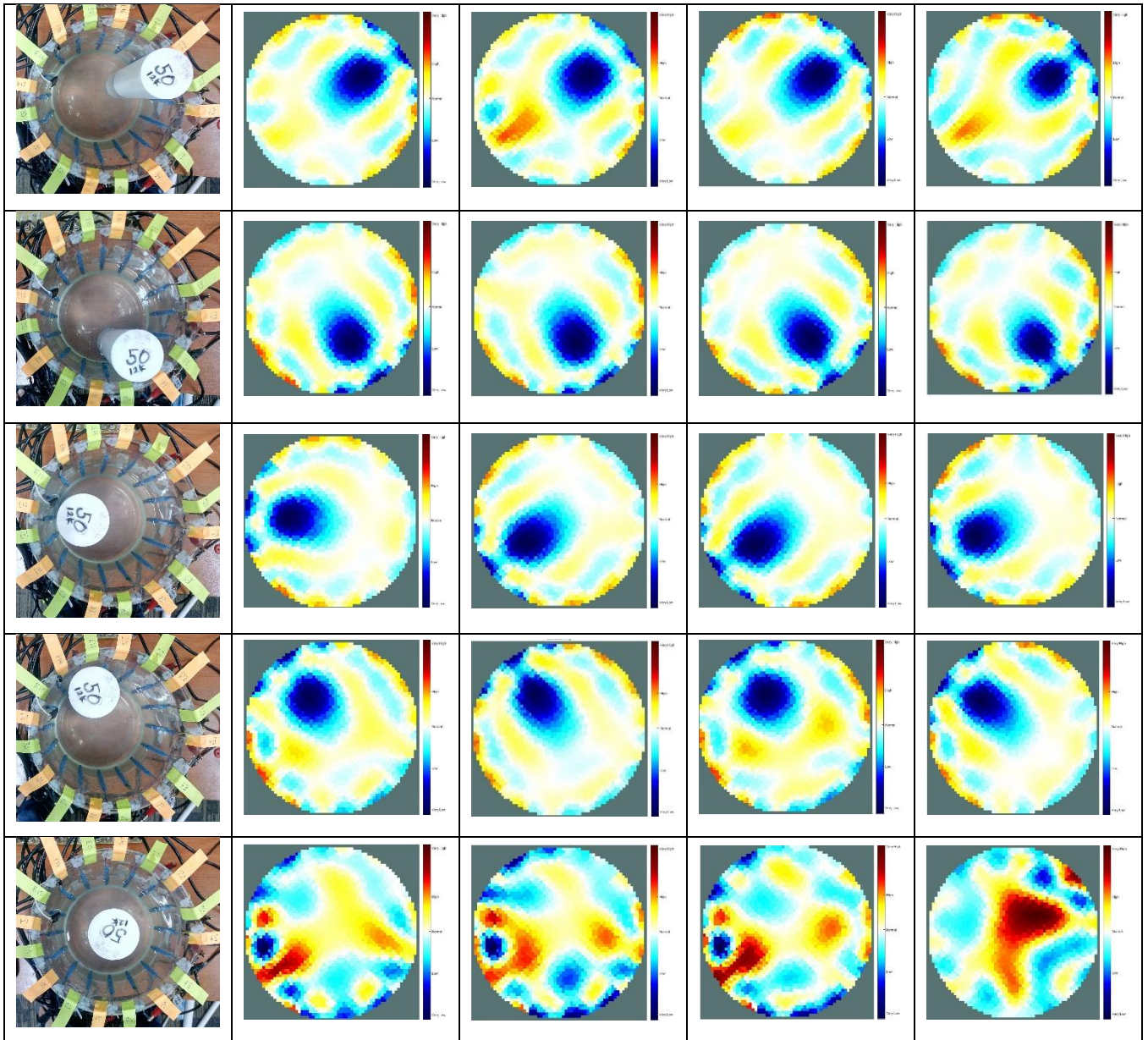


Table 5.7 shows the cross-sectional reconstructed images obtained with 35 kHz frequency. Using 35 kHz frequency to obtain the reconstructed image produces results similar to those found for 12.5 kHz. Similarly, for the 12.5 kHz reconstructed image using non-conductive rod, the object is undetectable when placed in the center of the beaker. Table 5.8 shows that the tracking and detection behavior is similar for 12.5 and 35 kHz except that the system can locate the plastic rod with diameters of 50 and 40 mm when the rod placed in the center of the beaker.

Table 5.7: Non-conductive objects at different positions; images for four different rod sizes using 35 kHz for injection frequency.

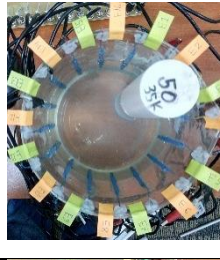
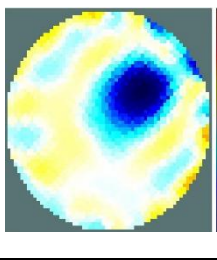
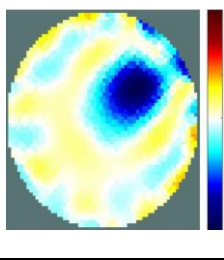
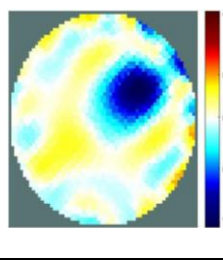
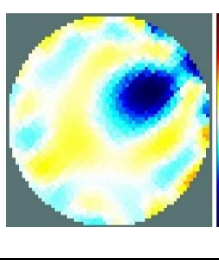
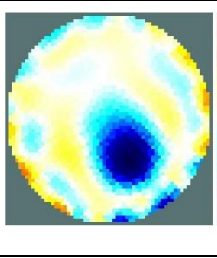
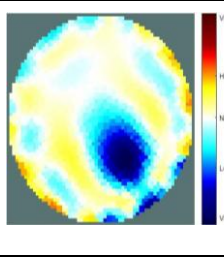
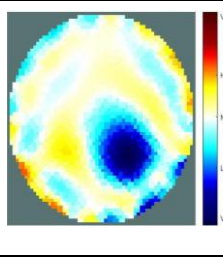
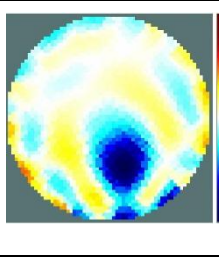
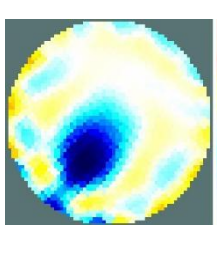
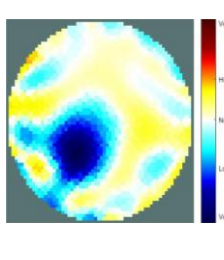
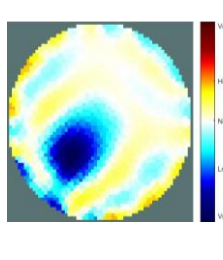
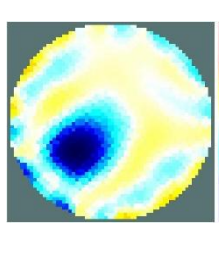
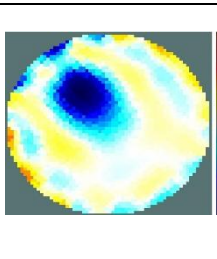
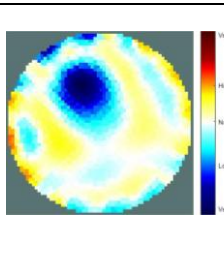
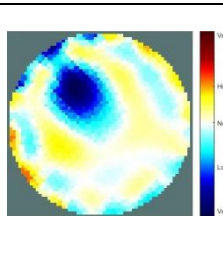
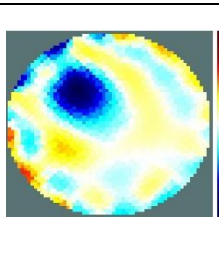
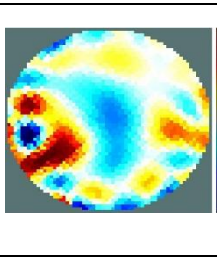
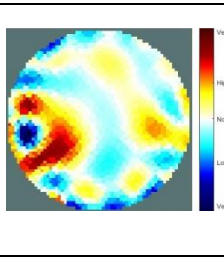
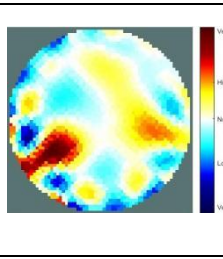
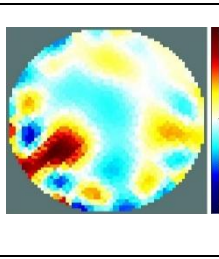
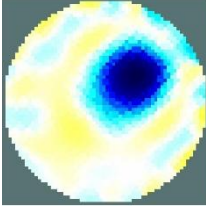
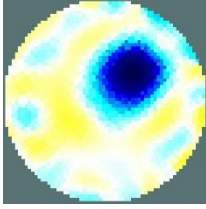
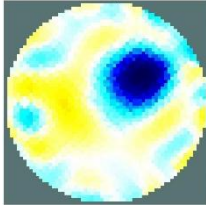
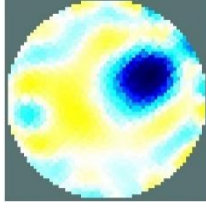
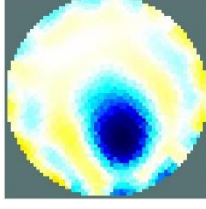
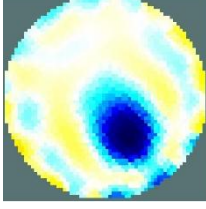
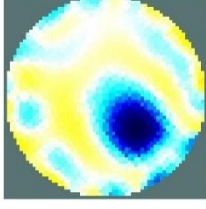
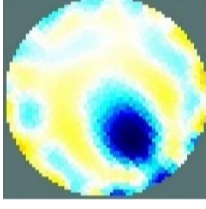
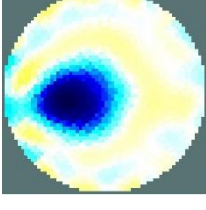
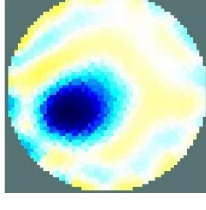
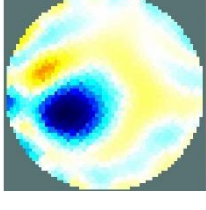
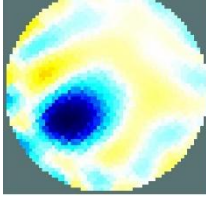
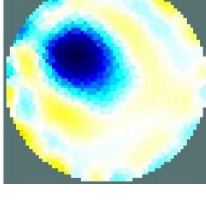
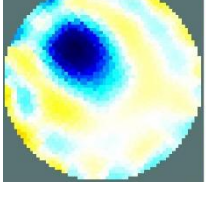
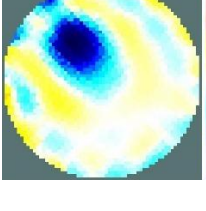
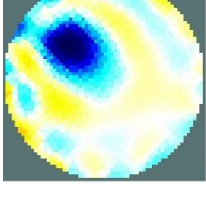
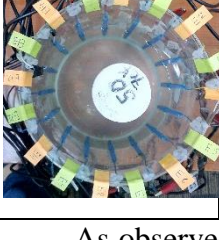
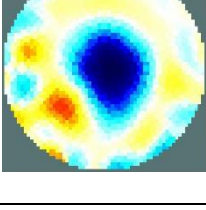
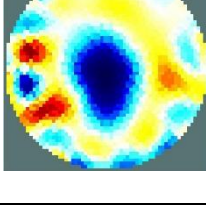
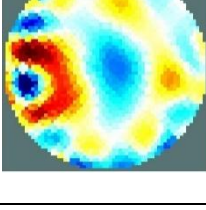
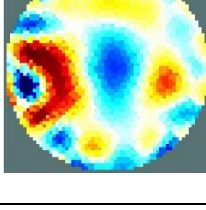
Injection frequency 35 kHz	Reconstructed images of non-conductive objects			
Real location	Teflon rod (50 mm diameter)	Teflon rod (40 mm diameter)	Teflon rod (25 mm diameter)	Teflon rod (14 mm diameter)
				
				
				
				
				

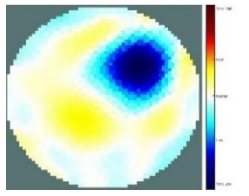
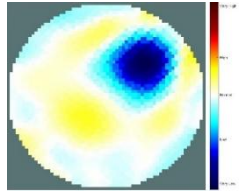
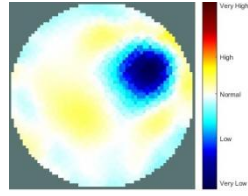
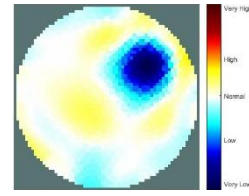
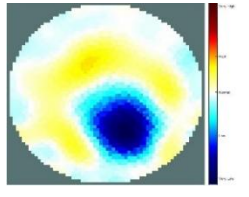
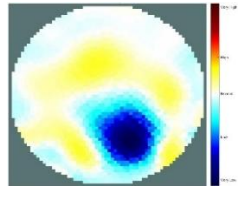
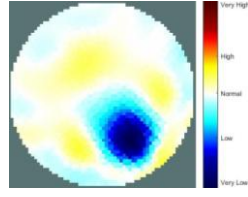
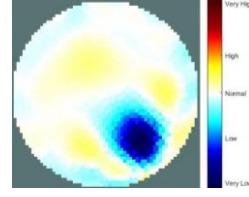
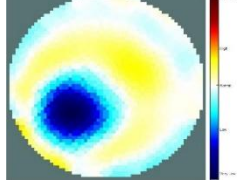
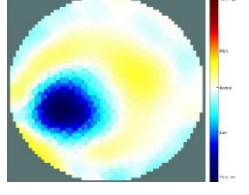
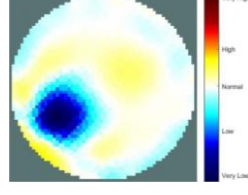
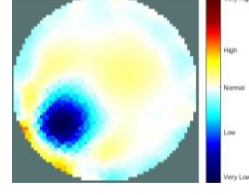
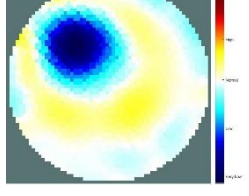
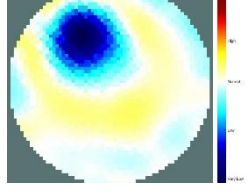
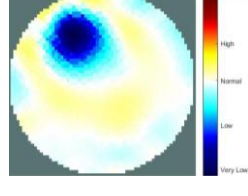
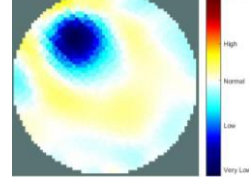
Table 5.8: Non-conductive objects at different positions; images for four different rod sizes using 70 kHz for injection frequency.

Injection frequency 70 kHz	Reconstructed images of non-conductive objects			
Real location	Teflon rod (50 mm diameter)	Teflon rod (40 mm diameter)	Teflon rod (25 mm diameter)	Teflon rod (14 mm diameter)
				
				
				
				
				

As observed from the results, using 350 kHz for the excitation frequency to detect and track the Teflon rod is much more accurate than using 12.5, 35, and 70 kHz. Moreover, as can be seen from the images, the rods of all diameters at different positions can be detected, even when the object is placed in the centre of the testing

beaker. However, identification of the rod diameter based on the reconstructed image is still imprecise, but the diameter can be estimated. Also of note, the background noise of the cross-sectional images as observed in Table 5.9 is reduced for the injection frequency of 350 kHz.

Table 5.9: Non-conductive objects at different positions; images for four different rod sizes using 350 kHz for injection frequency.

Injection frequency 350 kHz	Reconstructed images of non-conductive objects			
Real location	Teflon rod (50 mm diameter)	Teflon rod (40 mm diameter)	Teflon rod (25 mm diameter)	Teflon rod (14 mm diameter)
				
				
				
				

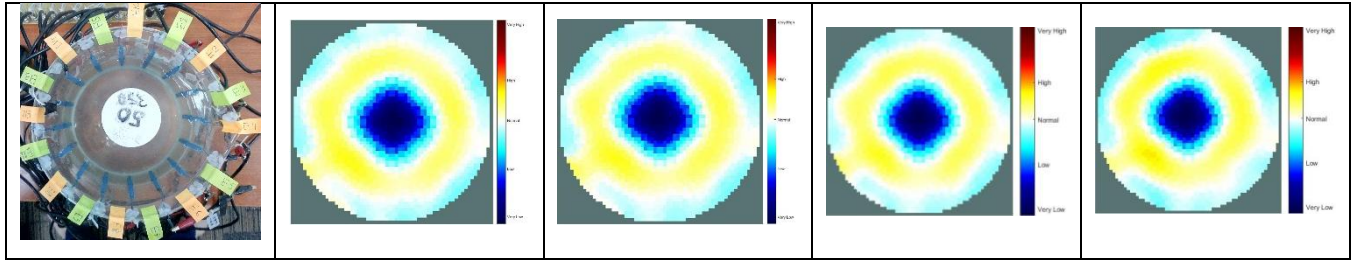
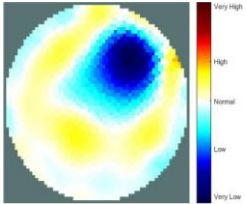
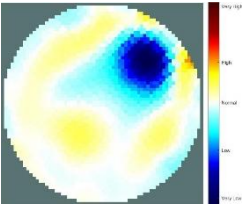
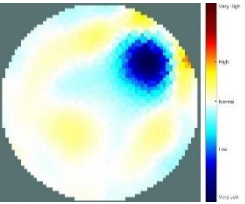
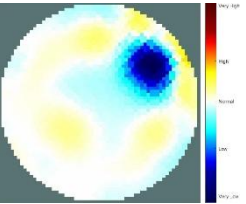
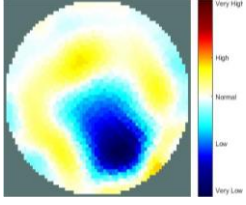
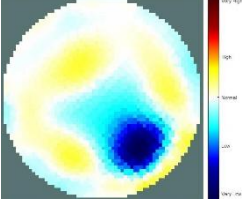
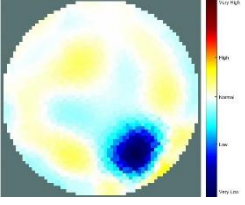
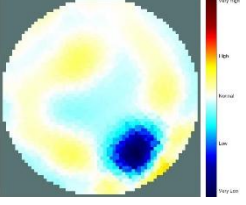
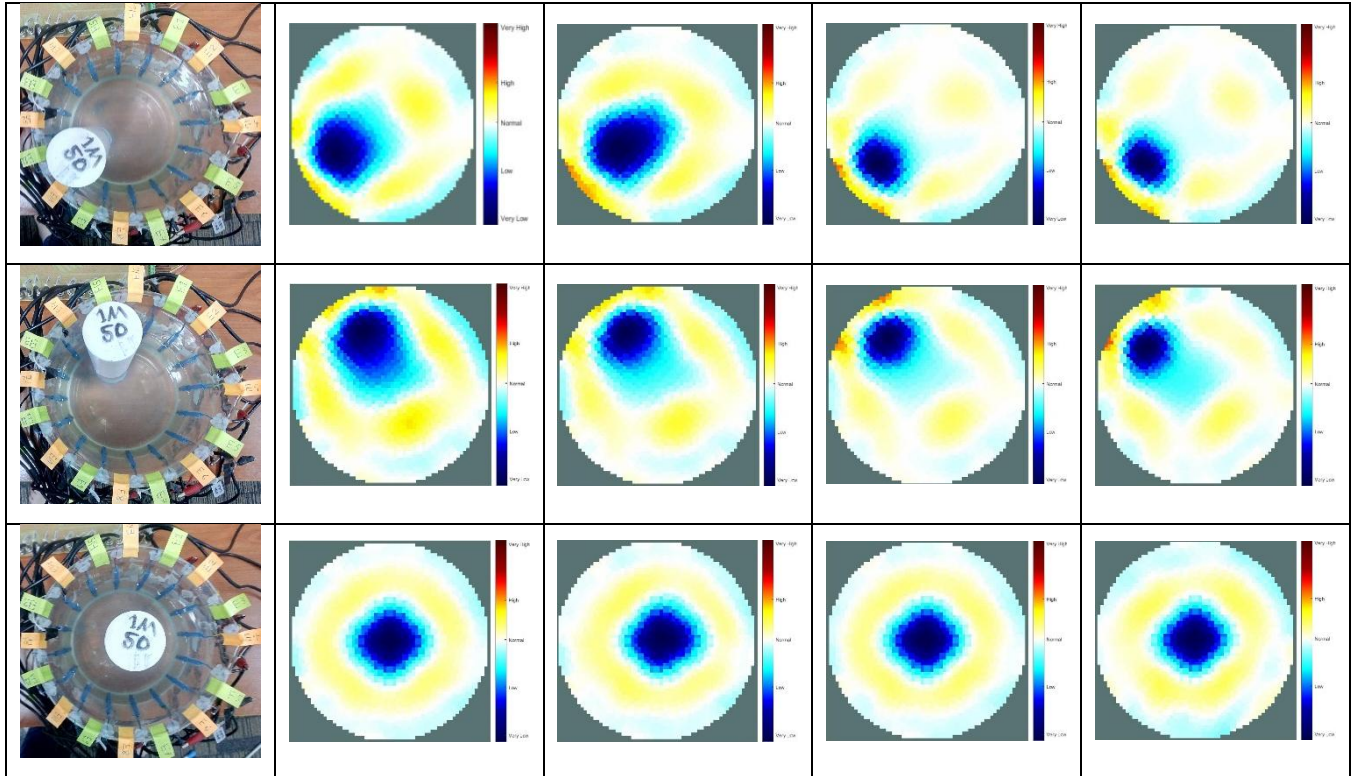


Table 5.10 shows that all the Teflon rods with different diameters can be located and traced by employing 1 MHz as the excitation frequency. Furthermore, the 1 MHz image results are as accurate as the 350 kHz reconstructed images. Additionally, the amount of image background noise using 350 and 1000 kHz is less than that of the reconstructed images using 12.5, 35, and 70 kHz as excitation frequencies. The most reliable excitation frequencies to detect and track non-conductive objects with minimum image background noise for the four different rod diameters is found to be 350 and 1000 kHz.

Table 5.10: Non-conductive objects at different positions; images for four different rod sizes using 1 MHz for injection frequency.

Injection frequency 1 MHz	Reconstructed images of non-conductive objects			
Real location	Teflon rod (50 mm diameter)	Teflon rod (40 mm diameter)	Teflon rod (25 mm diameter)	Teflon rod (14 mm diameter)
				
				



The experimental results from Table 5.1 to Table 5.10 show that the SEEIT system can detect and track hidden conductive and non-conductive objects inside a beaker (cylindrical shape) filled with tap water using 16 electrodes. Clearly, as observed, the most stable excitation frequency to detect and track conductive and non-conductive objects with different diameters is 350 kHz. All of the reconstructed images using the SEEIT system suffer from image background noise, even though the noise lessened some when a high frequency was used for injection. The reconstructed 2D image quality of the non-conductive object was significantly more accurate than the reconstructed 2D image quality of the conductive object. Based on several studies in EIT system shows that increasing the signals frequency injection will improve reconstructed image quality significantly this postulation of electrical current discharge.

Chapter 6 A novel measurement technique using single-ended signalling for electrical impedance tomography (SEEIT)

This chapter presents the design of a novel single-ended electrical impedance tomography (SEEIT) measurement method, which shows that it reduces the SEEIT system complexity significantly since it uses only one electrode to measurement (Receiver). By measuring the voltage signal Root Mean Square (RMS) of one stationary electrode (unlike the other measurement methods, which require using more than one electrode). Resistor network circuit tests were recorded to provide information on the capability of this technique to detect and track the resistance changes. Moreover, the measurement technique was tested in a real measurement environment, i.e., a beaker filled up with tap water, to confirm that the current SEEIT measurement technique can be used for SEEIT system real testing. Programmable algorithms were developed using LabVIEW to process and control the injected and the measured signals. This measurement strategy approach has the potential of increasing the accuracy and reducing the data error and the cost of the EIT system. A regular SEEIT system needs a large number of measurements to reconstruct a cross-sectional image. Thus, more recorded data has a higher chance of introducing data error and requiring a longer time to process the raw data. A standard SEEIT system consists of 16 channels requiring approximately 208 voltage measurements (Pikkemaat et al., 2012). The proposed method, on the other hand, requires only 15 voltage measurements, which means less data points to be processed per image. The main benefits of the proposed SEEIT system technique are less hardware required to implement (using one ADC), less computational memory, and less data processing.

6.1 Principle of measurement

The typical block diagram of the proposed SEEIT system method is shown in Figure 6.1. In this measurement technique, the proposed system continually measures voltage signals from one channel and injects a steady voltage signal through all other channels in turn. This measurement strategy consists of a computer system, a data acquisition (DAQ) system, a switching box, and a resistor network circuit. The resistor network circuit is a collection of thirty-two 1-k Ω resistors, arranged, as shown in Figure 6.2.

These resistors are used to provide convenient stable test loads for the SEEIT system and provide a lumped approximation to a conductive body (Griffiths, 1988). The I/O switching box, controlled by 16 digital channels, was pre-programmed using commercially software (LabVIEW) to monitor the excitation signals for all channels simultaneously while measuring the voltage signal of one individual channel.

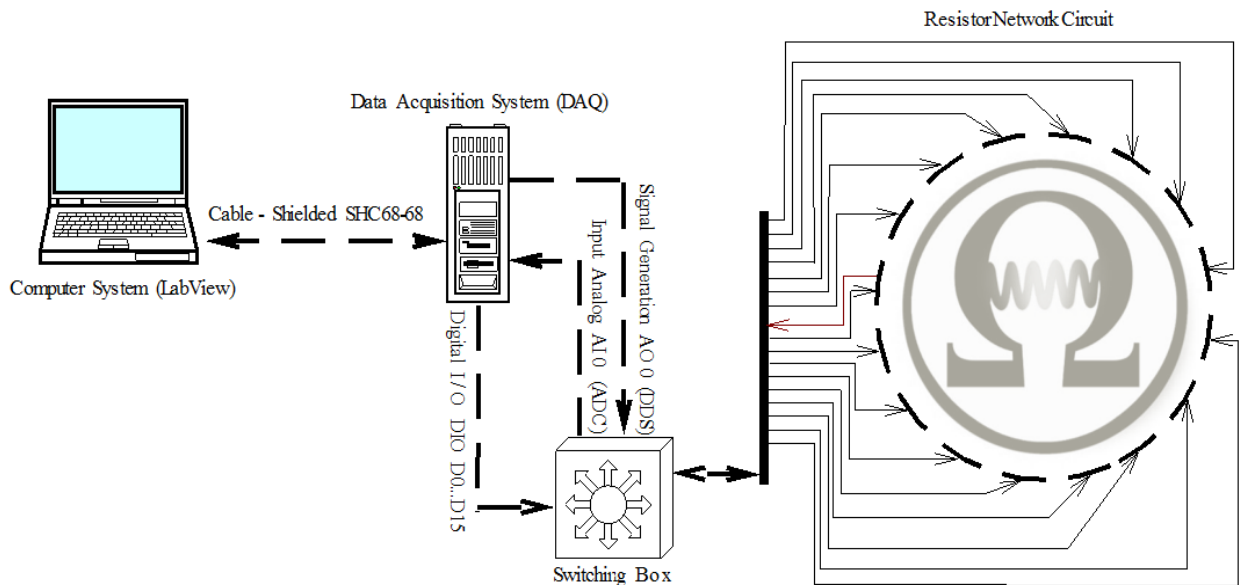


Figure 6.1: Simplified block diagram of the proposed electrical impedance measurement system.

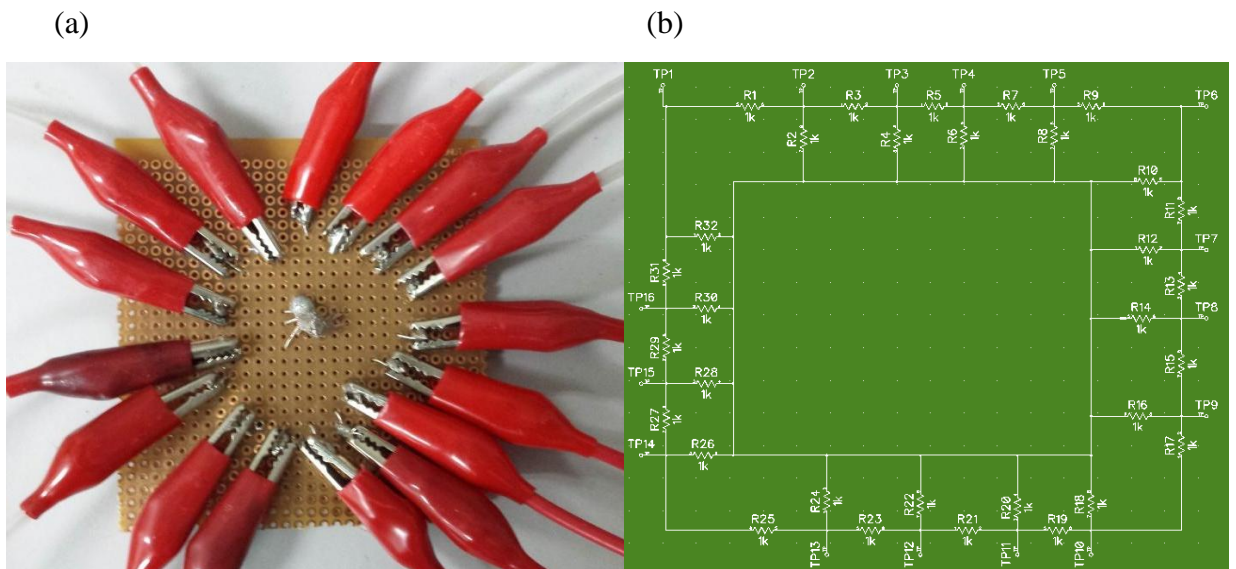


Figure 6.2: (a) Photograph of real resistor network circuit with 16 channels; (b) basic scheme of the resistor network circuit with 16 channels.

6.2 Data collection

In reference to Figure 6.3 (b), which shows the resistor network, voltage signals are injected in Channel 1 (TP1), then the voltage signal measurement is taken at the same time from Channel 1. The injection or excitation of Channel 1 is ON until the voltage signal measurements are achieved. Next, the signal injection is shifted to the neighbouring channel (TP2), and then voltage signal measurements are obtained from Channel 1. This procedure is repeated for each channel in turn. Note that the voltage measurement is taken only from Channel 1. The number of independent measurement $M = N-1$, where N is the total number of channels (in this case, 16); thus, there are 15 independent measurements in this case. This method requires a minimum amount of hardware to implement since it uses only one ADC channel. Furthermore, it is faster with regard to computational memory and image reconstruction. To gain more insight into the current SEIT measurement technique, Figure 3 (a) demonstrates the stages of the process in a flowchart. The delay time is controllable, and the speed is based on the host PC's performance. The switching box's fastest switching speed is 3-millisecond. Figure 6.3 (b), shows all the different steps of this measurement technique to clarify the procedure. AI0 is the measuring channel, and AO0 is the voltage signals injection channel.

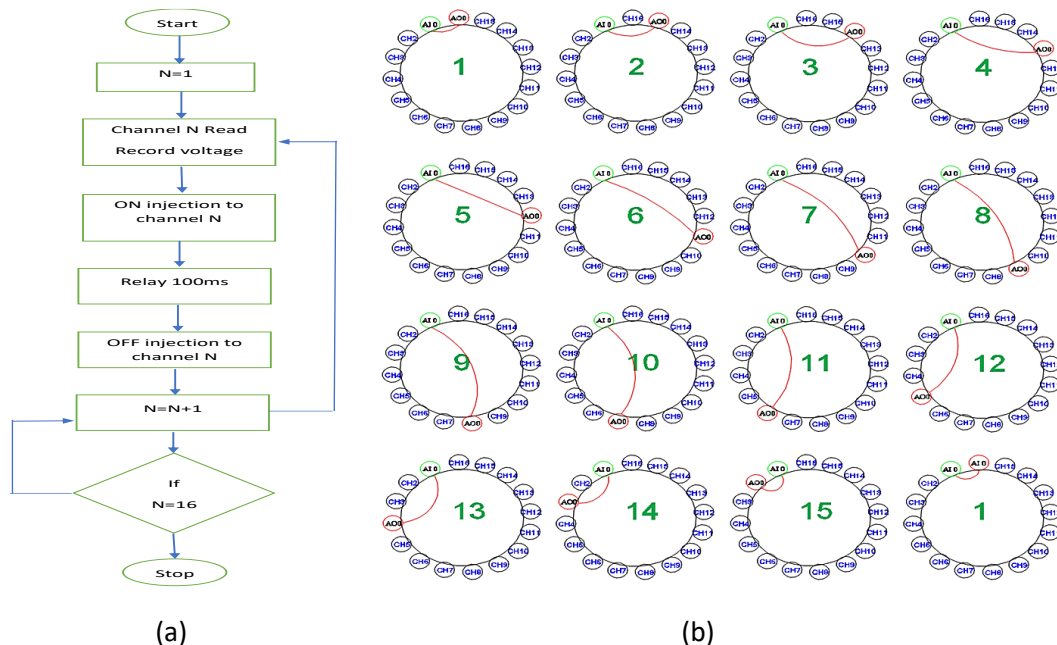


Figure 6.3 (a) The proposed measurement strategy flowchart and (b) Impedance data collection for complete steps of procedure is clarified.

6.3 Results and discussion

In order to prove that the proposed technique (measurement strategy) is able to detect and track the conductivity change, several experiments have been done and some of measurement results are presented. The results of all the experiments (conducted in 4 tests) were obtained using the same single-ended voltage signal injection system. Standard electrical impedance systems need RMS measurements to reconstruct the image. For the first three tests of the experiment, the same resistor network circuit and LabVIEW programme were used to obtain RMS results. Moreover, 1-k Ω , 2-k Ω and 3-k Ω resistors were used to create an imbalance in the resistor network circuit in order to observe the change in resistance. These resistors were used to simulate the change in conductivity by adding them near the targeted channel. On the other hand, real measurement results were obtained in Test 4 using a vessel filled up with water and attached to electrodes.

Test 1: In the first test of the experiment, a resistance circuit network was used. The injection signal configuration and the resistor value were used to achieve the imbalance are; Frequency: 30 kHz, Sampling Rate: 3,000,000, Amplitude: 2 volts, and Resistor: 1 k Ω . Figures 6.4 represents the homogenous RMS measurement result and the change in the RMS measurement results when resistors are added to any of the resistor circuit network channels. As displayed, the most significant change was observed in three different channels Channel 2, Channel 7, and Channel 12. The change occurred because the resistivity change occurred around these channels due to the resistance imbalance in the resistor circuit network caused by the 1-k Ω resistor. Based on the highest RMS measurement change, the 1-k Ω resistor can be located and tracked in the resistor circuit network.

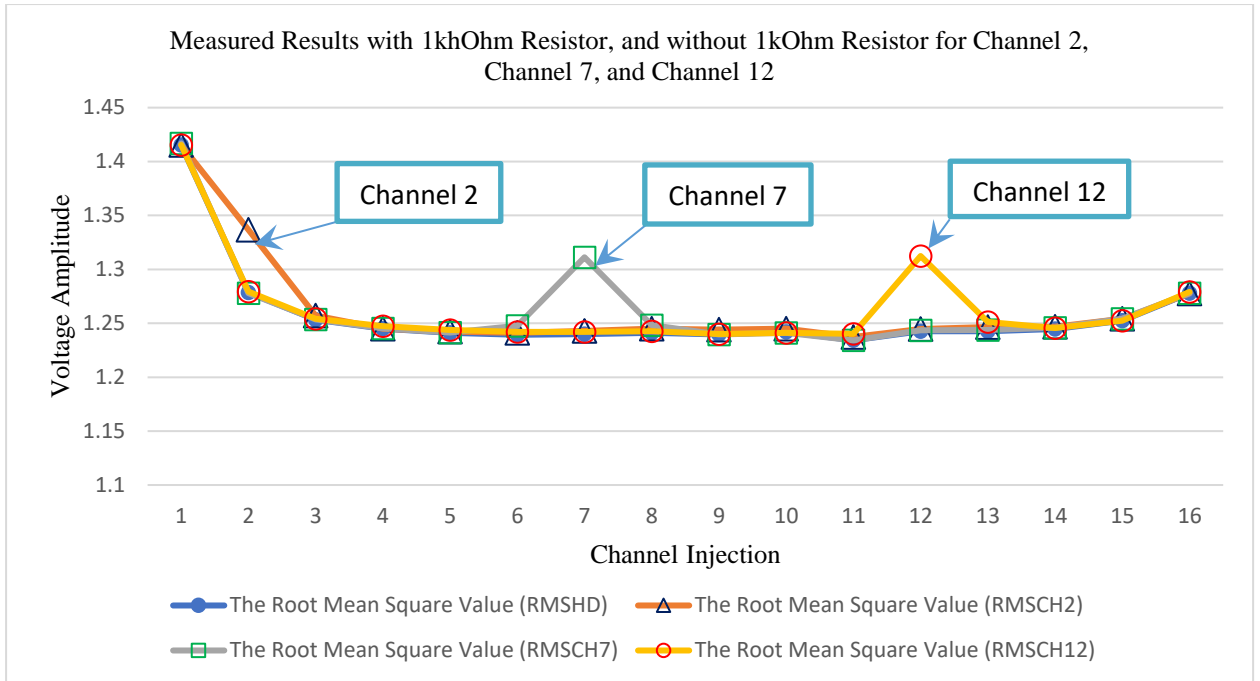


Figure 6.4: Homogeneous Root Mean Square data (RMSHD) and the data when a 1-k Ω resistor is added to Channel 2, Channel 7, and Channel 12.

Test 2: In the 2nd test of the experiment, a resistance circuit network was used. The injection signal configuration and the resistor value used to achieve the imbalance are; Frequency: 60 kHz, Sampling Rate: 3,000,000, Amplitude: 2 volts, Resistor: 1-k Ω . The only difference between Test 1 and Test 2 of the experiment is the use of different injection signal frequencies. However, Figures 6.5 illustrate the plotting of the RMS voltage when there is no resistor added and when there is a 1-k Ω resistor attached to the resistor network circuit. Furthermore, they show that the highest RMS voltage changes were observed on Channels 2, 7, and 12, due to the effect of connecting the 1-k Ω resistor to the resistor circuit network to simulate the change in resistance in the circuit.

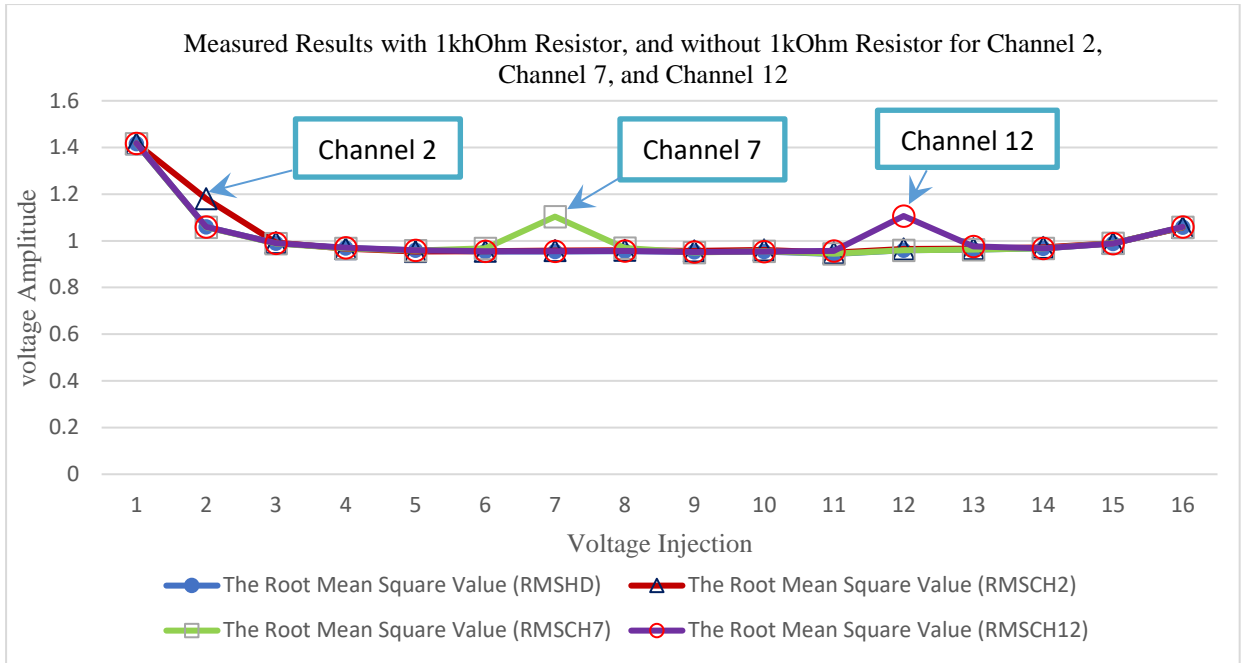


Figure 6.5: RMSHD and the data when a 1-k Ω resistor is added to Channel 2, Channel 7, and Channel 12.

Test 3: In the 3rd test of the experiment, a resistance circuit network was used. The injection signal configuration and the resistor value used to achieve the imbalance are; Frequency: 30 kHz, Sampling Rate: 3,000,000, Amplitude: 2 volts, Resistor: 1 k Ω , 2 k Ω , 3 k Ω . Test 3 examines the measurement strategy capability to detect and track multiple types of resistance. Figures 6.6 shows the plotting of the RMS voltage when there is no resistor added and when 1-k Ω , 2-k Ω , and 3-k Ω resistors are added to the resistor network circuit. The results show that the measurement method can sense the change in resistance.

On the other hand, Figure 6.6, Figure 6.7, and Figure 6.8 shows that this measurement method can track different types of resistances change at the same time. They show the homogenous RMS measurement results and the change in RMS measurement results when three different resistors at the same time are added to different channels in the resistor circuit network. Therefore, the measurement strategy was able to detect and track the conductivity change location for more than one resistor.

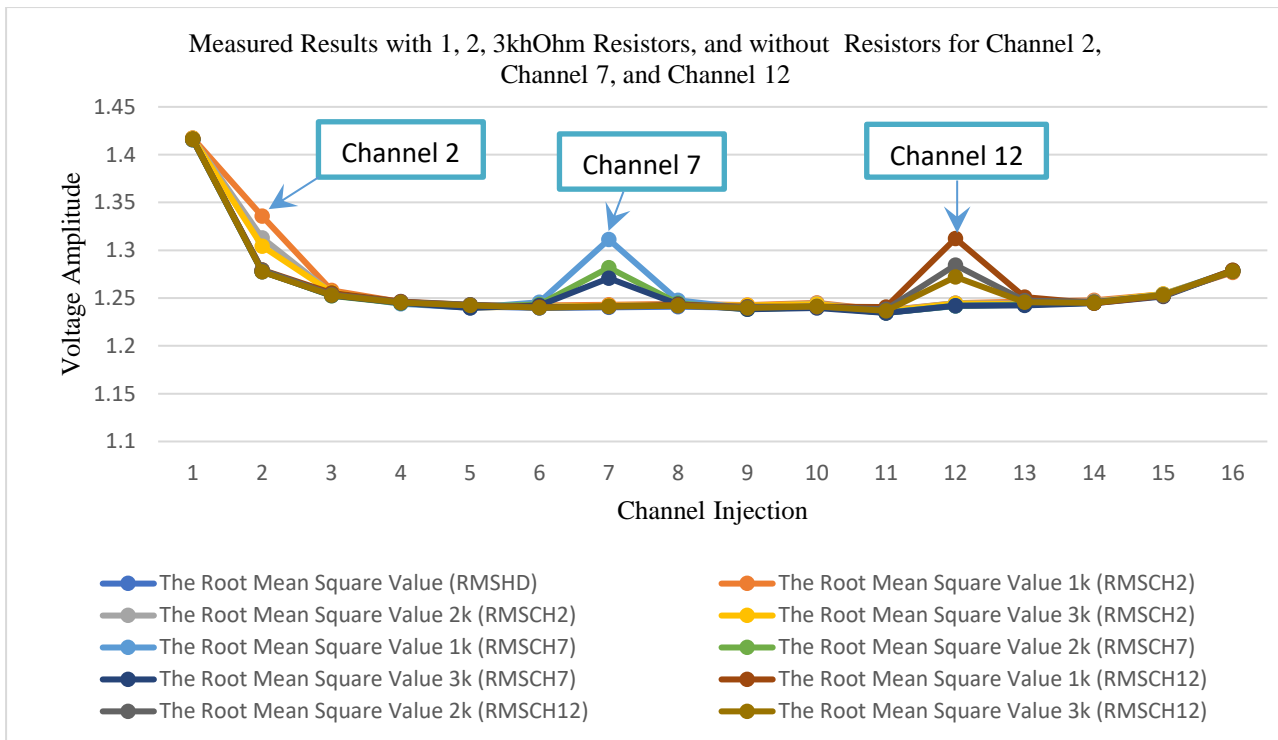


Figure 6.6: RMSHD and data when 1-kΩ, 2-kΩ, and 3-kΩ resistors are added to Channel 2, Channel 7, and Channel 12.

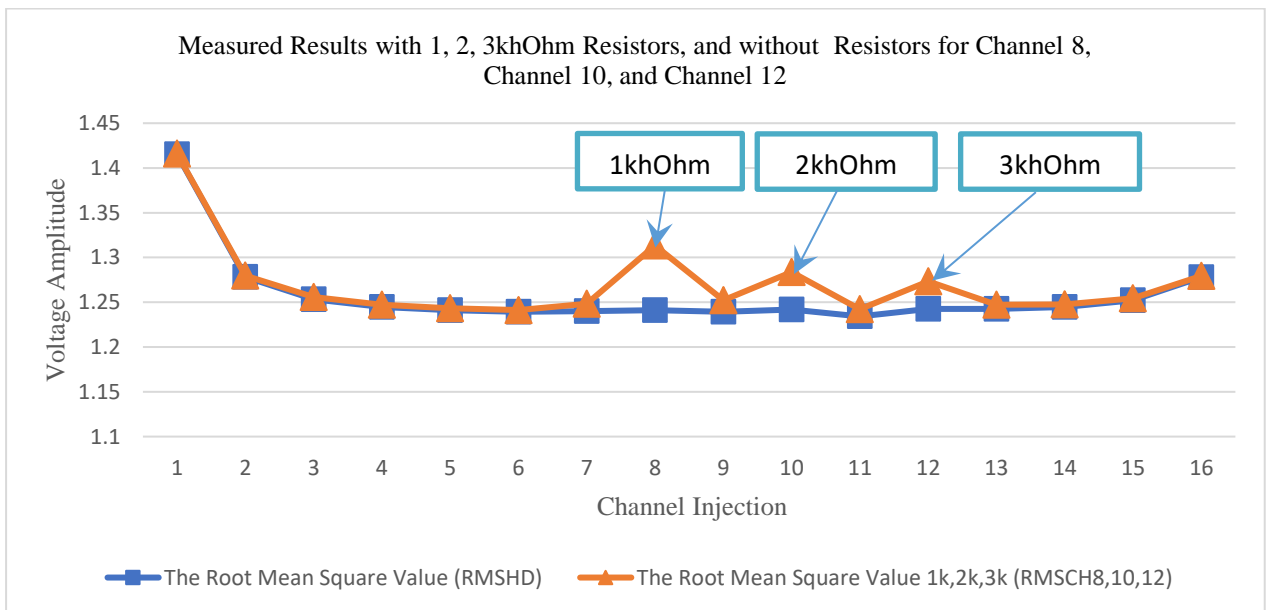


Figure 6.7: RMSHD and data when 1-kΩ, 2-kΩ, and 3-kΩ resistors are attached to Channels 8, 10, and 12 at the same time.

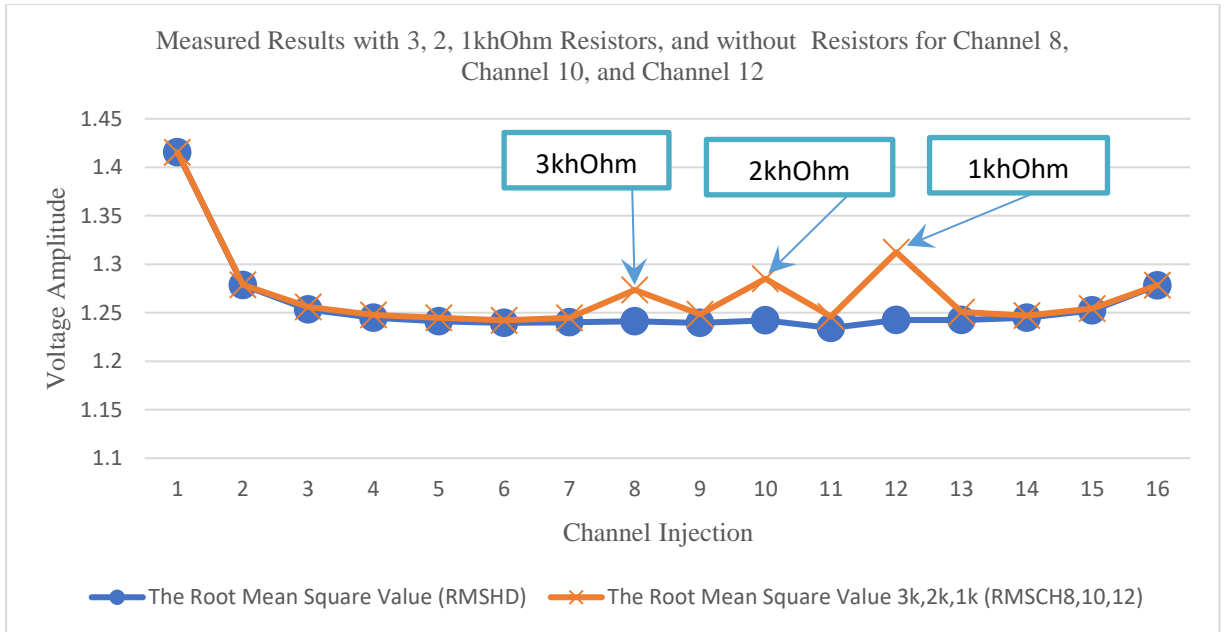


Figure 6.8. RMSHD and data when 1-kΩ, 2-kΩ, and 3-kΩ resistors are attached to Channels 8, 10, and 12 at the same time.

Test 4: In test 4 of the experiment, the measurement technique was tested using a real measurement environment, i.e., a beaker filled up with tap water. This test was done to prove that the current SEEIT measurement technique can be used for actual testing of the SEEIT system. Figure 6.9 shows the line graph of the voltage amplitude RMS for one full SEEIT measurement cycle difference when there is no object in the testing beaker and when there is an object added to the centre of the testing beaker. Moreover, the RMS voltage measurement difference results show a high impact on all channels, as observed in Figure 6.9. A significant change in the voltage amplitude for all the channels, which indicates that the object is in the centre of the beaker, matches the reallocation of the object, as shown in Figure 6.10.

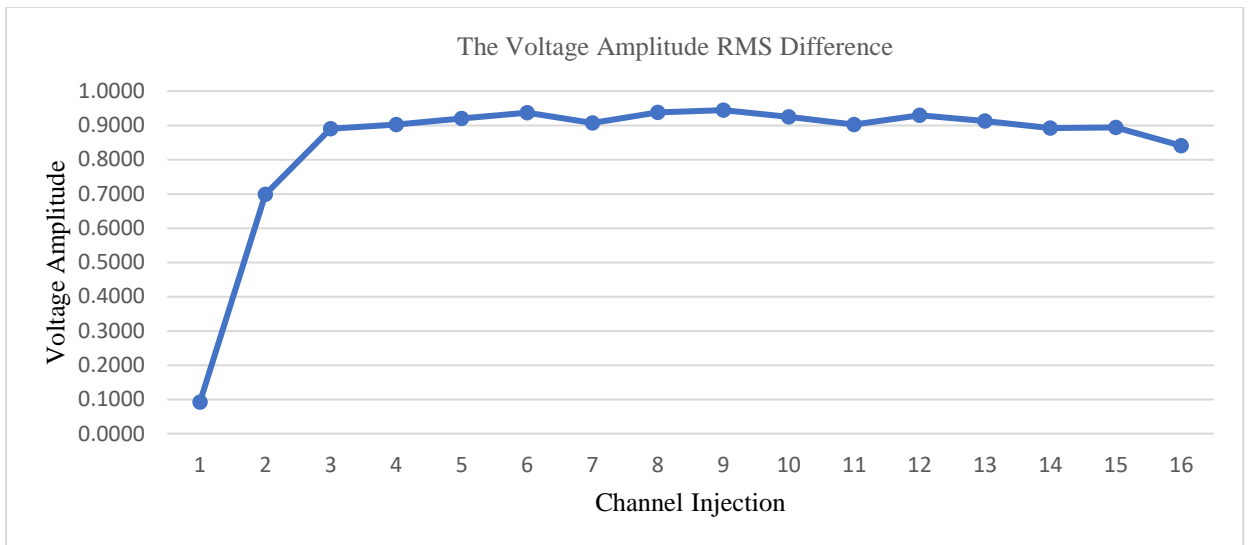


Figure 6.9: RMS voltage difference when there is no object and when there is a non-conductive object in the centre of the vessel.

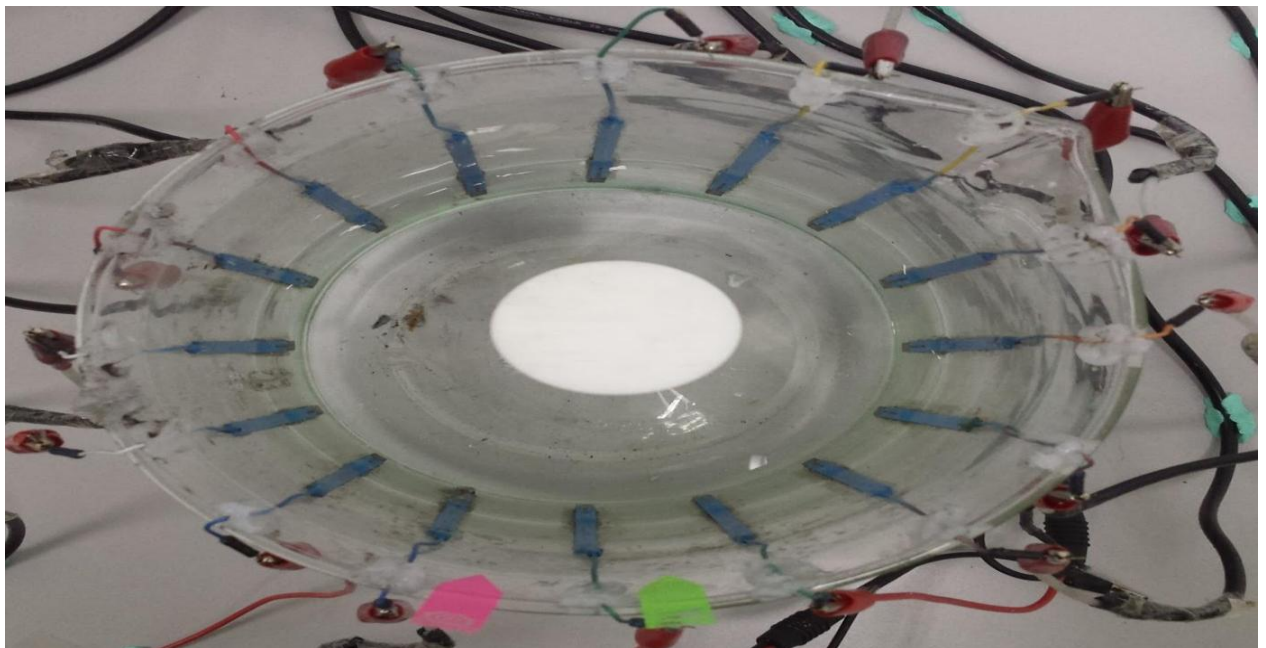


Figure 6.10: Non-conductive object in the centre of the testing beaker (top view).

Figure 6.11 illustrates the line graph of the RMS voltage difference for one full SEEIT measurement cycle dataset when there is no object added and when there is a non-conductive object near Channels 3, 4, and 5. The highest change occurred on injection Channel 6, and it flowed by Channels 3 and 5. These readings were caused by the high change in impedance detected around Channels 3, 4, and 5. Moreover, these changes match the real object location in the testing beaker as shown in Figure 6.12.

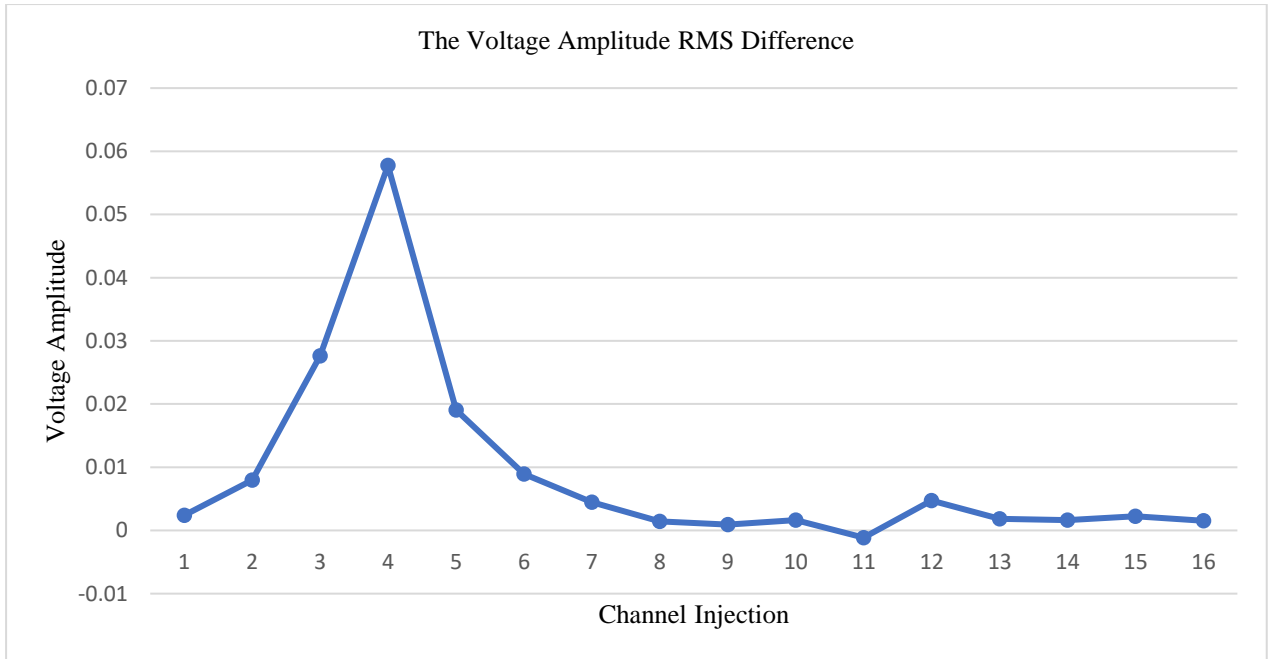


Figure 6.11: RMS voltage difference when there is no object and when there is a non-conductive object near Channels 3, 4, and 5 of the testing beaker.

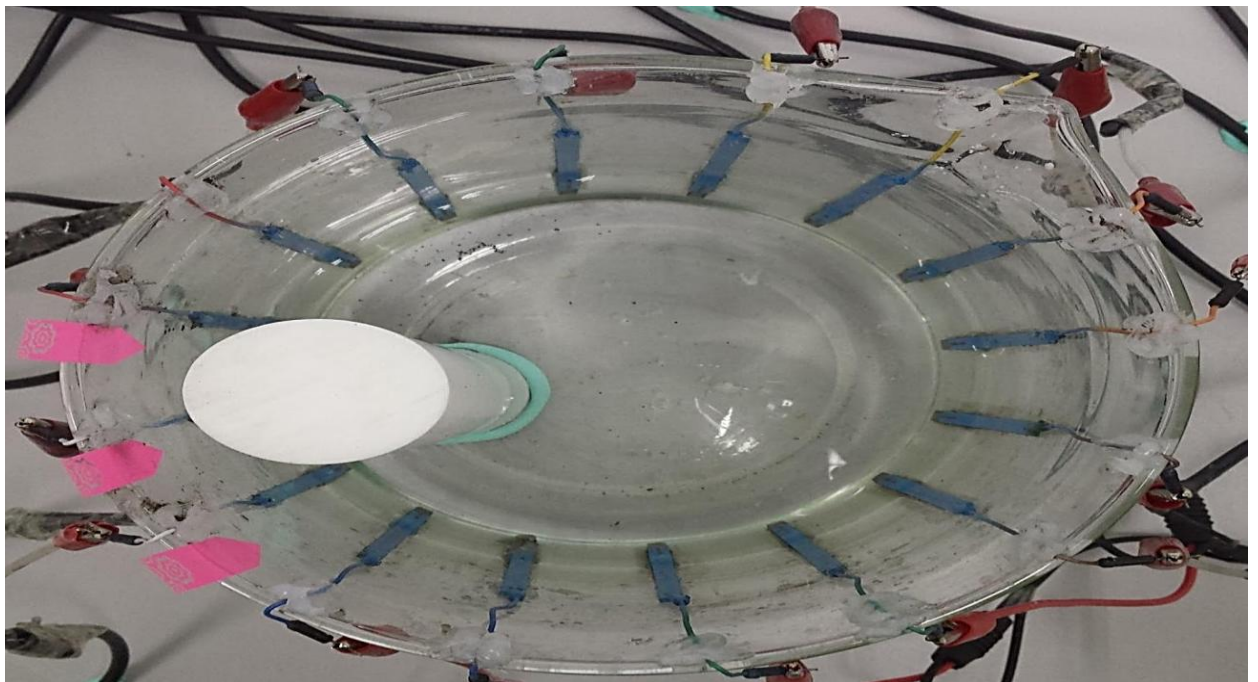


Figure 6.12: Non-conductive object near Channels 3, 4, and 5 in the testing beaker (real location).

Figure 6.13 shows the line graph of the RMS voltage difference for one full SEEIT measurement cycle dataset when there is no object added and when there is a non-conductive object near Channels 8, 9, and 10. The highest change was observed on injection Channel 9, and it flowed by Channels 8 and 10. These readings were caused by the high change in impedance identified around Channels 8, 9, and 10. Furthermore,

these changes match the real object position in the testing beaker, as shown in Figure 6.14.

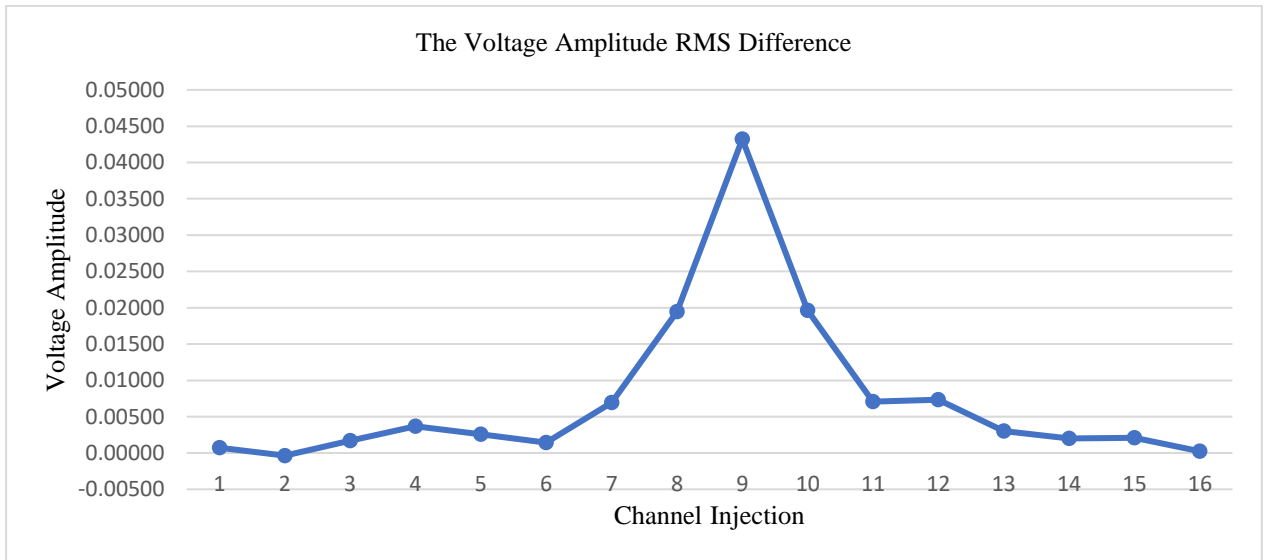


Figure 6.13: RMS voltage difference when there is no object and when there is a non-conductive object near Channels 8, 9, and 10.

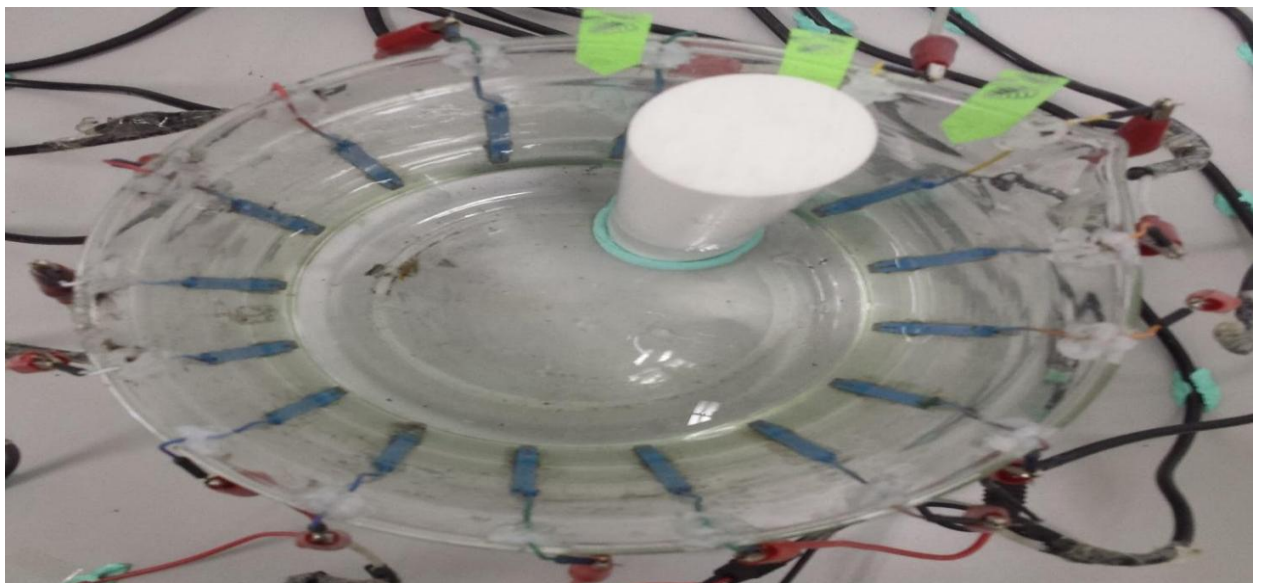


Figure 6.14: Non-conductive object near Channels 8, 9, and 10 in the testing beaker (top view).

Figure 6.15 shows a line graph of the RMS voltage difference for one full SEIT measurement cycle dataset when there is no object added and when there is a non-conductive object near injection Channels 11, 12, and 13. The highest change observed was on the injection Channel 12, and it flowed by Channels 13 and 11. These readings were caused by the high change in impedance recognised around Channels 11, 12, and

13. Moreover, these changes match the real object location in the testing beaker, as shown in Figure 6.16.

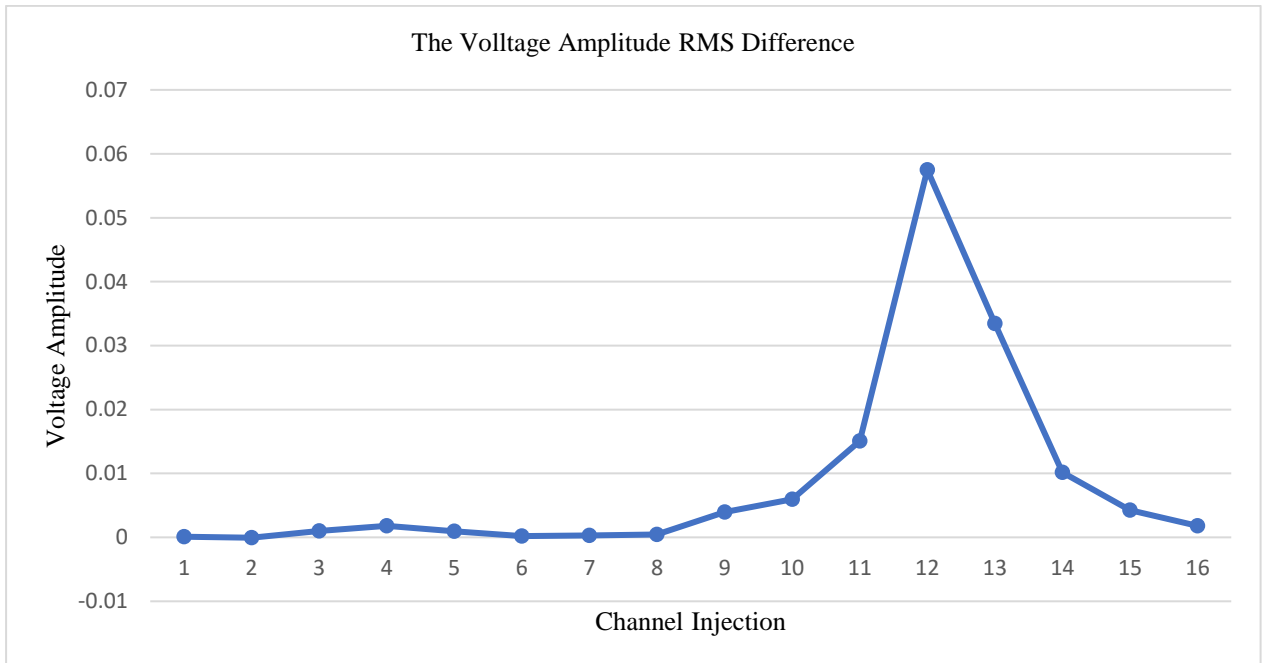


Figure 6.15: RMS voltage difference when there is no object and when there is a non-conductive object near Channels 11, 12, and 13.

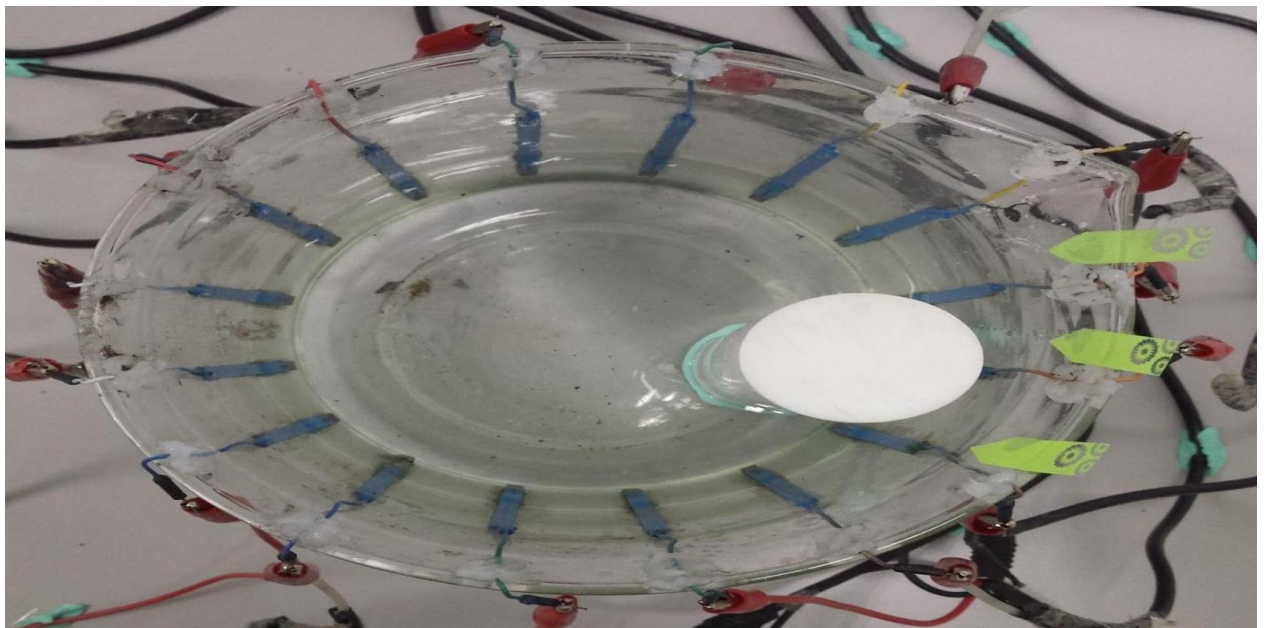


Figure 6.16: Non-conductive object near Channels 11, 12, and 13 in the testing beaker (top view).

Figure 6.17 illustrates I/O measurements channels location and connectivity change estimations point coordination based on the obtained measurement results.

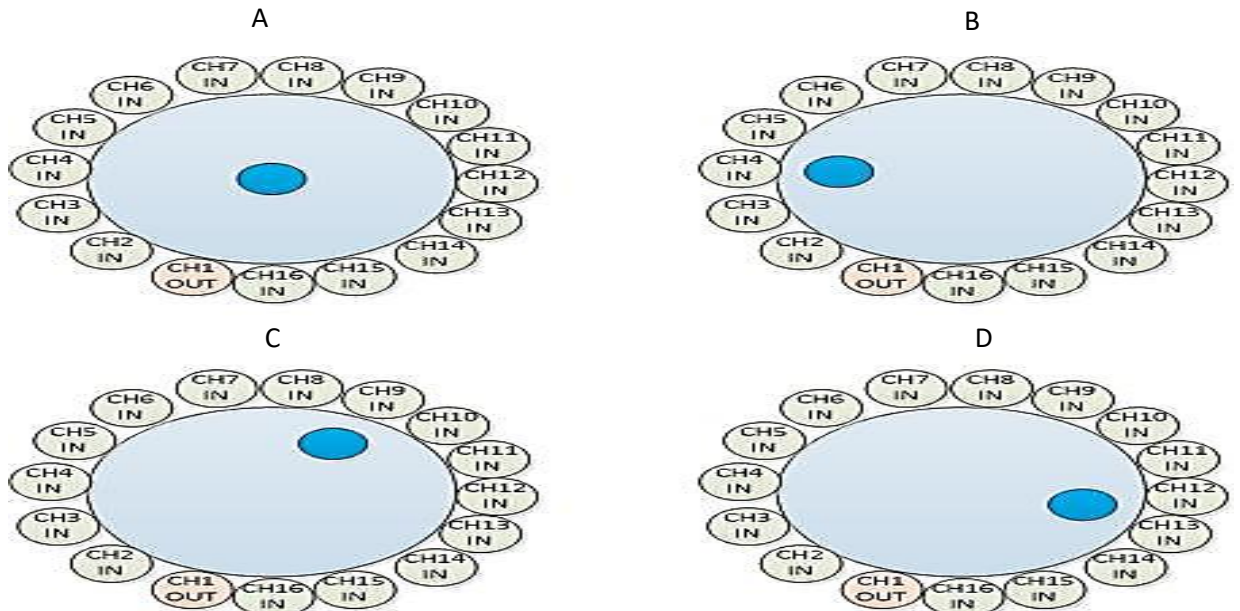


Figure 6.17. Connectivity measurements different estimation object coordination based on the obtained measurements results. (a) The object in the centre. (b) The object near channels 3, 4, and 5. (c) The object near channels 8, 9, and 10. (d) Object near channels 11, 12, and 13.

6.4 Conclusion

A novel measurement method for SEIT system that requires less hardware to implement, less computational memory, and less processed data. Furthermore, the proposed technique needs only one electrode to measure voltage signals and 15 measurements to reconstruct an image. This measurement technique was investigated by running several tests using a computer system, a data acquisition system, a switching box, and a resistor network circuit. On the other hand, numerous tests have been performed with different frequency injection using real measurement results obtained from a testing beaker filled up with tap water and attached to electrodes. The results show that the system was able to detect and track an object (conductivity change) within the testing beaker by using only 15-measurements dataset.

Chapter 7 Application of SEEIT

Electrical impedance tomography (EIT) is an inexpensive, non-invasive electrical tomography technique. It offers an excellent opportunity for different challenging problems for medical and industrial applications (Zhou, Harrach and Seo, 2018; Wei and Soleimani, 2013). There are many existing applications for EIT imaging technique, such as brick wall imaging, imaging leaks from buried pipes, lung imaging, breast imaging, brain imaging, soil water infiltration, monitoring of multicomponent flows in pipes, pneumatic transport, nuclear fuel process and plant decommission (Tapp et al., 2003; Abdul Wahab et al., 2015; Gneccchi et al., 2012; Wang et al., 2007; Bickenbach et al., 2017; Bera, 2018). Although EIT has many advantages, it has problems, such as low-quality spatial resolution and a high number of the electrode's requirements. This makes it harder to utilize in some applications (Bera, 2018). The traditional EIT application required a unique system hardware and software setup, which limited its use to one application. The developed SEEIT system can be adapted to be used for different applications since it uses a unique monitoring and control setup. This setup is evaluated through several experiments without changing the hardware or software.

This chapter presents a multiple experimental testing using the developed SEEIT prototype system. This system was developed to overcome some of the drawbacks of the conventional EIT system, including flexibility and durability to monitor and image industrial processes. There are six experiments conducted to mimic several industrial process applications using the SEEIT system. All the tests showed the capability of the SEEIT system to monitor and image hidden objects, whether electrically conductive or non-conductive. The ability of the developed SEEIT system to detect, locate, and reshape objects are evaluated. The experiments are listed below:

1. Tap Water Detection Test Using SEEIT System

- **Application**

"Real-Time Industrial Water Quality Assessment Using the SEEIT System"
(Monitoring coolant or process water in manufacturing)

2. Muddy Water Detection Test Using SEEIT System

- **Application**

"Wastewater Slurry Analysis for Oil/Gas Pipelines Using the SEEIT System"
(Identifying sediment or blockages in industrial wastewater systems)

3. Gas and Tap Water Detection Test Using SEEIT System
 - **Application**
"Gas Leak Detection in Petrochemical Pipelines Using the SEEIT System"
(Monitoring for gas leaks in hazardous industrial environments)
4. Electrically Non-Conductive Object Shape Detection Test Using SEEIT System
 - **Application**
"Plastic Contaminant Detection in Food Processing Using the SEEIT System"
(Identifying foreign plastic objects in food production lines)
5. Chicken Tissue Chunks Detection Test Using SEEIT System
 - **Application**
"Tumor/Foreign Object Detection in Soft Tissue Using the SEEIT System"
(Simulating tumor localization in human tissue for diagnostics)
6. SEEIT System Stability Test
 - **Application**
"System Reliability for Continuous Critical Care Monitoring"
(Ensuring robust performance in ICU or emergency room settings)

The developed SEEIT system is flexible and can be adapted for different applications by controlling and monitoring the configuration of I/O signals. These signals include frequency, voltage amplitude, signal type, offset, sample rate, and code width. The SEEIT system's flexibility lies in its ability to dynamically adjust key parameters—frequency (e.g., 12.5 kHz for deep tissue penetration in medical diagnostics vs. 1 MHz for high-resolution industrial flaw detection), voltage amplitude (low power for patient safety vs. high sensitivity for pipeline inspections), and signal type (pulsed waves to reduce noise in factories or thermal effects in tissue)—enabling seamless adaptation to diverse applications. This reconfigurability eliminates the need for specialized hardware, allowing the same system to detect tumors in soft tissue, monitor gas leaks in petrochemical plants, or assess water quality in environmental surveys, all while optimizing performance for each unique scenario. The system shows good accuracy for locating and imaging cross-section objects with simple shapes, such as circles, squares, and triangles. However, most of the reconstructed images have background noise, although this does not affect the object detection and tracking. Moreover, the results of the stability test show that the developed SEEIT system could continuously monitor and image a hidden object for one hour successfully. The system

can potentially detect electrical conductivity changes from objects as small as 1.5 mm in a testing tank with a diameter of 134 mm. Based on the results of these experiments, the programmable EIT system can adapt the SEEIT system for a different industrial process without the need to implement any new hardware to the system, which may help to save time and costs. The setup for all the experiments consisted of a testing tank with an attached 16-electrode array. The titanium alloy electrode was used to enhance SEEIT system durability and lifespan.

7.1 Data collection

For all the experiments, the data was recorded using 16 electrodes. Three testing Bessel were needed, two of them had the same diameter approximately (14 cm) with different heights, and the third one is a testing beaker with a diameter of approximately 18 cm. The neighbouring measurement strategy was used for all the tests and integrate with the reconstruction algorithm used by EIDORS, although this system can support different measurement strategies (Schulcke et al, 2016; Adler and Lionheart, 2006). Figure 7.1 illustrates the stages of the process in a flowchart to provide insight into the current SEEIT system data collection and measurement strategy. The system setup was configured based on the applications and the electrode specification. For example, the amplitude was set based on the electrical conductivity environments and the diameter of the region. Therefore, low conductivity requires high signal injection, and high conductivity needs a low signal injection. However, the injection amplitude and frequency are limited; the amplitude range is 0.1–10 V_{pp}, and the frequency range is 1 Hz to 1 MHz. The lowest measurable measurement change, termed code width, was determined by the data acquisition (DAQ) analog-to-digital converter (ADC) resolution and the range of the input signal (maximum value/minimum value).

To begin, signals were injected into channel 1, and the signal data measurements were taken simultaneously from all 16 channels. Then, the signal injection was moved to the next channel (channel 2), and signal data measurements were recorded from all the channels. This procedure was repeated for each channel, in turn. Afterwards, the number of independent data measurements obtained for a complete data set M was $N \times N$, where N is the total number of channels. Fundamentally, a complete set of data measurements must be performed for every image slide, and the delay time can be

controlled. The delay time to be set depends on the measurement sampling rate. Therefore, a high measurement sampling rate requires a longer time to process than a lower sampling rate. In these experiments, the measured signal variance, standard deviation, and RMS could be calculated, and the data sets were uploaded to the EIDORS for further signal processing.

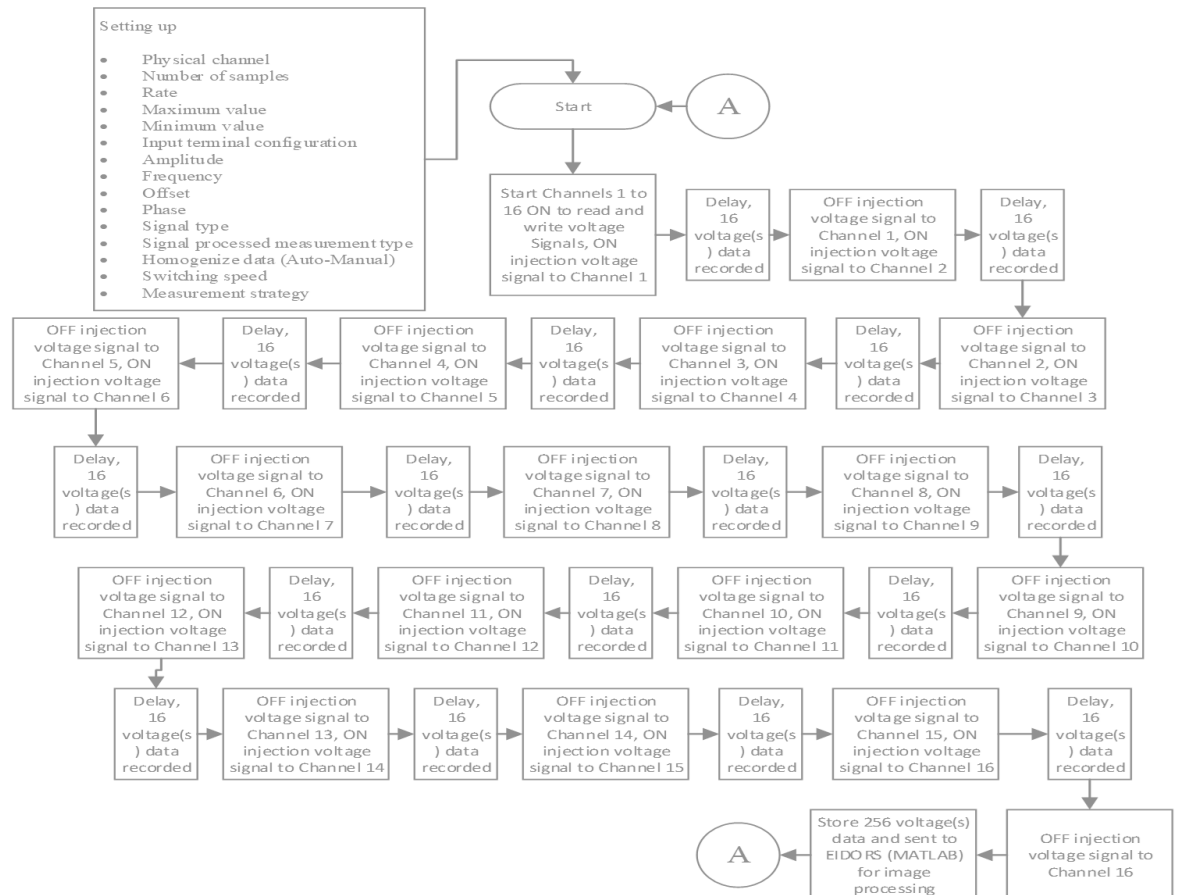


Figure 7.1: Flowchart of the stages of the process for the programmable SEEIT system.

7.2 Results and discussion

The developed SEEIT system was evaluated, including its ability to be used in different applications by tracking and detecting conductive changes of targeted objects. Therefore, several SEEIT system tests were conducted, and some of the data results are presented here. Basically, several experiments were conducted to show the ability of the SEEIT system to be adapted for numerous industrial processes. The results of all the experiments (parts) were obtained using an adjacent injection measurement protocol with an injection frequency range of 12–1000 kHz. Moreover, the signal measurements used were controlled and monitored using LabVIEW to reconstruct the cross-sectional

image. The variance data mainly used were calculated from the recorded measurement. However, the standard deviation and RMS were calculated only on the muddy water test results. For all the experiments, three electrode types with different diameters were used. The first electrode, which was made of titanium alloy grade 2 with an active contact area of $13 \times 13 \times 0.5 \text{ mm}^3$, was employed for the Tap Water Detection Test, Gas and Tap Water Test, and Electrically Non-Conductive Object Shapes Detection Test. In addition, the second electrode, which was also made of titanium alloy with an active area of $14 \times 14 \times 0.5 \text{ mm}^3$, was used for the Chicken Tissue Chunks Detection Test. The last electrode, which was made of copper with dimensions of $20 \times 5 \text{ mm}^2$, was used for both the Muddy Water Detection Test and Stability Test. All the tests were conducted using three testing tanks (cylindrical shape). Figure 7.2 shows a typical analog I/O signal configuration setup window. The settings were modified based on the test's requirements.

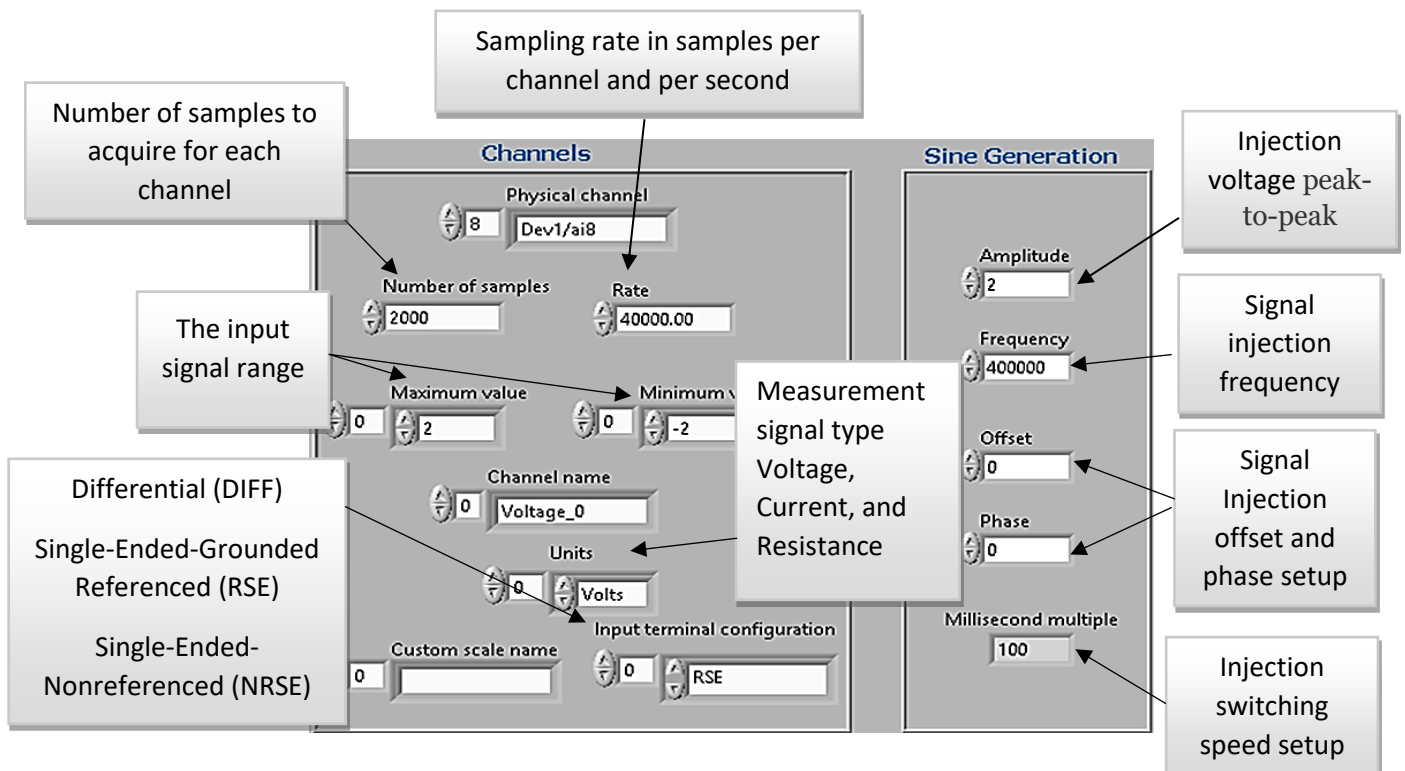


Figure 7.2: Channel configuration and signal generator configuration controls.

7.2.1 Tap water detection test using the SEEIT system

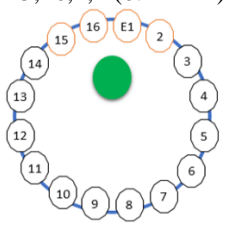
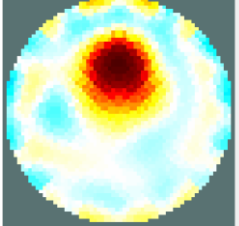
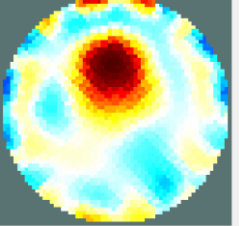
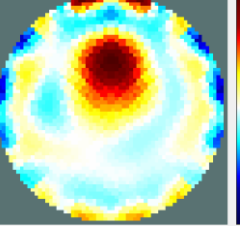
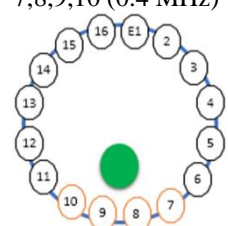
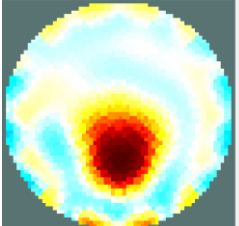
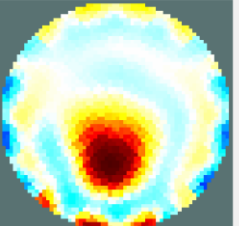
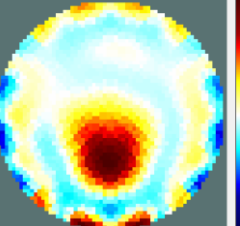
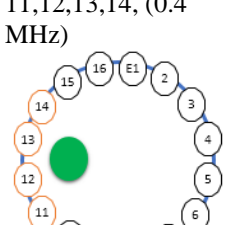
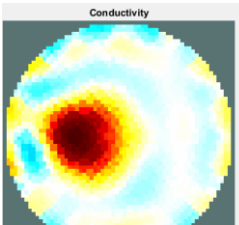
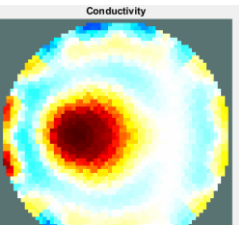
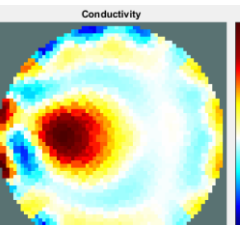
The Tap Water detection test was conducted to observe and test the capability of the system to detect and track electrically conductive and electrically non-conductive materials with different diameters. However, this part of the experiment showed the ability of the system to detect and track electrically conductive and non-conductive objects of different diameters when they were placed in a range of positions in the testing vessel filled with 3200 ml of tap water, one after another. The conductivity of the tap water, which was measured using an electrical conductivity meter, was approximately 97 $\mu\text{S}/\text{cm}$ at 27°C. For this series of tests, the first measurements were obtained when only tap water was in the tank. For the second measurements, the electrically conductive and non-conductive objects were placed in different locations inside the testing vessels. Then, the two measurements were compared and processed and saved using LabVIEW. Later, they were streamed to MATLAB (EIDORS) for further processing and image reconstruction. The conductive objects were a stainless-steel rod and steel wire rope with diameters of 26, 12, 4, 3, 2, and 1.5 mm. The non-conductive objects included a plastic rod and plastic wire rope with diameters of 25, 12, 7, 4, and 2 mm. Some of the targeted objects, whether electrically conductive or non-conductive, were placed in a few different locations inside the testing vessel and exposed to various injection signal frequencies: 400, and 500 kHz. The table includes the actual object location and the reconstructed image of the object. Five primary targeted object placement locations for all the experiments are listed below:

6. Near electrodes 15, 16, 1, 2
7. Near electrodes 3, 4, 5, 6
8. Near electrodes 6, 7, 8, 9
9. Near electrode 11, 12, 13, 14
10. In the centre

Table 7.1 shows the 2-D reconstruction images of three electrically conductive objects with three diameters placed in several locations using titanium alloy grade 2. The input signal range was max 3 – min –3, and the injected frequency, as shown in this table, was 400 kHz and 500 kHz. The colour scale illustrates the states of the electrical conductivity changes. The red colour means that the electrical conductivity is high in that area, and the blue colour signifies that the electrical conductivity in that

area decreased. As observed, the steel rod diameter of 26 mm was placed in the four stated locations and was tracked and imaged. Similarly, the electrically conductive object with a diameter of 12 mm was placed in the locations shown and was tracked and imaged. Some background noise was present in the reconstruction image, but at an inconsistent level. This noise did not overwhelm the reconstructed image, as can be seen in all the images. In contrast, the steel wire rope with a diameter of 4 mm was placed in four locations and detected and imaged. The reconstructed image when the object was located in the centre of the testing vessel had more amount of distortion, as shown in row 4 image of table 7.1. Therefore, the injected excitation frequency was increased from 400 kHz to 500 kHz, which improved the reconstruction image of the object when it was in the centre.

Table 7.1: Conductive objects at different positions; reconstructed images for three conductive object diameters (26 mm, 12 mm, 4 mm).

Targeted object, real location, and injected frequency with input signal range (max 3 – min -3)	The object is a cylindrical stainless-steel rod (26 mm diameter)	The object is a cylindrical stainless-steel rod (12 mm diameter)	The object is steel wire rope (4 mm diameter)
15,16,1,2 (0.4 MHz) 			
7,8,9,10 (0.4 MHz) 			
11,12,13,14, (0.4 MHz) 			

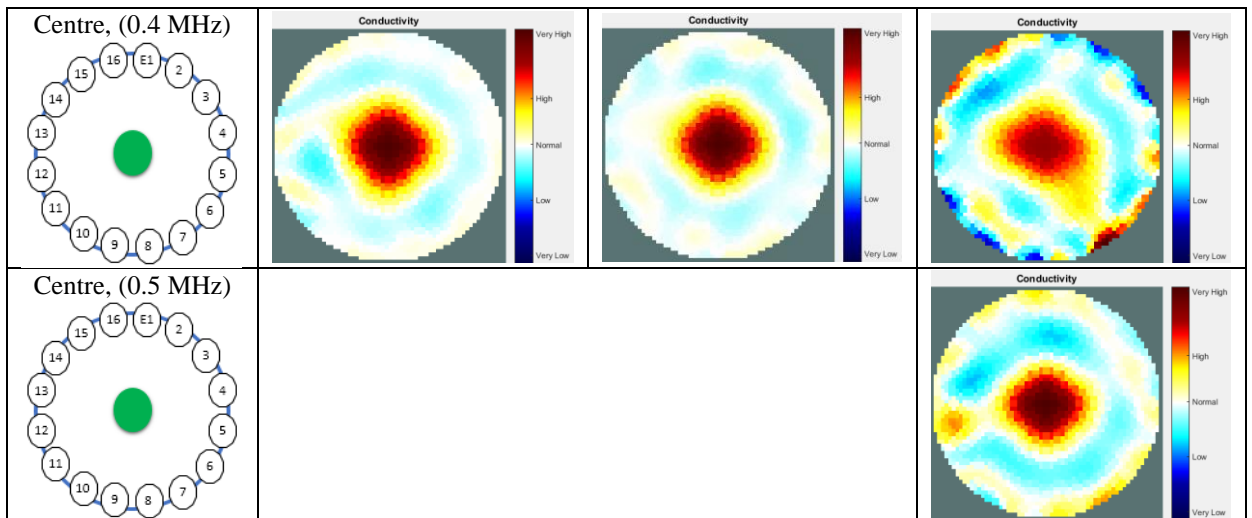


Table 7.2 shows the 2-D reconstruction images of three electrically conductive objects of three different diameters placed in several locations, but with the objects smaller in diameter than the objects in Table 7.1. As observed, the steel wire rope with a diameter of 4 mm was placed in four stated locations and tracked and imaged using 400 kHz as the excitation frequency. However, when the object was positioned in the central location, the reconstructed image of the object ‘shifted’. This ‘object-shifting’ problem was solved by increasing the injected excitation frequency from 400 kHz to 500 kHz. The reconstructed images are displayed in the table. The steel wire rope with a diameter of 3 mm that was placed in the four stated locations, was tracked and imaged using 500 kHz as the excitation frequency. Additionally, when the 2-D reconstructed image object was placed in the centre, a large distortion occurred, even when using 500 kHz for the injection excitation frequency. However, the image distortion was eradicated by decreasing the input signal range from max 3 – min –3 to max 1 – min – 1, which increased the measurement sensitivity of the signal. The last column of the table shows the results of the smallest electrically conductive object in this study, with a diameter of 1.5 mm. As shown, the current SEEIT system can image and track the object, even though background noise is present inconsistently. However, it does not affect the detection of the aimed object, as shown in table 7.2.

Table 7.2: Conductive objects at different positions; reconstructed images for three different conductive object diameters (3 mm, 2 mm, 1.5 mm).

Targeted object real location	The object is steel wire rope (3 mm diameter)	The object is steel wire rope (2 mm diameter)	The object is steel wire rope (1.5 mm diameter)
	0.4 MHz (max 3 – min – 3) 	0.5 MHz (max 3 – min – 3) 	0.5 MHz (max 1 – min – 1)
	0.4 MHz (max 3 – min – 3) 	0.5 MHz (max 3 – min – 3) 	0.5 MHz (max 1 – min – 1)
	0.4 MHz (max 3 – min – 3) 	0.5 MHz (max 3 – min – 3) 	0.5 MHz (max 1 – min – 1)
	0.4 MHz (max 3 – min – 3) 	0.5 MHz (max 3 – min – 3) 	0.5 MHz centre (max 1 – min – 1)
	0.5 MHz centre (max 3 – min – 3) 	0.5 MHz centre (max 1 – min – 1) 	

Table 7.3 shows the 2-D reconstruction images of three electrically non-conductive objects with three diameters placed in several locations. Plastic rods with diameters of

25 mm, 14 mm, and 7 mm were placed in four locations and tracked and imaged using 0.4 MHz as the stimulation frequency, with an input signal range of max 3 – min –3. Although the volume of the reconstructed image background noise is observed and not invariable, it does not affect the reconstructed image of the aimed object, as demonstrated.

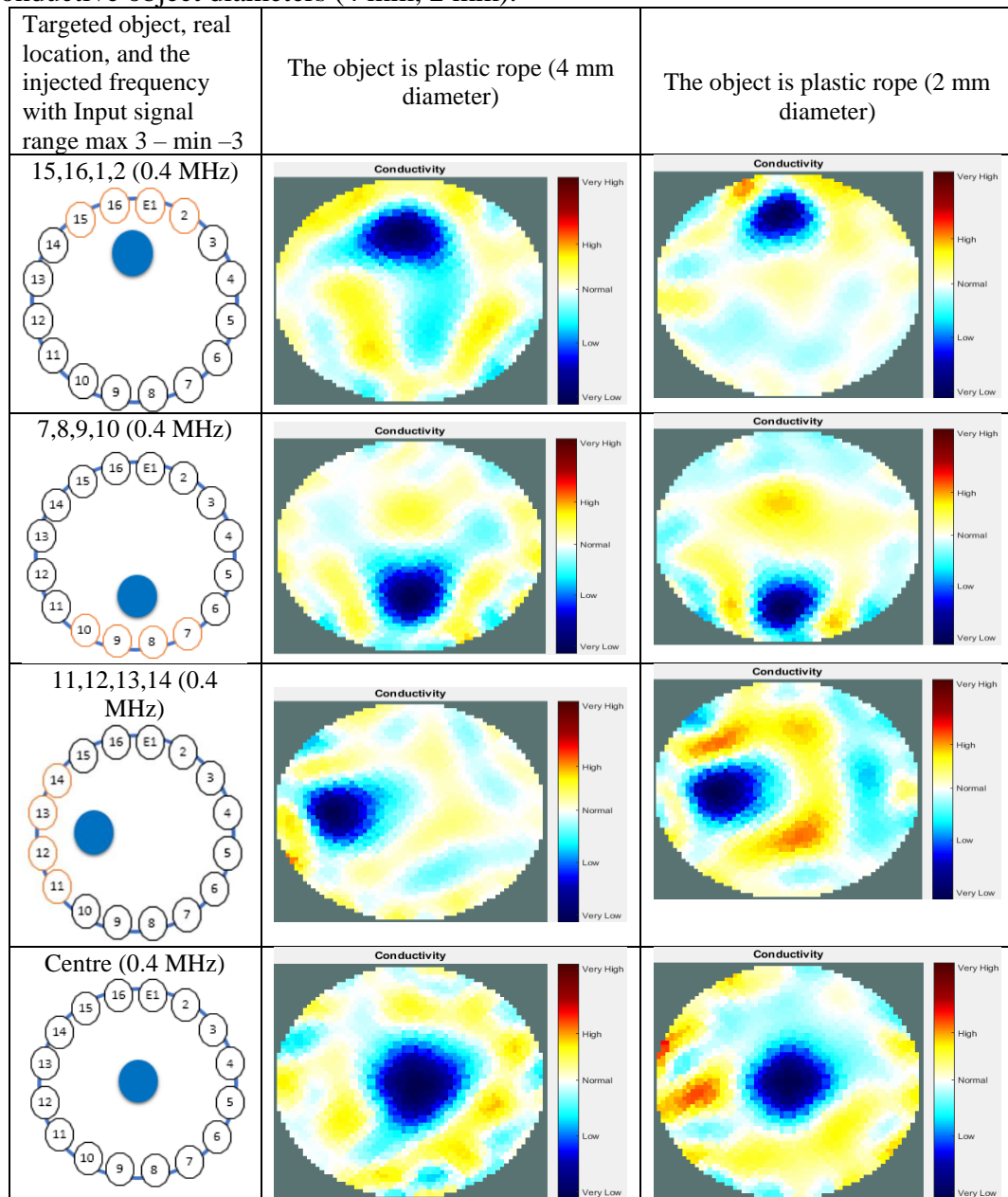
Table 7.3: Non-conductive objects at different positions; reconstructed images for three non-conductive object diameters (25 mm, 14 mm, 7 mm).

Targeted object, real location and injected frequency with input signal range max 3 – min –3	The object is a cylindrical plastic rod (25 mm diameter)	The object is a cylindrical plastic rod (14 mm diameter)	The object is a cylindrical rod (7 mm diameter)
15,16,1,2 (0.4 MHz) 			
7,8,9,10 (0.4 MHz) 			
11,12,13,14 (0.4 MHz) 			
Centre (0.4 MHz) 			

Table 7.4 displays the 2-D reconstructed images of two electrically conductive plastic ropes with two diameters placed in four regions. The plastic ropes with diameters of 4 mm and 2 mm were identified and imaged using 0.4 MHz as the

excitation frequency with a range of input signals of max 3 – min –3. The effects of the changes in object diameter on the reconstructed images were noticed to change slightly, depending on the object width. In contrast, the artefact of the reconstructed images was noticeable but did not affect the reconstructed images of the targeted objects.

Table 7.4: Non-conductive objects at different positions; images for two non-conductive object diameters (4 mm, 2 mm).



The results in Tables 7.1 to 7.4 show the capability of the SEEIT system to track and image electrically conductive and non-conductive objects with stated diameters that were placed in a testing tank filled with tap water. As seen, the electrically conductive materials require more calibration and configuration setup than the non-conductive

objects, particularly when the targeted object was smaller. It also was observed, in some cases, that the reconstructed images of the electrically conductive object were strong in most targeted object locations and became weak in the centre of the testing tank. This may be because the electrical conductivity at high frequency became low; hence, the current easily passed through the targeted object when the targeted object diameter became smaller and farther from the electrodes. However, this issue was solved in two ways. The first solution was to increase the injected excitation frequency from 0.4 MHz to 0.5 MHz. The second was to decrease the input signal range from max 3 – min –3 to max 1 – min –1 to increase the measurement signal sensitivity.

7.2.2 Muddy water detection test using SEEIT system

The capability of the SEEIT system to detect and track a hidden object in muddy water was evaluated using three frequencies as well as three single processing measurement types. For all the muddy water tests, the first measurements were obtained with the muddy water was in the testing beaker. For the second measurements, the electrically conductive and non-conductive objects were placed in different locations inside the beaker. Then, the two measurements were compared, processed and saved using LabVIEW. Afterwards, they were streamed to MATLAB (EIDORS) for further processing for image reconstruction. Furthermore, a voltage input signal range of ± 3 V was used for muddy water experiments. These results demonstrated the ability of the system to detect and track electrically conductive and non-conductive objects of different diameters when they were placed in a range of positions in the testing beaker filled with 3000 ml of tap water mixed with soil, one after another. The 16 electrodes, made of copper, which attached to the testing beaker, were approximately 500 mm from the bottom of the beaker. The electrical conductivity of the muddy water was greater than that of the regular water (tap water). This was measured using an electrical conductivity meter and was 930 microS/cm at 23.7°C, which indicates a high conductivity medium. Only three types of data were calculated from the recorded measurement signals of muddy water test. These signals were the variance, standard, and RMS. The electrically conductive objects were stainless-steel rods with diameters of 12, 26, and 50 mm. The electrically non-conductive objects were plastic rods with diameters of 14, 25, and 50 mm. The targeted objects, whether conductive or non-conductive, were placed in four locations inside the testing beaker and exposed to

various injection signal frequencies: 12.5, 300, and 1000 kHz. All the results of the muddy water experiment were obtained using an adjacent injection measurement strategy. Tables 7.5 to 7.22 portrays the actual object locations and the 2D images of the object. The four targeted object placement locations for all the muddy water experiments are Near electrodes 7, 8, 9, 10, Near electrodes 11, 12, 13, 14, Near electrodes 15, 16, 1, 2, and at the centre of the beaker.

7.2.2.1 RMS

The results in this section were obtained using root mean square data for image reconstruction. Table 7.5 shows the 2-D reconstruction images of three electrically non-conductive objects of three diameters placed in four locations using 12.5 kHz for the injection signals. The plastic rod, with a diameter of 50 mm was placed in the four stated locations was tracked and imaged. As noticed, the first three locations of the object (50 mm plastic rod) were imaged but with an artefact (background noise). However, when the object was positioned in the central location, the reconstructed image of the object disappeared or went undetected. This was due to the use of low frequency. The problem of object detection, when it is in the central position, can be minimized significantly by increasing injection frequency and decreasing the input signal range, which increases the measurement sensitivity. In addition, the plastic rod with a diameter of 25 mm, which also was placed in the four stated locations, was tracked and imaged using 12.5 kHz as the injection frequency. The SEEIT system was able to detect and track the 25 mm object for the first three locations, but with higher image distortion than that of the 50 mm object, as observed. In addition, when the 25 mm object was placed in the centre, the system was unable to detect or find the object. The last column of the table shows that the SEEIT system was able to detect and track the 14 mm object only near the electrode, but with greater image distortion than that of the 25 mm object, it can be observed.

Table 7.5: Non-conductive objects at different positions; images for three different non-conductive object diameters (50 mm, 25 mm, 14 mm) with injection frequency 12.5 kHz.

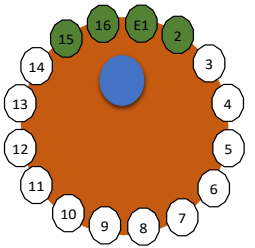
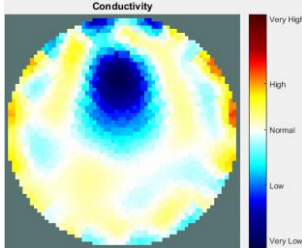
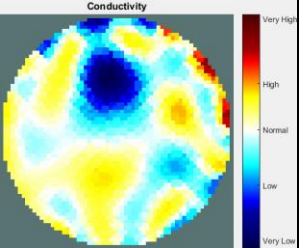
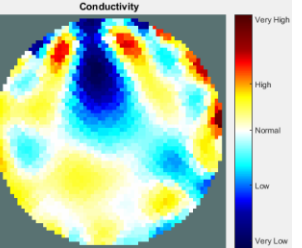
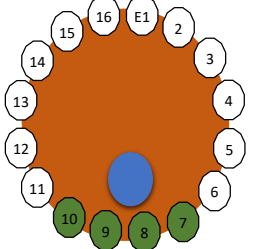
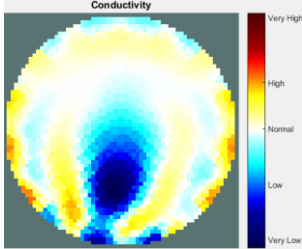
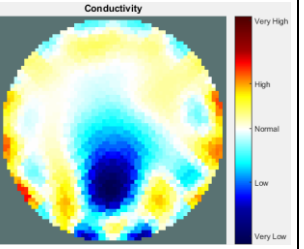
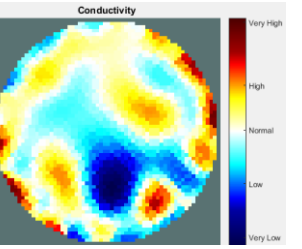
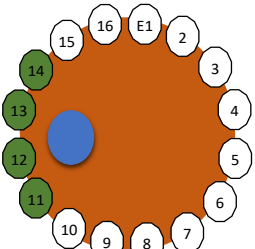
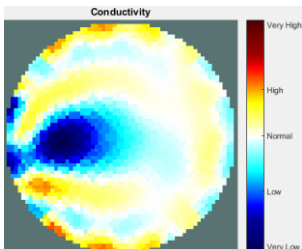
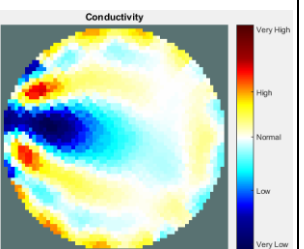
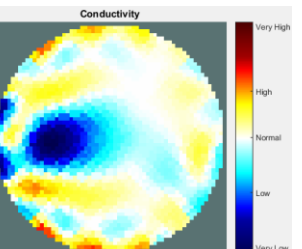
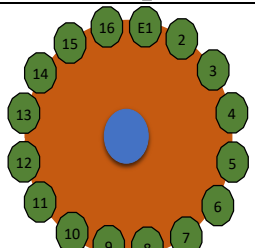
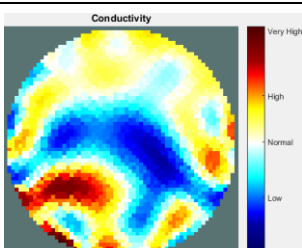
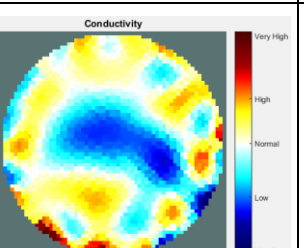
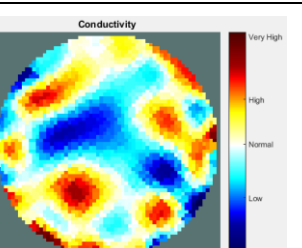
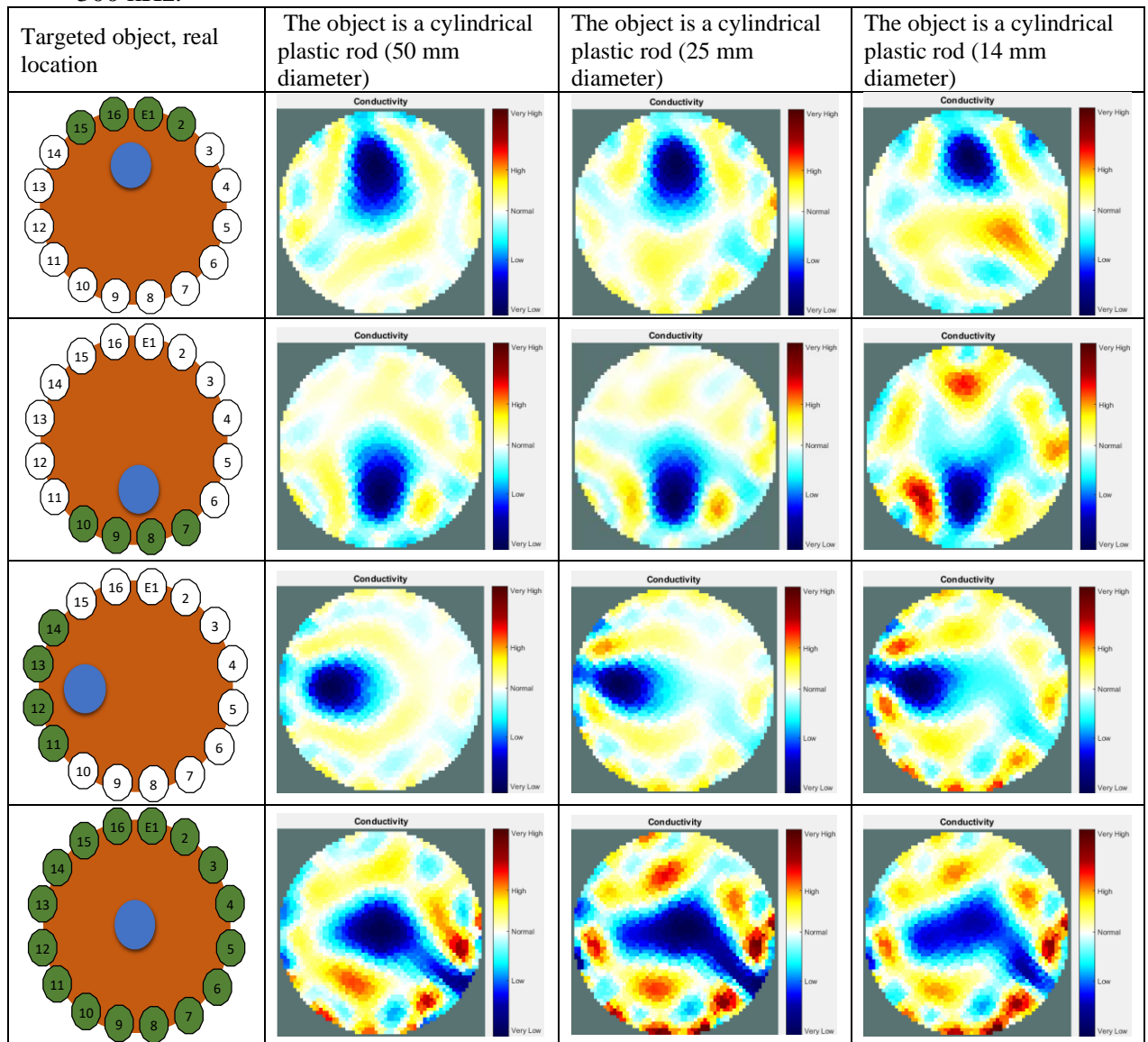
Targeted object, real location	The object is a cylindrical plastic rod (50 mm diameter)	The object is a cylindrical plastic rod (25 mm diameter)	The object is a cylindrical plastic rod (14 mm diameter)
			
			
			
			

Table 7.6 shows the 2-D reconstructed images of three electrically non-conductive objects of three diameters placed in four locations, but this time using 300 kHz as the excitation frequency. As noticed, the results of the detection and tracking are similar to the results when the 12.5 kHz was used, but with less image distortion. However, in this case, the object was detected even when it was in the centre, but with much background noise, which was due to the increase in injection frequency.

Table 7.6: Non-conductive objects at different positions; images of three non-conductive object diameters (50 mm, 25 mm, 14 mm) with an injection frequency of 300 kHz.



As can be seen in table 7.7, the SEEIT system was unable to locate and track the object using 1000 kHz in any location due to very high signal noise. As noticed, the results of the detection and tracking object using 12.5 and 300 kHz as the injection frequency were significantly better than that of the 1000 kHz.

Table 7.7: Non-conductive objects at different positions; images for three non-conductive object diameters (50 mm, 25 mm, 14 mm) with the injection frequency of 1000 kHz.

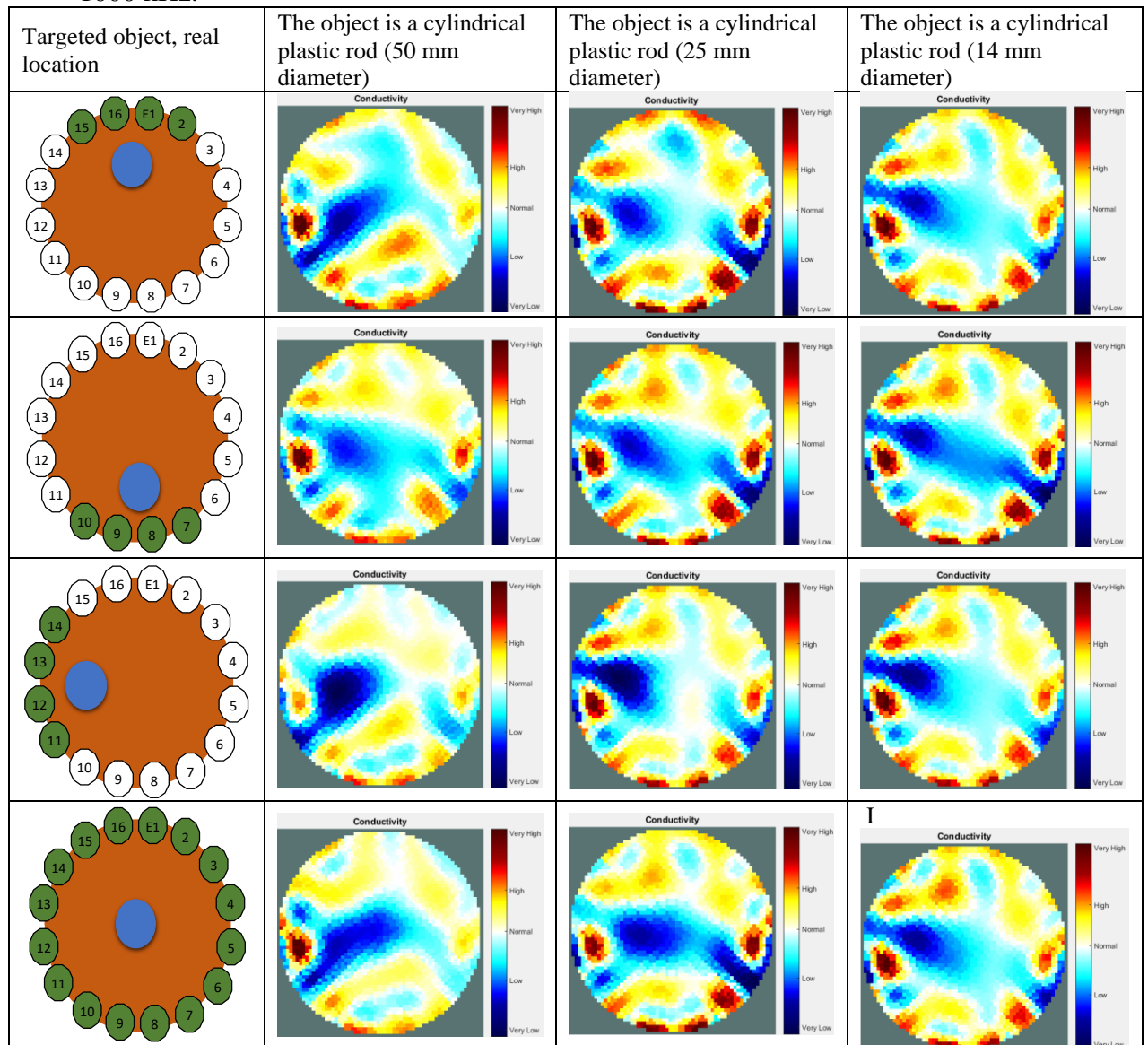


Table 7.8 shows the reconstructed images of three electrically conductive objects of three diameters, which are placed in four locations using 12.5 kHz as stimulation signals. The first object used for the test was a stainless-steel rod with a diameter of 50 mm. It was located and tracked. As noted, the SEEIT system can detect and image the 50 mm object in all positions with artefact (background noise). As seen in the reconstructed image, the object in the centre has a high level of background noise. This will be minimized significantly when the injection frequency increases. The 26 mm stainless-steel rod was placed in the four positions shown, and was located and imaged using 12.5 kHz, except when the object was in the centre. There, the SEEIT system was not able to detect it. As known in tomography imaging, the smaller the object, the harder

it is to detect and locate. As seen from the results of detection and imaging, the 26 mm object for the first three positions was detected and tracked but with higher background noise than the 50 mm reconstructed image. The 12 mm object in the last column of the table shows that the SEEIT system can track the object around the electrodes with high image distortion and deformation. However, when the object was placed in the centre of the beaker, the reconstructed image of the object shifted towards electrodes 14, 13, 12, and 11.

Table 7.8: Conductive objects at different positions; reconstructed images for three conductive object diameters (50 mm, 26 mm, 12 mm) with the injection frequency of 12.5 kHz.

Targeted object, real location	The object is a cylindrical stainless-steel rod (50 mm diameter)	The object is a cylindrical stainless-steel rod (26 mm diameter)	The object is a cylindrical stainless-steel rod (12 mm diameter)

Table 7.9 shows the reconstructed images when 300 kHz frequency is used for injection for three stainless-steel rod objects with three diameters and are placed in four

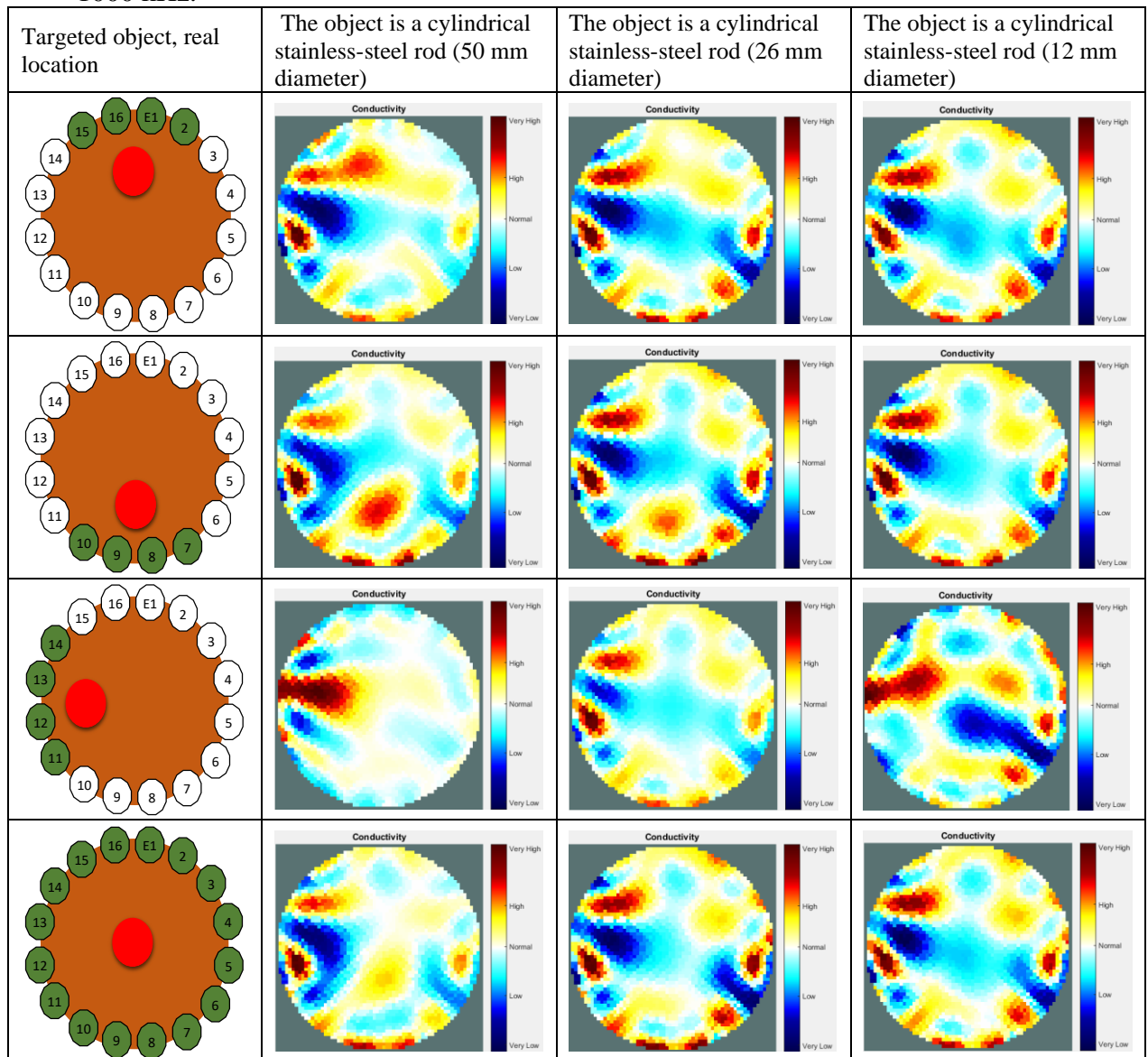
positions. However, the 50, and 26 mm objects were detected and imaged with low image background noise in all locations except the object of 26 mm in the central position, which had higher distortion. As noted, the results of the reconstructed 2D image from Tables 7.8, and 7.9 using 12 mm objects are alike the results of using 12.5 kHz injected signals.

Table 7.9: Conductive objects at different positions; reconstructed images for three conductive object diameters (50 mm, 26 mm, 12 mm) with the injection frequency of 300 kHz.

Targeted object, real location	The object is a cylindrical stainless-steel rod (50 mm diameter)	The object is a cylindrical stainless-steel rod (26 mm diameter)	The object is a cylindrical stainless-steel rod (12 mm diameter)

As can be seen in table 7.10, the SEIT system was unable to imagine any of the objects using 1000 kHz due to very high signal noises. As observed, the results of the detection of the stainless-steel rod using 12.5 and 300 kHz as the injection frequency were much better than those of 1000 kHz.

Table 7.10: Conductive objects at different positions; reconstructed images for three conductive object diameters (50 mm, 26 mm, 12 mm) with the injection frequency of 1000 kHz.

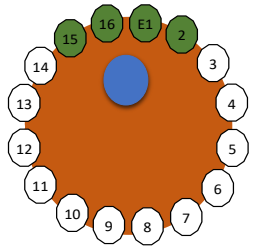
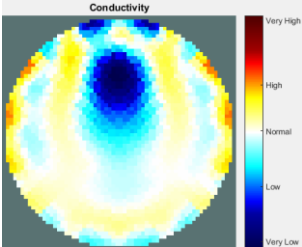
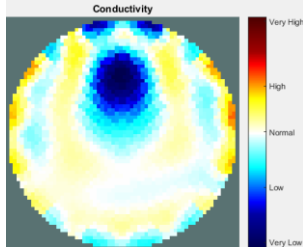
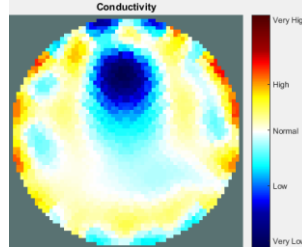
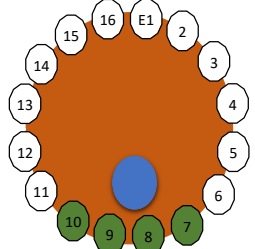
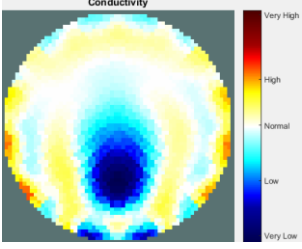
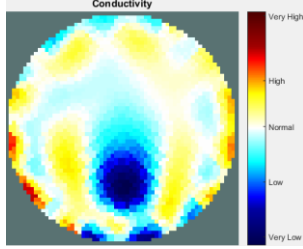
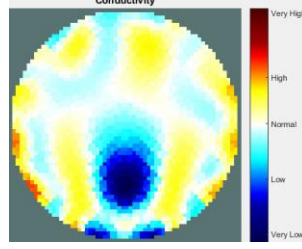


In summary, the results of both electrically conductive and electrically non-conductive targeted objects using the RMS measurement signals were obtained using 16 copper electrodes attached to the testing beaker. Reconstructed object results in all locations were obtained and displayed using three injection frequencies. Mainly, the reconstructed image quality was best when using 300 kHz, whether targeted objects were electrically conductive or non-conductive. However, the RMS result quality was still poor due to high noise levels, which occurred in the image background.

7.2.2.2 Standard deviation

The results in this part of the experiment were obtained using standard deviation processed data for image reconstruction. Table 7.11 shows the results of three plastic rod objects of three diameters placed in four locations using 12.5 kHz for the injection signals. The electrically non-conductive object with a diameter of 50 mm placed in four stated locations was tracked and imaged with very low image distortion. As observed, the 50 mm plastic rod was tracked and imaged even when it was placed in the central position, but with a higher artefact that occurs in the central position. The object's reconstructed image quality will improve by either increasing the measurement sample rate or increasing injection frequency. The 25 mm plastic rod was imaged and located for the first three locations, except when the object was placed in the centre. Then, the SEEIT system was unable to track the plastic rod. The last column of the table, which shows the results of 14 mm plastic rods, had similar reconstructed 2D image results to those of the 25 mm object.

Table 7.11: Non-conductive objects at different positions; images for three non-conductive object diameters (50 mm, 25 mm, 14 mm) with the injection frequency of 12.5 kHz.

Targeted object, real location	The object is a cylindrical plastic rod (50 mm diameter)	The object is a cylindrical plastic rod (25 mm diameter)	The object is a cylindrical plastic rod (14 mm diameter)
			
			

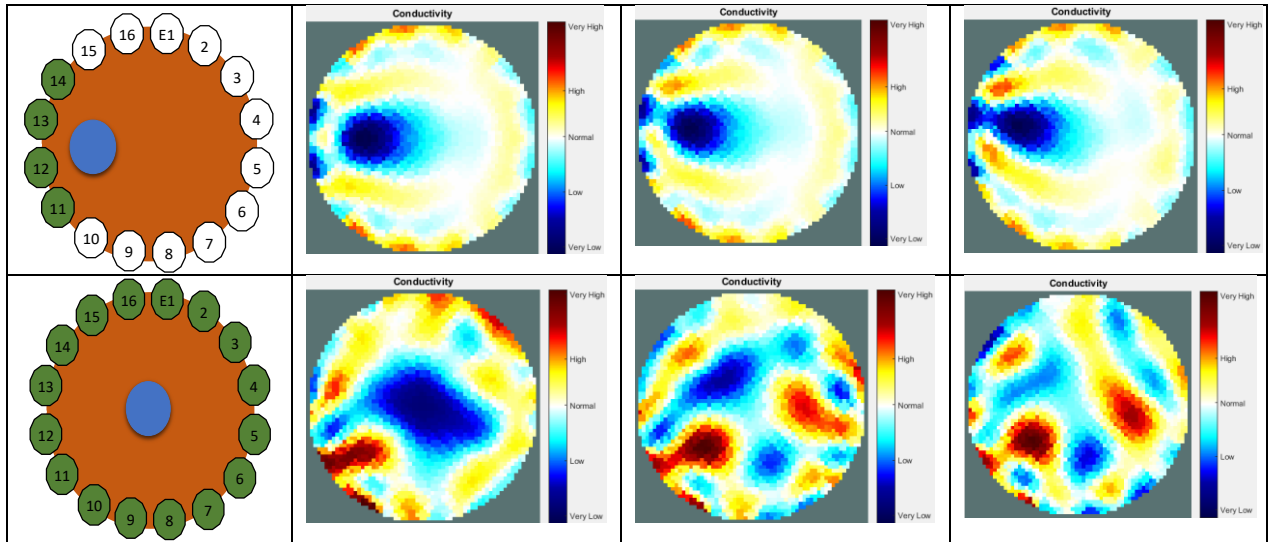
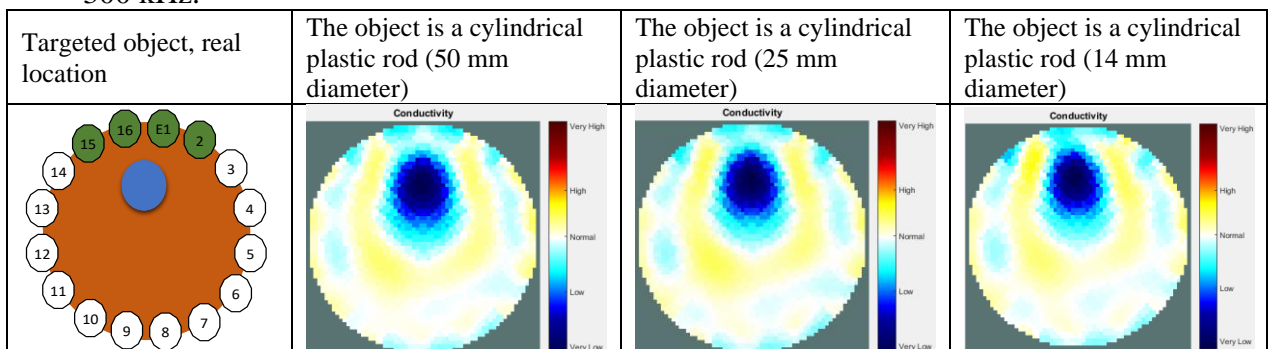
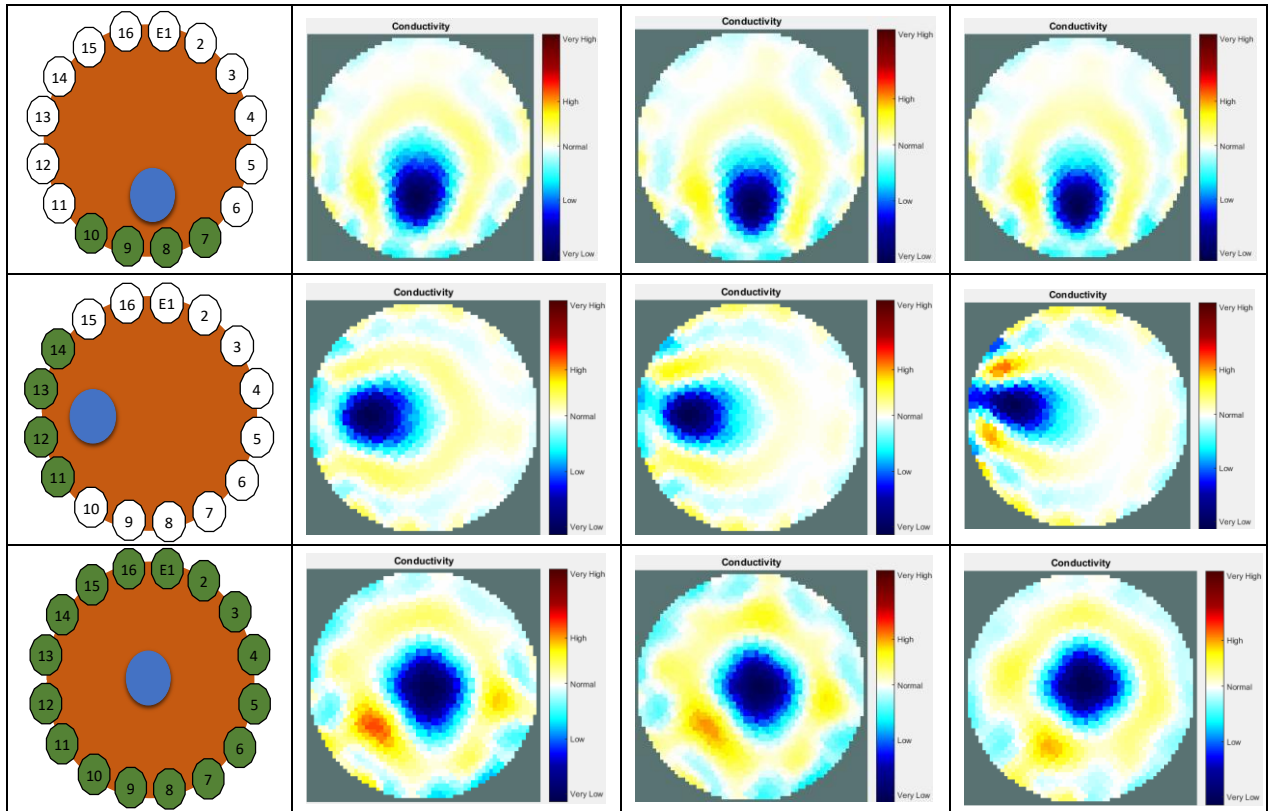


Table 7.12 shows the 2-D reconstructed images of three electrically non-conductive substances with different diameters placed in four locations using 300 kHz as the excitation frequency. As observed, the three objects with different diameters were located and imaged even when the targeted object was placed in the centre of the beaker, which had a low reconstructed image artefact. These results provide more advantages to the standard deviation measurement process since they are performed much better than the RMS measurements process. Furthermore, the reconstructed 2D image results, using 300 kHz, were better than those using 12.5 kHz as the injection frequency. This is because the reconstructed image of 300 kHz shows the ability to image the object when it is placed in the centre of the testing beaker using the smallest plastic rod 14 mm, as seen.

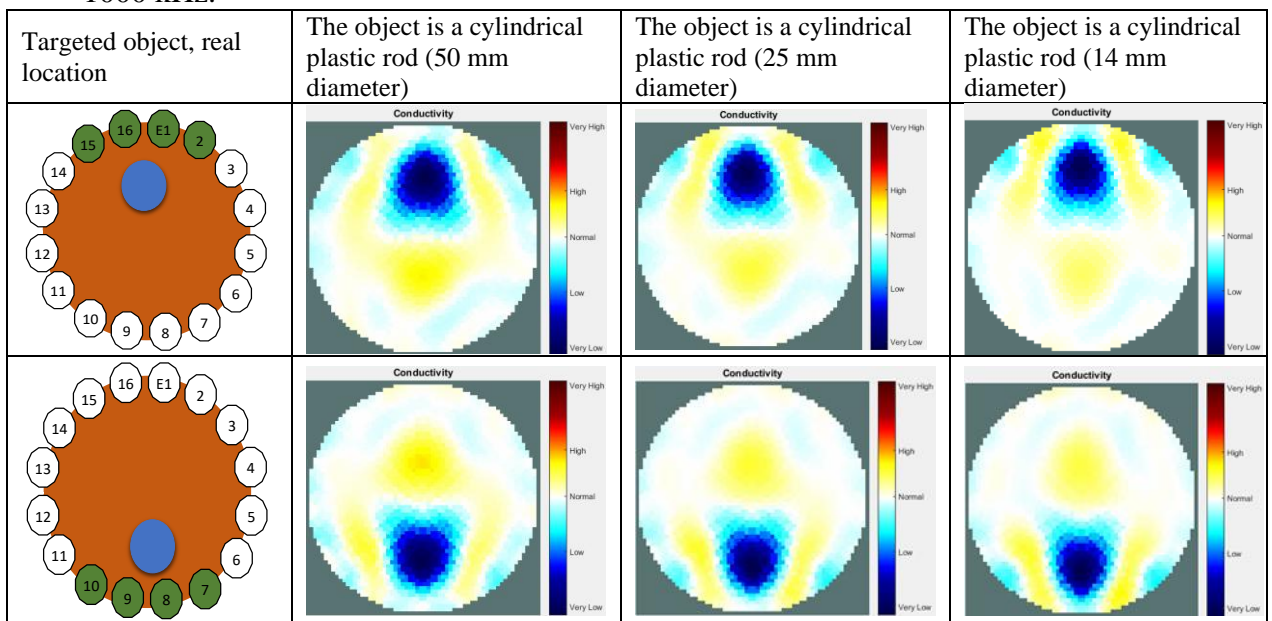
Table 7.12: Non-conductive objects at different positions; images for three non-conductive object diameters (50 mm, 25 mm, 14 mm) with the injection frequency of 300 kHz.





The SEEIT system could image and track the object using 1000 kHz in all locations with low distortion, as seen in Table 7.13. With the three-injection frequency, the best results were seen when using the 1000 kHz, since the reconstructed 2D images of 1000 kHz had the lowest amount of image background noise.

Table 7.13: Non-conductive objects at different positions; images for three non-conductive object diameters (50 mm, 25 mm, 14 mm) with the injection frequency of 1000 kHz.



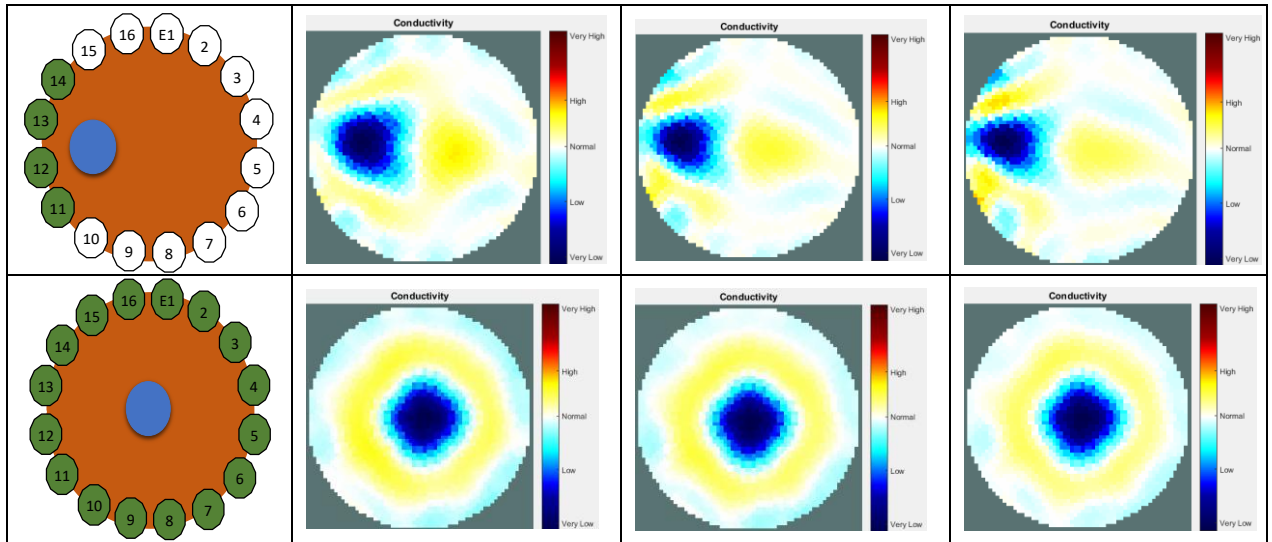


Table 7.14 shows the 2D images using the 12.5 kHz injection frequency of electrically conductive objects with different diameters that are placed in four locations. The stainless-steel rod with a diameter of 50 mm was located and tracked even in the central positions, but with background noise. When the object became smaller than 26 and 12 mm, the system was unable to detect the targeted object when it placed in the central position.

Table 7.14: Conductive objects at different positions; reconstructed images for three conductive object diameters (50 mm, 26 mm, 12 mm) with the injection frequency of 12.5 kHz.

Targeted object, real location	The object is a cylindrical stainless-steel rod (50 mm diameter)	The object is a cylindrical stainless-steel rod (26 mm diameter)	The object is a cylindrical stainless-steel rod (12 mm diameter)

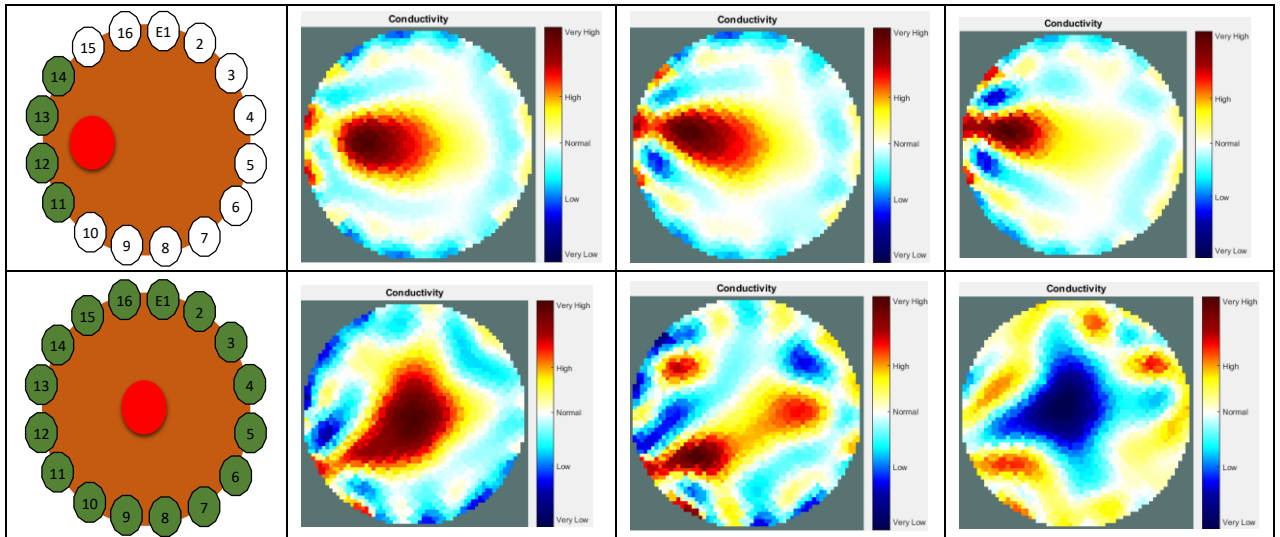


Table 7.15 shows the results of 2D reconstructed images for three electrically conductive objects with different diameters using 300 kHz for the injection frequency. As observed, all the objects with different diameters were located and imaged with low reconstructed image background noise. However, for an electrically conductive object using 300 kHz, when the object was placed near the electrodes, the reconstructed aimed object shifted towards the centre. This may have been caused by the current leakage. Furthermore, the reconstructed 2D image results using 300 kHz were better than those of 12.5 kHz when used as the injection frequency. Comparing the image background noise level, when applying standard deviation measurement processes, was significantly lower than that of the RMS measurement process.

Table 7.15: Conductive objects at different positions; reconstructed images for three conductive object diameters (50 mm, 26 mm, 12 mm) with the injection frequency of 300 kHz.

Targeted object, real location	The object is a cylindrical stainless-steel rod (50 mm diameter)	The object is a cylindrical stainless-steel rod (26 mm diameter)	The object is a cylindrical stainless-steel rod (12 mm diameter)

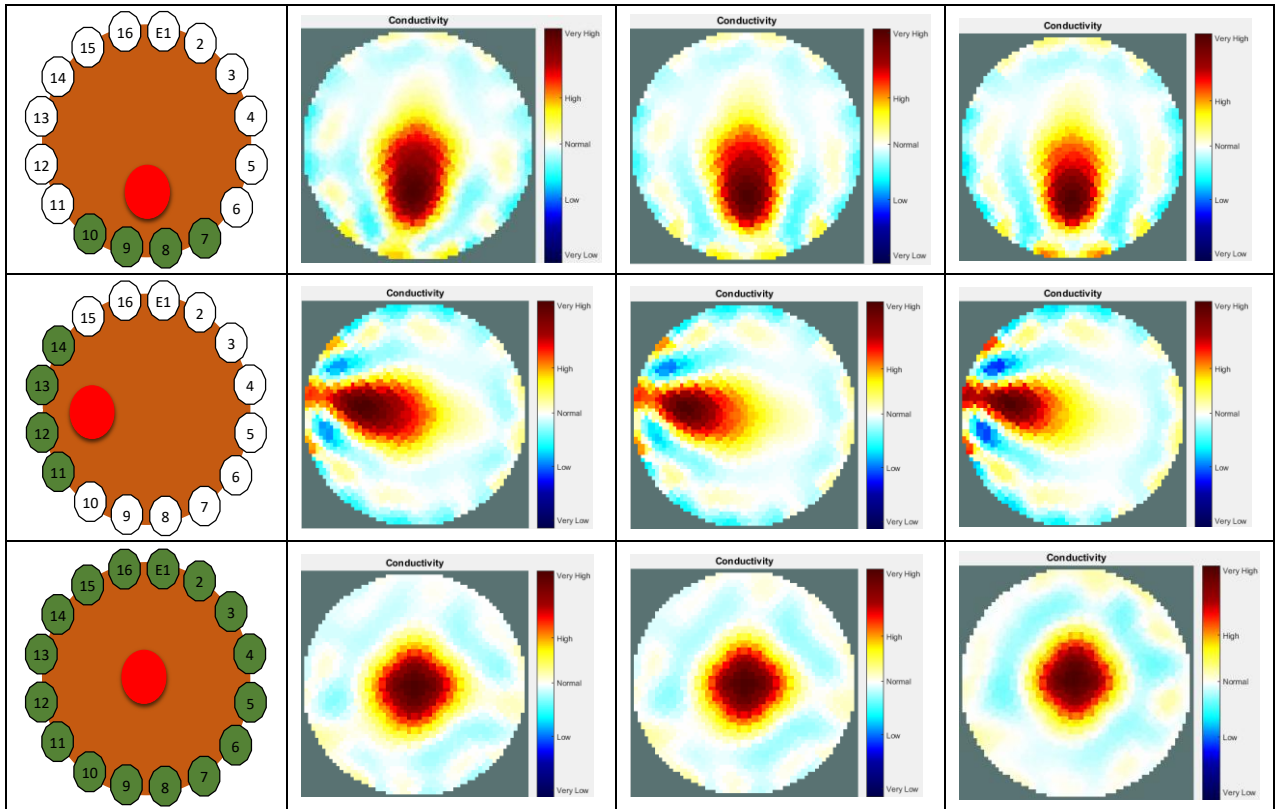
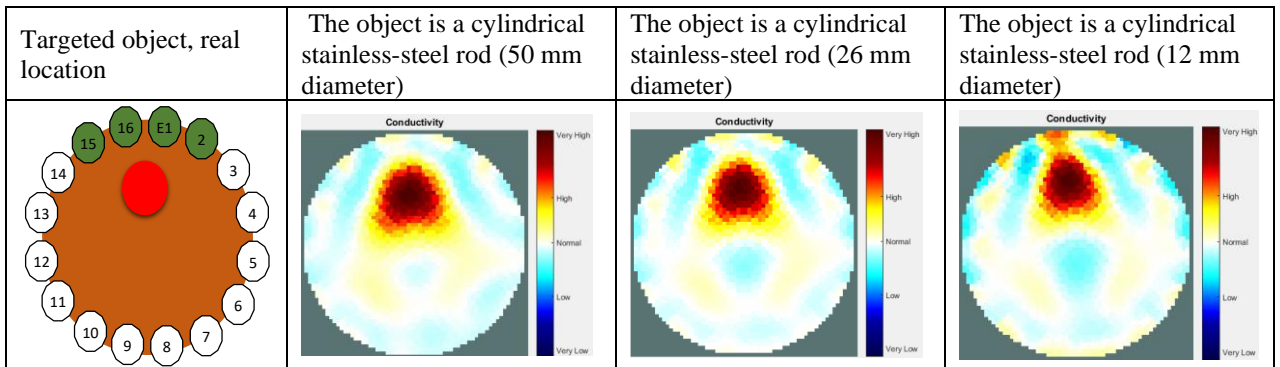
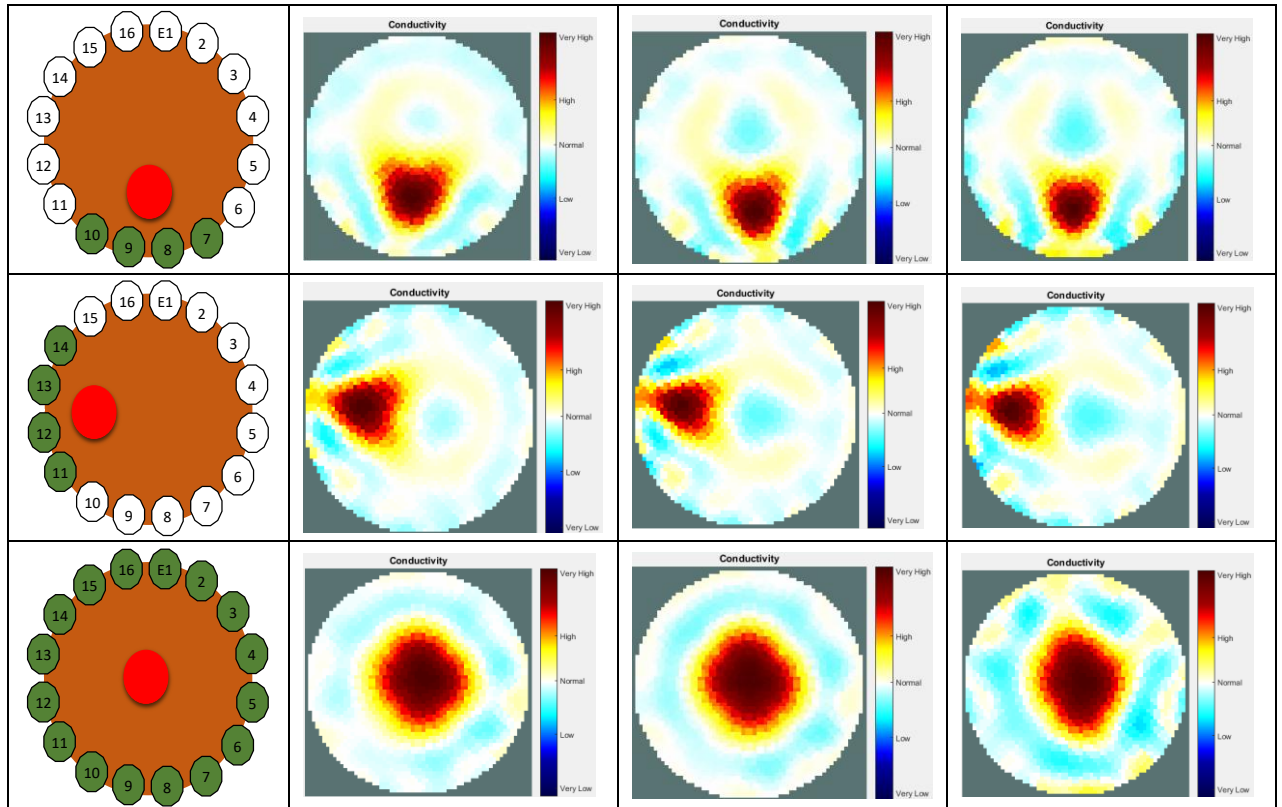


Table 7.16 shows the results of 2D reconstructed images, which are similar to those of Table 7.15. However, this uses 1000 kHz instead of 300 kHz as the injection frequency. As noted, all the stainless-steel rods with different diameters were located and imaged with very low image background noise. However, the targeted object shifted towards the centre of the testing beaker was a problem. This was seen when 300 kHz was the injection frequency. It was solved by increasing the injection frequency. However, when the diameter of the object became smaller, the reconstructed 2D image's background noise increased.

Table 7.16: Conductive objects at different positions; reconstructed images for three conductive object diameters (50 mm, 26 mm, 12 mm) with the injection frequency of 1000 kHz.





The results of the observed image of both plastic rods and stainless-steel rods targeted object using the standard deviation processed measurements were obtained using testing beaker filled up with muddy water. The 2D reconstructed image results in all locations were successfully obtained using three injection frequencies. The reconstructed 2D image quality was best when using both 300 and 1000 kHz as injection frequencies. However, the standard deviation result quality was better than that of the RMS results, even with much less reconstructed image artefacts.

7.2.2.3 Variance

These section results were obtained using variance data to reconstruct the 2D image. Table 7.17 shows the reconstructed image results using 12.5 kHz as the injection frequency for three plastic rods with diameters of 50, 25, and 14 mm. They were placed and tested in four locations. The targeted object with a diameter of 50 mm, was imaged for the first three positions. However, for the central position, the developed system using variance measurements was unable to image or even detect the targeted object. The results of the 25 mm plastic rod were similar to the results of the 50 mm plastic rod. They both had reconstructed image background noise. Moreover, the plastic rod

with a diameter of 14 mm was imaged only when the targeted object was near the electrodes. The higher levels of reconstructed image background noise were for 25- and 50-mm objects. The problem of object detection in the central position could be minimized significantly when the injection frequency was increased or when the input signal range was decreased.

Table 7.17: Non-conductive objects at different positions; images for three non-conductive object diameters (50 mm, 25 mm, 14 mm) with the injection frequency of 12.5 kHz.

Targeted object, real location	The object is a cylindrical plastic rod (50 mm diameter)	The object is a cylindrical plastic rod (25 mm diameter)	The object is a cylindrical plastic rod (14 mm diameter)

Table 7.18 shows the 2-D reconstructed images for three plastic rod objects with different diameters, using 300 kHz as the injected frequency. As observed, all the objects were imaged even when the targeted object was placed in the centre. However, the image background noise level was lower when the aimed object was placed near

the electrodes than when it was placed in the central location. Moreover, the reconstructed image results using 300 kHz were better than those using 12.5 kHz as the injection frequency. As seen, the smallest plastic rod of 14 mm was imaged even when it was placed in the centre of the testing beaker.

Table 7.18: Non-conductive objects at different positions; images for three non-conductive object diameters (50 mm, 25 mm, 14 mm) with the injection frequency of 300 kHz.

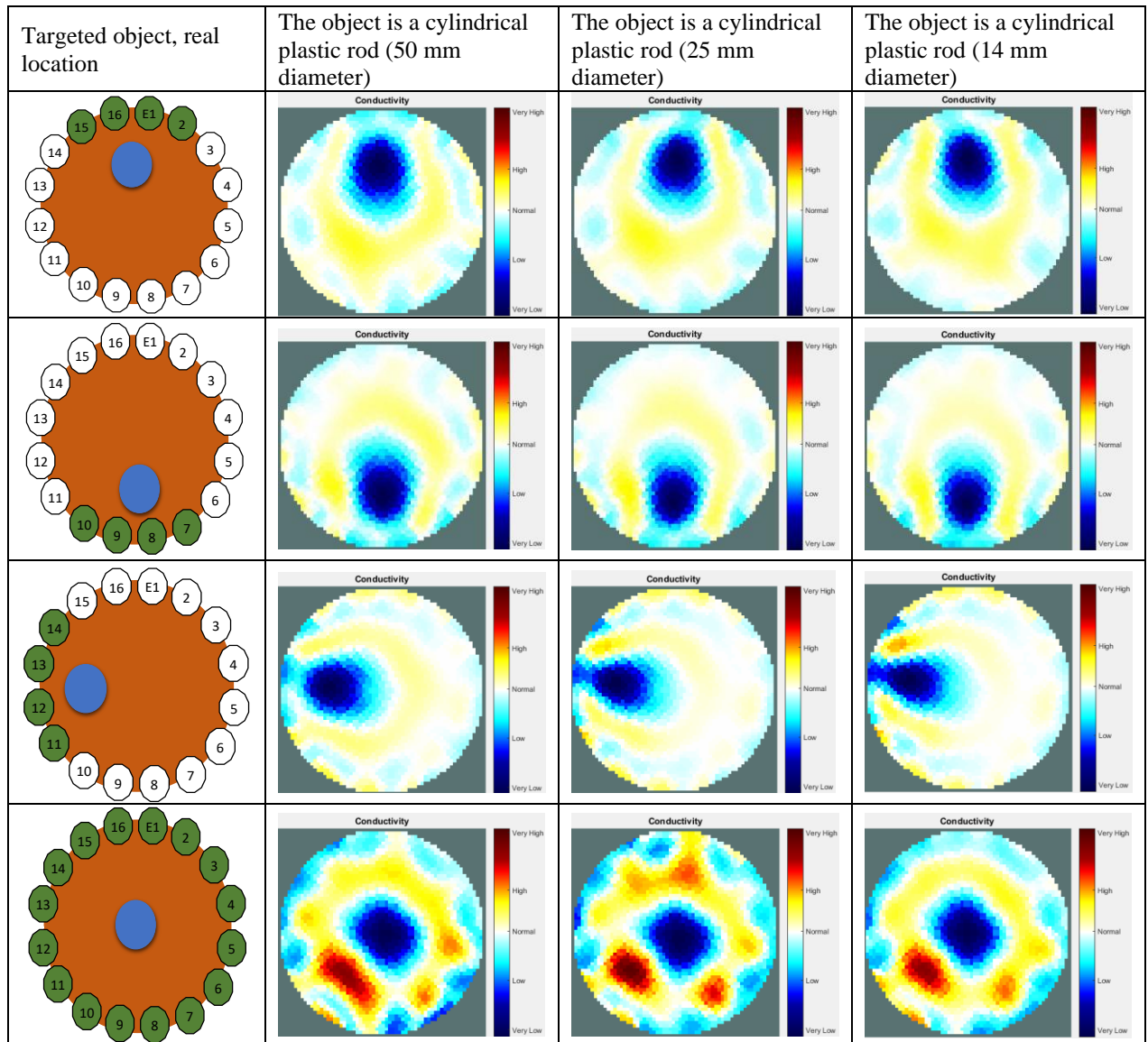


Table 7.19 shows the reconstructed images when the 1000 kHz frequency was injected to image plastic rods with different diameters. The SEEIT system was able to image all objects using 1000 kHz at all locations with very low image background noise, as seen. The best results of the reconstructed image were seen when using the 1000 kHz, and this was due to very low background image noise.

Table 7.19: Non-conductive objects at different positions; images for three non-conductive object diameters (50 mm, 25 mm, 14 mm) with the injection frequency of 1000 kHz.

Targeted object, real location	The object is a cylindrical plastic rod (50 mm diameter)	The object is a cylindrical plastic rod (25 mm diameter)	The object is a cylindrical plastic rod (14 mm diameter)

Table 7.20 shows the 2D images using the 12.5 kHz injection frequency of cylindrical stainless-steel rod objects with three diameters placed in four locations. The 50 mm object was located and tracked even in the central positions, but with background noise. When the object became smaller than 26 and 12 mm, the SEEIT system was unable to track the targeted object when it was placed in the central position. In addition, when the 12 mm object was placed in the centre, the reconstructed image showed an electrically non-conductive object instead of an electrically conductive object. These were incorrect reconstructed image results.

Table 7.20: Conductive objects at different positions; reconstructed images for three conductive object diameters (50 mm, 26 mm, 12 mm) with the injection frequency of 12.5 kHz.

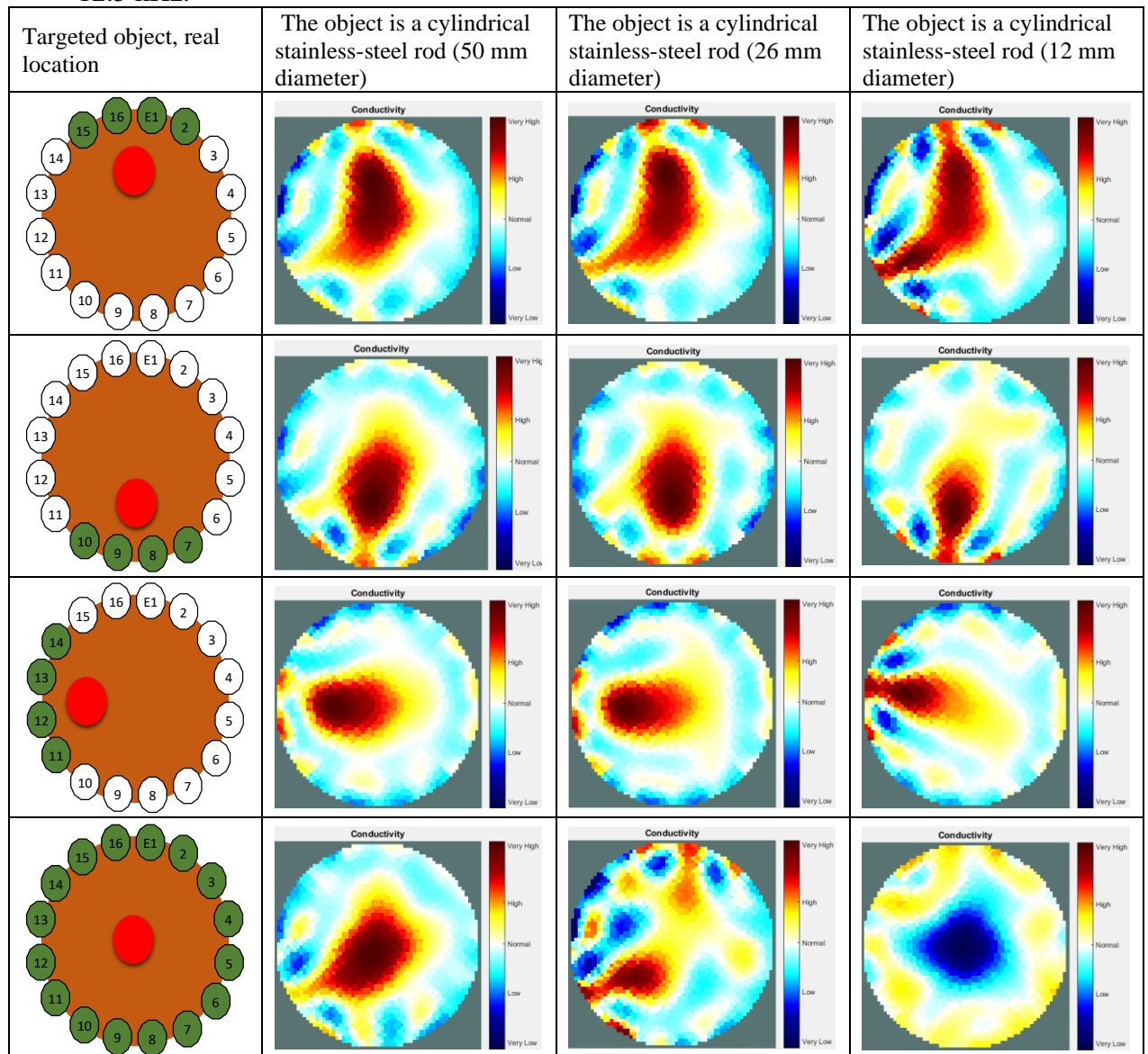


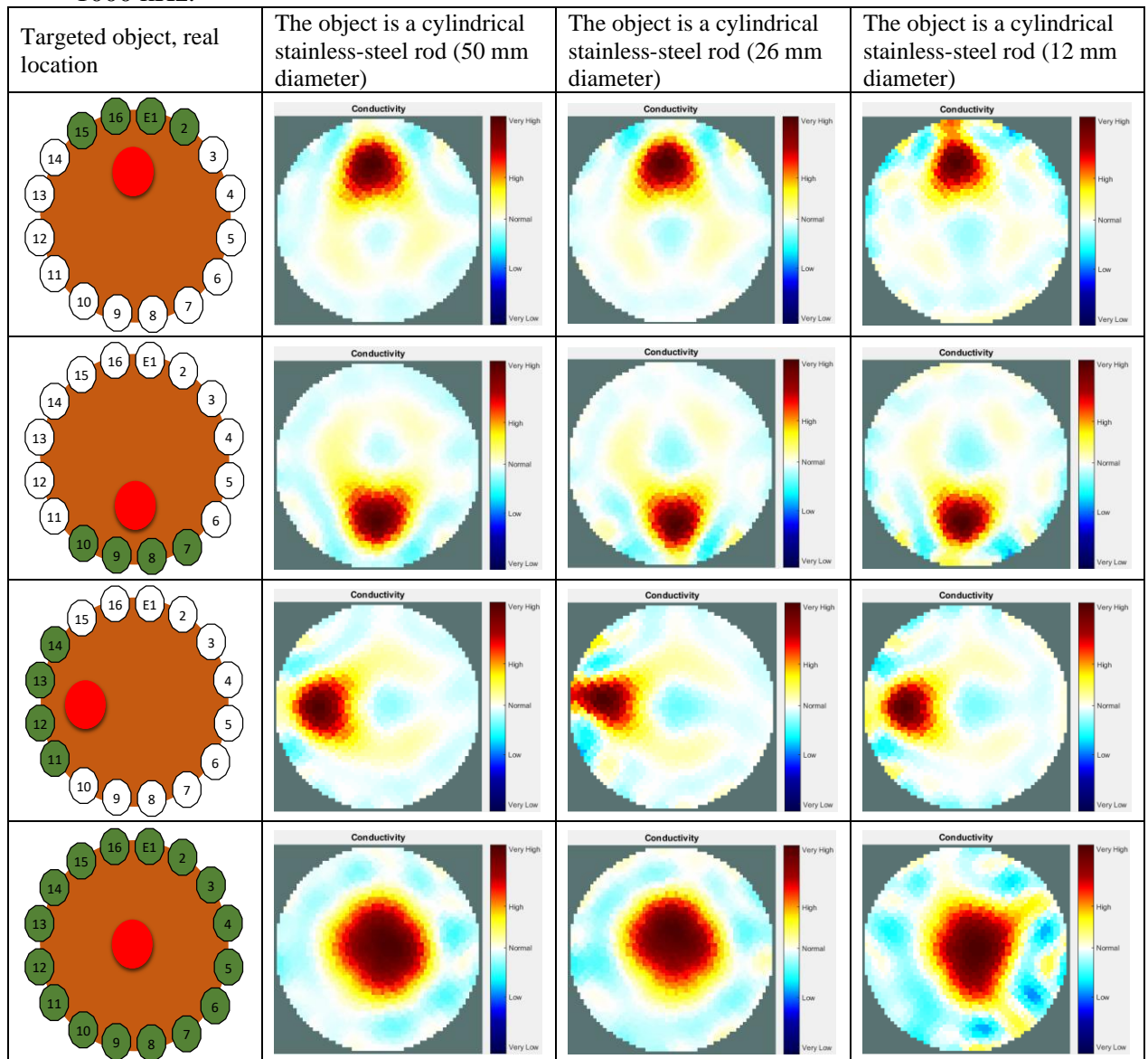
Table 7.21 shows 2D reconstructed images for three electrically conductive objects using 300 kHz for the injection frequency. As seen, all the animated objects with different diameters were imaged with reconstructed image background noise. However, when the object was placed near the electrodes, the reconstructed targeted object shifted towards the central position. Furthermore, images obtained using 300 kHz were better than those using 12.5 kHz as the injection frequency.

Table 7.21: Conductive objects at different positions; reconstructed images for three conductive object diameters (50 mm, 26 mm, 12 mm) with the injection frequency of 300 kHz.

Targeted object, real location	The object is a cylindrical stainless-steel rod (50 mm diameter)	The object is a cylindrical stainless-steel rod (26 mm diameter)	The object is a cylindrical stainless-steel rod (12 mm diameter)

Table 7.22 shows the results of 2D reconstructed images using 1000 kHz for the injection frequency. As observed, all the stainless-steel rods of 50, 26, and 12 mm in diameter were imaged with very low image distortion. However, the reconstructed 2D image distortion increased when the object was placed in the central position and became smaller, like the 12 mm reconstructed image.

Table 7.22: Conductive objects at different positions; reconstructed images for three conductive object diameters (50 mm, 26 mm, 12 mm) with the injection frequency of 1000 kHz.



The results of the images observed for both plastic rod and stainless-steel rod targeted objects using the variance measurements were obtained using testing beakers filled with tap water mixed with soil. The 2D reconstructed image results in all locations were successfully obtained using three injections; 12.5, 300, and 1000 kHz. The reconstructed 2D image quality was best when using both 300 and 1000 kHz for the injection frequency. However, the standard deviation and variance reconstructed image quality was better than that of RMS results, even with much lower levels of reconstructed image background noise.

The reconstructed image of the RMS data using low injection frequency (12.5 kHz) object observed whether it is electrically conductive or non-conductive but with high background noise. However, when the object becomes smaller, especially when the object placed in the center of the testing beaker, it becomes hard to observe the object through the reconstructed image. The reconstructed image of the RMS data performed the best using 300 kHz frequency since the object location located but with high background noise even when it placed in the center of the testing beaker. On the other hand, the reconstructed image using the RMS data, which uses 1000 kHz object undetectable in any location, whether electrically conductive or non-conductive object. The reconstructed image using the variance data with low frequency the object located, whether it electrically conductive or non-conductive except when the object placed in the center. However, in all the reconstructed images, background noise is present, and the noise increases when the object becomes smaller. The variance results using 300 kHz injection frequency improved significantly with low background noise even when the object placed in the center. For electrically conductive and non-conductive objects, the reconstructed image results using 1000 kHz is the best as observed with the least amount of background noise and clear comparing the variance results when the injection frequencies were 12.5 and 300 kHz. As observed, the results of the standard deviation data at low frequency, whether the object electrically conductive or non-conductive located and imaged but with high image distortion except when the object is placed in the centre, the object cannot be located. However, using 300 kHz standard deviation data, targeted objects were imaged and located even it placed in the center of the testing beaker with low reconstructed image distortion for electrically conductive and non-conductive objects. Additionally, the 1000 kHz image reconstructed results are improved since it has a lower amount of background noise than the 300 kHz reconstructed image.

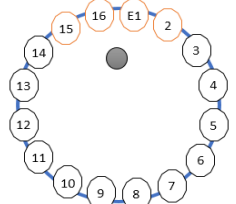
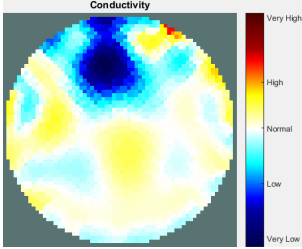
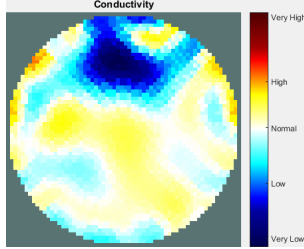
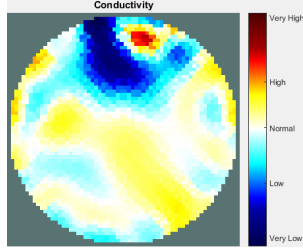
In the muddy water experiments, three types of measurements were used, which they are rms, variance, and standard deviation. Overall the reconstructed image results which use variance and standard deviation better than the rms since the rms reconstructed images results had higher background noises, and at high frequency, the object will not be detected. Locating and imaging objects, whether it is electrically conductive or non-conductive in a beaker filled up with muddy water, makes the reconstructed image

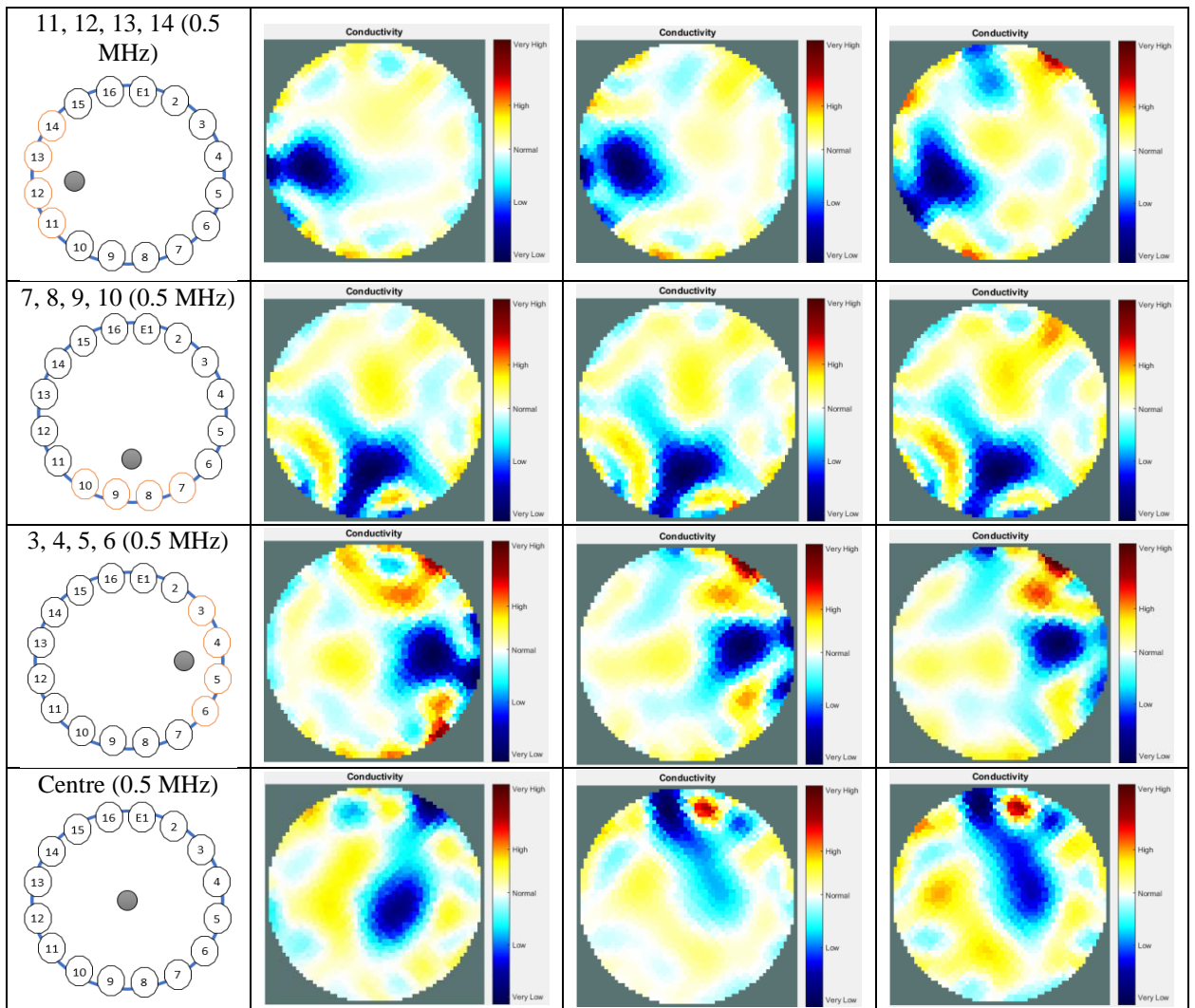
challenging since the medium electrical conductivity higher than tap water and not stable. In summary, the electrically conductive and non-conductive reconstructed images obtained using standard deviation data at 12.5 kHz is better than the one obtained using variance data but the results of other frequencies (300 kHz, 1000 kHz) they are similar.

7.2.3 Gas and tap water detection test using SEEIT system

Table 7.23 shows the results of detection bubbles of gas in the tap water test using titanium alloy grade 2 16-electrode array attached to a cylindrical testing tank. The first measurements were obtained when only tap water was used, and the air hose was placed in a fixed location. The second measurements were taken when the air was pumped through the air hose, which was fixed in different locations inside the testing tank. Then, the first and second measurements were compared to reconstructed 2-D images showing the air bubble flow location. As it is known that air bubble flow is unsteady, the three reconstructed images were unsteady for the samples presented for each location, as displayed. As observed, the air bubble flow area was located and imaged using 0.5 MHz as the excitation frequency, with input signals ranging from max 3 – min –3. However, as seen when the air was pumped into the central location, the reconstructed image of the air bubble area changed and varied (was unstable). This may have occurred because of the air bubble flow behaviour. The air bubbles appeared to shift into the testing tank wall regions.

Table 7.23: Air hose placed at different positions; reconstructed cross-section images for five air hose setups.

Air pumped area targeted real location and the injected frequency with input signal range max 3 – min –3	Sample 1	Sample 2	Sample 3
15, 16, 1, 2 (0.5 MHz) 			

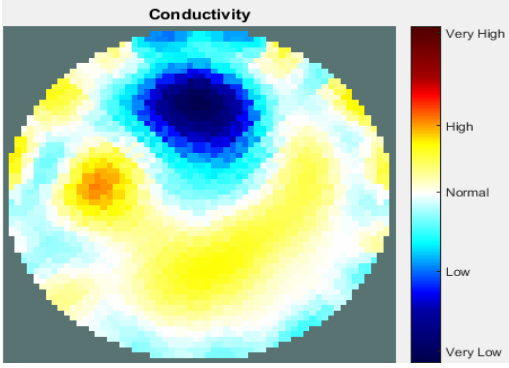


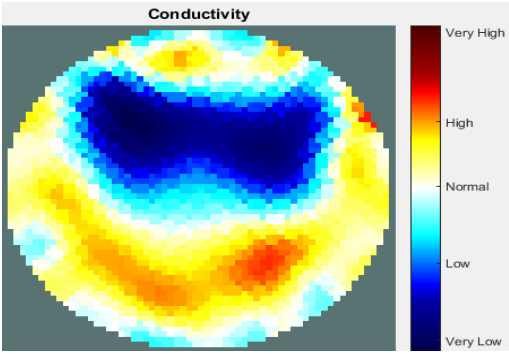
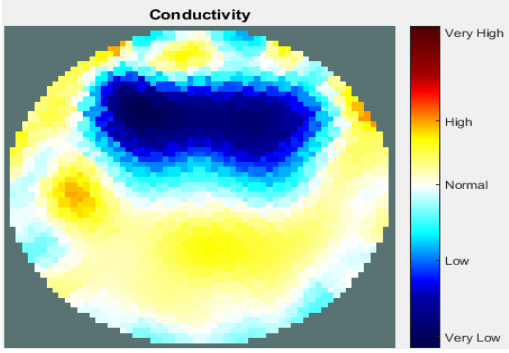
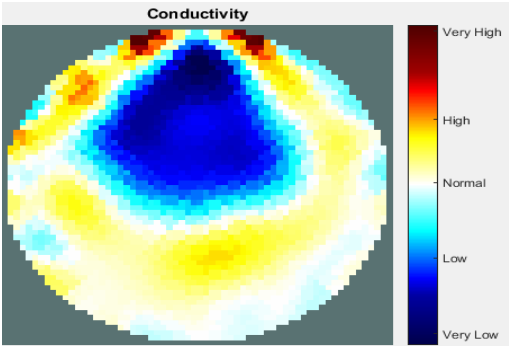
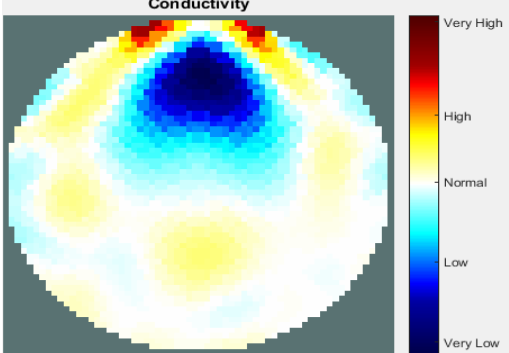
7.2.4 Electrically non-conductive object shape detection test using SEIT system

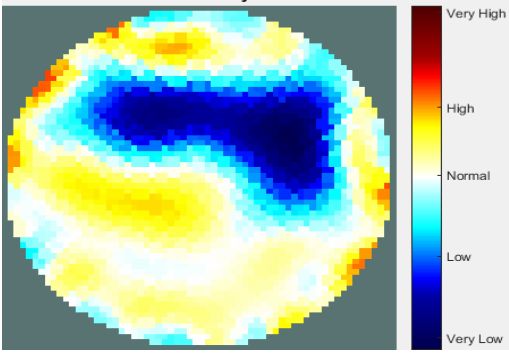
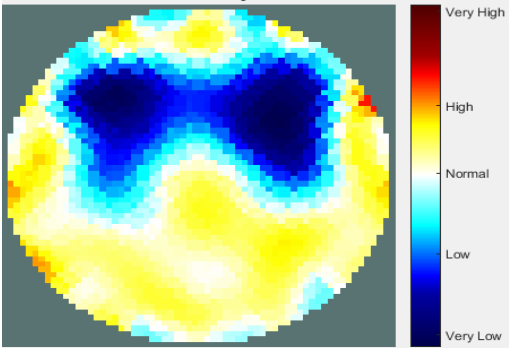
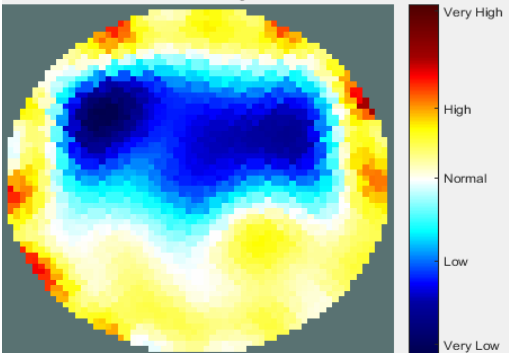
Table 7.24 shows the results of the third experiment, and it illustrates the ability of the system to detect and reconstruct the images of electrically non-conductive object shapes that were placed in the testing vessel filled with 2250 ml of tap water. The first column shows the Styrofoam real shapes, and the centre column demonstrates the reconstructed cross-section images for each aimed target shape. The last column shows the analog I/O signal main configuration setup parameters for each targeted object shape. The first object, which was made of Styrofoam, was carved into a circle shape, and it was placed near electrodes 15, 16, 1, and 2. The reconstructed image shows the ability of the system to estimate the targeted object shape; however, it is not very accurate because the background noise levels were high, particularly on the left side of

the imaged area, as seen in the dark red spot. The second object was carved into a square shape, and it was placed near electrodes 14, 15, 16, 1, 2, and 3. The target was detected and imaged as a rectangular shape with few defects, although background noise was present. The third object was carved as a rectangular shape as well, but with a smaller diameter size than the previous object, and was placed near electrodes 15, 16, 1, and 2. In addition, the small rectangular object was detected and imaged, but with a low defect. The fourth object was carved as a triangle shape and placed near electrodes 16 and 1. As seen in the table, the triangle shape was reconstructed with a low amount of background noise. Furthermore, a smaller triangle object was carved and imaged as shown; it was placed near electrodes 16 and 1. The L-shaped object, which was placed near electrodes 15, 16, 1, 2, 3, and 4, was imaged. As observed, the structural details of the reconstructed object are poor, particularly the object side towards the centre of the testing tank. The C-shaped object, which was located near electrodes 14, 15, 16, 1, 2, and 3, was identified with few defects. Finally, the E-shaped object, which has a structure with a complex shape, was compared with the previous object shapes and was placed near electrodes 14, 15, 16, 1, 2, and 3. It was recognised but had a high number of defects.

Table 7.24: Non-conductive objects (Styrofoam) with different shapes; reconstructed images for different non-conductive object shapes.

Targeted object shape, made of Styrofoam	The 2-D reconstructed image	The analog I/O signal main configuration setup
		<p>Amplitude: 2 V</p> <p>Frequency: 300 kHz</p> <p>Offset: 0</p> <p>Number of samples: 2000</p> <p>Rate: 40000</p> <p>Maximum value: 3</p> <p>Minimum value: -3</p>

		<p>Amplitude: 2 V</p> <p>Frequency: 1 MHz</p> <p>Offset: 0</p> <p>Number of samples: 2000</p> <p>Rate: 40000</p> <p>Maximum value: 1</p> <p>Minimum value: -1</p>
		<p>Amplitude: 2 V</p> <p>Frequency: 1 MHz</p> <p>Offset: 0</p> <p>Number of samples: 2000</p> <p>Rate: 40000</p> <p>Maximum value: 1</p> <p>Minimum value: -1</p>
		<p>Amplitude: 2 V</p> <p>Frequency: 1 MHz</p> <p>Offset: 0</p> <p>Number of samples: 2000</p> <p>Rate: 40000</p> <p>Maximum value: 0.5</p> <p>Minimum value: -0.5</p>
		<p>Amplitude: 2 V</p> <p>Frequency: 1 MHz</p> <p>Offset: 0</p> <p>Number of samples: 30000</p> <p>Rate: 40000</p> <p>Maximum value: 0.5</p> <p>Minimum value: -0.5</p>

		<p>Amplitude: 2 V</p> <p>Frequency: 900 kHz</p> <p>Offset: 0</p> <p>Number of samples: 2000</p> <p>Rate: 40000</p> <p>Maximum value: 1</p> <p>Minimum value: -1</p>
		<p>Amplitude: 2 V</p> <p>Frequency: 1 MHz</p> <p>Offset: 0</p> <p>Number of samples: 2000</p> <p>Rate: 40000</p> <p>Maximum value: 0.2</p> <p>Minimum value: -0.1</p>
		<p>Amplitude: 2 V</p> <p>Frequency: 1 MHz</p> <p>Offset: 0</p> <p>Number of samples: 2500</p> <p>Rate: 40000</p> <p>Maximum value: 0.2</p> <p>Minimum value: -0.1</p>

7.2.5 Chicken tissue chunk detection test using the SEEIT system

Figure 7.3 shows the results of the fourth experiment, which employed a testing tank with a height of 50 mm and electrodes. It had an active contact area of $14 \times 14 \times 0.5$ mm³. The first measurements were taken using a testing tank filled with chicken breast chunks and with an electrical conductivity level of 1184.04 μ S/cm. The second measurements were taken from the tank with chicken fat and skin (soaked in brackish water) with an electrical conductivity of 2870.4 μ S/cm. They were located near

electrodes 11, 12, 13, and 14. Then, the measurement data changes were processed to identify the location of the chicken skin and fat. As seen, the SEEIT system was able to find and image the electrical conductivity changes in the tank.

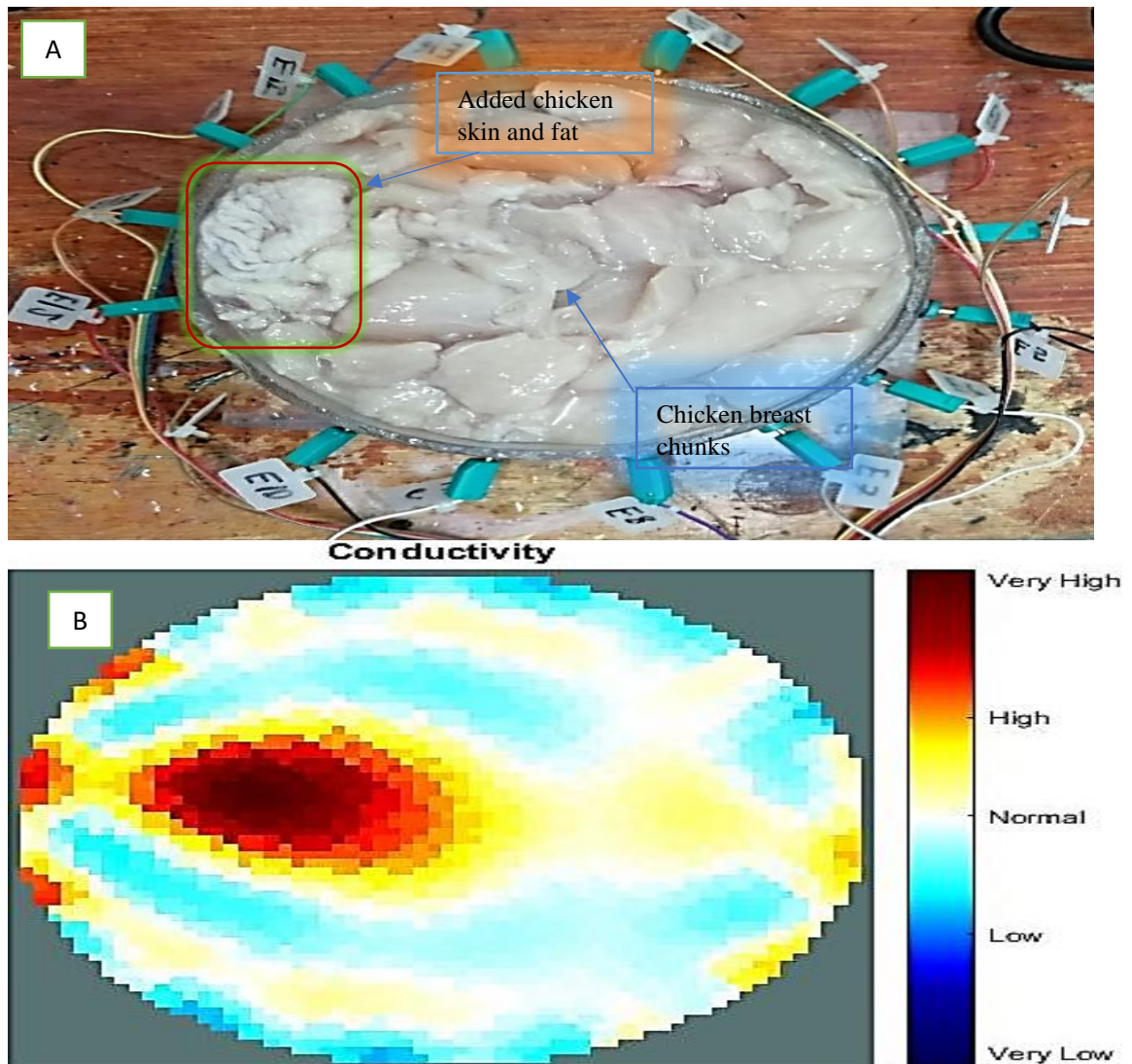


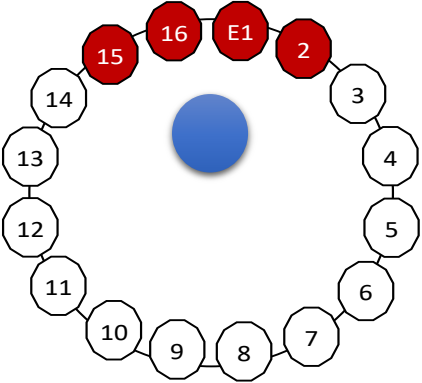
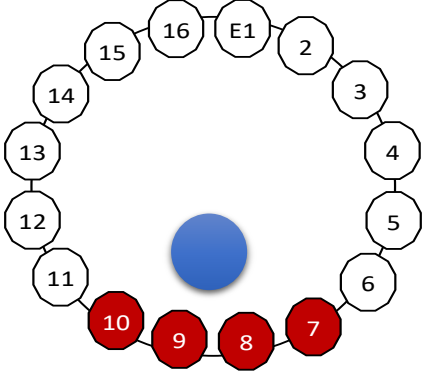
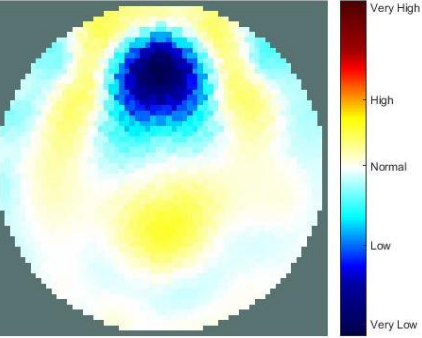
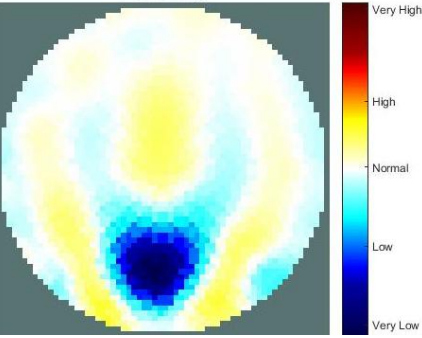
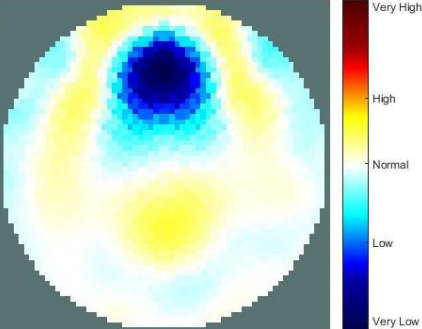
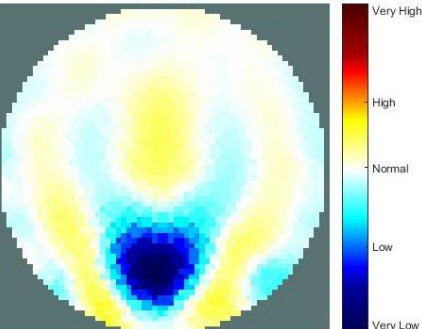
Figure 7.3: A. Chicken skin and fat location in the vessel filled with raw chicken breast chunks. B. 2-D reconstructed image of the chicken skin and fat.

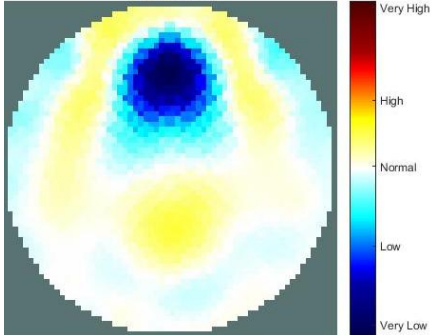
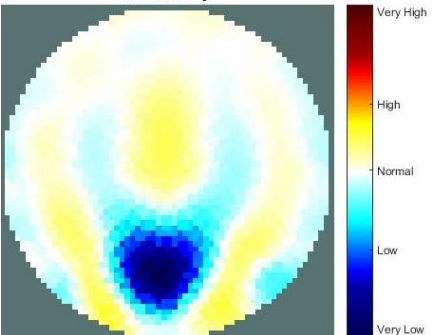
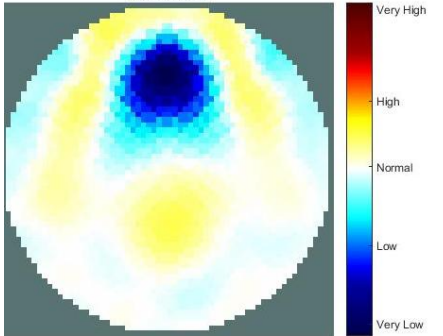
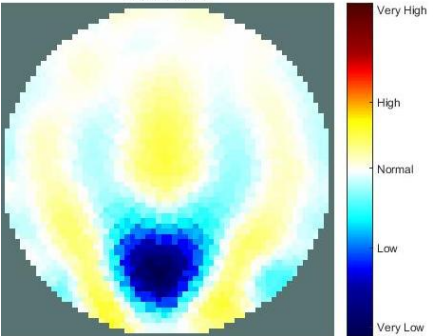
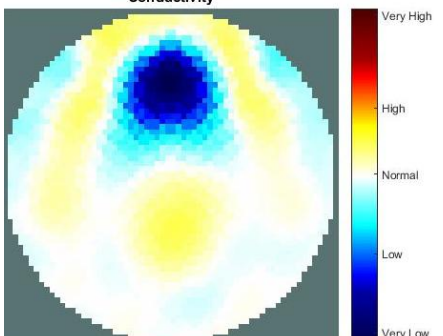
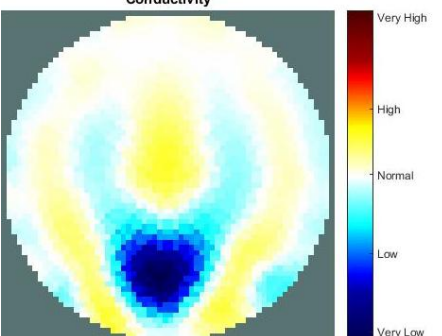
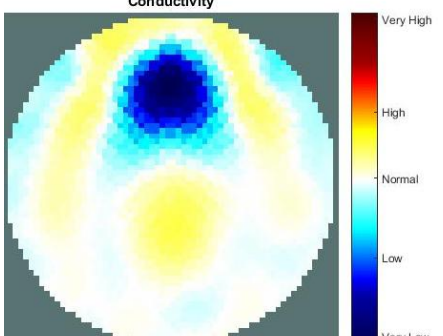
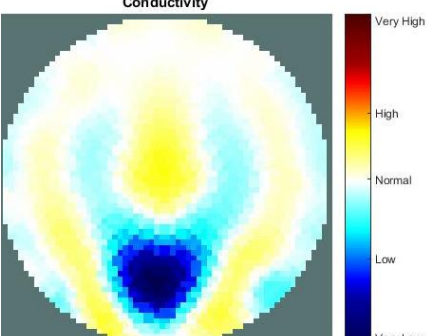
7.2.6 SEEIT system stability test

In this experiment, the results of an electrically non-conductive targeted object using the variance measurements signals were obtained using 16 copper electrodes attached to the testing beaker. The plastic rod was 25 mm and was placed in two locations in the testing beaker. The rod was continuously monitored and imaged for one hour using 1 MHz as the injection frequency. Moreover, the reconstructed image samples were

collected every period, as seen in Table 7.25. However, the water temperature was taken along with that of the reconstructed image samples. This was done because the temperature of the water would change the electrical conductivity, which would, in turn, affect the reconstructed image. As observed, the SEEIT system was able to monitor and image the targeted object continuously for one hour for two locations with high stability images.

Table 7.25: Plastic rod object with diameter of 25 mm at different positions; reconstructed image samples using 1000 kHz as the injection frequency.

Real samples taken in minutes	Water temperature	Plastic rod 25 mm real location 	Plastic rod 25 mm real location 
1	23.9°C	Conductivity 	Conductivity 
5	23.9°C	Conductivity 	Conductivity 

10	23.9°C		21.8°C	
20	23.7°C		21.9°C	
30	23.5°C		21.7°C	
40	22.8°C		21.2°C	

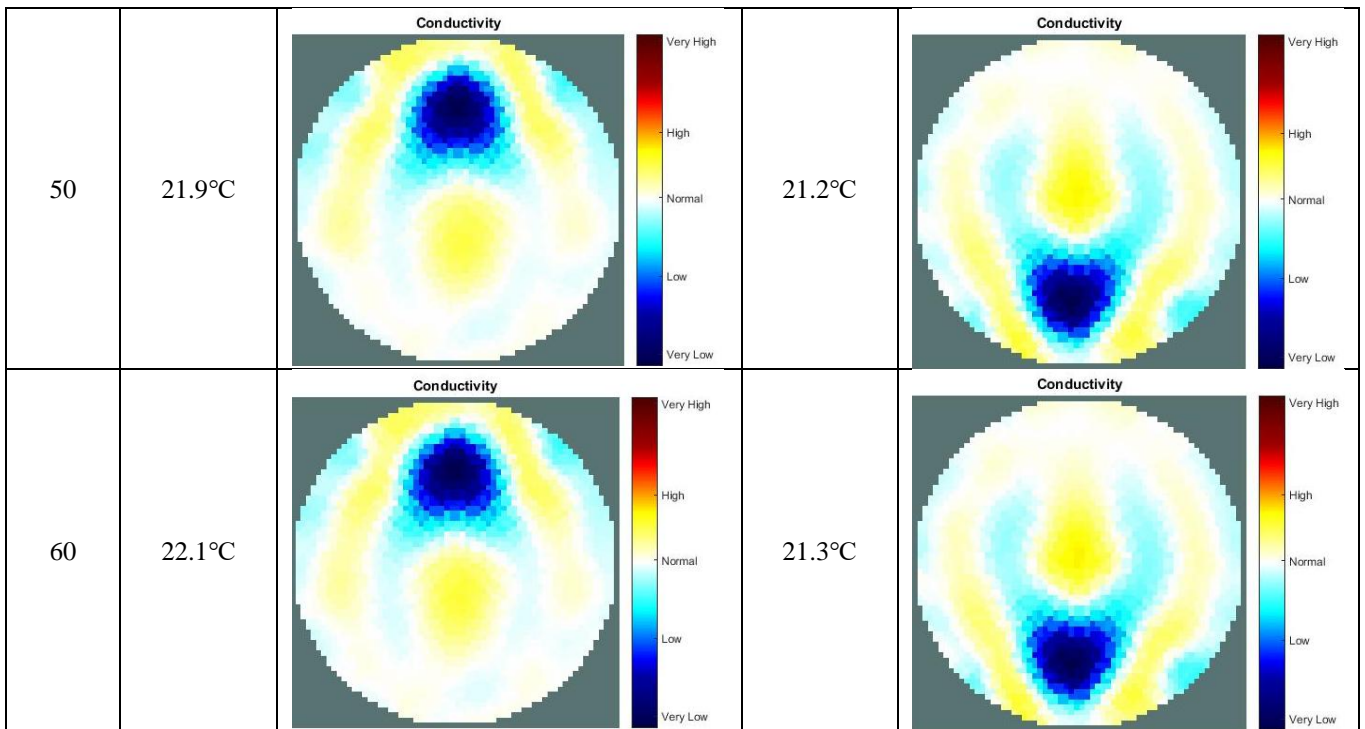


Figure 7.4 to Figure 7.6 shows the reconstructed image results of three different object diameter which they were placed around electrode 11, 12, 13, and 14 (left side) using an injection frequency of 1Mhz using testing beaker with a diameter of 180 mm. Figure 7.4 to Figure 7.6, V stands for variance, and SD stands for standard deviation. Figure 7.4 1A(V) and 2A(V) show the results using variance measurements to reconstruct the electrical non-conductive object with a diameter of 14 mm. As shown in Figure 7.4, 2A(V) 14 mm object located and the nearest border from the left side form the reconstructed image approximately 23.70 mm and from right side approximately 142.21 mm. The observed object diameter approximately 28.44 mm with a difference in diameter of 14.44 mm with a percentage change of 50.77%. However, Figure 7.4 1B(SD) and 2B(SD) show the results using standard deviation measurements to reconstruct the electrical non-conductive object with a diameter of 14 mm. As shown in Figure 7.4, 2B(SD) 14 mm object located and the nearest boundary from the left side form the reconstructed image approximately 28.10 mm and from the right side around 137.38 mm. The observed object diameter approximately 30.62 mm with a difference in diameter of 16.62 mm with a percentage change of 54.28%. The results concluded that the reconstructed image using variance measurements more accurate than the one using standard deviation measurements.

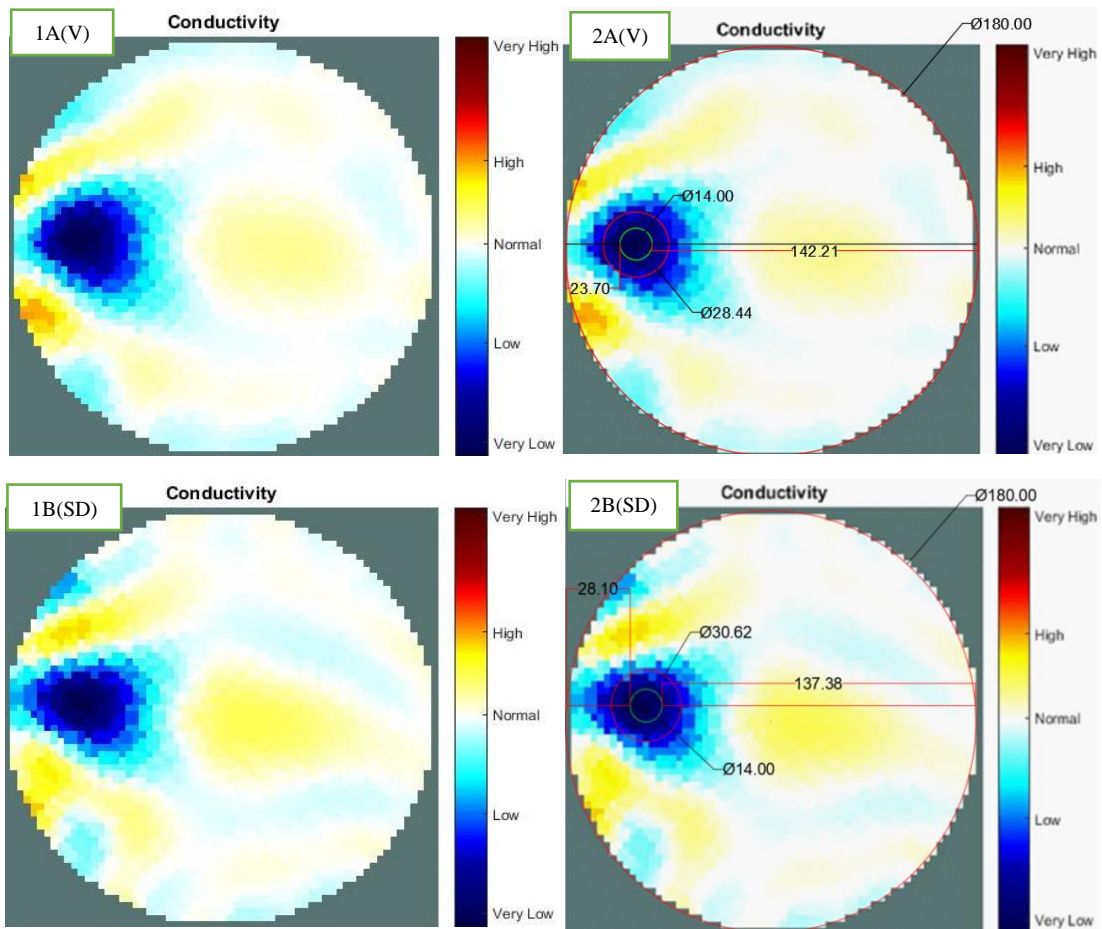


Figure 7.4: The reconstructed images of the electrically non-conductive object with a diameter of 14 mm using two types of measurement results.

Figure 7.5 1C(V) and 2C(V) show the results using variance measurements to reconstruct the electrically non-conductive object with a diameter of 25 mm. As shown in Figure 7.5, 2C(V) 25 mm object located and the nearest border from the left side form the reconstructed image approximately 19.40 mm and from right side approximately 135.11 mm. The observed object diameter approximately 30.00 mm with a difference in diameter of 5 mm with a percentage change of 16.67%. However, Figure 7.5 1D(SD) and 2D(SD) show the results using standard deviation measurements to reconstruct the electrical non-conductive object with a diameter of 25 mm. As shown in Figure 7.5, 2D(SD) 25 mm object located and the nearest boundary from the left side form the reconstructed image approximately 24.11 mm and from the right side around 130.51 mm. The observed object diameter approximately 35.59 mm with a difference in diameter of 10.59 mm with a percentage change of 29.76%. The results show that the reconstructed image using variance measurements more accurate than the one using standard deviation measurements.

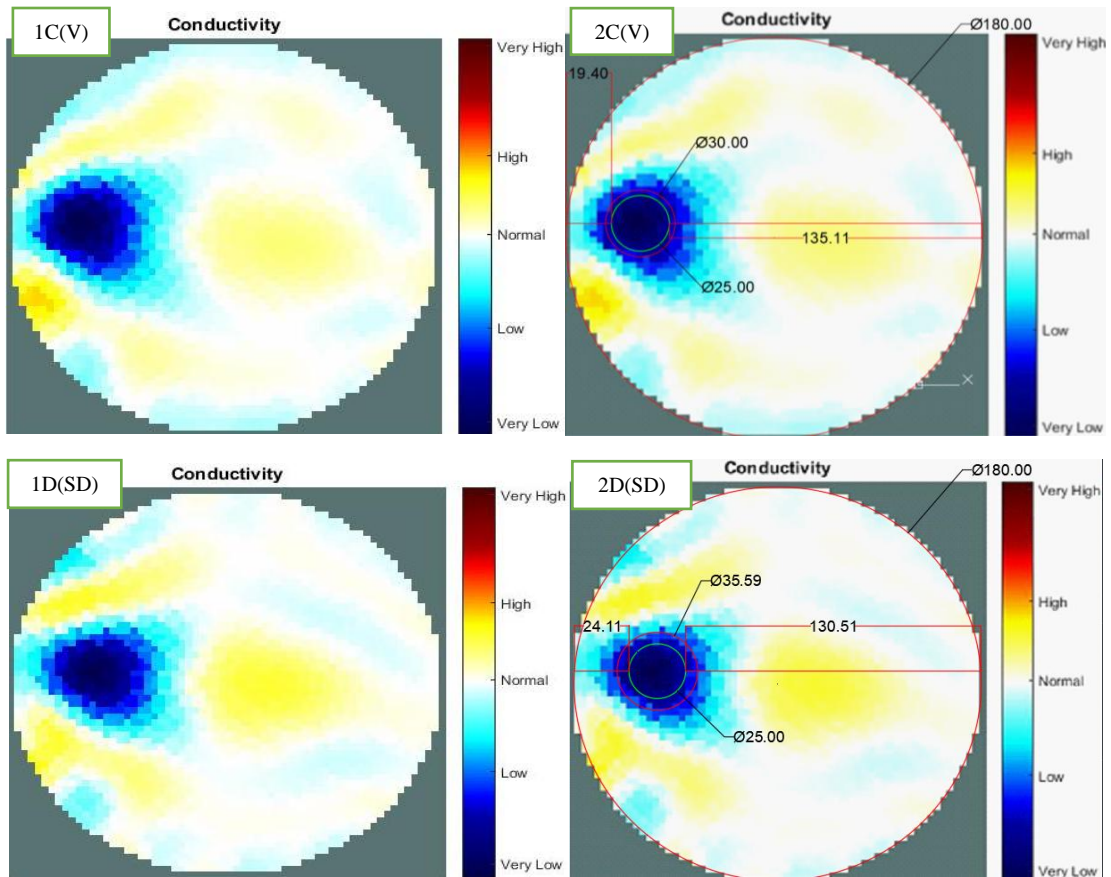


Figure 7.5: The reconstructed images of the electrically non-conductive object with a diameter of 25 mm using two types of measurement results.

Figure 7.6 1E(V) and 2E(V) show the results using variance measurements to reconstruct the electrically non-conductive object with a diameter of 50 mm. As shown in Figure 7.6, 2E(V) 50 mm object located and the nearest border from the left side form the reconstructed image approximately 13.53 mm and from right side approximately 116.36 mm. The observed object diameter approximately 41.57 mm with a difference in diameter of 8.43 mm with a percentage change of 16.86%. However, Figure 7.6 1F(SD) and 2F(SD) show the results using standard deviation measurements to reconstruct the electrical non-conductive object with a diameter of 50 mm. As shown in Figure 7.6, 2F(SD) 50 mm object located and the nearest boundary from the left side form the reconstructed image approximately 20.25 mm and from the right side around 109.55 mm. The observed object diameter approximately 43.79 mm with a difference in diameter of 6.21 mm with a percentage change of 12.42%. The results show that the reconstructed image using standard deviation measurements more accurate than the one using variance measurements.

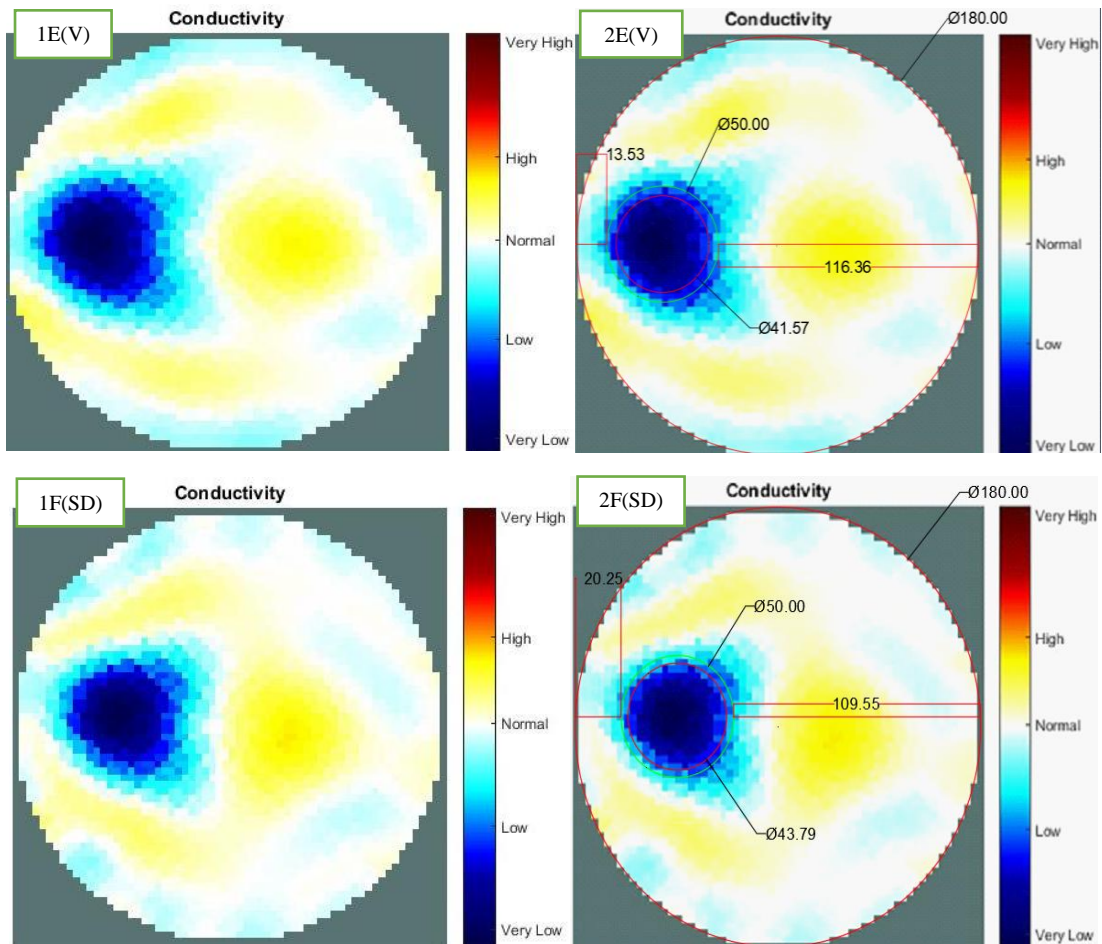


Figure 7.6: The reconstructed images of the electrically non-conductive object with a diameter of 5 mm using two types of measurement results.

Figure 7.4 to Figure 7.6 shows that the electrically non-conductive objects with diameters of 14 and 25 mm based on the reconstructed image that using the variance measurements more accurate than the one using standard deviation measurements. But when using the 50 mm object in diameter, the standard deviation measurements more accurate than the one using variance measurements.

Figure 7.7 to Figure 7.19 using testing tank with diameters of 134 mm. Figure 7.7 shows the reconstructed images of the electrically non-conductive object shape, made of Styrofoam (circle shape). The reconstructed image shows the estimated object shape which is not accurate circle shape that because of the background noise levels were high, particularly on the left side of the imaged area, as seen in the red spot.

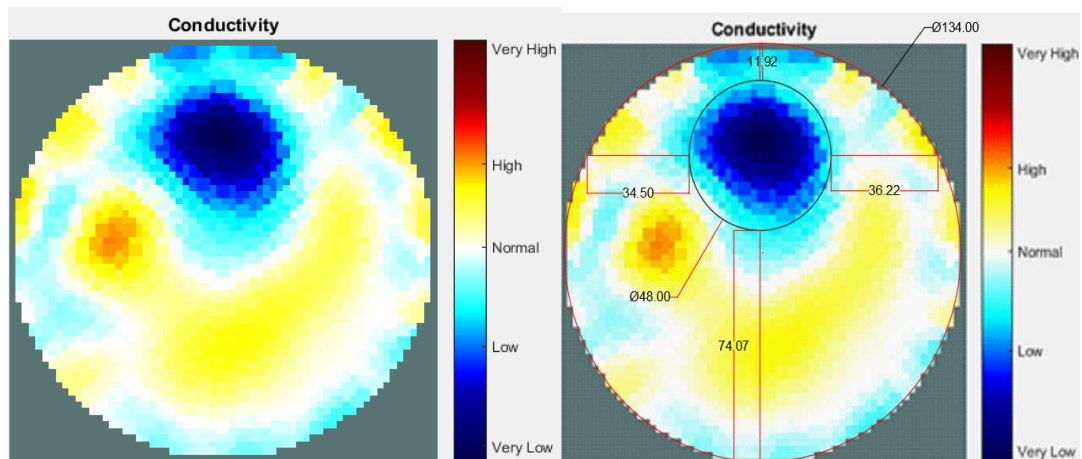


Figure 7.7: The reconstructed image of the electrically non-conductive object shape, made of Styrofoam (circle shape).

Figure 7.8 shows the reconstructed image of the electrically non-conductive object shape, made of Styrofoam large rectangular shape. The target object detected and imaged as a rectangular shape with defects, although background noise was present.

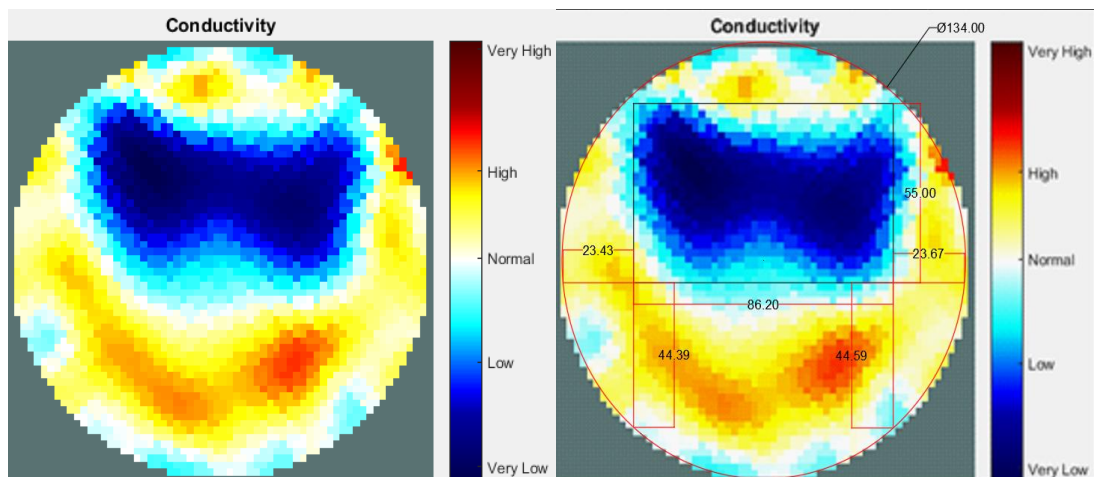


Figure 7.8: The reconstructed image of the electrically non-conductive object shape, made of Styrofoam (large rectangular shape).

Figure 7.9 shows the reconstructed image of the electrically non-conductive object shape, made of Styrofoam rectangular shape as well, but with a smaller diameter size than the previous object. The small rectangular object was detected and imaged, but with a defect.

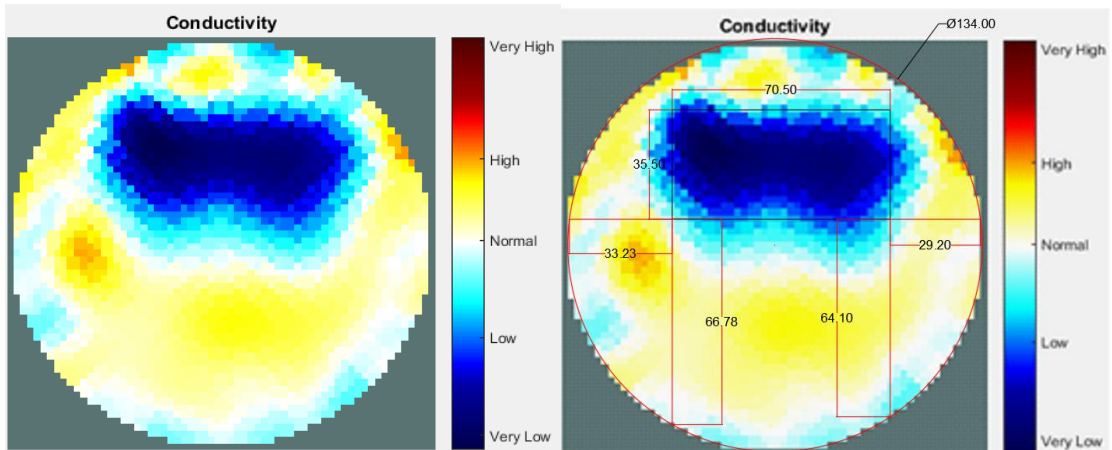


Figure 7.9: The reconstructed image of the electrically non-conductive object shape, made of Styrofoam (small rectangular shape).

Figure 7.10 shows the reconstructed image of the electrically non-conductive object shape, made of Styrofoam large triangle shape was reconstructed with a low amount of background noise.

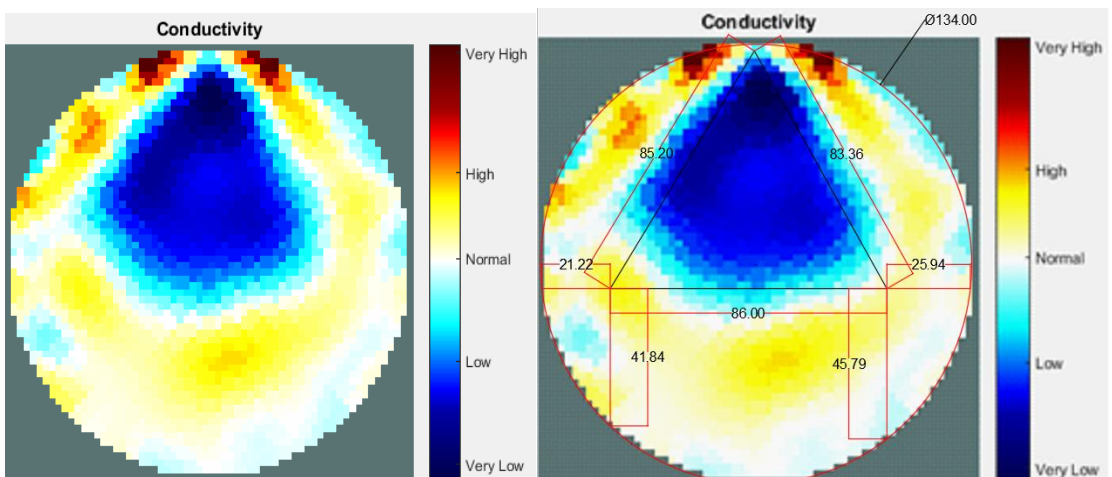


Figure 7.10: The reconstructed image of the electrically non-conductive object shape, made of Styrofoam (large triangle shape).

Figure 7.11 shows the reconstructed image of the electrically non-conductive object shape, made of Styrofoam triangle shape as well, but with a smaller diameter size than the previous object. The small triangle object was detected and imaged, but with a defect.

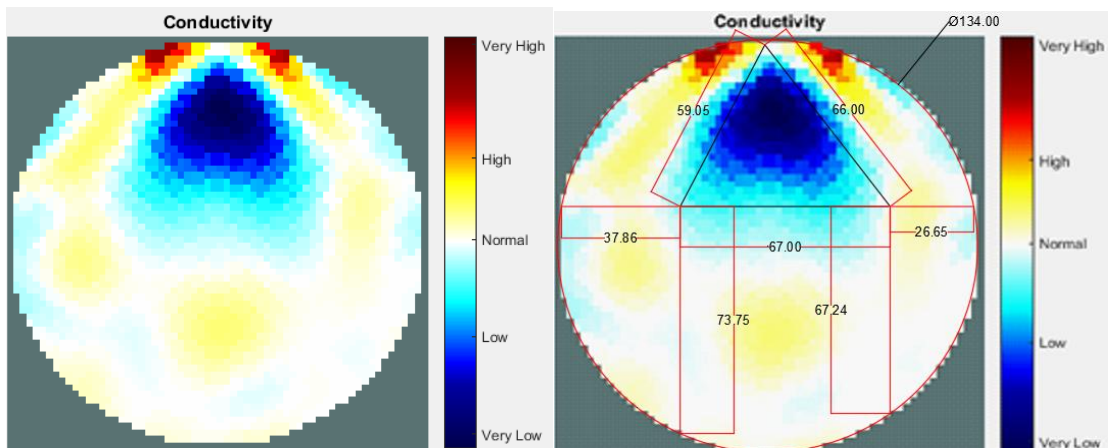


Figure 7.11: The reconstructed image of the electrically non-conductive object shape, made of Styrofoam (small triangle shape).

Figure 7.12 shows the reconstructed image of the electrically non-conductive object shape, made of Styrofoam L-shaped. As observed, the structural details of the reconstructed object image are poor, particularly the object side towards the centre of the testing tank.

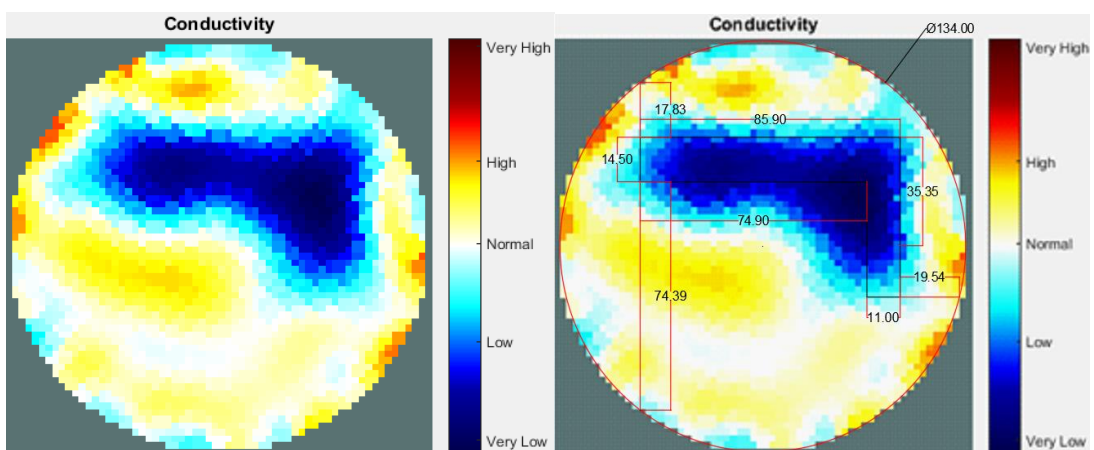


Figure 7.12: The reconstructed image of the electrically non-conductive object shape, made of Styrofoam (L shape shape).

Figure 7.13 shows the reconstructed image of the electrically non-conductive object shape, made of Styrofoam C-shaped imaged with defects. As observed, the structural details of the reconstructed object image not sharp.

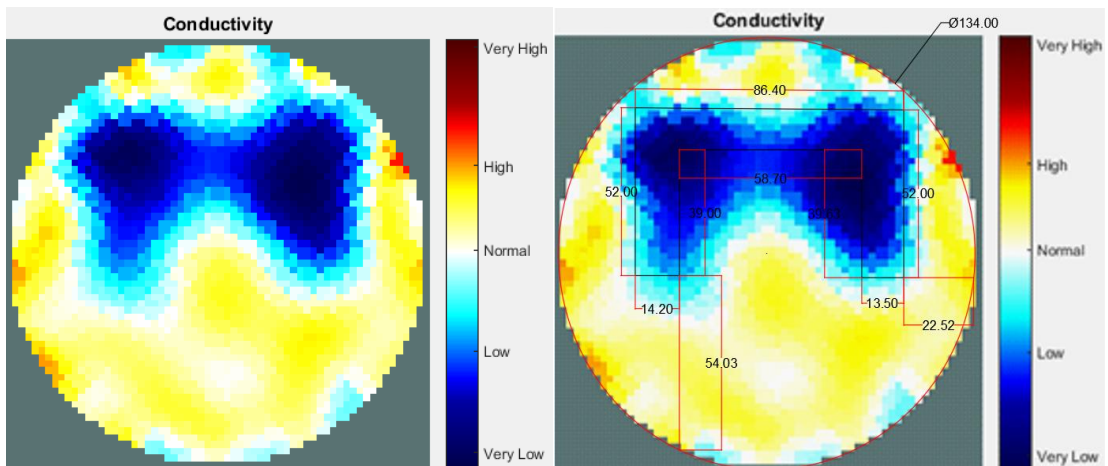


Figure 7.13: The reconstructed image of the electrically non-conductive object shape, made of Styrofoam (C shape shape).

Figure 7.14 shows the reconstructed image of the electrically non-conductive object shape, made of Styrofoam E-shaped imaged with defects. As observed, the structural details of the reconstructed object image not clear with a high number of defects.

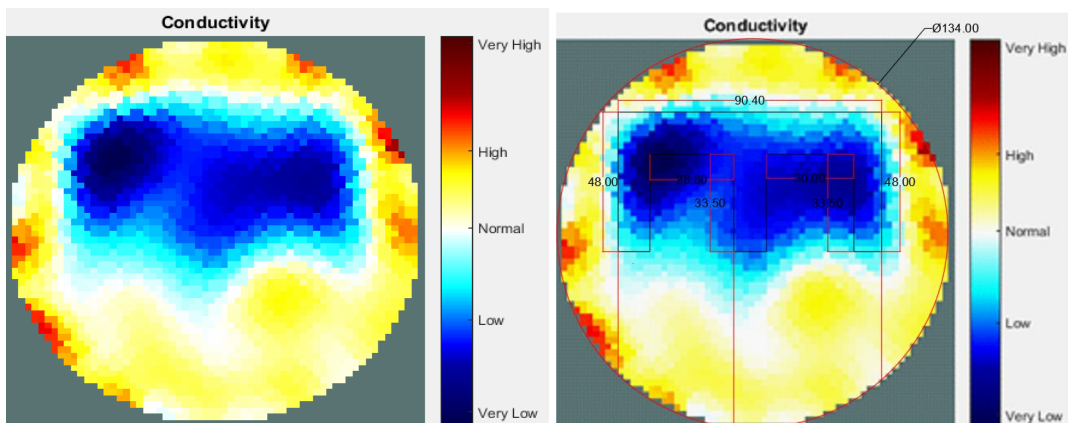


Figure 7.14: The reconstructed images of the electrically non-conductive object shape, made of Styrofoam (E shape shape).

Figure 7.7 to Figure 7.14 shows different reconstructed images of the electrically non-conductive object's shape, made of Styrofoam with actual objects shape dimension. As observed, the structural details of the images of the reconstructed objects vary. For simple objects shape, targeted object shapes identified, but low defect but with complex object shapes barely identified with a high number of a defect.

Figure 7.15 shows the reconstructed image of the smallest electrically conductive object with a diameter of 1.5 mm. As displayed object located and the nearest border from the north side form the reconstructed image approximately 95.11 mm and from the south side approximately 37.18 mm. The observed object diameter approximately

24.68 mm with a difference in diameter of 23.18 mm with a percentage change of 93.92%.

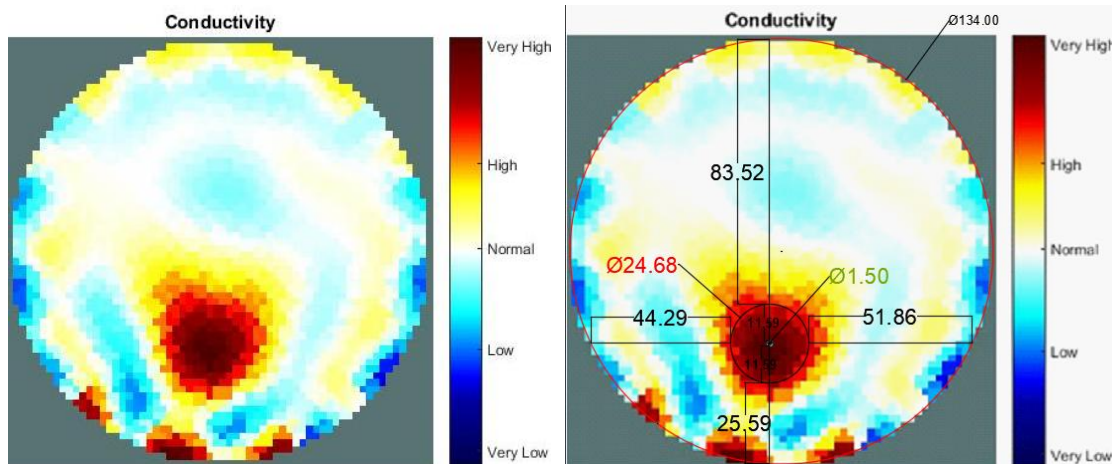


Figure 7.15: The reconstructed image of the electrically conductive object with a diameter of 1.5 mm.

Figure 7.16 shows the reconstructed image of the smallest electrically non-conductive object with a diameter of 2 mm. As displayed object located and the nearest border from the north side form the reconstructed image approximately 24.46 mm and from the south side about 107.29 mm. The observed object diameter approximately 19.45 mm with a difference in diameter of 17.45 mm with a percentage change of 89.72%.

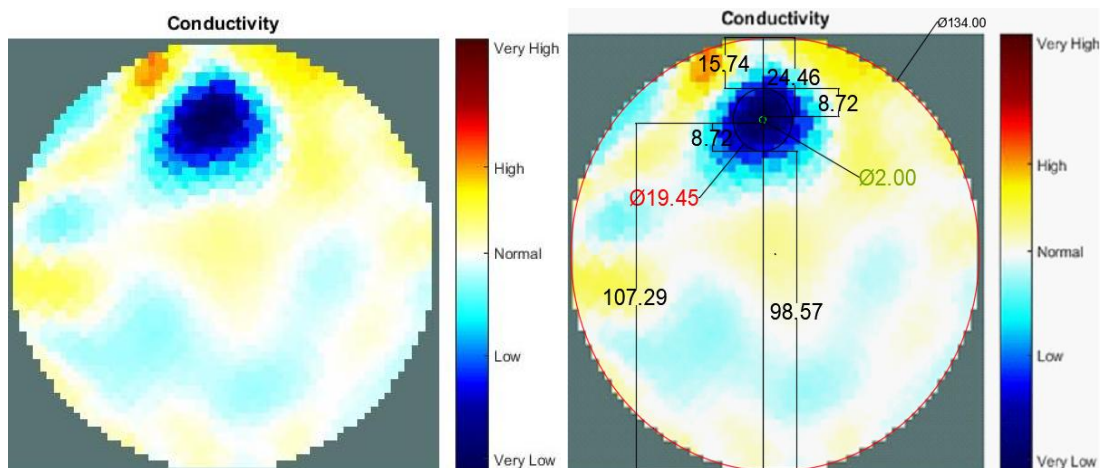


Figure 7.16: The reconstructed images of the electrically non-conductive object with a diameter of 2 mm.

Figure 7.17, Figure 7.18, and Figure 7.19 show the reconstructed image of detection bubbles of gas in the tap water test. Since the air bubble flow is unsteady, three reconstructed images samples were obtained and presented. The bubbles of gas are

electrically non-conductive medium pumped around electrodes 15, 16, 1, and 2, which observed by the reconstructed images. All the three reconstructed images sample gas bubble has been highlighted. The air bubbles appeared to shift into the testing tank wall regions.

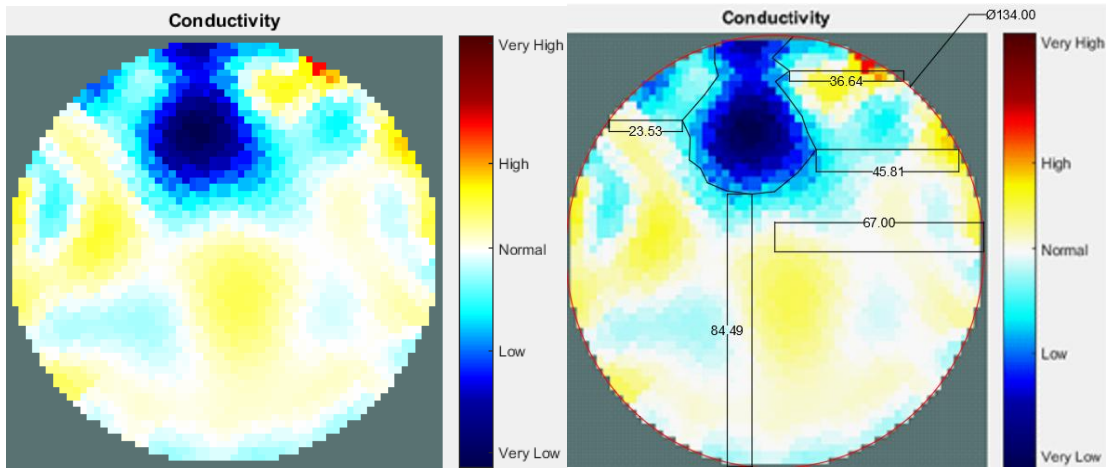


Figure 7.17: The reconstructed image of the gas bubble during gas has been pumped around electrodes 15, 16, 1, and 2 (Sample 1).

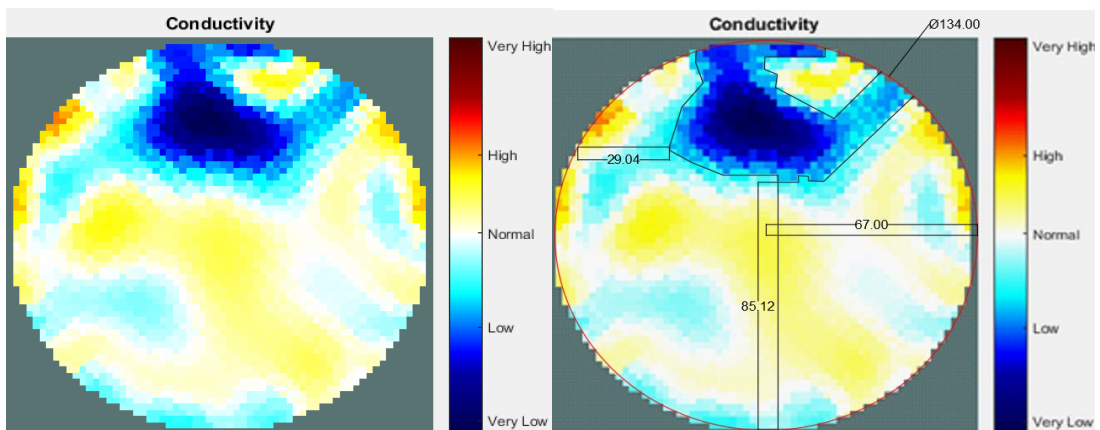


Figure 7.18: The reconstructed image of the gas bubble during gas has been pumped around electrodes 15, 16, 1, and 2 (Sample 2).

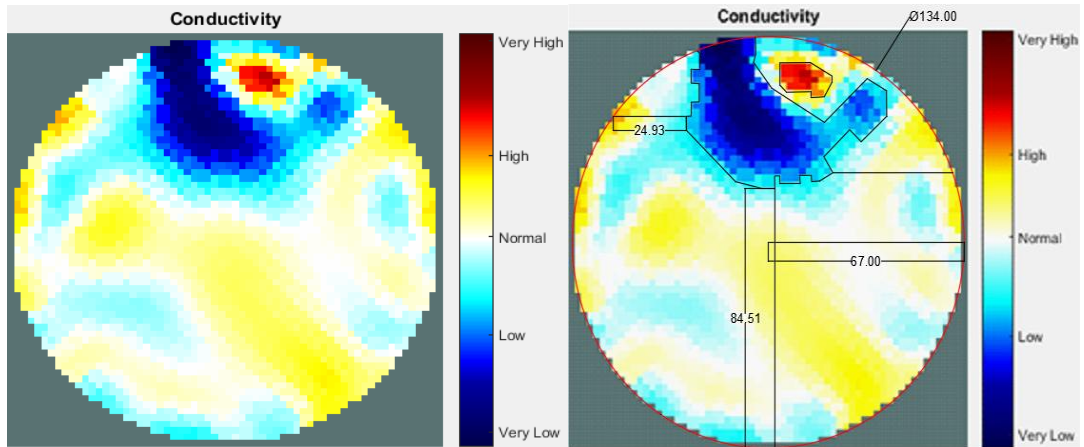


Figure 7.19: The reconstructed image of the gas bubble during gas has been pumped around electrodes 15, 16, 1, and 2 (Sample 3).

The chicken fat and skin which soaked in salty water have higher electrical conductivity than chicken breast chunks, which discussed in this chapter. The chicken fat and skin placed on the left side, as showed in Figure 7.20 (left side image). The nearest edge in the actual testing tank with a diameter of 134 mm for fat and skin tissue from the top view right side (left side image) is approximately 83.82 mm and in the reconstructed image (right side image) approximately 74.21 mm with different of about 9.61 mm. As showed the left side of the top view of the testing tank, the border of fat and skin has been highlighted, and even the reconstructed image conductivity change has been detected on the same side and highlighted.

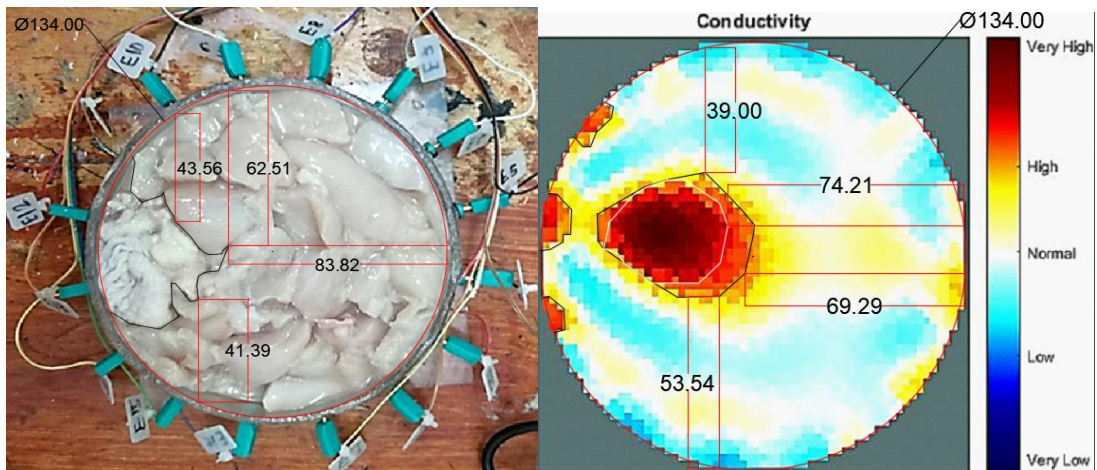


Figure 7.20: Left side Chicken skin and fat location in the tank filled with raw chicken breast chunks. Right side image reconstructed of the chicken skin and fat.

7.3 Conclusion

A multifunctioning SEEIT system was implemented to overcome some of the drawbacks of the conventional EIT system, including flexibility and durability. Three cylindrical testing tanks were used with three different 16-electrode arrays. The results observed show that the SEEIT system can detect and track a hidden stainless-steel rod object with a diameter as small as 1.5 mm that is placed in the testing tank. In addition, the SEEIT system shows good accuracy in locating and imaging cross-section objects with simple object shapes. Moreover, the results show the ability of the system to detect and track conductive and non-conductive materials, such as a plastic rod, gas, meat tissue, and a stainless-steel rod. This was true even when an object was submerged in different substances, such as water, muddy water, and chicken tissue. This shows that the system can be adapted for different EIT applications. However, most of the reconstructed images had background noise, although this does not affect the object detection and tracking. A stability test was carried out to continuously evaluate the SEEIT system and its ability to detect and image objects for one hour.

Chapter 8 Conclusion and Future Work

8.1 Conclusion

EIT is an imaging technique that analyses the electrical potential distribution within a medium of voltage or current measurements conducted through a series of electrodes. This Ph.D. research aims to design a novel EIT system that improves various features of the current EIT systems in terms of both hardware and software for visualising hidden objects, which can be used in different applications. This investigation involves the design, development, implementation, and experimental tests of EIT systems' hardware and software. A novel prototype EIT system, which uses single-ended signalling, has been developed. The SEEIT system has evolved through the use of several resistor circuit networks, which help to stabilise the system for use in a real testing tank or pipe. The ability of the system to detect and track hidden electrically conductive and non-conductive objects was examined using three cylindrical tanks with 16 electrodes attached. Stainless steel and Teflon rods of different sizes placed in different locations inside the container or beaker, and images obtained. All the objects tested under multiple signal injection frequencies in the range of 12–1000 kHz. The results demonstrated that the system can detect and track conductive and non-conductive objects with specific injection frequencies. The single-ended EIT system requires one wire connection to make one signal injection or measurement, and this is controlled using switching box. Alternatively, an ordinary EIT system requires additional wire connections for a single data measurement or injection, and a more complex circuit to control the I/O signals. This higher number of wires and increased circuit complexity will increase the data error rate and the cost significantly. The design of the novel EIT measurement technique has been shown to reduce the EIT system's complexity considerably since it uses only one electrode to measure electrical signals (receiver), with a total of 15 measurements per 2D image. This accomplished by measuring the voltage signal of one stationary electrode (unlike the other measurement methods, which require more than one electrode). This measurement technique approach has the potential of reducing the number of data errors since a lower number of measurements is required per 2D image. Several experiments evaluated the ability of the SEEIT system to detect, locate, and reshape electrically conductive and non-conductive materials. The results of the study indicate that the developed system can

detect and locate an electrically conductive object with a diameter as small as 1.5 mm. Moreover, the results demonstrate the ability of the current system to reconstruct an image of several non-conductive object shapes. The programmable LabVIEW code has improved the SEEIT system's flexibility and the system's ability to adapt the EIT system for different applications without the need to implement a new EIT system. The titanium alloy electrode was used to enhance the EIT system's durability. In this study, only two types of electrode materials used, titanium and copper. Several experiments were conducted to mimic some of the industrial applications, which show good responses to detected conductivity change. The main significant development in terms of the complexity reduction of the EIT system was the use of single-ended electrodes instead of double-ended conductors for sensing purposes. This provides more straightforward computation and faster data acquisition. EIDORS was used for all the experiments to reconstruct the 2D image based on the processed data received from LabVIEW.

Additionally, the developed SEEIT system has been subjected to a stability test, which shows reliable continuous results for one hour. An effective electrode reduction method has been presented to reduce the number of electrodes (sensors) by 50%, which helps to reduce the EIT system's interface limitation. This study primarily focuses on the development of unique EIT system aspects in hardware and software implementation.

8.2 Future work

Numerous problems need to be resolved to improve the EIT system, which should be considered for future work, including:

- Improving the electrode array arrangement and designing more precision data measurements. For instance, additional electrode measurements will improve the accuracy of object tracking and image resolution.
- Develop an image reconstruction algorithm for the developed measurement strategy method.
- Develop a new image reconstruction algorithm for the current SEEIT system.
- Increase the speed of EIT systems by employing a new high-speed relay.

- Increase the number of analog to digital converter ADCs since, at present, only one ADC 18bit is used. More ADCs will make the system much faster but more expensive to implement.
- Design a flexible electrode array that can be attached to a different testing media.
- Safety verification of the finalized SEEIT system.
- Employ a wireless connection between the DAQ and the electrodes for distance monitoring.

Bibliography

- 1]. Abdul Wahab, Y. et al. (2015) 'Non-invasive process tomography in chemical mixtures - A review', *Sensors and Actuators, B: Chemical*. Elsevier B.V., 210, pp. 602–617. doi: 10.1016/j.snb.2014.12.103.
- 2]. Abubucker, S. et al. (2012) 'Metabolic Reconstruction for Metagenomic Data and Its Application to the Human Microbiome', *PLoS Computational Biology*, p. e1002358. doi: 10.1371/journal.pcbi.1002358.
- 3]. Adler, A. and Lionheart, W. R. B. (2006) 'Uses and abuses of EIDORS: an extensible software base for EIT.', *Physiological measurement*, 27(5), pp. S25-42. doi: 10.1088/0967-3334/27/5/S03.
- 4]. Adler, A., Gaggero, P. O. and Maimaitijiang, Y. (2011) 'Adjacent stimulation and measurement patterns considered harmful', *Physiological Measurement*, 32(7), pp. 731–744. doi: 10.1088/0967-3334/32/7/S01.
- 5]. Aguiar Santos, S. et al. (2016) 'System Description and First Application of an FPGA-Based Simultaneous Multi-Frequency Electrical Impedance Tomography', *Sensors*, 16(8), p. 1158. doi: 10.3390/s16081158.
- 6]. Alberti, G. S. et al. (2016) 'The Linearized Inverse Problem in Multifrequency Electrical Impedance Tomography', *SIAM Journal on Imaging Sciences*, 9(4), pp. 1525–1551. doi: 10.1137/16M1061564.
- 7]. Almuhammadi, K. et al. (2015) 'Laser-based surface preparation of composite laminates leads to improved electrodes for electrical measurements', *Applied Surface Science*. Elsevier B.V., 359, pp. 388–397. doi: 10.1016/j.apsusc.2015.10.086.
- 8]. Ambrisko, T. D. et al. (2015) 'Assessment of distribution of ventilation by electrical impedance tomography in standing horses', *Physiological Measurement*, 37(2), pp. 175–186. doi: 10.1088/0967-3334/37/2/175.
- 9]. Ammari, H. et al. (2015) 'A mathematical and numerical framework for ultrasonically-induced lorentz force electrical impedance tomography', *Journal des Mathematiques Pures et Appliquees*. Elsevier Masson SAS, 103(6), pp. 1390–1409. doi: 10.1016/j.matpur.2014.11.003.
- 10]. Ammari, H. et al. (2017) 'Admittivity imaging from multi-frequency micro-electrical impedance tomography', *Journal of Mathematical Analysis and Applications*. Elsevier Inc., 449(2), pp. 1601–1618. doi: 10.1016/j.jmaa.2017.01.004.
- 11]. Anand, S. et al. (2015) 'Development of a Microcontroller based Electrical Impedance Tomography System', *IEEE Long Island Systems, Applications and Technology*, pp. 1–4.
- 12]. Angira, M. and Rangra, K. J. (2016) 'A novel design for low insertion loss, multi-band RF-MEMS switch with low pull-in voltage', *Engineering Science and Technology, an International Journal*. Elsevier B.V., 19(1), pp. 171–177. doi: 10.1016/j.jestch.2015.07.001.
- 13]. Ann, H. J., Su-shi, L. S. and Zakaria, Z. (2017) 'Non-invasive Breast Cancer Assessment Using Magnetic Induction Spectroscopy Technique', *Sensor & Its Application-Series 2*, 9(2), pp. 54–60.
- 14]. Antink, C. H. and Pikkemaat, R. (2015) 'A shape-based quality evaluation and reconstruction method for electrical impedance tomography', *Physiological Measurement*, 1161, p. 1161. doi: 10.1088/0967-3334/36/6/1161.

- 15]. Aristovich, K. Y. et al. (2016) 'Imaging fast electrical activity in the brain with electrical impedance tomography', *NeuroImage*. The Authors, 124, pp. 204–213. doi: 10.1016/j.neuroimage.2015.08.071.
- 16]. Arrayás, M., Bouwmeester, D. and Trueba, J. L. (2017) 'Knots in electromagnetism', *Physics Reports*. Elsevier B.V., 667, pp. 1–61. doi: 10.1016/j.physrep.2016.11.001.
- 17]. Avery, J. et al. (2017) 'A versatile and reproducible multi-frequency electrical impedance tomography system', *Sensors (Switzerland)*, 17(2). doi: 10.3390/s17020280.
- 18]. Babaeizadeh, S. et al. (2006) 'Electrode boundary conditions and experimental validation for BEM-Based EIT forward and inverse solutions', *IEEE Transactions on Medical Imaging*, 25(9), pp. 1180–1188. doi: 10.1109/TMI.2006.879957.
- 19]. Bagshaw, A. P. et al. (2003) 'Electrical impedance tomography of human brain function using reconstruction algorithms based on the finite element method', *NeuroImage*, 20(2), pp. 752–764. doi: 10.1016/S1053-8119(03)00301-X.
- 20]. Banasiak, R. et al. (2014) 'Study on two-phase flow regime visualization and identification using 3D electrical capacitance tomography and fuzzy-logic classification', *International Journal of Multiphase Flow*. Elsevier Ltd, 58, pp. 1–14. doi: 10.1016/j.ijmultiphaseflow.2013.07.003.
- 21]. Banavasi, S. C. (2015) 'Application of Virtual Instrumentation for Measuring Electrical Parameters in a Power Engineering Laboratory', *International journal of engineering studies and technical approach*, 01(3).
- 22]. Bas, E. et al. (2016) 'Electrode array-eluted dexamethasone protects against electrode insertion trauma induced hearing and hair cell losses, damage to neural elements, increases in impedance and fibrosis: A dose response study', *Hearing Research*. Elsevier B.V, 337, pp. 12–24. doi: 10.1016/j.heares.2016.02.003.
- 23]. Bayford, R. H. et al. (2001) 'Solving the forward problem in electrical impedance tomography for the human head using IDEAS (integrated design engineering analysis software), a finite element modelling tool', *Physiol. Meas.*, 22, pp. 55–64.
- 24]. Beck, M. S. and Williams, R. A. (1996) 'Process tomography: A European innovation and its applications', *Measurement Science and Technology*, 7(3), pp. 215–224. doi: 10.1088/0957-0233/7/3/002.
- 25]. Beff, L. et al. (2013) 'Three-dimensional monitoring of soil water content in a maize field using Electrical Resistivity Tomography', *Hydrology and Earth System Sciences*, 17(2), pp. 595–609. doi: 10.5194/hess-17-595-2013.
- 26]. Bera, T. K. (2018) 'Applications of Electrical Impedance Tomography (EIT): A Short Review', *IOP Conference Series: Materials Science and Engineering*, 331(April), p. 012004. doi: 10.1088/1757-899X/331/1/012004.
- 27]. Bera, T. K. and Nagaraju, J (2011) 'A LabVIEW Based Electrical Impedance Tomography (EIT) System for Radiation Free Medical Imaging', *National Instruments Graphical System Design Achievement Awards 2011*, (January 2011), pp. 1–6.
- 28]. Bera, T. K. and Nagaraju, J. (2011) 'A chicken tissue phantom for studying an electrical impedance tomography (EIT) system suitable for clinical imaging', *Sensing and Imaging*, 12(3–4), pp. 95–116. doi: 10.1007/s11220-011-0063-4.

- 29]. Bera, T. K. and Nagaraju, J. (2013) 'A MATLAB-Based Boundary Data Simulator for Studying the Resistivity Reconstruction Using Neighbouring Current Pattern', *Journal of Medical Engineering*, 2013, pp. 1–15. doi: 10.1155/2013/193578.
- 30]. Bera, T. K., Nagaraju, J. and Lubineau, G. (2016) 'Electrical impedance spectroscopy (EIS)-based evaluation of biological tissue phantoms to study multifrequency electrical impedance tomography (Mf-EIT) systems', *Journal of Visualization*. Springer Berlin Heidelberg, 19(4), pp. 1–23. doi: 10.1007/s12650-016-0351-0.
- 31]. Bickenbach, J. et al. (2017) 'Electrical impedance tomography for predicting failure of spontaneous breathing trials in patients with prolonged weaning', *Critical Care*. *Critical Care*, 21(1), pp. 1–8. doi: 10.1186/s13054-017-1758-2.
- 32]. Blankman, P. et al. (2014) 'Detection of "best" positive end-expiratory pressure derived from electrical impedance tomography parameters during a decremental positive end-expiratory pressure trial.', *Critical care (London, England)*, 18(3), p. R95. doi: 10.1186/cc13866.
- 33]. Bläser, D. et al. (2014) 'Unilateral empyema impacts the assessment of regional lung ventilation by electrical impedance tomography.', *Physiological measurement*, 35(6), pp. 975–83. doi: 10.1088/0967-3334/35/6/975.
- 34]. Botaya, L. et al. (2016) 'Visualized Multiprobe Electrical Impedance Measurements with STM Tips Using Shear Force Feedback Control', *Sensors*, 16(6), p. 757. doi: 10.3390/s16060757.
- 35]. Bouchette, G. et al. (2014) 'Imaging of compact objects buried in underwater sediments using electrical impedance tomography', *IEEE Transactions on Geoscience and Remote Sensing*, 52(2), pp. 1407–1417. doi: 10.1109/TGRS.2013.2250982.
- 36]. Brown, B. H. (2009) 'Electrical impedance tomography (EIT): a review.', *Journal of medical engineering & technology*, 27(3), pp. 97–108. doi: 10.1080/0309190021000059687.
- 37]. Casal, L. and Mura, G. La (2016) 'Skin-electrode impedance measurement during ECG acquisition: method's validation', *Journal of Physics: Conference Series*, 705, p. 012006. doi: 10.1088/1742-6596/705/1/012006.
- 38]. Chabchoub, S., Mansouri, S. and Salah, R. Ben (2015) 'Biomedical monitoring system using LabVIEW FPGA', 2015 World Congress on Information Technology and Computer Applications, WCITCA 2015, pp. 3–7. doi: 10.1109/WCITCA.2015.7367020.
- 39]. Chady, T. et al. (2007) 'Identification of three-dimensional distribution of metal particles using electromagnetic tomography system', *Journal of Materials Processing Technology*, 181(1–3), pp. 177–181. doi: 10.1016/j.jmatprotec.2006.03.022.
- 40]. Chang, F.-K. (1997) *Structural Health Monitoring: Current Status and Perspectives*. Pennsylvania: Technomic Publishing Company.
- 41]. Chen (1990) *Reconstruction algorithms for electrical impedance tomography*, University of Wollongong Thesis Collection University.
- 42]. Chen, D., Yang, W. and Deng, X. (2010) 'Comparison of three electrical capacitance tomography systems', 2010 IEEE International Conference on Imaging Systems and Techniques, (1), pp. 57–62. doi: 10.1109/IST.2010.5548441.
- 43]. Chen, X. et al. (2014) 'Multi-channel electrical impedance tomography for regional tissue hydration monitoring', *Physiological Measurement*, 35(6), pp. 1137–1147. doi: 10.1088/0967-3334/35/6/1137.

- 44]. Cherepenin et al., "A 3D electrical impedance tomography (EIT) system for breast cancer detection.," *Physiol. Meas.*, vol. 22, no. 1, pp. 9–18, 2001.
- 45]. Chieh, J. et al. (2018) 'Eight-Channel AC Magnetosusceptometer of Magnetic Nanoparticles for High-Throughput and Ultra-High-Sensitivity Immunoassay', *Sensors (Basel, Switzerland)*. doi: 10.3390/s18041043.
- 46]. Choi, H. and Popovics, J. S. (2015) 'NDE application of ultrasonic tomography to a full-scale concrete structure', *IEEE Transactions on Ultrasonics, Ferroelectrics, and Frequency Control*, 62(6), pp. 1076–1085. doi: 10.1109/TUFFC.2014.006962.
- 47]. Chung, E., Chan, T. and Tai, X. (2005) 'Electrical impedance tomography using level set representation and total variational regularization', *Journal of Computational Physics*, 205(1), pp. 357–372. doi: 10.1016/j.jcp.2004.11.022.
- 48]. Cornelis, P. et al. (2018) 'A Novel Modular Device for Biological Impedance Measurements: The Differential Impedimetric Sensor Cell (DISC)', *Physica Status Solidi (A) Applications and Materials Science*, 1701029, pp. 1–8. doi: 10.1002/pssa.201701029.
- 49]. Crabb, M. G. (2017) 'Convergence study of 2D forward problem of electrical impedance tomography with high-order finite elements', *Inverse Problems in Science and Engineering*. Taylor & Francis, 25(10), pp. 1397–1422. doi: 10.1080/17415977.2016.1255739.
- 50]. Cui, Z., Wang, H. and Yin, W. (2015) 'Electrical Capacitance Tomography With Differential Sensor', *IEEE Sensors Journal*, 15(9), pp. 5087–5094.
- 51]. Dai, H. et al. (2016) 'A Novel Methodology for Spatial Damage Detection and Imaging Using a Distributed Carbon Nanotube-Based Composite Sensor Combined with Electrical Impedance Tomography', *Journal of Nondestructive Evaluation*. Springer US, 35(2), pp. 1–15. doi: 10.1007/s10921-016-0341-0.
- 52]. Darrer, B. J. et al. (2015) 'Toward an Automated Setup for Magnetic Induction Tomography', *IEEE TRANSACTIONS ON MAGNETICS*, 51(1), pp. 18–21.
- 53]. de Munck, J. C., Faes, T. J. and Heethaar, R. M. (2000) 'The boundary element method in the forward and inverse problem of electrical impedance tomography.', *IEEE transactions on biomedical engineering*, 47(6), pp. 792–800. doi: 10.1109/10.844230.
- 54]. Dekdouk, B. et al. (2016) 'Absolute Imaging of Low Conductivity Material Distributions Using Nonlinear Reconstruction Methods in Magnetic Induction Tomography', *Progress In Electromagnetics Research*, 155(December 2015), pp. 1–18.
- 55]. Deng, X. and Yang, W. (2012) 'Fusion Research of Electrical Tomography with Other Sensors for Two-phase Flow Measurement', *Measurement Science Review*, 12(2), pp. 62–67. doi: 10.2478/v10048-012-0008-7.
- 56]. Devakumari, D. and Punithavathi, V. (2018) 'Study of Breast Cancer Detection Methods using Image Processing with Data Mining Techniques', *International Journal of Pure and Applied Mathematics*, 118(18), pp. 2867–2873.
- 57]. Donthi, S. (2004) Capacitance based tomography for industrial applications, M. Tech. credit seminar report, *Electronic Systems* Available at: http://www.ee.iitb.ac.in/~esgroup/es_mtech04_sem/es_sem04_paper_04307905.pdf (Accessed: 27 January 2014).
- 58]. Dowrick, T., Blochet, C. and Holder, D. (2015) 'In vivo bioimpedance measurement of healthy and ischaemic rat brain: implications for stroke imaging using electrical impedance

- tomography', *Physiological Measurement*. IOP Publishing, 36(6), pp. 1273–1282. doi: 10.1088/0967-3334/36/6/1273.
- 59]. Dunlop, M. M. and Stuart, A. M. (2016) 'The bayesian formulation of eit: Analysis and algorithms', *Inverse Problems and Imaging*, 10(4), pp. 1007–1036. doi: 10.3934/ipi.2016030.
- 60]. Eyüboğlu, B. M. (1996) 'An interleaved drive electrical impedance tomography image reconstruction algorithm.', *Physiological measurement*, 17 Suppl 4, pp. A59-71. Available at: <http://www.ncbi.nlm.nih.gov/pubmed/9001603>.
- 61]. Fabrizi, L. et al. (2009) 'A comparison of two EIT systems suitable for imaging impedance changes in epilepsy.', *Physiological measurement*, 30(6), pp. S103–S120. doi: 10.1088/0967-3334/30/6/S07.
- 62]. Fan, W., Wang, H. and Cui, Z. (2015) 'Damage detection of CFRP composites using open electrical impedance tomography', *IEEE International Instrumentation and Measurement Technology Conference*.
- 63]. Ferrari, A. et al. (2017) 'Digital chest tomosynthesis: the 2017 updated review of an emerging application', *Annals of Translational Medicine*, 6(2), pp. 1–8. doi: 10.21037/atm.2017.08.18.
- 64]. Floroian, L. et al. (2015) 'Stainless steel surface biofunctionalization with PMMA-bioglass coatings: compositional, electrochemical corrosion studies and microbiological assay', *Journal of Materials Science: Materials in Medicine*, 26(6). doi: 10.1007/s10856-015-5527-y.
- 65]. Fouchard, a et al. (2014) 'Inversion without Explicit Jacobian Calculations in Electrical Impedance Tomography', *Journal of Physics: Conference Series*, 542, p. 012002. doi: 10.1088/1742-6596/542/1/012002.
- 66]. Frerichs, I. et al. (2016) 'Chest electrical impedance tomography examination, data analysis, terminology, clinical use and recommendations: Consensus statement of the TRanslational EIT developmeNt stuDy group', *British Medical Association*, 72(1), pp. 83–93. doi: 10.1136/thoraxjnl-2016-208357.
- 67]. Fu, F. et al. (2014) 'Use of Electrical Impedance Tomography to Monitor Regional Cerebral Edema during Clinical Dehydration Treatment', *PLoS ONE*, 9(12), p. e113202. doi: 10.1371/journal.pone.0113202.
- 68]. Fuks, L. F. et al. (1991) 'Detection and imaging of electric conductivity and permittivity at low frequency.', *IEEE transactions on bio-medical engineering*, 38(11), pp. 1106–10. doi: 10.1109/10.99074.
- 69]. Gaggero, P. O. et al. (2015) 'Automated robust test framework for electrical impedance tomography', *Physiological Measurement*. IOP Publishing, 36(6), pp. 1227–1244. doi: 10.1088/0967-3334/36/6/1227.
- 70]. Gallo, G. J. and Thostenson, E. T. (2016) 'Spatial damage detection in electrically anisotropic fiber-reinforced composites using carbon nanotube networks', *Composite Structures*. Elsevier Ltd, 141, pp. 14–23. doi: 10.1016/j.compstruct.2015.07.082.
- 71]. Garde, H. and Knudsen, K. (2016) 'Sparsity prior for electrical impedance tomography with partial data', *Inverse Problems in Science and Engineering*, 24(3), pp. 524–541. doi: 10.1080/17415977.2015.1047365.
- 72]. Gevers, M. et al. (2014) 'Code-Division-Multiplexing Using Orthogonal Codes for Fast Electrical Impedance Tomography', pp. 2–5.

- 73]. Ghanem, K. G. et al. (2017) 'A comparative study of near-surface velocity model building derived by 3D travelttime Tomography and Dispersion Curves Inversion techniques', *Journal of Petroleum Science and Engineering*. Elsevier B.V., 154(April), pp. 126–138. doi: 10.1016/j.petrol.2017.04.023.
- 74]. Ghonghadze, S. et al. (2015) 'Reinterpretation of Geophysical Data for the Study of Deep Structure of the Greater Caucasus', *Journal of Georgian Geophysical Society*, pp. 49–58.
- 75]. Gnecchi, J. A. G. et al. (2012) 'Soil water infiltration measurements using electrical impedance tomography', *Chemical Engineering Journal*. Elsevier B.V., 191, pp. 13–21. doi: 10.1016/j.cej.2010.03.023.
- 76]. Goharian, M. et al. (2008) 'A DSP based multi-frequency 3D electrical impedance tomography system', *Annals of Biomedical Engineering*, 36(9), pp. 1594–1603. doi: 10.1007/s10439-008-9537-5.
- 77]. Gong, B. et al. (2015) 'Improving EIT image reconstruction with clustering', *IFAC-PapersOnLine*. Elsevier B.V., 28(20), pp. 418–422. doi: 10.1016/j.ifacol.2015.10.176.
- 78]. Gordon, R., Bender, R. and Herman, G. T. (1970) 'Algebraic Reconstruction Techniques (ART) for three-dimensional electron microscopy and X-ray photography', *Journal of Theoretical Biology*, 29(3), pp. 471–481. doi: 10.1016/0022-5193(70)90109-8.
- 79]. Graf, M. and Riedel, T. (2017) 'Electrical impedance tomography: Amplitudes of cardiac related impedance changes in the lung are highly position dependent', *PLoS ONE*, 12(11), pp. 1–14. doi: 10.1371/journal.pone.0188313.
- 80]. Grychtol, B., Müller, B. and Adler, A. (2016) '3D EIT image reconstruction with GREIT', *Physiological Measurement*, 37(6), pp. 785–800. doi: 10.1088/0967-3334/37/6/785.
- 81]. Guarnieri, M. (2014) 'Once upon a time? The compass', *IEEE Industrial Electronics Magazine*, 8(2), pp. 60–63. doi: 10.1109/MIE.2014.2316044.
- 82]. Guermandi, M. et al. (2015) 'Active electrode IC for EEG and electrical impedance tomography with continuous monitoring of contact impedance', *IEEE Transactions on Biomedical Circuits and Systems*, 9(1), pp. 21–33. doi: 10.1109/TBCAS.2014.2311836.
- 83]. Gulrajani, R. M. (1998) 'The Forward and Inverse Problems of Electrocardiography', *IEEE Engineering in Medicine and Biology*, 17(5), pp. 84–122. doi: 10.1109/51.715491.
- 84]. Halter, R. J. et al. (2015) 'Real-time electrical impedance variations in women with and without breast cancer', *IEEE Transactions on Medical Imaging*, 34(1), pp. 38–48. doi: 10.1109/TMI.2014.2342719.
- 85]. Hamilton, S. J. et al. (2016) 'A Hybrid Segmentation and D-Bar Method for Electrical Impedance Tomography', *SIAM Journal on Imaging Sciences*, 9(2), pp. 770–793. doi: 10.1137/15M1025992.
- 86]. Hamilton, S. J., Mueller, J. L. and Alsaker, M. (2017) 'Incorporating a Spatial Prior into Nonlinear D-Bar EIT Imaging for Complex Admittivities', *IEEE Transactions on Medical Imaging*, 36(2), pp. 457–466. doi: 10.1109/TMI.2016.2613511.
- 87]. Harikumar, R., Prabu, R. and Raghavan, S. (2013) 'Electrical Impedance Tomography (EIT) and Its Medical Applications: A Review', *International Journal of Soft Computing and Engineering (IJSCE)*, 3(4), pp. 193–198.

- 88]. Harrach, B. and Ullrich, M. (2015) ‘Resolution Guarantees in Electrical Impedance Tomography’, *IEEE Transactions on Medical Imaging*, 34(7), pp. 1513–1521. doi: 10.1109/TMI.2015.2404133.
- 89]. Harrach, B. et al. (2009) ‘Detecting Inclusions in Electrical Impedance Tomography Without Reference Measurements Detecting Inclusions in Electrical Impedance Tomography Without Reference Measurements*’, *Source: SIAM Journal on Applied Mathematics SIAM J. Appl. Math*, 69(6), pp. 1662–1681. doi: 10.1137/08072142X.
- 90]. He, S., Wang, H. and Zhou, R. (2009) ‘A 3D Image Reconstruction Algorithm of Electrical Capacitance Tomography Based on Support Vector Machines’, *2009 2nd International Congress on Image and Signal Processing. Ieee*, pp. 1–4. doi: 10.1109/CISP.2009.5303658.
- 91]. He, T. et al. (2016) ‘Robust Monitor Placement for Network Tomography in Dynamic Networks’, *The 35th Annual IEEE International Conference on Computer Communications Robust*, (1).
- 92]. Hermann, M., Pentek, T. and Otto, B. (2016) ‘Design Principles for Industrie 4.0 Scenarios’, *49th Hawaii International Conference on System Sciences Design*. doi: 10.1109/HICSS.2016.488.
- 93]. Herterich, M. M., Uebernickel, F. and Brenner, W. (2015) ‘The Impact of Cyber-Physical Systems on Industrial Services in Manufacturing’, *Procedia CIRP. Elsevier B.V.*, 30, pp. 323–328. doi: 10.1016/j.procir.2015.02.110.
- 94]. Hilbich, C. et al. (2009) ‘Applicability of electrical resistivity tomography monitoring to coarse blocky and ice-rich permafrost landforms’, *Permafrost and Periglacial Processes*, 20(3), pp. 269–284. doi: 10.1002/ppp.652.
- 95]. Holder, D. S. (1992) ‘Electrical impedance tomography (EIT) of brain function.’, *Brain topography*, 5(2), pp. 87–93. Available at: <http://www.ncbi.nlm.nih.gov/pubmed/19491446>.
- 96]. Hong, S. et al. (2015) ‘A4.9 mΩ-Sensitivity Mobile Electrical Impedance Tomography IC for Early Breast-Cancer Detection System’, *IEEE Journal of Solid-State Circuits*, 50(1), pp. 245–257.
- 97]. Holder, E. D. et al. (2004) *Methods, History and Applications The Reconstruction Problem*.
- 98]. Huang, Z., Wang, B. and Li, H. (2003) ‘Application of electrical capacitance tomography to the void fraction measurement of two-phase flow’, *IEEE Transactions on Instrumentation and Measurement*, 52(1), pp. 7–12. doi: 10.1109/TIM.2003.809087.
- 99]. Hussain, K. M. et al. (2015) ‘Control and Interfacing of Motors With NI- LabView Using NI-MYRIO’, *International Journal for Innovative Research in Science & Technology*, 1(8), pp. 146–150.
- 100]. Hyvönen, N. and Leinonen, M. (2015) ‘Stochastic Galerkin Finite Element Method with Local Conductivity Basis for Electrical Impedance Tomography’, *SIAM/ASA Journal on Uncertainty Quantification*, 3(1), pp. 998–1019. doi: 10.1137/140999050.
- 101]. Isaacson, D. et al. (2006) ‘Imaging cardiac activity by the D-bar method for electrical impedance tomography’, *Physiological Measurement*, 27(5), pp. 43–50. doi: 10.1088/0967-3334/27/5/S04.
- 102]. Isaksen, Ø. (1996) ‘A review of reconstruction techniques for capacitance tomography’, *Measurement Science and Technology*, 7(3), pp. 325–337. doi: 10.1088/0957-0233/7/3/013.

- 103]. Ismail, I. et al. (2005) 'Tomography for multi-phase flow measurement in the oil industry', *Flow Measurement and Instrumentation*, 16(2–3), pp. 145–155. doi: 10.1016/j.flowmeasinst.2005.02.017.
- 104]. Jaakko, M. and Robert, P. (1995) *Bioelectromagnetism: Principles and Applications of Bioelectric and Biomagnetic Fields*. 1st edn. New York: Oxford University Press.
- 105]. Jamil, N. et al. (2017) 'Design and fabrication of microelectrodes for electrical impedance tomography of cell spheroids', *IECBES 2016 - IEEE-EMBS Conference on Biomedical Engineering and Sciences*, pp. 426–431. doi: 10.1109/IECBES.2016.7843486.
- 106]. Jehl, M. and Holder, D. (2016) 'Correction of electrode modelling errors in multi-frequency EIT imaging', *Physiological Measurement*. IOP Publishing, 37(6), pp. 893–903. doi: 10.1088/0967-3334/37/6/893.
- 107]. Jehl, M. et al. (2015) 'A Fast Parallel Solver for the Forward Problem in Electrical Impedance Tomography.', *IEEE transactions on bio-medical engineering*, PP(99), p. 1. doi: 10.1109/TBME.2014.2342280.
- 108]. Jehl, M., Avery, J., et al. (2015) 'Correcting electrode modelling errors in EIT on realistic 3D head models', *Physiological Measurement*. IOP Publishing, 36(12), pp. 2423–2442. doi: 10.1088/0967-3334/36/12/2423.
- 109]. Jin, L. et al. (2016) 'Highly precise nanofiber web-based dry electrodes for vital signal monitoring', *RSC Advances*, 6(46), pp. 40045–40057. doi: 10.1039/c6ra00079g.
- 110]. Johansen, G. A. and Wang, M. (2008) 'Industrial Process Tomography', *Measurement Science and Technology*, 19(9), p. 090101. doi: 10.1088/0957-0233/19/9/090101.
- 111]. Karsten, J. et al. (2016) 'Influence of different electrode belt positions on electrical impedance tomography imaging of regional ventilation: A prospective observational study', *Critical Care*. *Critical Care*, 20(1), p. 3. doi: 10.1186/s13054-015-1161-9.
- 112]. Karthik, K. et al. (2015) 'Tools Identification System with Audio Indication using OCR in LabVIEW', *International Journal for Scientific Research & Development*, 3(01), pp. 849–851.
- 113]. Kauppinen, P., Hyttinen, J. and Malmivuo, J. (2005) 'Sensitivity Distribution Simulations of Impedance Tomography Electrode Combinations', *International Journal of Bioelectromagnetism*, 7(1), pp. 344–347.
- 114]. Khan, S. et al. (2015) 'FPGA-Based Voltage and Current Dual Drive System for High Frame Rate Electrical Impedance Tomography', *IEEE TRANSACTIONS ON MEDICAL IMAGING*, 34(4), pp. 888–901.
- 115]. Kharfi, F., Yahiaoui, M. L. and Boussahoul, F. (2015) 'X-ray computed tomography system for laboratory small-object imaging: Enhanced tomography solutions', *Applied Radiation and Isotopes*, 101, pp. 33–39. doi: 10.1016/j.apradiso.2015.03.016.
- 116]. Kourunen, J. et al. (2008) 'Imaging of mixing of two miscible liquids using electrical impedance tomography and linear impedance sensor', *Flow Measurement and Instrumentation*, 19(6), pp. 391–396. doi: 10.1016/j.flowmeasinst.2008.07.002.
- 117]. Krueger-Ziolek, S. et al. (2015) 'Positioning of electrode plane systematically influences EIT imaging.', *Physiological measurement*, 36(6), pp. 1109–18. doi: 10.1088/0967-3334/36/6/1109.
- 118]. Kusche, R. et al. (2015) 'A FPGA-Based Broadband EIT System for Complex Bioimpedance Measurements—Design and Performance Estimation', *Electronics*, 4(3), pp. 507–525. doi: 10.3390/electronics4030507.

- 119]. Kwon, H. et al. (2013) 'A local region of interest imaging method for electrical impedance tomography with internal electrodes', *Computational and Mathematical Methods in Medicine*, 2013. doi: 10.1155/2013/964918.
- 120]. Latha, N. and Murthy, B. (2016) 'GSM Based Rain Fall Detector Using Arduino', *International Journal of Electronics and Communication Engineering (IJECE)*, 5(3), pp. 11–16. Available at: http://www.iaset.us/view_archives.php?year=2016&id=16&jtype=2&page=2.
- 121]. Lei, J. et al. (2013) 'An image reconstruction algorithm for electrical capacitance tomography based on robust principle component analysis.', *Sensors (Basel, Switzerland)*, 13(2), pp. 2076–92. doi: 10.3390/s130202076.
- 122]. Li, F. et al. (2017) 'Total Variation Regularization With Split Bregman-Based Method in Magnetic Induction Tomography Using Experimental Data', *IEEE SENSORS JOURNAL*, 17(4), pp. 976–985.
- 123]. Li, L. et al. (2016) 'Localized electrical impedance myography of the biceps brachii muscle during different levels of isometric contraction and fatigue', *Sensors (Switzerland)*, 16(4). doi: 10.3390/s16040581.
- 124]. Li, R. et al. (2016) 'Preliminary Study of Assessing Bladder Urinary Volume Using Electrical Impedance Tomography', *Journal of Medical and Biological Engineering*. Springer Berlin Heidelberg, 36(1), pp. 71–79. doi: 10.1007/s40846-016-0108-1.
- 125]. Li, T. et al. (2014) 'Adaptive techniques in electrical impedance tomography reconstruction', *Physiological Measurement*, 35(6), pp. 1111–1124. doi: 10.1088/0967-3334/35/6/1111.
- 126]. Li, X. et al. (2016) 'In situ representation of soil/sediment conductivity using electrochemical impedance spectroscopy', *Sensors (Switzerland)*, 16(5), pp. 1–9. doi: 10.3390/s16050625.
- 127]. Li, Y. and Soleimani, M. (2013) 'Imaging conductive materials with high frequency electrical capacitance tomography', *Measurement*, 46(9), pp. 3355–3361. doi: 10.1016/j.measurement.2013.05.020.
- 128]. Li, Y. et al. (2013) 'Gas/oil/water flow measurement by electrical capacitance tomography', *Measurement Science and Technology*, 24(7), p. 074001. doi: 10.1088/0957-0233/24/7/074001.
- 129]. Lim, K. H. et al. (2006) 'An efficient forward solver in electrical impedance tomography by spectral element method', *IEEE Transactions on Medical Imaging*, 25(8), pp. 1044–1051. doi: 10.1109/TMI.2006.876143.
- 130]. Lima, L. C. De, Félix, B. P. G. and Reis, E. dos (2015) 'ELECTRICAL NON-INTRUSIVE PROBES APPLIED TO THE MONITORING OF TWO-PHASE FLOWS THROUGH PIPES: A LITERATURE BASED REVIEW', 23rd ABCM International Congress of Mechanical Engineering, (d). doi: 10.20906/CPS/COB-2015-1950.
- 131]. Lionheart, B. (2014) 'EIT for beginners Electrical impedance tomography', (July)
- 132]. Liu, D. et al. (2015) 'Multi-phase flow monitoring with electrical impedance tomography using level set based method', *Nuclear Engineering and Design*. Elsevier B.V., 289, pp. 108–116. doi: 10.1016/j.nucengdes.2015.04.023.
- 133]. Liu, D., Kolehmainen, V., et al. (2015) 'A nonlinear approach to difference imaging in EIT; Assessment of the robustness in the presence of modelling errors', *Inverse Problems*, 31(3). doi: 10.1088/0266-5611/31/3/035012.

- 134]. Liu, J., Xiong, H., et al. (2015) 'Evaluation of measurement and stimulation patterns in open electrical impedance tomography with scanning electrode', *Medical and Biological Engineering and Computing*. Springer Berlin Heidelberg, 53(7), pp. 589–597. doi: 10.1007/s11517-015-1274-y.
- 135]. Liu, S. et al. (2014) 'Prior-online iteration for image reconstruction with electrical capacitance tomography', *IEE Proceedings - Science Measurement and Technology*. doi: 10.1049/ip-smt.
- 136]. LRMC, (2014), Lung [ONLINE]. Available at: <http://www.lakewayregional.com/services/lung-health-program/> [Accessed 10 July 14].
- 137]. Loser, T., Wajman, R. and Mewes, D. (2001) 'Electrical capacitance tomography: image reconstruction along electrical field lines', *Measurement Science and Technology*, 12(8), pp. 1083–1091. doi: 10.1088/0957-0233/12/8/314.
- 138]. Loyola, B. R. et al. (2013) 'Spatial sensing using electrical impedance tomography', *IEEE Sensors Journal*, 13(6), pp. 2357–2367. doi: 10.1109/JSEN.2013.2253456.
- 139]. Malone, E. et al. (2013) 'Multifrequency Electrical Impedance Tomography using spectral constraints.', *IEEE transactions on medical imaging*, 33(c), pp. 1–12. doi: 10.1109/TMI.2013.2284966.
- 140]. Malone, E. et al. (2015) 'A Reconstruction-Classification Method for Multifrequency Electrical Impedance Tomography', *IEEE Transactions on Medical Imaging*, 34(7), pp. 1486–1497. doi: 10.1109/TMI.2015.2402661.
- 141]. Manage, P. et al. (2016) 'Electrical Impedance Tomography', *International Journal of Advanced Research in Computer and Communication Engineering*, 5(7), pp. 268–272. doi: 10.17148/IJARCCCE.2016.5754.
- 142]. Mann, R. et al. (1997) 'Application of electrical resistance tomography to interrogate mixing processes at plant scale', *Chemical Engineering Science*, 52(13), pp. 2087–2097. doi: 10.1016/S0009-2509(97)00036-5.
- 143]. Manuel, J. (2010) *Electromagnetic Tomography: Real-Time Imaging using Linear Approaches Biomedical Engineering*. University of Lisbon.
- 144]. Martin, S. and Choi, C. (2016) 'Nonlinear Electrical Impedance Tomography reconstruction using Artificial Neural Networks and Particle Swarm Optimization', *IEEE Transactions on Magnetics*, 52(3), pp. 1–4. doi: 10.1109/TMAG.2015.2488901.
- 145]. Maskery, I. et al. (2016) 'Quantification and characterisation of porosity in selectively laser melted Al-Si10-Mg using X-ray computed tomography', *Materials Characterization*, 111, pp. 193–204. doi: 10.1016/j.matchar.2015.12.001.
- 146]. Mellenthin, M. M. et al. (2015) 'The ACE1 thoracic Electrical Impedance Tomography system for ventilation and perfusion', *Proceedings of the Annual International Conference of the IEEE Engineering in Medicine and Biology Society, EMBS, 2015-Novem*, pp. 4073–4076. doi: 10.1109/EMBC.2015.7319289.
- 147]. Metrics, A. (2015) 'An overview on fault diagnosis and nature-inspired optimal control of industrial process applications', *Computers in Industry*.
- 148]. Miyajima, Hirofumi, Shigei, N. and Miyajima, Hiromi (2015) 'PERFORMANCE COMPARISON OF HYBRID ELECTROMAGNETISM-LIKE MECHANISM ALGORITHMS WITH DESCENT METHOD', *Journal of Artificial Intelligence and Soft Computing Research*, 5(4), pp. 271–282.

- 149]. Mohanna, S., Valian, E. and Tavakoli, S. (2013) 'Nondestructive Position Detection of a Metallic Target within Soil Substrate Using Electromagnetic Tomography', *Research in Nondestructive Evaluation*, 24(4), pp. 177–190. doi: 10.1080/09349847.2013.780645.
- 150]. Mueller, J. L., Siltanen, S. and Isaacson, D. (2002) 'A direct reconstruction algorithm for electrical impedance tomography', *IEEE Transactions on Medical Imaging*. IOP Publishing, 21(6), pp. 555–559. doi: 10.1109/TMI.2002.800574.
- 151]. Murphy, E. K. and Mueller, J. L. (2009) 'Effect of domain shape modeling and measurement errors on the 2-D D-bar method for EIT', *IEEE Transactions on Medical Imaging*, 28(10), pp. 1576–1584. doi: 10.1109/TMI.2009.2021611.
- 152]. Murphy, E. K., Mahara, A. and Halter, R. J. (2016) 'A Novel Regularization Technique for Microendoscopic Electrical Impedance Tomography', *IEEE Transactions on Medical Imaging*, 35(7), pp. 1593–1603. doi: 10.1109/TMI.2016.2520907.
- 153]. Nguyen, Q. and Yang, C. Y. (2016) 'Design of a longitudinal cooling fin with minimum volume by a modified Newton-Raphson method', *Applied Thermal Engineering*. Elsevier Ltd, 98, pp. 169–178. doi: 10.1016/j.applthermaleng.2015.12.035.
- 154]. Niemczewska-Wójcik, M. (2017) 'Multi-sensor measurements of titanium alloy surface texture formed at subsequent operations of precision machining process', *Measurement: Journal of the International Measurement Confederation*, 96, pp. 8–17. doi: 10.1016/j.measurement.2016.10.049.
- 155]. Nissinen, A., Kolehmainen, V. P. and Kaipio, J. P. (2011) 'Compensation of modelling errors due to unknown domain boundary in electrical impedance tomography', *IEEE Transactions on Medical Imaging*, 30(2), pp. 231–242. doi: 10.1109/TMI.2010.2073716.
- 156]. Nonn, S. et al. (2018) 'Application of electrical impedance tomography to an anisotropic carbon fiber-reinforced polymer composite laminate for damage localization', *Composites Science and Technology*. Elsevier, 160(March), pp. 231–236. doi: 10.1016/j.compscitech.2018.03.031.
- 157]. O'Donnell, R. and Wright, J. (2016) 'Efficient quantum tomography II', *ACM Special Interest Group on Algorithms and Computation Theory*, pp. 899–912. doi: 10.1145/3055399.3055454.
- 158]. Ogi, H., Hirao, M. and Ohtani, T. (1999) 'Line-focusing electromagnetic acoustic transducers for the detection of slit defects.', *IEEE transactions on ultrasonics, ferroelectrics, and frequency control*, 46(2), pp. 341–6. doi: 10.1109/58.753022.
- 159]. Orschulik, J. and Antink, C. H. (2015) 'Multi-Layer Electrical Impedance Tomography : An Experimental Study', pp. 1–5.
- 160]. Ortiz-Alemán, C. and Martin, R. (2005) 'Inversion of electrical capacitance tomography data by simulated annealing: Application to real two-phase gas-oil flow imaging', *Flow Measurement and Instrumentation*, 16(2–3), pp. 157–162. doi: 10.1016/j.flowmeasinst.2005.02.014.
- 161]. Peyton, A. J. et al. (1995) 'Electromagnetic Imaging Using Mutual Inductance Tomography: Potential for process applications', *Particle & Particle Systems Characterization*, 12(2), pp. 68–74. doi: 10.1002/ppsc.19950120204.
- 162]. Pellegrini, S. P., Trigo, F. C. and Lima, R. G. (2018) 'Solving the electrical impedance tomography inverse problem for logarithmic conductivity: Numerical sensitivity', *The international journal for computation and mathematics in electrical and electronic engineering*.

- 163]. Pidcock, W. R. B. and M. K. (1987) 'Mathematical aspects of impedance imaging', *Mathematical Aspects of Impedance Imaging*, 8, pp. 77–84.
- 164]. Pikkemaat, R. et al. (2012) 'Electrical impedance tomography : New diagnostic possibilities using regional time constant maps', pp. 212–225.
- 165]. Pisa, S., Pittella, E. and Piuizzi, E. (2017) 'Comparisons among EIT data collection techniques and reconstruction algorithms', *Applied Computational Electromagnetics Society Journal*, 32(6), pp. 473–483.
- 166]. Precup, R. et al. (2015) 'Computers in Industry An overview on fault diagnosis and nature-inspired optimal control of industrial process applications', *Computers in Industry*. Elsevier B.V., 74, pp. 75–94. doi: 10.1016/j.compind.2015.03.001.
- 167]. Rao, S. M. et al. (2001) 'Electrical Capacitance Tomography Measurements on the Pneumatic Conveying of Solids', *Industrial & Engineering Chemistry Research*, 40(20), pp. 4216–4226. doi: 10.1021/ie0100028.
- 168]. Rasteiro, M. G. et al. (2011) 'Electrical tomography: A review of configurations and applications to particulate processes', *KONA Powder and Particle Journal*, 29(29), pp. 67–80. doi: 10.14356/kona.2011010.
- 169]. Roth, C. J. et al. (2015) 'Correlation between alveolar ventilation and electrical properties of lung parenchyma', *Physiological Measurement*, 36(6), pp. 1211–1226. doi: 10.1088/0967-3334/36/6/1211.
- 170]. Ruan, M., Shen, J. and Wheeler, C. B. (2001) 'Latching microelectromagnetic relays', *Sensors and Actuators, A: Physical*, 90(3), pp. 346–350. doi: 10.1016/S0924-4247(01)00606-9.
- 171]. Ruan, T. and Poursaee (2017) 'Subsurface Damage Assessment In Mortar Using Electrical Impedance Tomography', *i-Manager's Journal on Future Engineering and Technology*, 12(3), pp. 1–9.
- 172]. Rymarczyk, T. (2016) 'New methods to determine moisture areas by electrical impedance tomography', *International Journal of Applied Electromagnetics and Mechanics*, 52(1–2). doi: 10.3233/JAE-162071.
- 173]. Rymarczyk, T. et al. (2016) 'New electrical tomographic method to determine dampness in historical buildings', *Archives of Electrical Engineering*, 65(2), pp. 273–283. doi: 10.1515/ae-2016-0019.
- 174]. Saiful, M. et al. (2015) 'Jurnal Teknologi Magnetic Induction Tomography : A Brief Review', *Jurnal Teknologi*, 3, pp. 91–95.
- 175]. Samore, A. et al. (2017) 'Parametric Detection and Classification of Compact Conductivity Contrasts with Electrical Impedance Tomography', *IEEE Transactions on Instrumentation and Measurement*, 66(10), pp. 2666–2679. doi: 10.1109/TIM.2017.2711818.
- 176]. Sanders, T. et al. (2017) 'Recovering fine details from under-resolved electron tomography data using higher order total variation ℓ_1 regularization', *Ultramicroscopy*. Elsevier B.V., 174(January), pp. 97–105. doi: 10.1016/j.ultramic.2016.12.020.
- 177]. Sarode, V., Patil, H. and Cheeran, A. N. (2014) 'LabVIEW based Automatic Data acquisition system for Electrical Impedance Tomography', *International Journal of Computer Science and Information Technologies*, 5(0975–9646), pp. 4320–4324.

- 178]. Sarode, V., Patkar, S. and N Cheeran, A. (2013) 'Comparison of 2-D Algorithms in EIT based Image Reconstruction', *International Journal of Computer Applications*, 69(8), pp. 6–11. doi: 10.5120/11860-7642.
- 179]. Sbarbaro, D., Vauhkonen, M. and Johansen, T. a (2015) 'State estimation and inverse problems in electrical impedance tomography: observability, convergence and regularization', *Inverse Problems*. IOP Publishing, 31(4), p. 045004. doi: 10.1088/0266-5611/31/4/045004.
- 180]. Schullcke, B. et al. (2016) 'Effect of the number of electrodes on the reconstructed lung shape in electrical impedance tomography', *Current Directions in Biomedical Engineering*, 2(1), pp. 499–502. doi: 10.1515/cdbme-2016-0110.
- 181]. Scott, D. and Mccann, H. (2005) *Process Imaging For Automatic Control*. Edited by D. Scott and H. Mccann. Florida: Taylor & Francis Group.
- 182]. Selvi, K. and Rajeswari, S. (2015) 'an Equipped Sensorized Glove With Bent Sensor for Measuing Finger Flexion', *International Journal of Advanced Research in Biology Ecology, Science and Technology (IJARBEST)*, 1(1).
- 183]. Seok, B. et al. (2014) 'Image reconstruction using voltage-current system in electrical impedance tomography', *Nuclear Engineering Design*. Elsevier B.V., 278, pp. 134–140. doi: 10.1016/j.nucengdes.2014.07.023.
- 184]. Shercliff, J. A. (1987) *The theory of electromagnetic flow-measurement*. Cambridge: Cambridge University Press.
- 185]. Siegel, D. M. (2002) *Innovation in Maxwell's Electromagnetic Theory: Molecular Vortices, Displacement Current, and Light*. Cambridge: Cambridge University Press.
- 186]. Silvera-Tawil, D. et al. (2015) 'Electrical impedance tomography for artificial sensitive robotic skin: A review', *IEEE Sensors Journal*, 15(4), pp. 2001–2016. doi: 10.1109/JSEN.2014.2375346.
- 187]. Soleimani, M. (2006) 'Electrical impedance tomography system: an open access circuit design.', *Biomedical engineering online*, 5, p. 28. doi: 10.1186/1475-925X-5-28.
- 188]. Soleimani, M. and Lionheart, W. R. B. (2005) 'Nonlinear image reconstruction for electrical capacitance tomography using experimental data', *Measurement Science and Technology*, 16(10), pp. 1987–1996. doi: 10.1088/0957-0233/16/10/014.
- 189]. Soleimani, M. et al. (2009) 'Four-Dimensional Electrical Capacitance Tomography Imaging Using Experimental Data', *Progress In Electromagnetics Research*, 90, pp. 171–186. doi: 10.2528/PIER09010202.
- 190]. Spartalis, E. et al. (2017) 'Successful combined surgical approach in a rare case of retrotracheal goitre in a patient with anatomical impediments', *Via Medica*, 77(1), pp. 166–169. doi: 10.5603/FM.a2017.0072.
- 191]. Steinmann, D. et al. (2008) 'Electrical impedance tomography to confirm correct placement of double-lumen tube: A feasibility study', *British Journal of Anaesthesia*. *British Journal of Anaesthesia*, 101(3), pp. 411–418. doi: 10.1093/bja/aen166.
- 192]. Sun, B. et al. (2015) 'A new linear back projection algorithm to electrical tomography based on measuring data decomposition', *Measurement Science and Technology*, 26(12). doi: 10.1088/0957-0233/26/12/125402.

- 193]. Sun, J. and Yang, W. (2015) 'A dual-modality electrical tomography sensor for measurement of gas-oil-water stratified flows', *Measurement: Journal of the International Measurement Confederation*. Elsevier Ltd, 66, pp. 150–160. doi: 10.1016/j.measurement.2015.01.032.
- 194]. Sun, J., Yang, W. and Tian, W. (2015) '3D imaging based on fringe effect of an electrical capacitance tomography sensor', *Measurement*.
- 195]. Tallman, T. N. and Wang, K. W. (2016) 'Damage and strain identification in multifunctional materials via electrical impedance tomography with constrained sine wave solutions', *Structural Health Monitoring*, 15(2), pp. 235–244. doi: 10.1177/1475921716635574.
- 196]. Tallman, T. N. et al. (2015) 'Tactile imaging and distributed strain sensing in highly flexible carbon nanofiber/polyurethane nanocomposites', *Carbon*. Elsevier Ltd, 95, pp. 485–493. doi: 10.1016/j.carbon.2015.08.029.
- 197]. Tamburrino, A., Rubinacci, G. and Ventre, S. (2014) 'Noniterative Methods for Real Time Imaging of Conducting Materials', in *17th International Workshop on Electromagnetic Nondestructive Evaluation*.
- 198]. Tami Freeman, (2008), An image showing the lungs [ONLINE]. Available at: <http://medicalphysicsweb.org/cws/article/research/34139> [Accessed 09 April 14].
- 199]. Tapp, H. S. et al. (2003) 'Chemical engineering applications of electrical process tomography', *Sensors and Actuators, B: Chemical*, 92(1–2), pp. 17–24. doi: 10.1016/S0925-4005(03)00126-6.
- 200]. Thorn, R., Johansen, G. a and Hjertaker, B. T. (2013) 'Three-phase flow measurement in the petroleum industry', *Measurement Science and Technology*, 24(1), p. 012003. doi: 10.1088/0957-0233/24/1/012003.
- 201]. Tommaso, D. E. M. (2011) *Parallel Modeling of the Electric Field Distribution in the Brain*. University of Bologna.
- 202]. Tossavainen, O. (2007) *Shape Estimation in Electrical Impedance Tomography*, *Environmental Sciences*. Available at: <http://dx.doi.org/10.1111/j.1749-6632.1999.tb09492.x>.
- 203]. Trepte, C. J. C. et al. (2016) 'Electrical impedance tomography (EIT) for quantification of pulmonary edema in acute lung injury', *Critical Care*. *Critical Care*, 20(1), p. 18. doi: 10.1186/s13054-015-1173-5.
- 204]. Trepte, C. J. C. et al. (2017) 'Electrical impedance tomography for non-invasive assessment of stroke volume variation in health and experimental lung injury', *British Journal of Anaesthesia*, 118(1), pp. 68–76. doi: 10.1093/bja/aew341.
- 205]. Uday, B. and Ajay, B. (2007) *Electromagnetic Engineering*. Technical Publications.
- 206]. van der Burg, P. S. et al. (2014) Unilateral atelectasis in a preterm infant monitored with electrical impedance tomography: a case report, *European Journal of Pediatrics*. doi: 10.1007/s00431-014-2399-y.
- 207]. Villa, F. et al. (2016) 'Wearable multi-frequency and multi-segment bioelectrical impedance spectroscopy for unobtrusively tracking body fluid shifts during physical activity in real-field applications: A preliminary study', *Sensors (Switzerland)*, 16(5), pp. 1–15. doi: 10.3390/s16050673.
- 208]. Visentin, F., Fiorini, P. and Suzuki, K. (2016) 'A deformable smart skin for continuous sensing based on electrical impedance tomography', *Sensors (Switzerland)*, 16(11), pp. 1–21. doi: 10.3390/s16111928.

- 209]. Vitalii, L., Andrey, L. and Georgy, G. (2015) 'Eddy Current Analysis for Nuclear Power Materials', *Advanced Materials Research*, 1085, pp. 335–339.
- 210]. Wang, G. et al. (2016) 'Ultrasound-assisted preparation of electrospun carbon fiber/graphene electrodes for capacitive deionization: Importance and unique role of electrical conductivity', *Carbon*. Elsevier Ltd, 103, pp. 311–317. doi: 10.1016/j.carbon.2016.03.025.
- 211]. Wang, J. et al. (2017) 'Study on Sensitivity Field for MIT', *International Core Journal of Engineering*, 3(12), pp. 299–302.
- 212]. Wang, J.-G. et al. (2013) 'RECONSTRUCTION OF MICROWAVE ABSORPTION OF MULTIPLE TUMORS IN HETEROGENEOUS TISSUE FOR MICROWAVE-INDUCED THERMO-ACOUSTIC TOMOGRAPHY', *Progress In Electromagnetics Research*, pp. 57–72.
- 213]. Wang, M. (2015) *Industrial Tomography: Systems and Applications*. Cambridge: Woodhead Publishing.
- 214]. Wang, M. et al. (2007) 'Electrical Impedance Tomography for Nuclear Engineering', in *international conference on nuclear engineering; Nagoya, Aichi (Japan)*, pp. 1–8.
- 215]. Warsito, W. and Fan, L.-S. (2001) 'Neural network based multi-criterion optimization image reconstruction technique for imaging two- and three-phase flow systems using electrical capacitance tomography', *Measurement Science and Technology*, 12(12), pp. 2198–2210. doi: 10.1088/0957-0233/12/12/323.
- 216]. Wei, H. and Soleimani, M. (2013) 'Electromagnetic Tomography for Medical and Industrial Applications: Challenges and Opportunities [Point of View]', *Proceedings of the IEEE*, 101(3), pp. 559–565. doi: 10.1109/JPROC.2012.2237072.
- 217]. Wei, H.-Y. and Soleimani, M. (2012) 'A Magnetic Induction Tomography System for Prospective Industrial Processing Applications', *Chinese Journal of Chemical Engineering*, 20(2), pp. 406–410. doi: 10.1016/S1004-9541(12)60404-2.
- 218]. Wei, K. et al. (2015) 'ITS Reconstruction Tool-Suite: An inverse algorithm package for industrial process tomography', *Flow Measurement and Instrumentation*. Elsevier, 46, pp. 292–302. doi: 10.1016/j.flowmeasinst.2015.08.001.
- 219]. Wi, H. et al. (2014) 'Multi-frequency electrical impedance tomography system with automatic self-calibration for long-term monitoring', *IEEE Transactions on Biomedical Circuits and Systems*, 8(1), pp. 119–128. doi: 10.1109/TBCAS.2013.2256785.
- 220]. Xu, W. et al. (2012) 'Normalized least-square method for water hold-up measurement in stratified oil–water flow', *Flow Measurement and Instrumentation*. Elsevier Ltd, 27, pp. 71–80. doi: 10.1016/j.flowmeasinst.2012.05.002.
- 221]. Xu, Y. et al. (2010) 'Separation of Gas-Liquid Two-Phase Flow Through Independent Component Analysis', *Ieee Transactions on Instrumentation and Measurement*, 59(5, Sp. Iss. SI), pp. 1294–1302. doi: 10.1109/TIM.2010.2044077.
- 222]. Yan, H. et al. (2001) 'Image reconstruction in electrical capacitance tomography using multiple linear regression and regularization', *Measurement Science and Technology*, 12(5), pp. 575–581. doi: 10.1088/0957-0233/12/5/304.
- 223]. Yang, T. et al. (2017) 'Level measurement for saline with a small surface area using high frequency electromagnetic sensing technique', *Measurement: Journal of the International Measurement Confederation*. Elsevier Ltd, 101, pp. 118–125. doi: 10.1016/j.measurement.2017.01.025.

- 224]. Yang, W. Q. (1996) 'Hardware design of electrical capacitance tomography systems', *Measurement Science and Technology Hardware*.
- 225]. Yang, Y. *et al.* (2017) 'A Miniature Electrical Impedance Tomography Sensor and 3D Image Reconstruction for Cell Imaging', *IEEE Sensors*, 17(2), pp. 514–523. doi: 10.1109/JSEN.2016.2631263.
- 226]. Yang, Y., Peng, L. and Jia, J. (2017) 'A novel multi-electrode sensing strategy for electrical capacitance tomography with ultra-low dynamic range', *Flow Measurement and Instrumentation*. Elsevier Ltd, 53, pp. 67–79. doi: 10.1016/j.flowmeasinst.2016.05.005.
- 227]. Yaqin, L. (2010) 'A Novelty Dynamic Image Reconstruction Algorithm in Electrical Impedance Tomography Based on Nachman Theory', *Information Technology and Applications, International Forum on*, 2(1), pp. 118–120. doi: <http://doi.ieeecomputersociety.org/10.1109/IFITA.2010.131>.
- 228]. Yerworth, R. J., Frerichs, I. and Bayford, R. (2017) 'Analysis and compensation for errors in electrical impedance tomography images and ventilation-related measures due to serial data collection', *Journal of Clinical Monitoring and Computing*, pp. 1–9. doi: 10.1007/s10877-016-9920-y.
- 229]. Yorkey, T. J., Webster, J. G. and Tompkins, W. J. (1987) 'Comparing Reconstruction Algorithms for Electrical Impedance Tomography', *IEEE Transactions on Biomedical Engineering*, BME-34(11), pp. 843–852. doi: 10.1109/TBME.1987.326032.
- 230]. Zain, N. M. and Kanaga, K. C. (2015) 'A Review on breast electrical impedance tomography clinical accuracy', *ARPN Journal of Engineering and Applied Sciences*, 10(15), pp. 6230–6234.
- 231]. Zarina, S., Muji, M. and Amirulah, R. (2016) 'Development of Image Reconstruction Using FPGA', 6th IEEE International Conference on Control System, Computing and Engineering, (November), pp. 25–27.
- 232]. Zeng, W.-C., Zhao, W.-J. and Zang, D.-F. (2001) 'Application Research of Crosshole Electromagnetic Tomography', *Chinese Journal of Geophysics*, 44(3), pp. 408–418. doi: 10.1002/cjg2.156.
- 233]. Zhai, L. S. *et al.* (2016) 'The measurement of local flow parameters for gas-liquid two-phase bubbly flows using a dual-sensor probe array', *Chemical Engineering Science*. Elsevier, 144, pp. 346–363. doi: 10.1016/j.ces.2016.01.058.
- 234]. Zhang, M., Ma, L. and Soleimani, M. (2015) 'Dual modality ECT-MIT multi-phase flow imaging', *Flow Measurement and Instrumentation*, 46, pp. 240–254. doi: 10.1016/j.flowmeasinst.2015.03.005.
- 235]. Zhang, P. *et al.* (2018) 'Cement and Concrete Research Application of neutron imaging to investigate fundamental aspects of durability of cement-based materials: A review', *Cement and Concrete Research*. Elsevier, 108(March), pp. 152–166. doi: 10.1016/j.cemconres.2018.03.003.
- 236]. Zhang, S. *et al.* (2006) 'Multi-frequency EIT hardware system based on DSP.', *Conference proceedings: ... Annual International Conference of the IEEE Engineering in Medicine and Biology Society. IEEE Engineering in Medicine and Biology Society. Conference*, Suppl, pp. 6677–80. doi: 10.1109/IEMBS.2006.260919.
- 237]. Zhang, T. *et al.* (2015) 'Electrical impedance spectroscopy-based defect sensing technique in estimating cracks', *Sensors (Switzerland)*, 15(5), pp. 10909–10922. doi: 10.3390/s150510909.

- 238]. Zhang, W. et al. (2014) 'Application of electrical capacitance tomography in particulate process measurement – A review', *Advanced Powder Technology*. The Society of Powder Technology Japan, 25(1), pp. 174–188. doi: 10.1016/j.appt.2013.12.003.
- 239]. Zhou, L., Harrach, B. and Seo, J. K. (2018) 'Monotonicity-based Electrical Impedance Tomography for Lung Imaging', *Nanoscience and Nanotechnology Letters*.
- 240]. Zhou, W. et al. (2016) 'Experimental investigation on surface wettability of copper-based dry bioelectrodes', *Sensors and Actuators, A: Physical*. Elsevier B.V., 244, pp. 237–242. doi: 10.1016/j.sna.2016.04.044.
- 241]. Zhou, Y., Chen, F. and Sun, B. (2008) 'Identification Method of Gas-Liquid Two-phase Flow Regime Based on Image Multi-feature Fusion and Support Vector Machine', *Chinese Journal of Chemical Engineering*. Chemical Industry and Engineering Society of China (CIESC) and Chemical Industry Press (CIP), 16(6), pp. 832–840. doi: 10.1016/S1004-9541(09)60002-1.

Appendix A

Front panel window toolbar

The front panel window toolbar keys are used to control, modify and calibrate the virtual instruments (VI).



The Run key in LabVIEW is used to run the developed VI without the need to compile the code since LabVIEW does this automatically. The Run key is a solid white arrow as seen on the left of this paragraph.



When the Run key in LabVIEW appears broken, that means the VI, which has been created, contains an error. However, when the Run key still appears broken that means the writing in the VI block diagram is broken or includes incorrect writing. It is found as a dark grey broken arrow as seen on the left of this paragraph.



The Rotary motion arrows key in LabVIEW, as shown to the left of this paragraph, is used as a sign that the program is running continuously (infinite). It will be disabled once it is clicked for the second time.



The red circle key in LabVIEW as shown on the left of this paragraph is used to abort the execution of VI when it is running. It is also used when the Pause or Run keys are not responding. Furthermore, it used in an emergency saturation which occurs in industrial processes. Using this key will immediately stop the whole process.



The Pause button is used to pause a running VI. It resembles the icon that is shown on left side of this paragraph. After pressing the Pause button, the LabVIEW will highlight where the VI in the block diagram execution has been paused. Press the Pause key again to continue running the VI.

“Acquisition” loop

The “Acquisition” loop is responsible for electrodes switching control and signal acquisition. It operates as state machine and has four cases: “Initialization”, “Acquire”, “ProcessData”, and “Reset”.

Code before and after “Acquisition” loop

The initialization part is located before the “Acquisition” loop, as shown in Figure 3.19. The “States” enumerator is for initializing the first state of the case structure in the “Acquisition” loop. The “Data” is meant to initialize the parameters and variables which are used in the loop. The “Homogen data” is intended to initialize the homogeneous data (“Homogen Data” array). Then, the initialization of the error cluster is located. The part for obtaining the “Eidors” queue is at the bottom of the code. Using this queue (in the “ProcessData” case), the “Data” array, which contains measured signal RMS values for each channel, is transferred to the “Processing & Save” loop.

Once the program is finished, the digital array with “false” values is written to the front panel indicators and the “DAQ Assistant” to return the indicators and DO states to initial “false” values. The VI for the “Eidors” queue release is located at the bottom of Figure A. The error clusters are merged at the end to provide information about errors that occurred in the program.

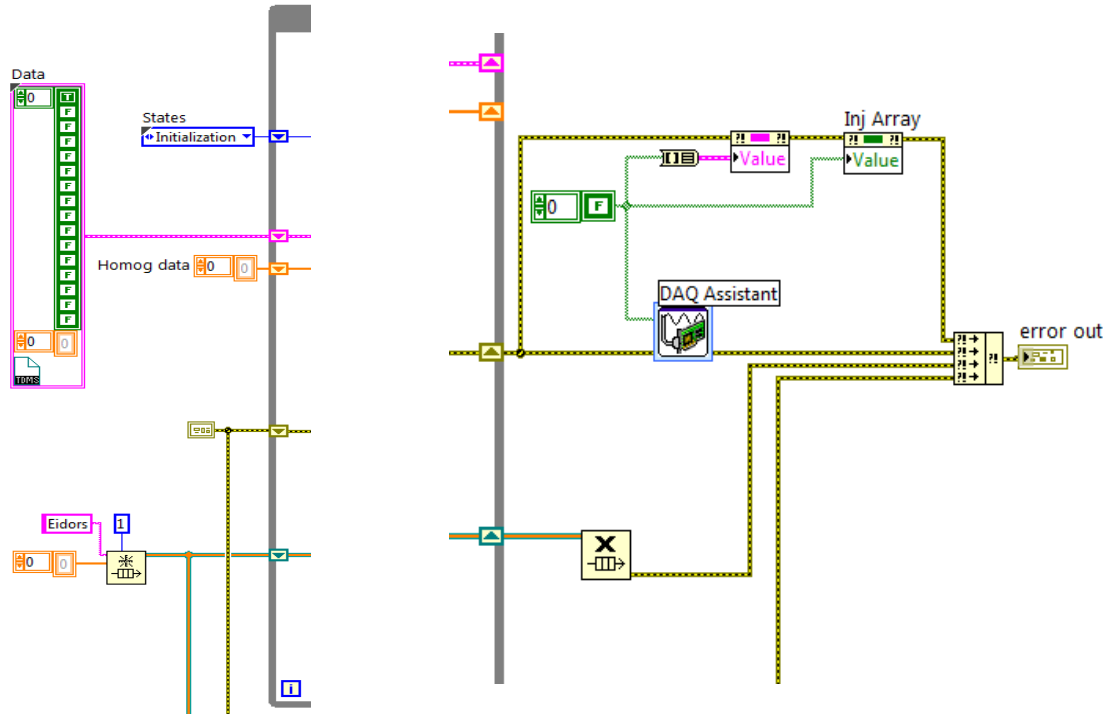


Figure A: Code before and after “Acquisition” loop.

“Initialization” case

The “Initialization” case is designed to open (if the case exists) or create the “Data.tdms” TDMS file in the application directory and call ...\eidors-v3.8\eidors\startup.m MATLAB script to run EIDORS software, as shown in Figure B.

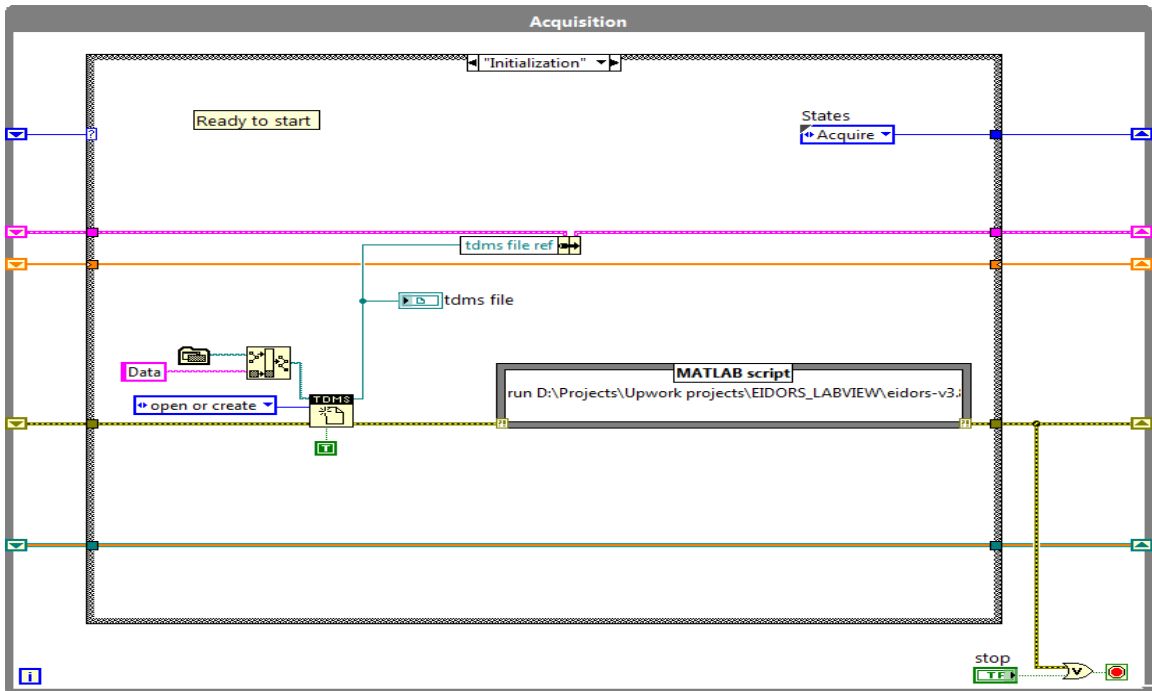
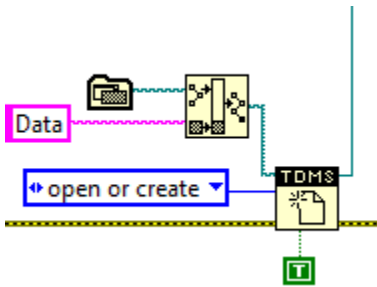
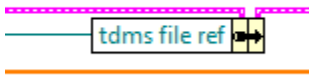


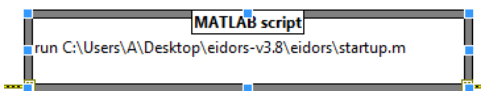
Figure B: “Initialization” case.



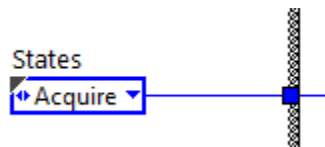
This part opens or creates “Data.tdms” TDMS file in the application directory.



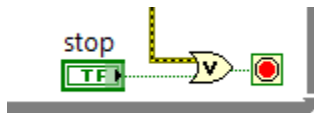
The reference “Data.tdms” file is bundled to “Data” cluster to pass in other cases.



The MATLAB script node is used to call EIDORS software.



This enumerator determines the next state.



The loop stops when an error occurs or the “Stop” button is pressed.

“Acquire” case

The electrode switching logic is implemented in this case, as shown in Figure C. For each switching occurrence, the signal for 500 samples is measured from all electrodes and RMS values are calculated and collected in the “Data” array. If the number of elements in the “Data” array reaches 256 (which means one switching cycle has been completed), the program should execute next “ProcessData” state. The time benchmark is placed at the bottom of this case.

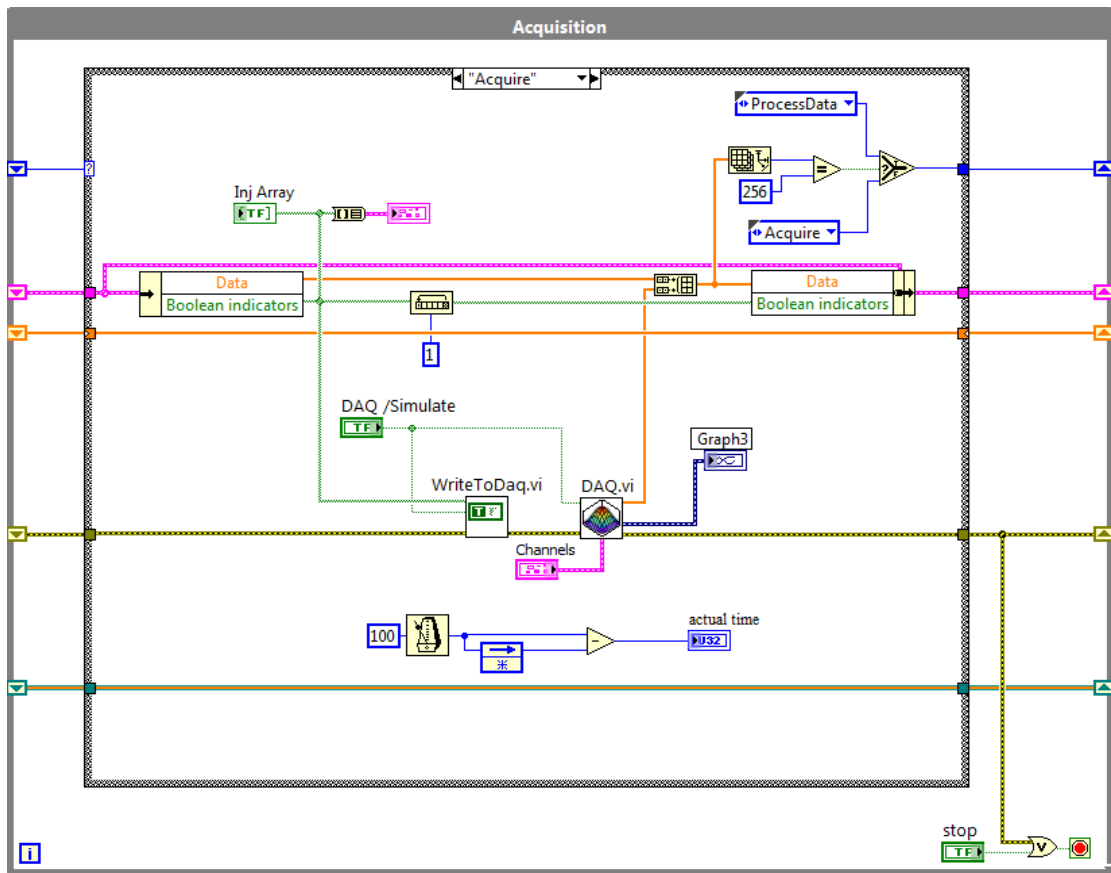
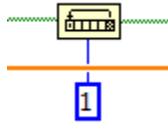


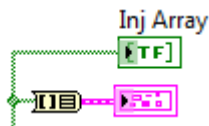
Figure C: “Acquire” case.



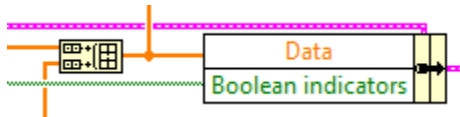
This node is intended to unbundle the “Data” array and “Boolean indicators” array from the “Data” cluster.



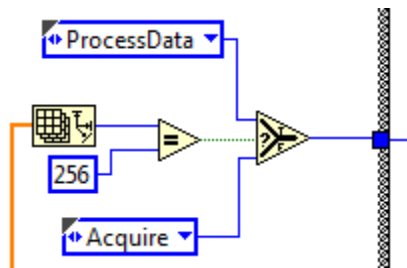
Rotates the injection array by one element. This function is used to modify the electrode switching array. The same array is written to indicators on UI.



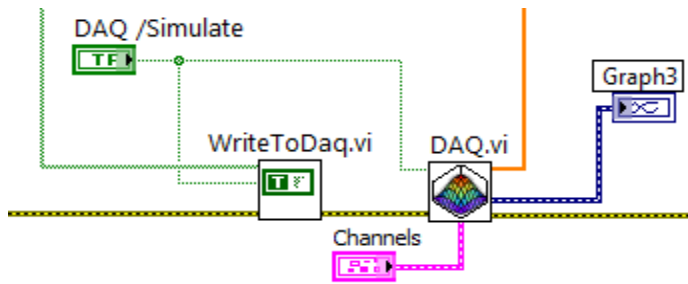
The “Boolean indicators” array is written to indicators on UI.



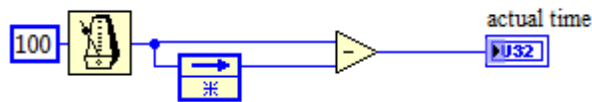
The new data are written to the “Data” array via the “Build Array” function. Then, the modified “Data” array and “Boolean indicators” array is bundled to the “Data” cluster.



If the size of the “Data” array is equal to 256, this means that one full cycle has finished, and all 16 electrodes have been excited. In this case, the next “ProcessData” state should be executed. Otherwise, the same “Acquire” case is executed.



In this section, the “Boolean indicators” array is passed to “WriteToDaq.vi” to generate a digital signal on the DAQ device. Then, “DAQ.vi” is used to measure and calculate RMS values of signals gathered from electrodes. “DAQ/Simulate” control determines the mode of the above mentioned VI operation.



This part measures the actual time for “Acquire” case execution. In addition, it assures that the duration of signal acquisition from each electrode is 100 ms.

WriteToDaq.vi

This VI can work in two modes: “DAQ” and “Simulate”. If “DAQ” mode is selected from the UI of the program, then it passes the injection array to generate a digital signal on the DAQ device. The “True” case works when “Simulate” mode is selected. There is no need to generate any signal on the DAQ device in this mode. Here, the only error cluster is passed through the “True” case (Figure D).



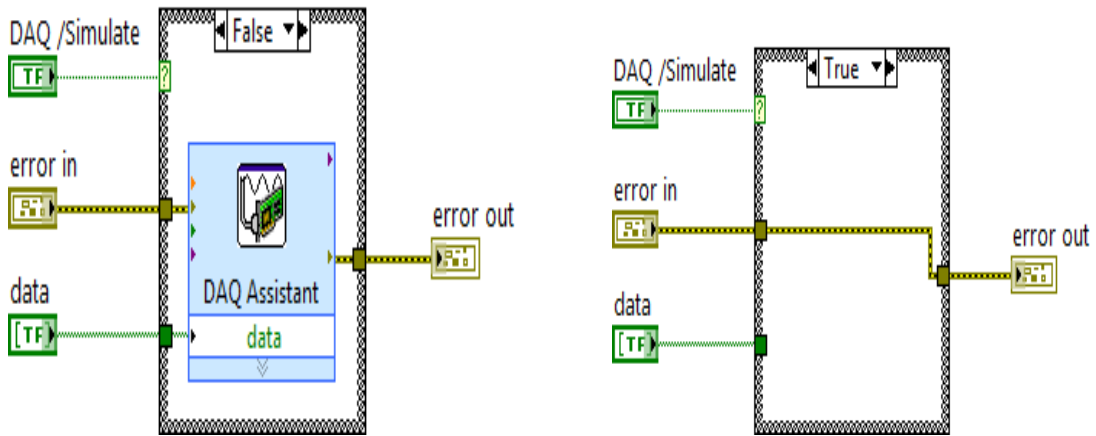


Figure D: “True” case corresponds to “Simulate” mode (Right side) and the “False” case corresponds to “DAQ” mode (Lift side).

DAQ.vi

This VI can work in two modes: “DAQ” and “Simulate”. If “DAQ” mode is selected from the UI of the program, then the “False” case works, as shown in Figure E. This VI is responsible for 500 sample measurements from all electrodes and RMS value calculation and collection to the “Data” array. These samples are default values, but this number can be configured from the UI “Settings” tab.



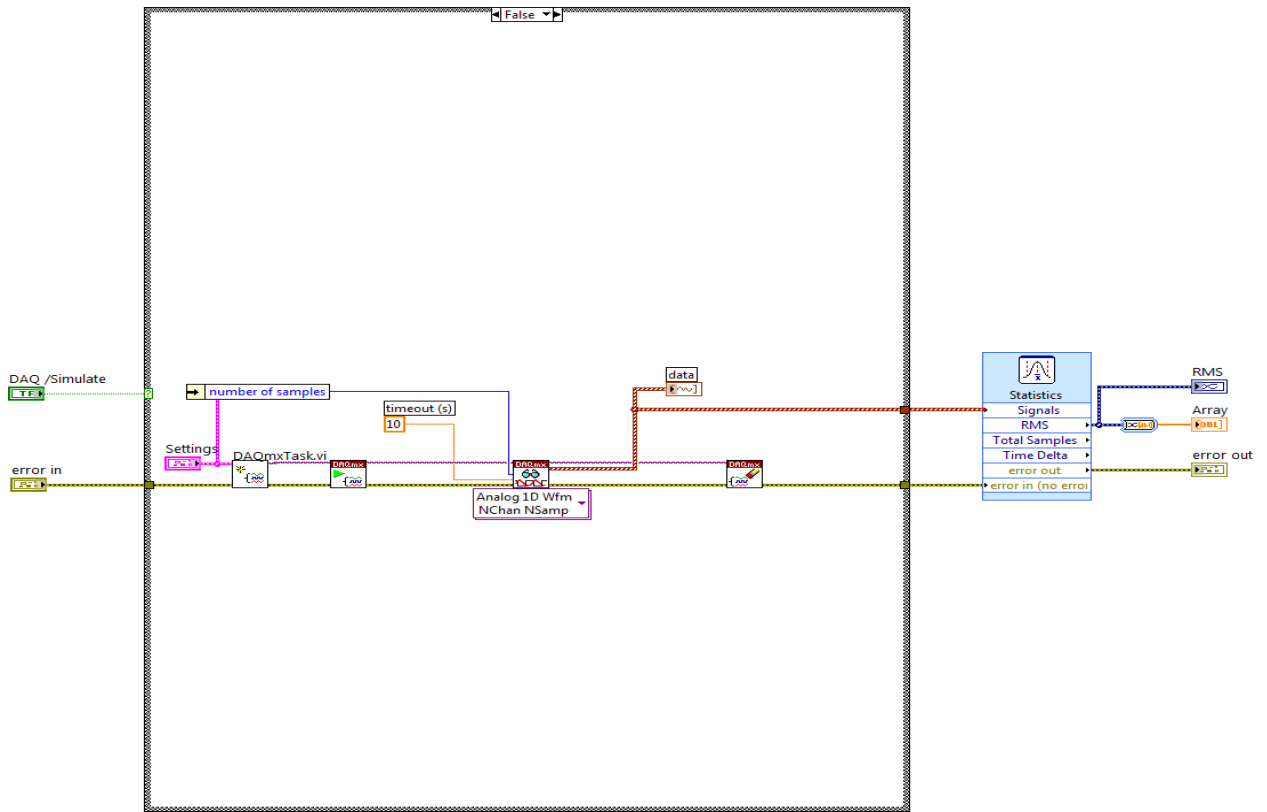


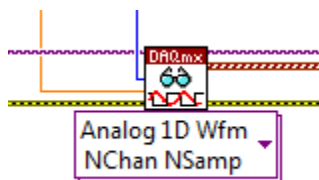
Figure E: “False” case corresponds to “DAQ” mode.



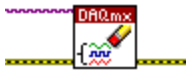
This VI creates a virtual channel to measure voltage and configure the sampling clock. The “Settings” is clustered with channels parameters which are passed from the UI.



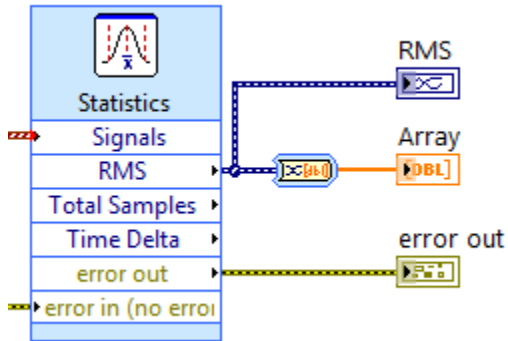
This is for starting measurements.



Reads from all channels and provides “number of samples” from each channel.



Clears the task after measurement completion.



Calculates RMS values for all channel measurements.

If “Simulate” mode is selected from the UI of the program, then the “True” case works, as shown in Figure F. The sine signals for 16 channels are simulated in this mode. In this mode, the software can work without NI hardware and is designed for algorithm testing purposes. The “Simulate Signal” VIs are designed to simulate measurement signals from 16 electrodes.

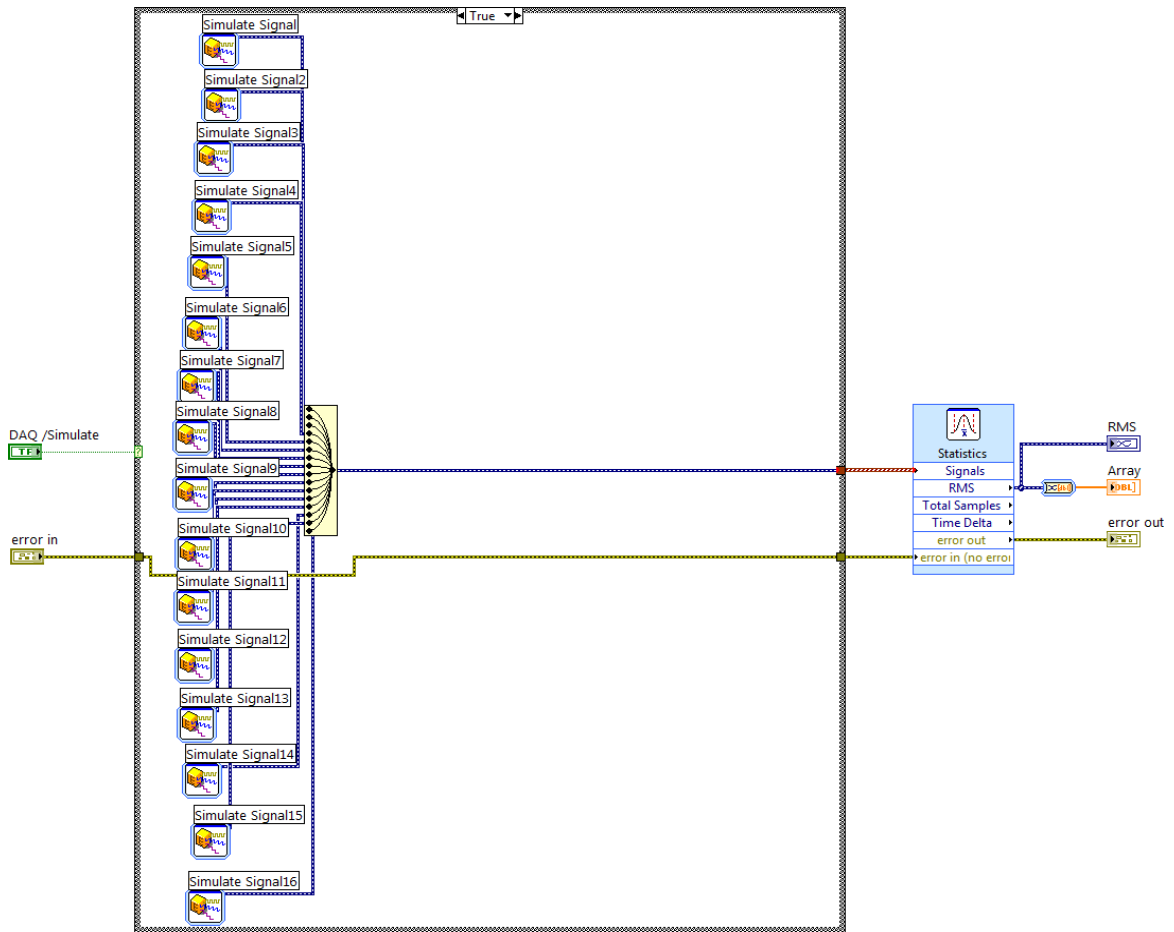
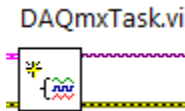


Figure F: “True” case corresponds to “Simulate” mode.

DAQmxTask.vi

This VI creates a virtual channel to measure the voltage and configure the sampling clock, as shown in Figure G.



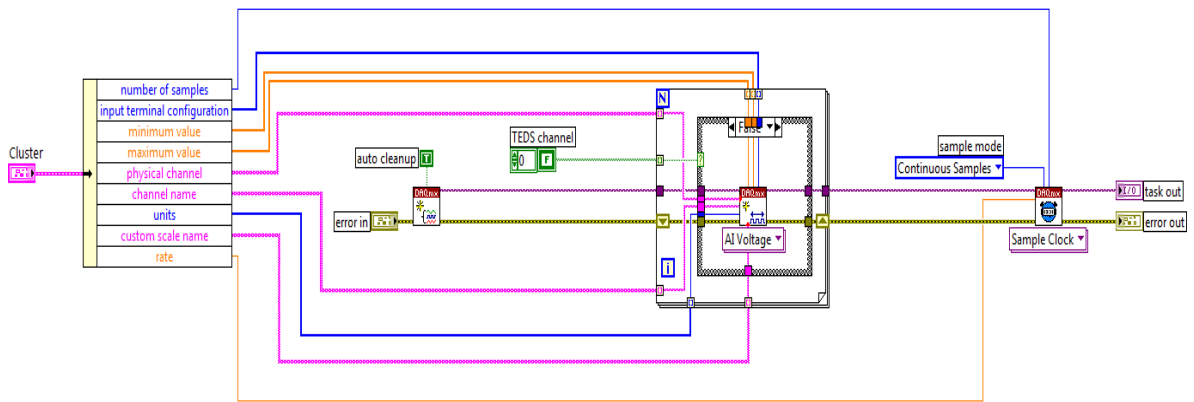
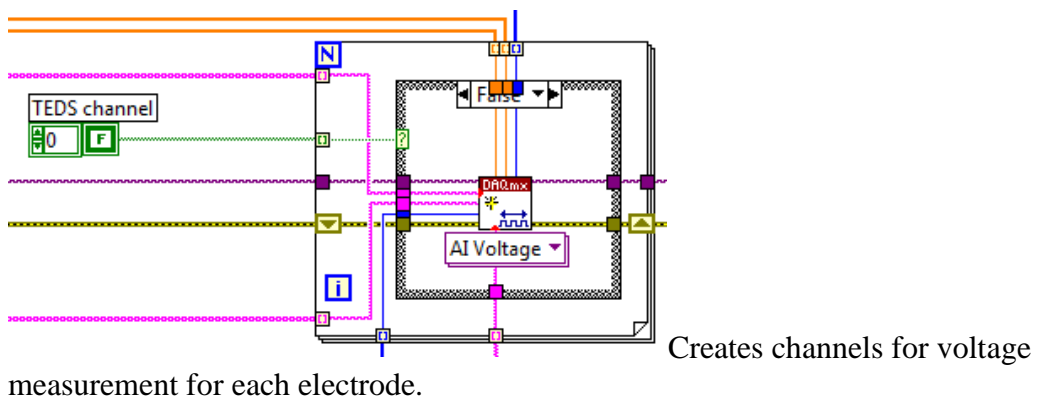
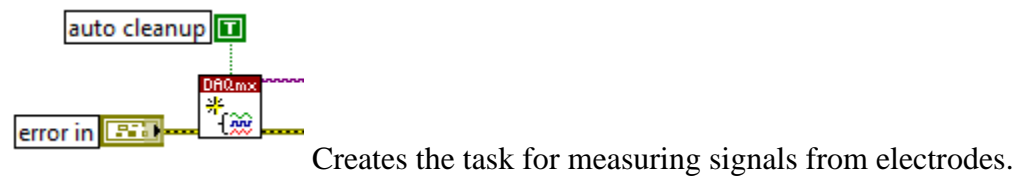
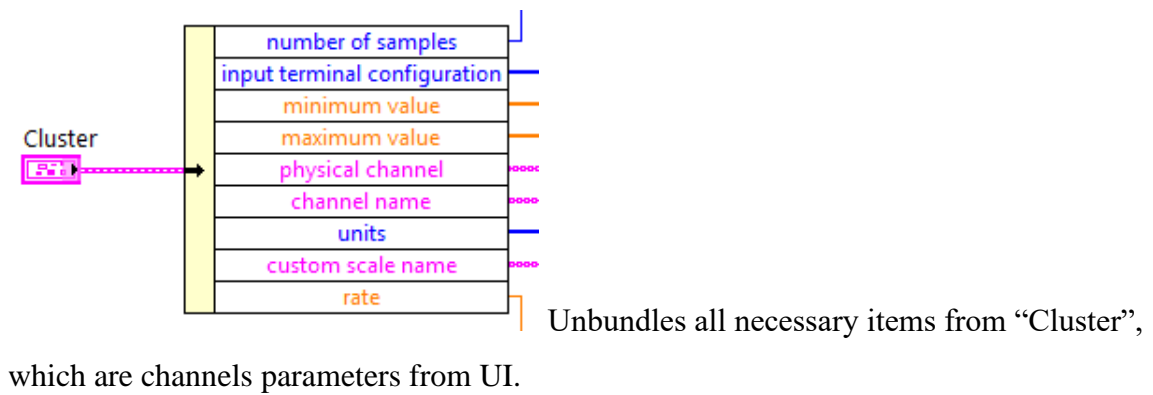
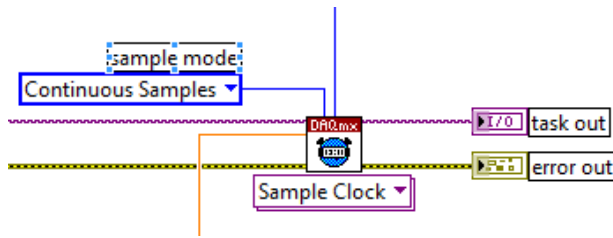


Figure G: DAQmxTask.vi.





Configures the sampling clock.

“ProcessData” case

In this case, the “Data” array is written to queue to send to the “Processing & Save” loop, as shown in Figure H. For the first cycle of excitation and measurement, calculated data are considered as homogeneous data. After running the program, when it proceeds to the “ProcessData” case for the first time, the “Homogen Data” array is empty. In this case, the “Data” array is written to the “Homogen Data” array. The next time when the program goes to this case, the “Homogen Data” array is not empty and there is no need to write new “Data” to it. Thereafter, the “ProcessData” case program should execute the next “Reset” state.

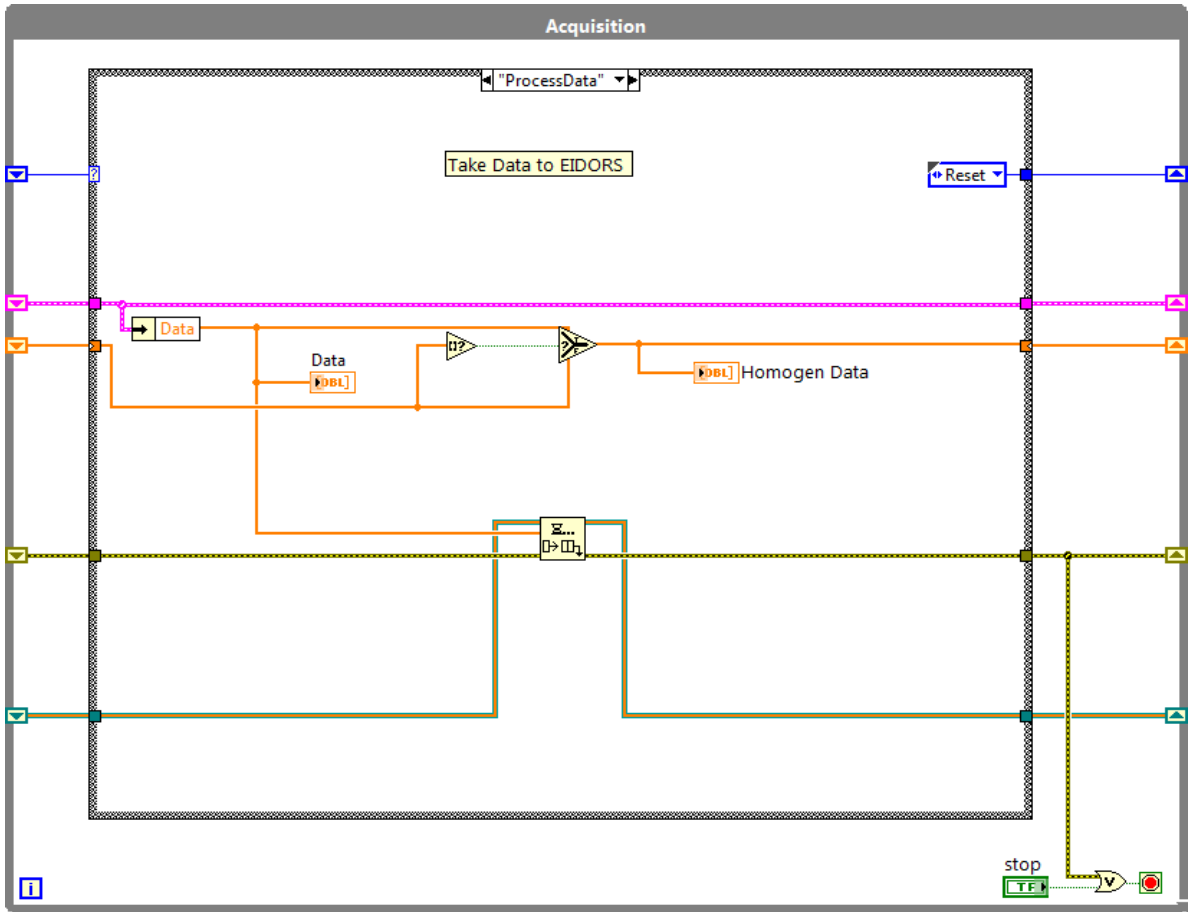
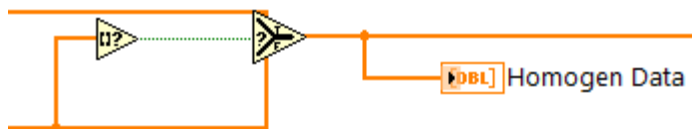
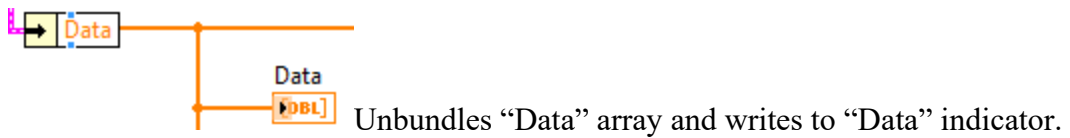
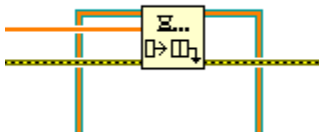


Figure H: "ProcessData" case.





The “Data” array is written to the “Eidors” queue to pass to the “Processing & Save” loop.

“Reset” case

In this case, the “Data” array is emptied, and the program goes to the “Acquire” state, as shown in Figure I.

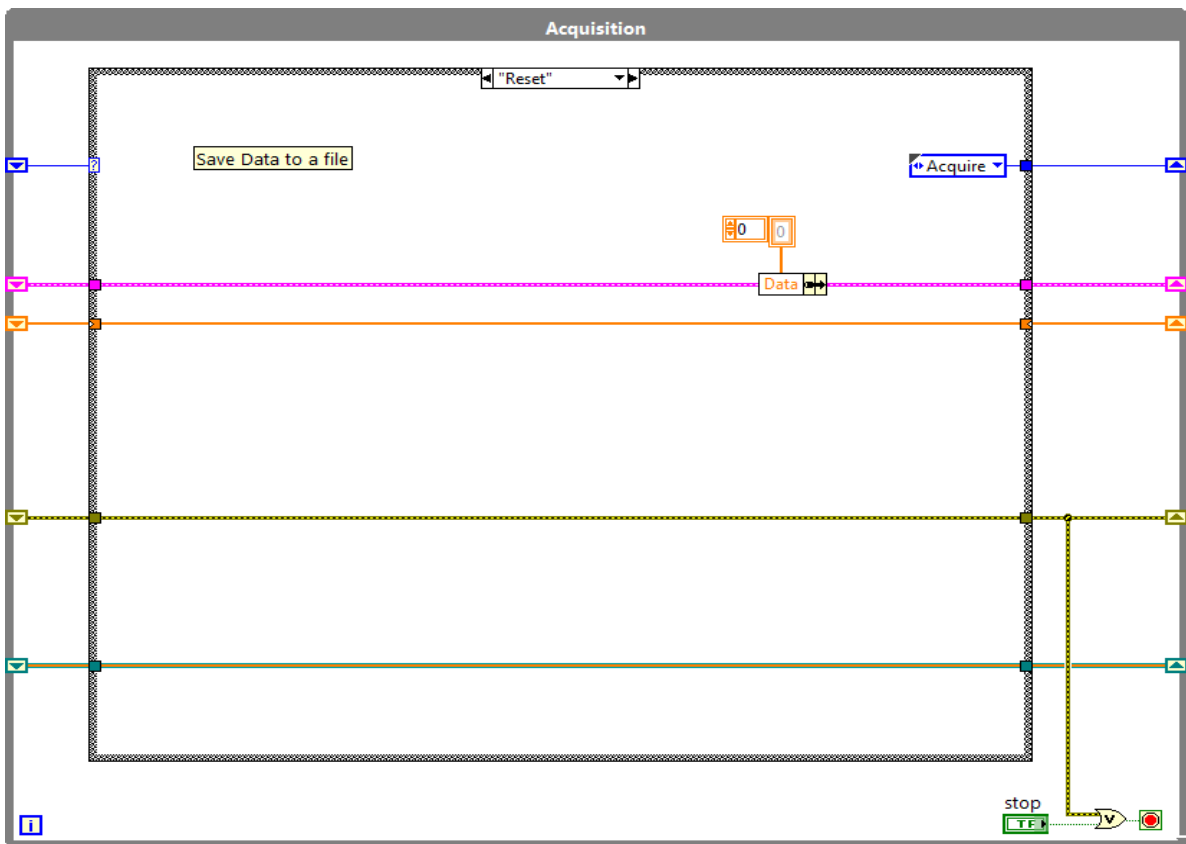


Figure I: "Reset" case.

“Processing & Save” loop

The “Processing & Save” loop is synchronized with the “Acquisition” loop, as shown in Figure J. This loop waits for the “Data” array to be written to the queue. Once this process is finished, the data are read from the queue, proceed to the “MATLAB script

node”, and are recorded to the TDMS file. The homogeneous data are read from the “Homogen Data” property node and also proceed to the “MATLAB script node”. After the program is run and launches the “Processing & Save” loop for the first time, it records “Homogen Data” to the “Homogen.tdms” file in the application directory. The “MATLAB script node” executes the following MATLAB code from EIDORS software:

```
show_slices(inv_solve(mk_common_model('d2c2',16),h_data',data')).
```

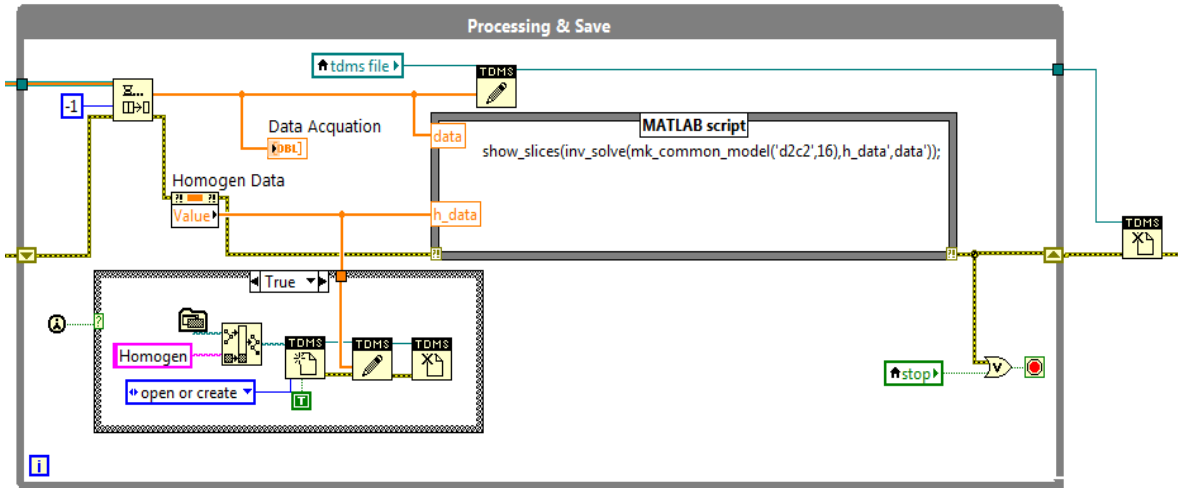
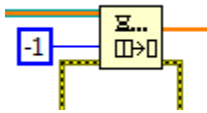
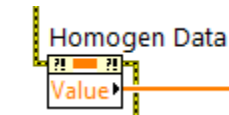


Figure J: “Processing & Save” loop.



Waits until “Data” array is written to queue. When new data are written, it reads them.



The “Value” property node of the “Homogen Data” indicator in the “Process Data” case of the “Acquisition” loop is used to read homogeneous data.



“Data” array is recorded to TDMS file.

The first function is

`mk_common_model`

This function creates an inverse model from the template and has many options. More about this function can be found [here](#).

The second function is

`inv_solve`

It calculates the image from an inverse model and data.

The final function

`show_slices`

It is designed to display the image.

“Signal Generation” loop

This loop generates a sine signal with a given “Amplitude”, “Frequency”, “Offset”, and “Phase”, which are set from the UI. Figure K displays the signal generation process loop.

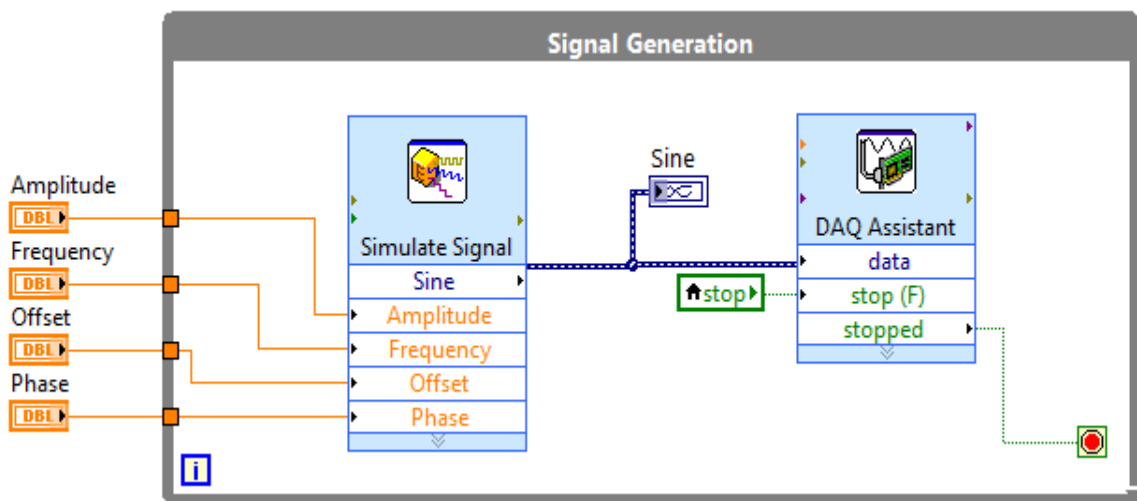
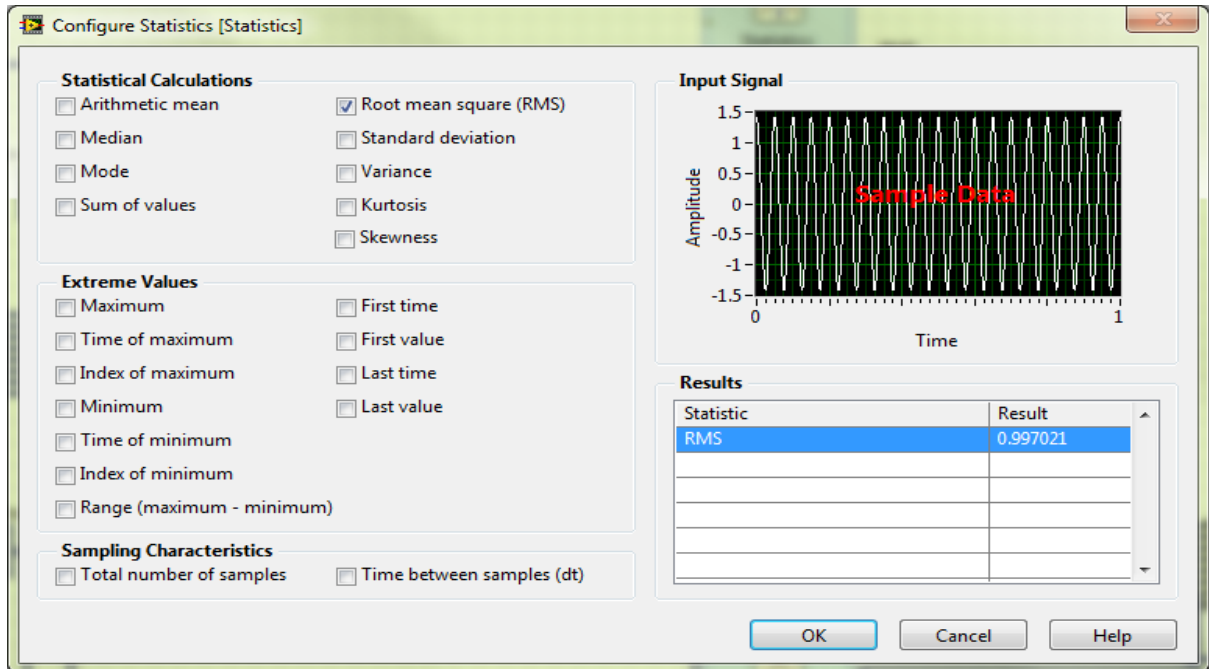


Figure K: “Signal Generation” loop.

Appendix B



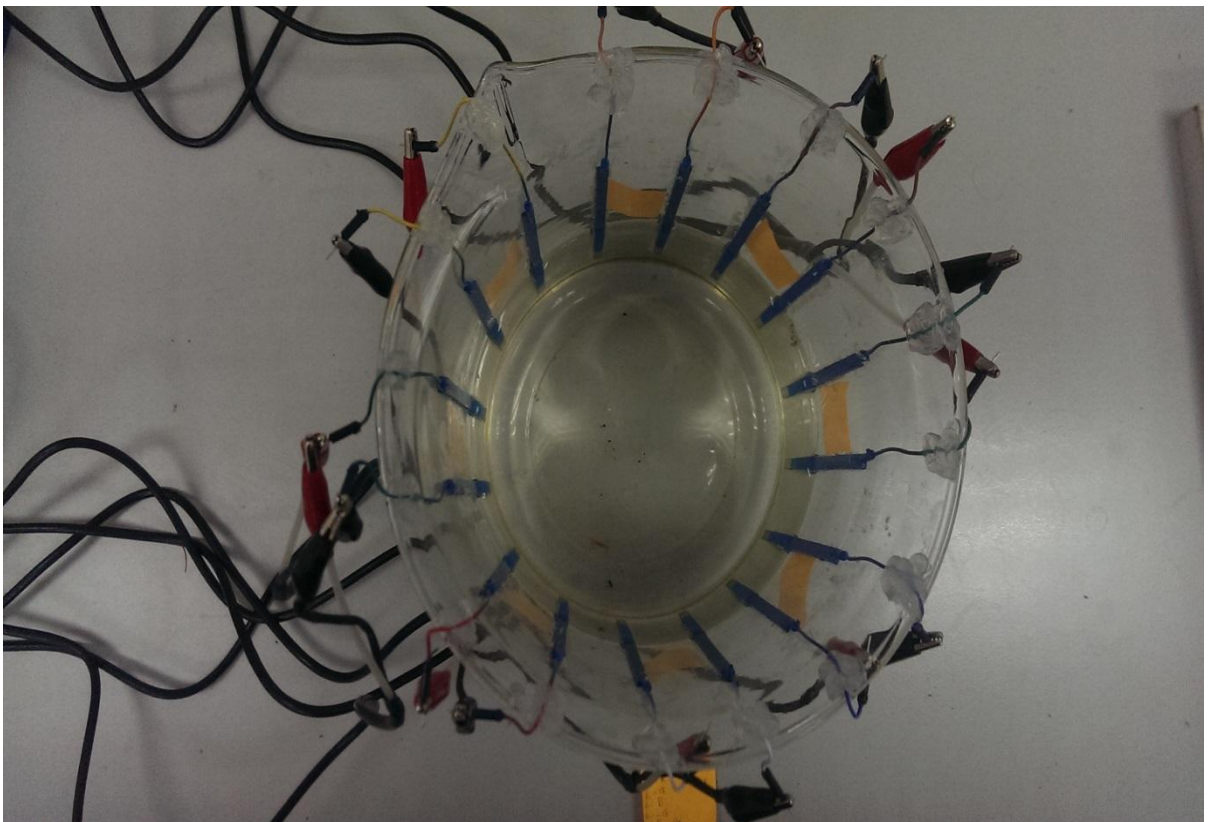
Configuration statistics window.



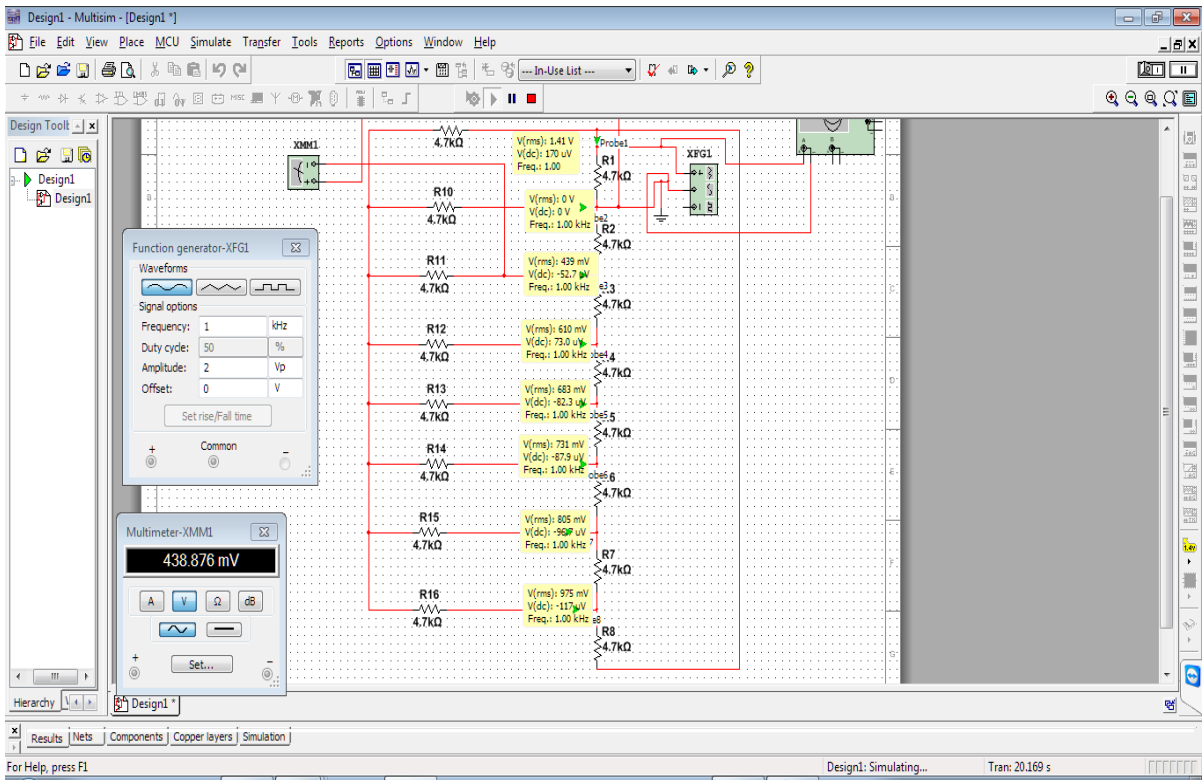
Locating the right position to install the electrodes.



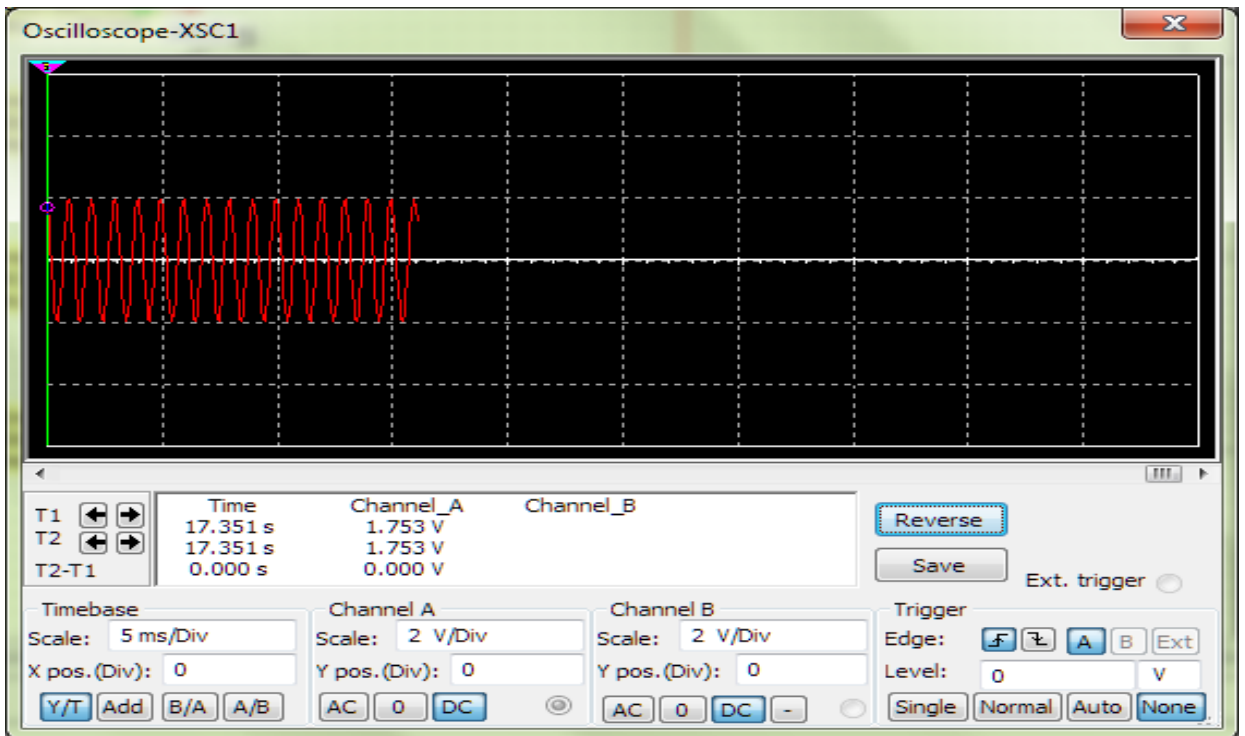
Attaching the copper electrodes to the beaker.



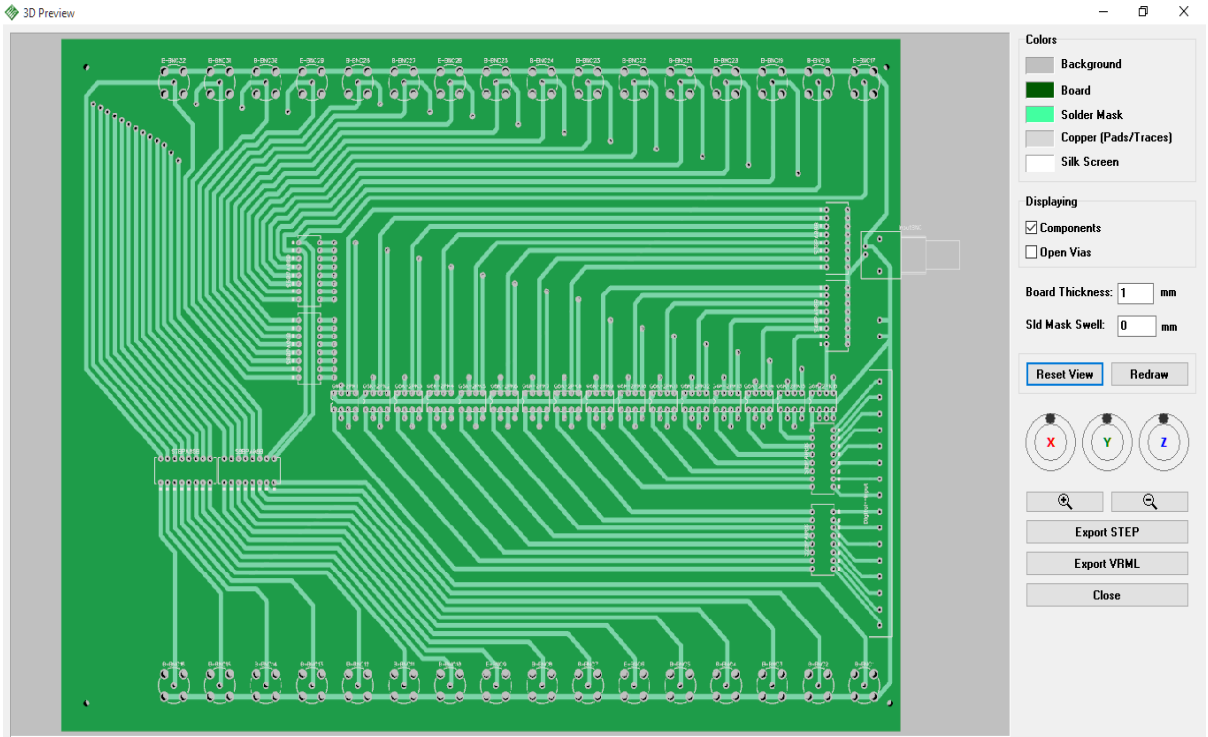
Testing the electrode connectivity after attaching the electrode.



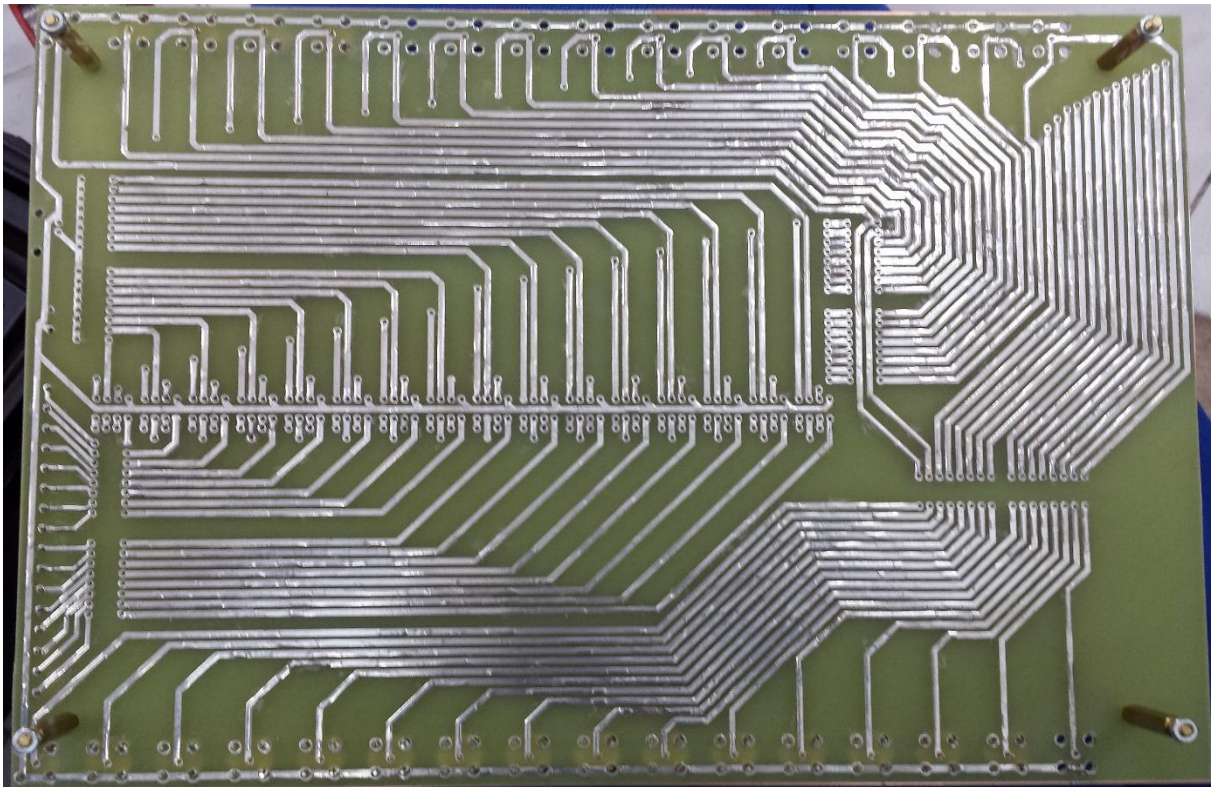
The basic resistors network circuit simulation and calibration test using Multisim Software.



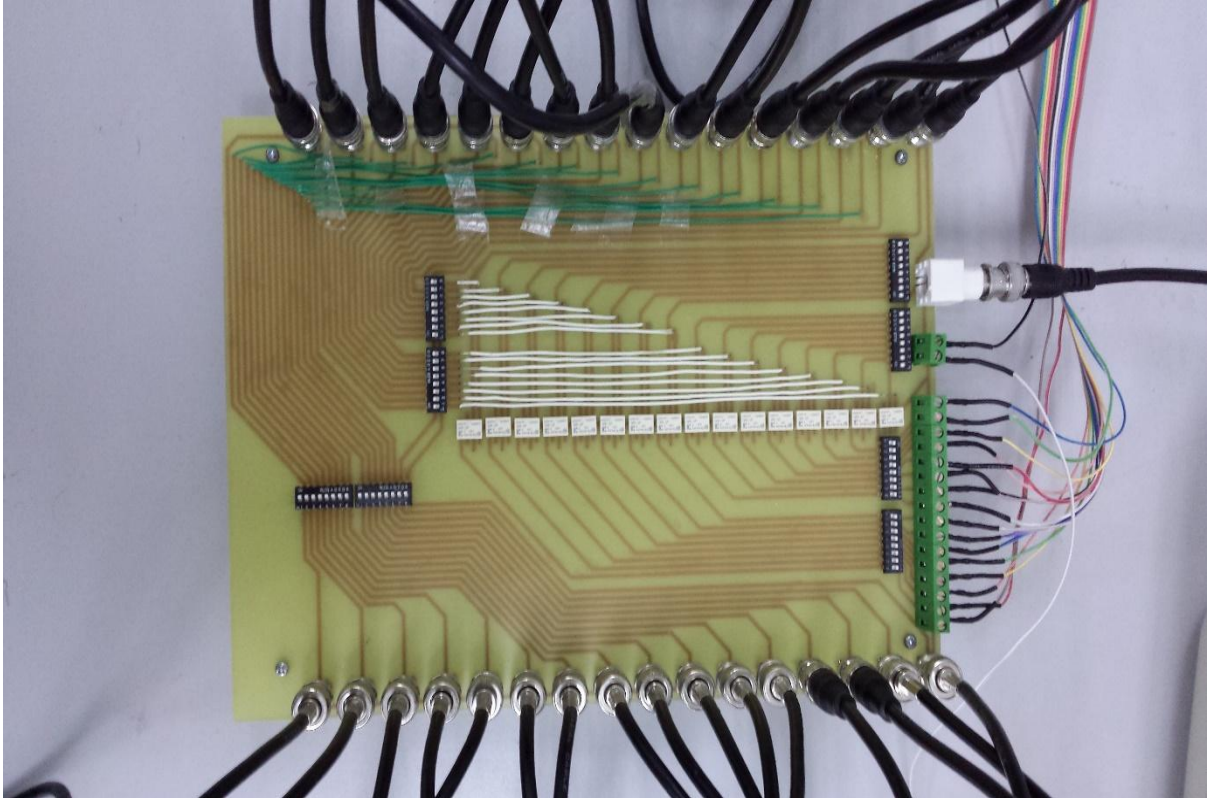
Measurement of the basic resistor's network circuit signals.



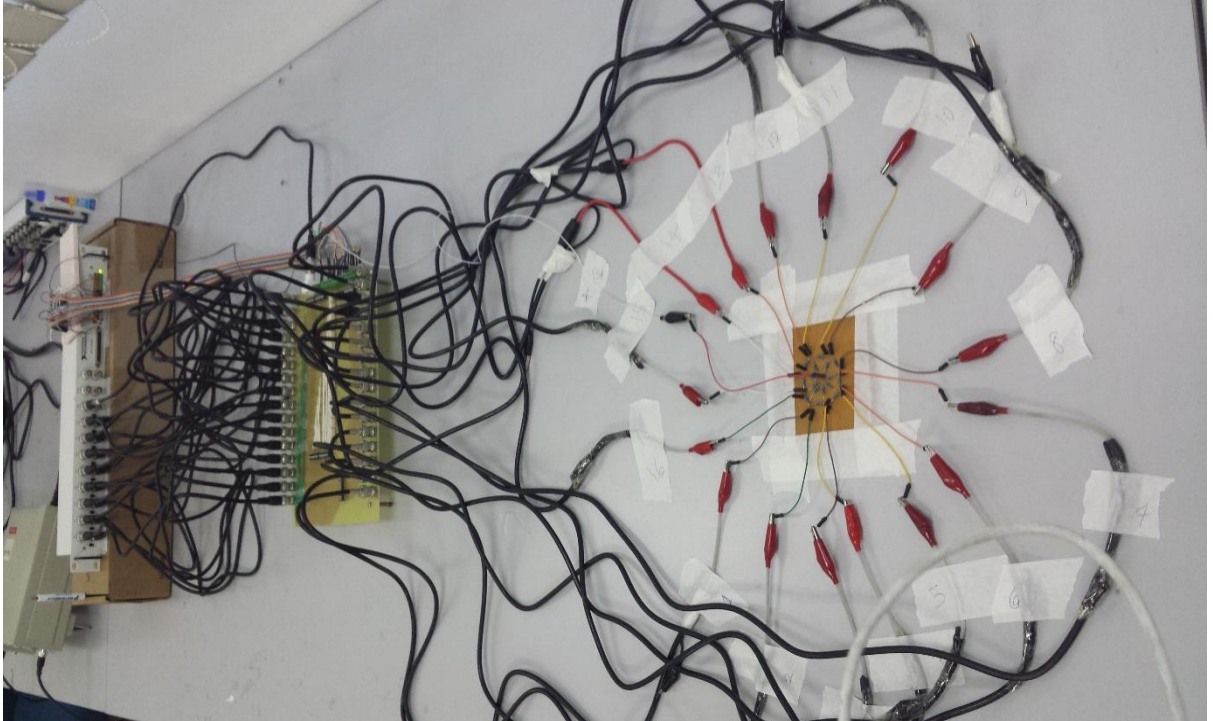
The switching box 3D layout.



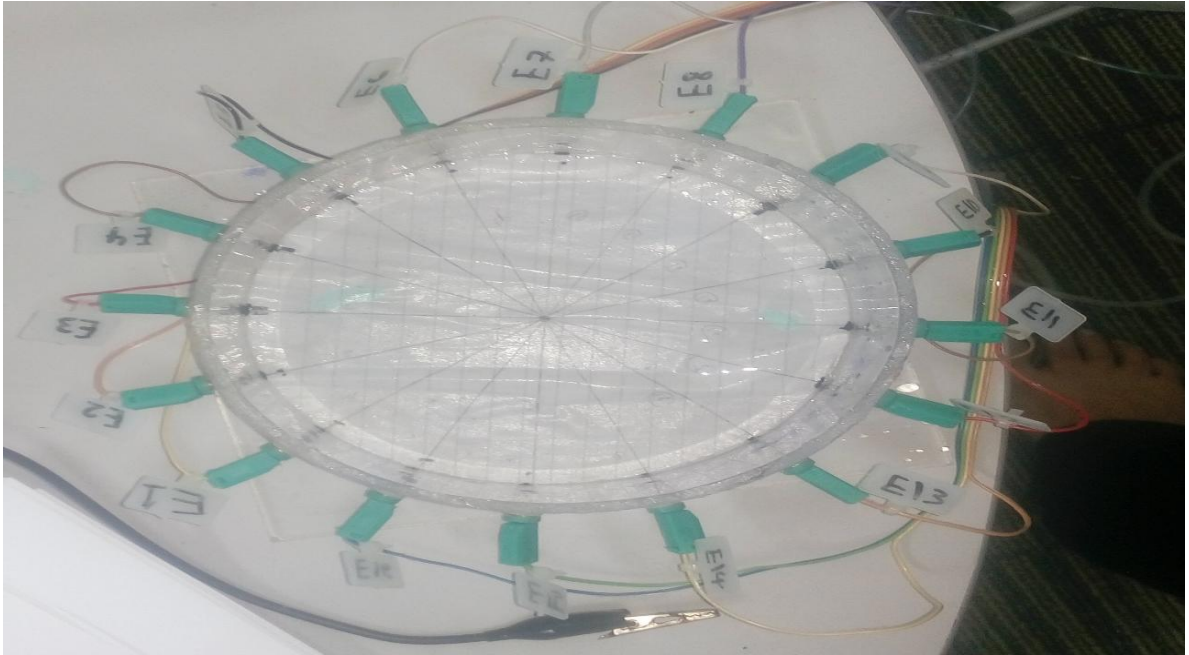
Bottom view of switching box.



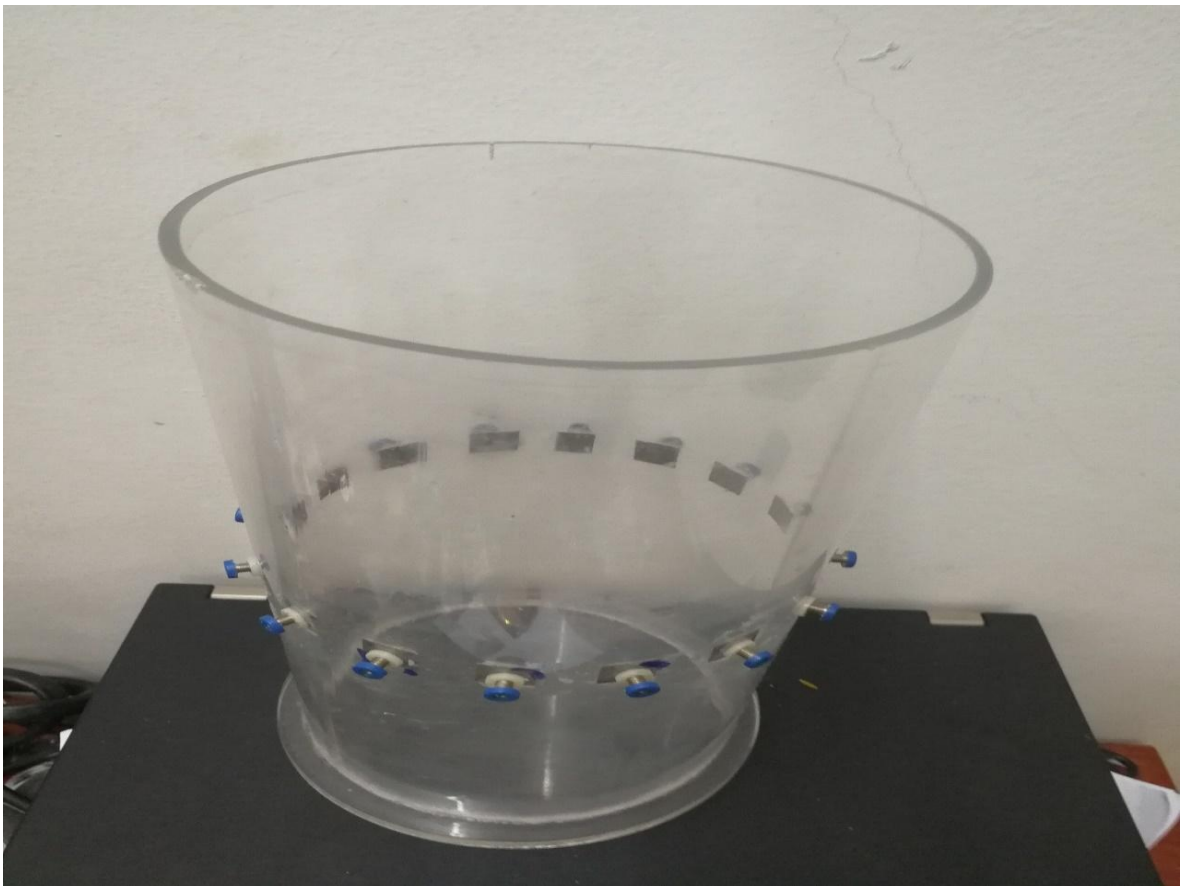
Top view of switching box.



Real resistors network circuit test.



A testing tank which used for chicken tissue test.



A testing tank which used for most of the experiments.